Experimental studies on the performance of low-carbon, high-efficiency heavy-duty dual-fuel combustion engines

A Thesis Submitted for the Degree of Doctor of Philosophy

By

Kevin Pinto da Mota Longo

Department of Mechanical and Aerospace Engineering,

Brunel University London

2025

Abstract

This thesis presents an experimental investigation into dual-fuel combustion strategies aimed at decarbonising heavy-duty engines through the use of low- and zero-carbon gaseous fuels. A single-cylinder research engine and its fuelling system were upgraded for dual-fuel operations with hythane and hydrogen. Systematic experiments were performed at a constant engine speed of 1200 rpm and loads of 0.6, 1.2, and 1.8 MPa IMEP, corresponding to 25%, 50%, and 75% of full engine load. The study explored both conventional and advanced combustion strategies by varying effective compression ratio and diesel injection timing to maximise thermal efficiency and minimise engine-out emissions.

The diesel-hythane dual-fuel system demonstrated strong potential for short-term decarbonisation. An advanced combustion strategy using early diesel injection combined with Miller cycle delivered significant improvements in thermal efficiency by up to 4% at low load and reduced CO_2 emissions by up to 40% relative to conventional diesel combustion. Total GHG emissions were lowered by approximately 25%, and NOx and soot emissions were reduced by as much as 89% and 69%, respectively, compared to diesel-only operation.

The diesel-hydrogen system, while facing limitations in diesel substitution due to combustion phasing constraints, achieved the highest CO_2 and GHG reductions – by up to 56% – when operated with a lower effective compression ratio. Although NOx levels increased under the baseline configuration, mitigation strategies such as external EGR, water injection, and leaner mixtures were shown to effectively reduce NOx without compromising efficiency. Notably, green hydrogen use allowed the diesel-hydrogen powertrain to exceed the EU's 2030 CO_2 reduction target.

A comparative assessment across diesel-CNG, diesel-hythane, and diesel-hydrogen systems confirmed that while methane-based fuels offer substantial NOx reduction, their GHG benefits are limited by methane slip. Hythane emerged as the best short-term solution due to its balance of efficiency and emissions performance, while green hydrogen showed the greatest promise for long-term decarbonisation, provided that NOx control strategies and injection optimisation are fully implemented.

Overall, this research confirms that dual-fuel combustion with hythane and hydrogen – when paired with advanced engine strategies – can significantly lower the carbon and pollutant emissions of heavy-duty diesel engines. The findings provide a solid foundation for the further development of clean, efficient dual-fuel systems aligned with upcoming emissions regulations and climate targets.

List of Contents

Abstract II
Nomenclature VII
List of figures XII
List of tables XVII
List of publications related to this research XVIII
Acknowledgements XIX
Chapter 1 Introduction 1
1.1 Preface 1
1.2 Research objectives 2
1.3 Thesis outline 3
Chapter 2 Literature Review 4
2.1 Introduction 4
2.2 Emission and fuel efficiency regulations 9
2.3 Heavy-duty diesel engine emissions 12
2.4 Heavy-duty diesel engine emissions control technologies 15
2.4.1 Alternative combustion strategies 16
2.4.2 Boosting technology 18
2.4.3 Exhaust gas recirculation 19
2.4.4 Miller cycle 21
2.4.5 Water injection 23
2.4.6 Aftertreatment technologies 23
2.5 Dual-fuel combustion 26
2.5.1 Low- and zero-carbon fuels 28
2.5.2 Potential and limitations of the dual-fuel combustion 29
2.6 Summary 36
Chapter 3 Experimental methodology 37
3.1 Introduction 37
3.2 Experimental setup 37
3.2.1 Engine specifications 39
3.2.2 Variable valve actuation system 39
3.2.3 Dynamometer 41
3.2.4 Intake and exhaust systems 41

3.2.5 Fuel systems and proprieties 42
3.2.6 Exhaust emissions measurement 47
3.2.7 Data acquisition and control 49
3.3 Data analysis 51
3.3.1 Heat release rate 52
3.3.2 Overall engine parameters 54
3.3.3 Mean in-cylinder gas temperature 56
3.3.4 Engine-out exhaust emissions 57
3.3.5 Combustion stoichiometry 62
3.4 Engine testing 64
3.5 Summary 65
Chapter 4 Characterisation of diesel-hythane dual-fuel combustion 66
4.1 Introduction 66
4.2 Evaluation of the optimum diesel injection strategy 67
4.2.1 Experimental test procedure 67
4.2.2 Overview of the dual-fuel operation and combustion characteristics 70
4.2.3 Engine performance 73
4.2.4 Engine-out emissions 75
4.2.5 GHG emissions estimation 80
4.2.6 NOx emissions mitigation and additional practical considerations 82
4.3 The combination of internal EGR and external EGR at low engine load 87
4.3.1 Experimental test procedure 87
4.3.2 Engine modelling 89
4.3.3 Validation of the 1D engine model 92
4.3.4 Overview of the iEGR and combustion characteristics 93
4.3.5 Engine performance 96
4.3.6 Engine-out emissions 98
4.4 The effect of external EGR at medium and high engine loads 100
4.4.1 Experimental test procedure 100
4.4.2 Overview of the eEGR and combustion characteristics 101
4.4.3 Engine-out emissions and performance 104
4.5 Overview of optimal dual-fuel engine operation 107
4.5.1 Maximisation of hythane energy fraction 107
4.5.2 Maximisation of GHG reduction potential 108
4.5.3 Well-to-Wheel analysis 109
4.5.4 Summary matrix of strategies for optimal engine efficiency and emissions 112
4.6 Summary 113

Chapter 5 Characterisation of diesel-hydrogen dual-fuel combustion 116
5.1 Introduction 116
5.2 Evaluation of effective compression ratio 117
5.2.1 Experimental test procedure 117
5.2.2 Overview of the dual-fuel operation and combustion characteristics 119
5.2.3 Engine performance 123
5.2.4 Engine-out emissions 125
5.3 The exploration of hydrogen energy fraction 128
5.3.1 Experimental test procedure 128
5.3.2 Overview of the dual-fuel operation and combustion characteristics 129
5.3.3 Engine performance 133
5.3.4 Engine-out emissions 136
5.3.5 GHG emissions estimation 138
5.4 The effect of relative air-fuel ratio 141
5.4.1 Experimental test procedure 141
5.4.2 Overview of the dual-fuel operation and combustion characteristics 142
5.4.3 Engine-out emissions and performance 145
5.4.4 Enhancement of H2EF at high engine load 150
5.5 The employment of external EGR at low and medium engine loads 153
5.5.1 Experimental test procedure 153
5.5.2 Operation overview and combustion characteristics 154
5.5.3 Engine-out emissions and performance 156
5.6 The impact of water injection at high engine load 159
5.6.1 Experimental test procedure 159
5.6.2 Overview of the dual-fuel operation 160
5.7 Overview of optimal dual-fuel engine operation 164
5.7.1 Maximisation of hydrogen energy fraction 164
5.7.2 Maximisation of GHG reduction potential 165
5.7.3 Well-to-Wheel analysis 167
5.7.4 Advanced dual-fuel optimisation for NOx reduction 169
5.8 Summary 172
Chapter 6 Multi-fuel comparison in dual-fuel operation from low to high engine load 176
Chapter 7 Conclusions and future work 191
7.1 Conclusions 191
7.1.1 Diesel-hythane dual-fuel combustion 191
7.1.2 Diesel-hydrogen dual-fuel combustion 192
7.1.3 Multi-fuel comparison in dual-fuel operation 194

7.2 Recommendations for future work 195
Appendix A – Diesel fuel specifications 196
Appendix B – Hythane fuel specifications 198
Appendix C – Hydrogen fuel specifications 199
Appendix D – Measurement device specification 201
List of references 203

Nomenclature

1D: one-dimensional
2EVO: exhaust valve re-opening
2IVO: intake valve re-opening
$T_{cyl,i}$: mean in-cylinder gas temperature
ADF: advanced dual-fuel combustion
AFR_{stoich}: stoichiometric air-fuel ratio
ATDC: after top dead centre
ATS: aftertreatment system
BDC: bottom dead centre
BOC: British Oxygen Company
CA10: crank angle of 10% cumulative heat release
CA10-CA90: combustion duration
CA50: combustion phasing or crank angle of 50% cumulative heat release
CA90: crank angle of 90% cumulative heat release
CAD: crank angle degree
CBM: compressed biomethane
CCS: carbon capture and storage
CDC: conventional diesel combustion
CDF: conventional dual-fuel combustion
CE: combustion efficiency
CI: compression ignition
CNG: compressed natural gas
CO: carbon monoxide
CO_2: carbon dioxide
CO_{2eq}: carbon dioxide equivalent
$CO_{2_{intake}}$: concentration of CO_2 in the intake manifold
$CO_{2_{exhaust}}$: concentration of CO_2 in the exhaust manifold
COP: Conference of the Parties
COV_{IMEP}: coefficient of variation of IMEP
DAQ: data acquisition
DEF: diesel exhaust fluid
DF: dual-fuel
DOC: diesel oxidation catalyst
DPF: diesel particulate filter
ECE: Engine Control Electronics GmbH
ECR: effective compression ratio
ECU: engine control unit
EER: effective expansion ratio
EF: energy fraction
eEGR: external exhaust gas recirculation
EGR: exhaust gas recirculation
EGT: exhaust gas temperature
EIVC: early intake valve closing
EU: European Union
EVC: exhaust valve closing
EVO: exhaust valve opening
FGT: fixed geometry turbocharger
FID: flame ionisation detector
FSN: filter smoke number
GDCI: gasoline direct injection compression ignition
GHG: greenhouse gas
GCP: Glasgow Climate Pact
GWP: global warming potential
H_2O: water

H_a: intake air humidity
HC: hydrocarbons
HCCI: homogeneous charge compression ignition
HCLD: heated chemiluminescence
HD: heavy-duty
HDV: heavy-duty vehicle
HEF: hythane energy fraction
H2EF: hydrogen energy fraction
ICCT: International Council on Clean Transportation
ICE: internal combustion engine
iEGR: internal exhaust gas recirculation
IMEP: net indicated mean effective pressure
$IMEP_{gross}$: gross indicated mean effective pressure
IPCC: intergovernmental panel on climate change
$ISCH_4$: net indicated specific emissions of methane
ISCO: net indicated specific emissions of carbon monoxide
$ISCO_2$: net indicated specific emissions of carbon dioxide
$ISFC_{eq}$: net indicated specific fuel consumption equivalent
ISH_2: net indicated specific emissions of unburned hydrogen
ISN_2O: net indicated specific emissions of nitrous oxides
ISNMHC: net indicated specific emissions of non-methane hydrocarbons
ISNOx: net indicated specific emissions of nitrogen oxides
ISsoot: net indicated specific emissions of soot
ISTHC: net indicated specific emissions of total unburned hydrocarbons
ITE: net indicated thermal efficiency
IVC: intake valve closing
IVO: intake valve opening
k_f: fuel specific factor of wet exhaust
k_h: humidity correction factor for nitrogen oxides
k_w: dry/wet correction factor for the raw exhaust gas
LNG: liquified natural gas
LPG: liquified petroleum gas
LTC: low temperature combustion
LHV: lower heating value
LHV_{CO}: lower heating value of carbon monoxide
LHV_{DF}: lower heating value of the in-cylinder fuel mixture
LHV_{diesel}: lower heating value of diesel
$LHV_{hydrogen}$: lower heating value of hydrogen
$LHV_{hythane}$: lower heating value of hythane
$\dot{m}_{air}$: mass flow rate of fresh air
$\dot{m}_{diesel}$: mass flow rate of diesel
$\dot{m}_{dry\ air}$: mass flow rate of dry air
$\dot{m}_{exh}$: mass flow rate of exhaust gas
$\dot{m}_{gas\ fuel}$: mass flow rate of hydrogen / hythane

$\dot{m}_{hydrogen}$: mass flow rate of hydrogen

$\dot{m}_{hythane}$: mass flow rate of hythane

$\dot{m}_{humidity}$: mass flow rate of humidity

$\dot{m}_{H2O}$: mass flow rate of water

$\dot{m}_{CH4}$: mass flow rate of methane

$\dot{m}_{CO}$: mass flow rate of carbon monoxide

$\dot{m}_{CO2}$: mass flow rate of carbon dioxide

$\dot{m}_{NOx}$: mass flow rate of nitrogen oxides

$\dot{m}_{soot}$: mass flow rate of soot

$\dot{m}_{THC}$: mass flow rate of total unburned hydrocarbons

$\dot{m}_{\mathrm{UH2}}$: flow rate of unburned hydrogen

m_{air}: mass of intake fresh air per cycle

m_{fuel}: mass of fuel injected per cycle

m_{rg}: mass of residual gas trapped at exhaust valve closing

m_{RP}: mass (burned and unburned) per mole of O_2 in the mixture

m_{total}: total in-cylinder mass per cycle

M_b: molecular weight of the burned gas

$M_{dry\ air}$: molar mass of dry air

$M_{\mathrm{H_2O}}$: molar mass of water

M_{N_2}: molar mass of nitrogen

M_{O_2}: molar mass of oxygen

MF: mass fraction

MFB: mass fraction burned

MK: modulated kinetics

MOC: methane oxidation catalyst

MPA: magneto-pneumatic detector

M2: passenger vehicles

M3: larger passenger vehicles, buses and coaches

n_b: number of moles of burned gas

N_2: nitrogen

N_2O: nitrous oxide

NG: natural gas

NDIR: non-dispersive infrared detector

NH_3: ammonia

NMHC: non-methane hydrocarbons

NO: nitrogen monoxide

NO_2: nitrogen dioxide

NOx: nitrogen oxides

NZE: net-zero emissions

N2: medium goods vehicles

N3: heavy goods vehicles

O_2: oxygen

O_3: ozone

p: pressure

p_{amb}: ambient air pressure

p_{EVC}: in-cylinder gas pressure at exhaust valve closing

p_{vapour}: partial pressure of water vapour in the air

p_{sat}: saturation pressure of water vapour

P_{ind}: net indicated power

PCCI: premixed charge compression ignition

PFI: port fuel injection

PI: positive ignition

PLC: programmable logic controller

PMEP: pumping mean effective pressure

PPC: partially premixed combustion

PPCI: partially premixed charge compression ignition

ppm: parts per million

PRR: pressure rise rate
$\mathrm{Q_{ch}}$: chemical energy release
$\mathrm{Q_{ht}}$: heat transfer
Q_{net}: net heat release
$\widetilde{\mathrm{R}}$: universal gas constant
RCCI: reactivity-controlled compression ignition
REF: trigger signal
RGF: residual gas fraction
RH: relative humidity
SCR: selective catalytic reduction
SOC: start of combustion
SOI: start of injection
SOI_1: start of first diesel injection or pre-injection
SOI_2: start of second diesel injection or main injection
SMR: steam methane reforming
STP: standard temperature and pressure
T_{amb}: ambient temperature
TDC: top dead centre
THC: total unburned hydrocarbons
TTW: Tank-to-Wheel
u_{CH4}: methane to exhaust gas density ratio
u_{CO}: carbon monoxide to exhaust gas density ratio
u_{CO2}: carbon dioxide to exhaust gas density ratio
u_{gas}: exhaust gas density ratio
$\mathrm{u}_{gas,\ DF}$: exhaust gas density ratio for the dual-fuel combustion
u_{HC}: hydrocarbon to exhaust gas density ratio
u_{NOx}: nitrogen oxides to exhaust gas density ratio
u_{soot}: soot to exhaust gas density ratio
UNFCCC: United Nations Framework Convention on Climate Change
UNIBUS: uniform bulky combustion system
US: United States of America
VGT: variable geometry turbocharger
VVA: variable valve actuation
v/v: volume basis
V: volume
$\mathrm{V_c}$: clearance volume
$\mathrm{V_d}$: displaced volume
V_{EVC}: in-cylinder volume at exhaust valve closing
$\mathrm{W_{c,ind}}$: net indicated work per cycle
WHSC: World Harmonised Stationary Cycle
WHTC: World Harmonised Transient Cycle
WTW: Well-to-Wheel
WTT: Well-to-Tank
ZEV: zero-emission vehicle
x: molar carbon to carbon ratio
y: molar hydrogen to carbon ratio
z: molar oxygen to carbon ratio
[CH_4]: concentration of unburned methane in the exhaust gas
[CO]: concentration of carbon monoxide in the exhaust gas

[CO_2]: concentration of carbon dioxide in the exhaust gas

[H_2]: concentration of unburned hydrogen in the exhaust gas

[NOx]: concentration of nitrogen oxides in the exhaust gas

[soot]: concentration of soot in the exhaust gas

[THC]: concentration of total unburned hydrocarbons in the exhaust gas

γ: ratio of specific heats (c_p/c_v)

θ: crank angle position

λ: relative air-fuel ratio

ρ_{exh}: exhaust gas density

List of figures

Figure 2.1 – Global energy demand by sector and source. Adapted from [4]. 4
Figure 2.2 – Fuel demand by transportation sector. Adapted from [5]..... 5
Figure 2.3 – Atmospheric carbon dioxide concentration in parts per million for the past 800,000 years based on ice-core data (light purple line) compared to 2023 concentration (bright purple dot). Adapted from [7]. 6
Figure 2.4 – Carbon dioxide emissions from fossil fuels and land-use change. Adapted from [8] 6
Figure 2.5 – GHG emissions from economic sectors in 2022. Adapted from [15] 8
Figure 2.6 – Global Well-to-Wheel CO_2 emissions from road transport compared to a 1.5°C and 2°C compatible emissions pathways. Source: [18]..... 8
Figure 2.7 – Development of European HD legislated emissions limits for NOx and PM. Source [27] 10
Figure 2.8 – Evolution of heavy-duty emissions standards in the EU. Source: [27] . 12
Figure 2.9 – The composition of diesel exhaust gas. Source: [36]. 13
Figure 2.10 – Typical particular matter emissions composition from a heavy-duty diesel engine. Source: [45]. 14
Figure 2.11. Local equivalence ratio versus temperature map for the classification of combustion strategies. Adapted from [58]. 17
Figure 2.12 – Impact of intake oxygen concentration on NOx reduction. Source: [65] 20
Figure 2.13 – Aftertreatment system configuration of a modern HD diesel engine. Adapted from [65]. 24
Figure 2.14 – Diesel oxidation catalyst. Source: [36]..... 24
Figure 2.15. Use of diesel and gas fuels in a CI engine under dual-fuel technology. Adapted from [112]. 27
Figure 2.16. Progression of the combustion process of the hydrogen-fuelled diesel engine near TDC. Adapted from [113]..... 27
Figure 3.1 – Schematic diagram of the engine experimental setup. 38
Figure 3.2 – Overview of the engine test bench. 38
Figure 3.3 – Lost-motion intake VVA system with collapsing tappet on the valve side of the rocker arm [157]. 40

Figure 3.4 – Overview of variable intake valve lift and fixed exhaust valve lift curves. 40
Figure 3.5 – Water injection system. 42
Figure 3.6 – Diesel fuel injection system. 44
Figure 3.7 – Hythane fuel injection system. 45
Figure 3.8 – Hydrogen fuel injection system. 47
Figure 3.9 – DAQ transient combustion analyser software. 50
Figure 3.10 – Molar H/C and O/C ratios for the in-cylinder fuel mixture as a function of the hythane MF 63
Figure 3.11 – Molar H/C and O/C ratios for the in-cylinder fuel mixture as a function of the hydrogen MF. 63
Figure 3.12 - The selected test points and the WHSC [21] test cycle points over the experimental HD engine speed-load map. 65
Figure 4.1. The effect of combustion mode on combustion characteristics and stability. 72
Figure 4.2. The effect of combustion mode on in-cylinder pressure, mean in-cylinder gas temperature, HRR and diesel injection at: (a) low engine load, (b) medium engine load, and (c) high engine load. 73
Figure 4.3. The effect of combustion mode on engine performance. 75
Figure 4.4. The effect of combustion mode on engine-out emissions. 76
Figure 4.5. The effect of combustion mode on combined GHG emissions. 81
Figure 4.6. Estimated ISNOx levels for different SCR conversion efficiencies. 83
Figure 4.7. Diesel SOI as a NOx generation control at low engine load. 84
Figure 4.8. Difference between baseline ITE and SCR corrected ITE. 85
Figure 4.9. Total fluid consumption for CDC, CDF and ADF operations. 86
Figure 4.10. 1D model of the single cylinder HD engine 89
Figure 4.11. Multi-Wiebe fitting tool panel 91
Figure 4.12. Validation of intake mass flow rate for multiple cases applying iEGR. . 92
Figure 4.13. Experimental and numerical log P-V diagram of Case Miller + iEGR. .. 92
Figure 4.14. The effect of iEGR on in-cylinder pressure, mean in-cylinder gas temperature and HRR for constant diesel injection. 93
Figure 4.15. The effect of iEGR on combustion characteristics at low engine load. . 94
Figure 4.16. In-cylinder gas temperatures and RGF for the three dual-fuel cases obtained from the 1D engine model. 95

Figure 4.17. The effect of iEGR on engine performance at low engine load. 97
Figure 4.18. The effect of iEGR on engine-out emissions at low engine load. 99
Figure 4.19. The effect of eEGR on in-cylinder pressure and HRR for constant diesel injection at medium engine load. 102
Figure 4.20. The effect of eEGR on in-cylinder pressure and HRR for constant diesel injection at high engine load. 102
Figure 4.21. The effect of eEGR on combustion parameters at medium and high engine loads. 103
Figure 4.22. The effect of eEGR on engine performance at medium and high engine loads. 105
Figure 4.23. The effect of eEGR on engine-out emissions at medium and high engine loads. 106
Figure 4.24. Comparison of dual-fuel strategies for HEF maximisation across low, medium and high engine loads. 108
Figure 4.25. Comparison of dual-fuel strategies for maximum GHG emissions reduction across low, medium and high engine loads. 109
Figure 4.26. Theoretical TTW and WTW CO2eq emissions for CDC and ADF modes, simulating different hythane production sources. 111
Figure 5.1. The effect of ECR on in-cylinder pressure and HRR for constant diesel injection at low engine load. 121
Figure 5.2. The effect of ECR on in-cylinder pressure and HRR for constant diesel injection at medium engine load. 122
Figure 5.3. The effect of ECR on in-cylinder pressure and HRR for constant diesel injection at high engine load. 122
Figure 5.4. The effect of ECR on combustion characteristics and stability. 123
Figure 5.5. The effect of ECR on engine performance. 124
Figure 5.6. The effect of ECR on hydrogen slip in the exhaust line. 125
Figure 5.7. The effect of ECR on engine-out emissions. 127
Figure 5.8. The effect of H2EF on in-cylinder pressure and HRR for constant diesel injection at low engine load. 130
Figure 5.9. The effect of H2EF on in-cylinder pressure and HRR for constant diesel injection at medium engine load. 131
Figure 5.10. The effect of H2EF on in-cylinder pressure and HRR for constant diesel injection at high engine load. 131

Figure 5.11. The effect of H2EF on combustion characteristics and stability. 132
Figure 5.12. The effect of H2EF on hydrogen slip in the exhaust line and crankcase. 134
Figure 5.13. The effect of H2EF on engine performance. 135
Figure 5.14. The effect of H2EF on engine-out emissions. 137
Figure 5.15. The effect of H2EF on combined GHG emissions. 140
Figure 5.16. The effect of relative air-fuel ratio on in-cylinder pressure and HRR for constant diesel injection at low engine load. 143
Figure 5.17. The effect of relative air-fuel ratio on in-cylinder pressure and HRR for constant diesel injection at medium engine load. 144
Figure 5.18. The effect of relative air-fuel ratio on in-cylinder pressure and HRR for constant diesel injection at high engine load. 144
Figure 5.19. The effect of relative air-fuel ratio on combustion characteristics and stability. 145
Figure 5.20. The effect of relative air-fuel ratio on engine performance. 147
Figure 5.21. The effect of relative air-fuel ratio on engine-out emissions. 149
Figure 5.22. The effect of increased H2EF at leaner mixture on engine performance and combustion stability. 151
Figure 5.23. The effect of increased H2EF at leaner mixture on exhaust emissions. 152
Figure 5.24. The impact of the H2EF enhancement with highest relative air-fuel ratio on combined GHG emissions at high engine load. 152
Figure 5.25. The effect of external EGR on in-cylinder pressure and HRR for constant diesel injection at low engine load. 155
Figure 5.26. The effect of external EGR on in-cylinder pressure and HRR for constant diesel injection at medium engine load..... 155
Figure 5.27. The effect of external EGR on combustion characteristics and stability. 156
Figure 5.28. The effect of external EGR on engine performance. 157
Figure 5.29. The effect of external EGR on engine-out emissions. 158
Figure 5.30. The impact of water injection on in-cylinder pressure and heat release rate for constant diesel injection timing at high engine load. 161
Figure 5.31. The impact of water injection on combustion characteristics and stability. 162

Figure 5.32. The impact of water injection on exhaust emissions. 163
Figure 5.33. Comparison of dual-fuel strategies for H2EF maximisation across low, medium and high engine loads. 165
Figure 5.34. Comparison of dual-fuel modes in terms of maximum GHG emissions reduction across low, medium and high engine loads, relative to CDC, with identification of the most effective strategy for each case. 166
Figure 5.35. Theoretical TTW and WTW CO_{2eq} emissions for CDC and ADF modes, simulating different hydrogen production pathways. 168
Figure 5.36. Relative changes in NOx emissions (bottom graph) and ITE (top graph) for each NOx control strategy tested compared to the ADF baseline. 170
Figure 5.37. Comparison of NOx emissions between the ADF baseline and ADF optimised relative to CDC, and identification of the most effective ADF optimised strategy for NOx mitigation. 171
Figure 6.1. Maximum achievable energy fraction for each dual-fuel system at different engine loads. 177
Figure 6.2. Indicated thermal efficiency of the combustion systems (diesel-only, diesel-CNG, diesel-hythane, and diesel-hydrogen) at low (top), medium (middle), and high (bottom) engine loads 180
Figure 6.3. Comparison of indicated specific CO_2 and total GHG emissions for the combustion systems (diesel-only, diesel-CNG, diesel-hythane, and diesel-hydrogen) at low (top), medium (middle), and high (bottom) engine loads. 183
Figure 6.4. Well-to-Wheel assessment involving diesel and multiple alternative fuel production pathways from fossil sources. 186
Figure 6.5. Well-to-Wheel assessment involving diesel and multiple alternative fuel production pathways from renewable sources. 186
Figure 6.6. Indicated specific NOx emissions of the combustion systems at low (top), medium (middle), and high (bottom) engine loads. 188

List of tables

Table 2.1 – Euro VI for Type 2B HD DF engines [21, 25] and Euro 7 tailpipe emission limits for HDV of categories M2, M3, N2, and N3 [26]. 11
Table 3.1 – Specification of the research engine. 39
Table 3.2 – Fuel proprieties. 43
Table 3.3 – Specifications of diesel injector. 44
Table 3.4 – Raw exhaust gas for diesel, hythane and hydrogen [21, 162]. 58
Table 3.5 – Constant values for calculation of saturation pressure of water vapour [163]. 60
Table 4.1. Engine operating conditions for optimum diesel injection experiment. 67
Table 4.2. Diesel injection strategies for different combustion modes. 68
Table 4.3. Engine operating conditions for the iEGR evaluation. 88
Table 4.4. The testing modes matrix. 88
Table 4.5. Engine operating conditions for the investigation of eEGR. 100
Table 4.6. Matrix representative of optimal strategy for efficiency and emissions. . 112
Table 5.1. Engine operating conditions for the ECR sweep. 117
Table 5.2. Diesel injection strategy employed for conventional diesel and both dual-fuel combustions. 118
Table 5.3. Engine operating conditions for the energy fraction sweep. 128
Table 5.4. Engine operating conditions for the relative air-fuel ratio sweep. 142
Table 5.5. Engine operating conditions for the eEGR sweep. 153
Table 5.6. Engine operating conditions for the water injection sweep. 159
Table 5.7. Estimated Well-to-Tank CO_{2eq} emissions for diesel and various hydrogen production pathways. 167
Table 6.1. Engine operating conditions for the different dual-fuel systems. 178
Table 6.2. Estimated Well-to-Tank CO_{2eq} emissions for diesel and multiple alternative low-carbon fuel production pathways. 184

List of publications related to this research

[1] K. Longo, X. Wang and H. Zhao, “Impact of diesel-hythane dual-fuel combustion on engine performance and emissions in a heavy-duty engine at low-load condition,” International Journal of Engine Research, vol. 25, no. 2, 2023.

[2] K. Longo, X. Wang and H. Zhao, “Comparison of conventional vs reactivity-controlled compression ignition diesel-hythane dual-fuel combustion: An investigation on engine performance and emissions at low-load,” SAE Technical Paper 2023-01-1203, 2023.

[3] K. Longo, X. Wang and H. Zhao, “Advanced diesel-hythane combustion for maximum reduction in CO2 and GHG emissions,” Powetrain Systems for a Sustainable Future, https://www.taylorfrancis.com/chapters/edit/10.1201/9781032687568-5/advanced-diesel-hythane-combustion-maximum-reduction-co2-ghg-emissions-longo-wang-zhao, 2023.

Acknowledgements

The conclusion of this thesis marks the end of my journey at Brunel University of London – and in the United Kingdom. It has been 5.5 years of an incredibly exciting and challenging experience, beginning with an MSc and extending into this PhD. I never imagined myself living in London, but now, as this chapter closes, I find myself already missing this amazing city.

I would like to begin by expressing my deepest gratitude to my main supervisor, Professor Hua Zhao, for the unique opportunity provided to conduct research in a field I am truly passionate about, and for the unwavering support provided throughout these years. I am equally thankful to Professor Xinyan Wang, my second supervisor, for all the guidance, advice, and valuable lessons since day one – lessons I will carry with me for life. Thank you for your friendship and mentorship. I must also acknowledge how grateful I am for the flexibility and support of my supervisory team, which made it possible for me to continue pursuing my motorsport career alongside my full-time PhD studies. Your trust meant everything.

Several other individuals at Brunel played key roles in this journey. My heartfelt thanks to Andy, my technician, for his dedicated support in my test cell over the years. Despite his busy schedule, he always found time to help. I will miss our chats about Formula One and rollercoasters. I would also like to thank Eamon, as well as my colleagues Raghul, Mohamed, and Alex for their help and companionship throughout the project.

A special mention goes to João Ribeiro, whom I met at Brunel and who became a true friend during my time in London. Thank you for all the chats, lunch breaks, and football matches we watched together – I will truly miss it.

Finally, I extend my deepest and sincerest thanks to the most important people in my life: my parents, Lucília and Jorge, and my brother, Micael, for their unconditional love, support, and belief in my dreams. You have taught me the value of persistence and never giving up. To my childhood friends - Areias, Gualter, and Wilson – thank you for your unwavering friendship, no matter the distance.

Chapter 1
Introduction

1.1 Preface

Internal combustion engines (ICE), which originated in the 19th century [1] have become one of the most efficient and dependable sources of power generation globally. With advancements in technology and increasing environmental regulations on energy consumption, there has been significant progress in understanding engine processes and fuel properties. The global rise in concerns about air pollution, increasing carbon dioxide (CO_2) emissions, and their impact on human health and climate has led to the implementation of fuel efficiency and exhaust emission standards for the transportation sector. These regulations have driven extensive research and development efforts aimed at producing cleaner, more efficient ICEs and fuels.

Innovations such as the use of alternative fuels and improved aftertreatment systems (ATS) have played a key role in enhancing fuel conversion efficiency and reducing pollutants. By combining low-carbon fuels with high-efficiency ICE, it is possible to decrease human-induced greenhouse gas emissions, which contribute to global warming.

Heavy-duty vehicles, which typically use compression ignition (CI) diesel engines, are major contributors to global CO_2 emissions from the transport sector. However, to meet recent stringent carbon reduction targets, replacing a portion of diesel with lower or zero-carbon fuels such as methane or hydrogen can help reduce the greenhouse gas (GHG) emissions intensity of these vehicles in the short term [2, 3].

Most dual-fuel engines operate on the principle of using a high-reactivity fuel, such as diesel, with direct injection, alongside a low-reactivity fuel like gasoline, natural gas, methanol, or hydrogen, which is injected through port fuel injection. The energy substitution of each fuel used in the engine depends on the operating conditions.

Dual-fuel engines face significant challenges, including low fuel conversion efficiency at low loads due to incomplete combustion, and high levels of combustion noise at high loads caused by rapid burn rates. These issues restrict the premixed fuel energy fraction to lower levels. To mitigate these challenges, alternative combustion control strategies must be developed. In this regard, an experimental study was conducted to examine two distinct dual-fuel combustion approaches: one using a diesel with hydrogen-methane blend and the other using diesel with pure hydrogen. The aim was to optimise engine performance and emissions in a heavy-duty engine context.

1.2 Research objectives

The primary aim of this research is to investigate the use of hydrogen-based gaseous fuels as partial substitutes for diesel in heavy-duty compression ignition engines, with the goal of achieving significant reductions in GHG emissions while maintaining high thermal efficiency across a wide range of engine loads. To achieve this aim, the study focused on the following specific objectives:

- To address the limitations of conventional dual-fuel combustion by implementing and evaluating advanced in-cylinder control strategies, including early and multiple diesel injections, introduction of Miller cycle via late intake valve closing, and intake enhancement techniques such as exhaust gas recirculation and water injection.

- To maximise diesel substitution through the use of low- and zero-carbon gaseous fuels, and assess the trade-offs between fuel efficiency, emissions, and combustion stability in dual-fuel operation.

- To perform a comprehensive Well-to-Wheel assessment of each dual-fuel configuration using different fuel sourcing pathways, in order to quantify the full climate impact and decarbonisation potential of each strategy.

- To identify the most viable short- and medium-term decarbonisation pathways for heavy-duty transport applications based on technical feasibility, emissions performance, and fuel availability.

1.3 Thesis outline

The thesis is organised into six chapters. Chapter 1 provides an introduction, defining the scope and objectives of the thesis. Chapter 2 presents a review of the literature relevant to this research, which aided supporting the methodology employed and the discussion of results.

Topics such as GHG emissions, climate change, and regulatory standards are assessed. Technologies implemented in the transportation sector, especially for heavy-duty vehicles, are described. Potential in-cylinder control strategies, ATS, and alternative fuels are explored. The limitations faced by current dual-fuel engines are discussed.

Chapter 3 presents the research engine and test cell facilities. The equations employed and methodology utilised for acquisition and analysis of engine data are also described.

Chapters 4 and 5 explore means of improving the efficiency and minimising exhaust emissions of dual-fuel combustion at different engine loads. Chapter 4 focuses on diesel-hythane dual-fuel, investigating the impact of advanced diesel injection strategies, internal and external exhaust gas recirculation, and maximising hythane energy fraction. Chapter 5 examines diesel-hydrogen dual-fuel, assessing the effect of hydrogen energy fraction, relative air-fuel ratio, external EGR, and water injection.

Chapter 6 presents a comparative assessment of all dual-fuel strategies tested, including diesel-CNG, diesel-hythane, and diesel-hydrogen, evaluated under consistent operating conditions. The analysis focuses on thermal efficiency, carbon dioxide and total greenhouse gas emissions, nitrogen oxides formation, and Well-to-Wheel climate impact, offering a broader perspective on the strengths and limitations of each fuel pathway.

Finally, Chapter 7 concludes by summarising the principal findings of this research and providing recommendations for future research.

Chapter 2

Literature Review

2.1 Introduction

The transportation sector currently represents around 20% of global energy use, and projections suggest this figure could increase by over 30% between 2021 and 2050 [4], as shown in Figure 2.1. This anticipated growth is largely attributed to expanding economic development and the rising demand for goods and services, particularly in emerging economies. As a result, commercial transport activity is expected to surge, with heavy-duty (HD) transportation showing the most pronounced increase, as illustrated in Figure 2.2.

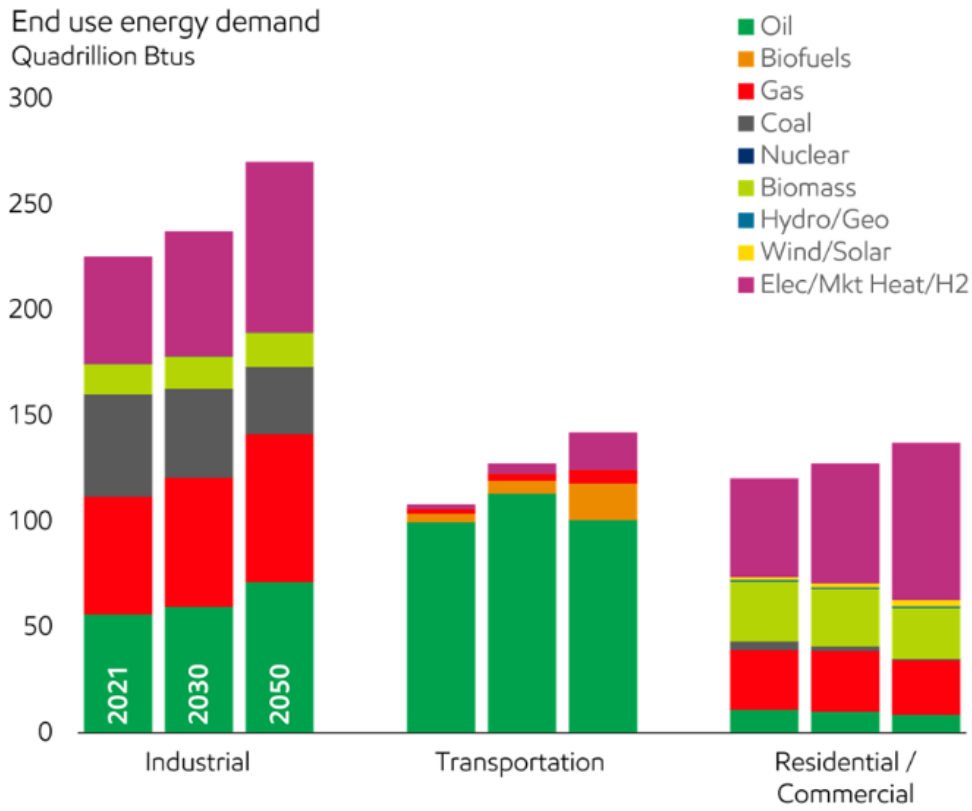

Figure 2.1 – Global energy demand by sector and source. Adapted from [4].

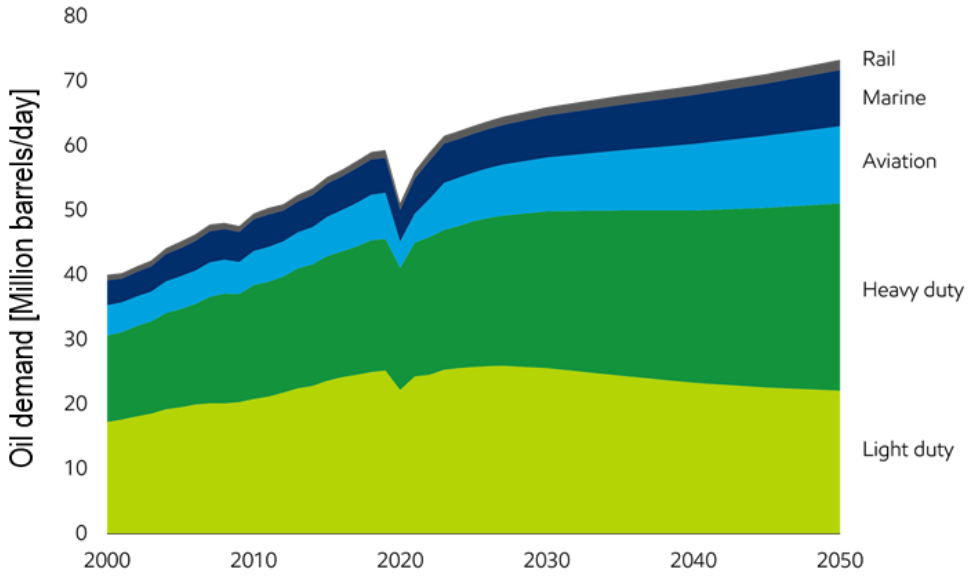

Figure 2.2 – Fuel demand by transportation sector. Adapted from [5]

Additionally, oil remains essential for transportation, with commercial transportation still relying on fossil fuels to meet more than 80% of demand by 2050 [5]. According to the Intergovernmental Panel on Climate Change (IPCC) [6], the combustion of fossil fuels has greatly affected the atmospheric concentration of greenhouse gases (GHG). Those GHG emissions are constituted by methane (CH_4), nitrous oxide (N_2O), and mostly carbon dioxide (CO_2). In particular, CO_2 have risen since the Industrial revolution, has now reached the highest atmospheric concentration in at least the past 800,000 years, as depicted in Figure 2.3 [7]. Since mid-1950, the majority of that CO_2 generation has come from the use of fossil fuels [8], as demonstrated by Figure 2.4.

Scientists are observing changes in the Earth's climate in every region and across the whole climate system, according to the 2023 IPCC Synthesis Report [6]. Many of the changes observed in the climate are unprecedented in thousands, if not hundreds of thousands of years, and some of the changes already set in motion, such as continued sea level rise, which are irreversible over hundreds to thousands of years [6].

The report finds that unless there are immediate, rapid and large-scale reductions in greenhouse gas emissions, there is more than 50% chance that global temperature rise will reach or exceed 1.5°C between 2021 and 2040. In some high-emissions pathway scenarios, the world may hit this threshold even sooner – between 2018 and 2037 [6].

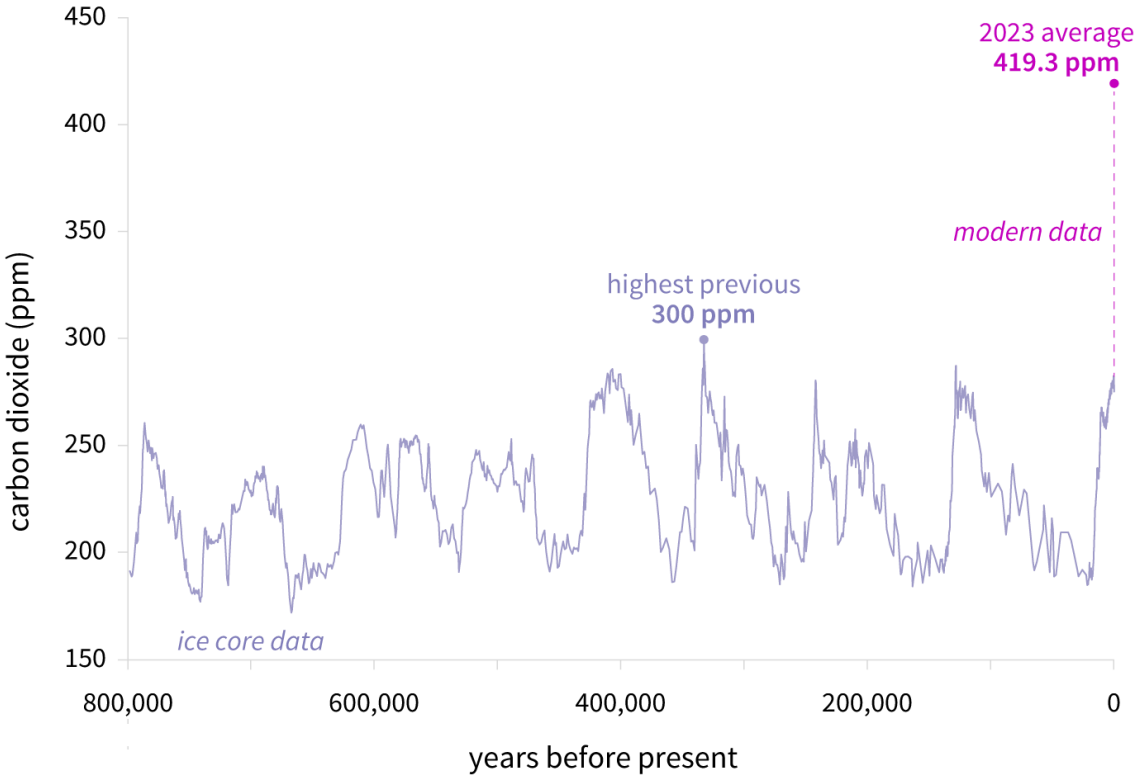

Figure 2.3 – Atmospheric carbon dioxide concentration in parts per million for the past 800,000 years based on ice-core data (light purple line) compared to 2023 concentration (bright purple dot). Adapted from [7].

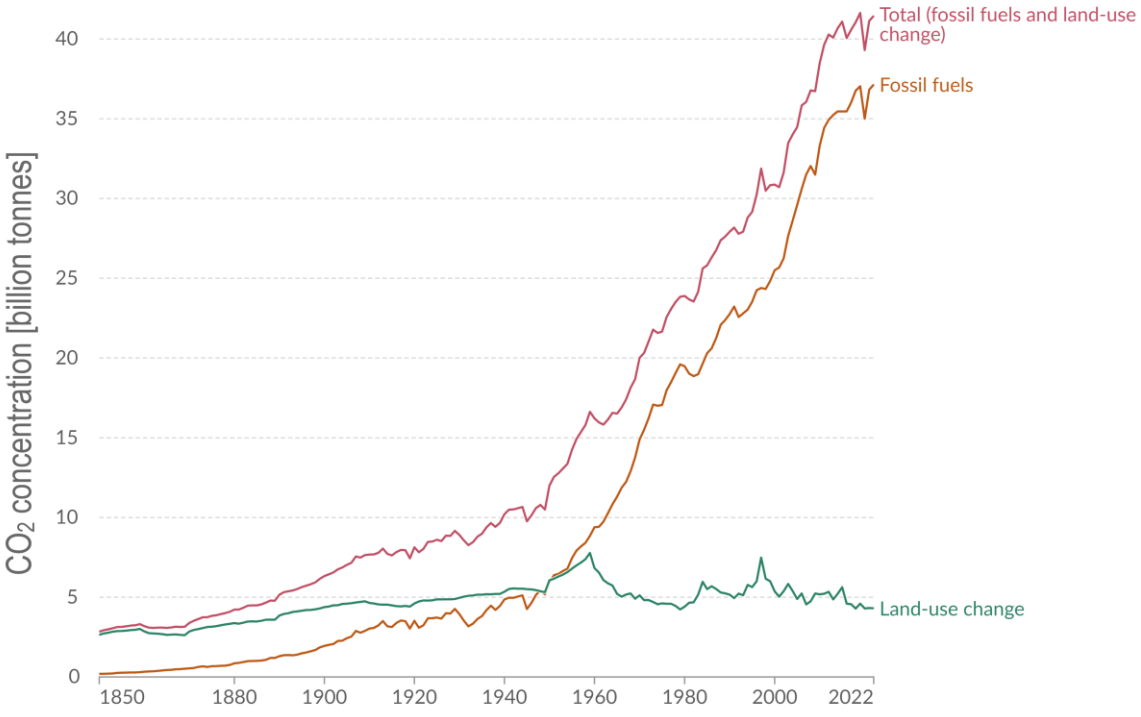

Figure 2.4 – Carbon dioxide emissions from fossil fuels and land-use change. Adapted from [8]

In 2021, nearly 200 parties of the United Nations Framework Convention on Climate Change (UNFCCC) agreed the Glasgow Climate Pact (GCP) [9] during the Conference of the Parties (COP) 26. The goal of this agreement was to maintain the target of limiting global warming to 1.5°C alive, which was previously established in the Paris Agreement [10] in 2015. More recently, during the last 2023 COP28 in Dubai, the United Arab Emirates, nations agreed the “beginning of the end” of the fossil fuel era by laying the ground for a swift, just and equitable transition to renewable energy sources [11].

For the aforementioned reasons, the introduction of measures to reduce energy use and decarbonise the supply as well as revisit and strengthen current emissions targets is fundamental in every major sector, particularly in transportation. The European Green Deal [12], approved in 2019 and codified into European Climate Law [13] in 2021, was the first pact including policy initiatives to reduce GHG emissions by at least 55% by 2030 compared to 1990 levels, and to achieve climate neutrality by 2050.

Until 2019, GHG emissions from transportation continued increasing steadily in European Union (EU) and United States of America (US), a trend that diverges significantly from those in other sectors. In particular, there was an increase of 18% in car transport and 22% in freight transport between 2000 and 2019 in the EU [14]. Despite a 13.5% drop verified in 2020 caused by the Covid-19 pandemic, which disrupted transport demands, GHG emissions have rebounded by 8.6% in 2021 and 2.7% in 2022 [15]. It was anticipated that pre-pandemic levels would be reached by 2024.

This sector is a major contributor to these emissions, representing 26% of total GHG emissions in the EU, and 28% in the US in 2022 [15, 16]. As seen in Figure 2.5, heavy-duty vehicles (HDV) are responsible for more than a quarter (27%) of the road transport GHG emissions. This is equivalent to about 6% of the global GHG emissions. This considerable environmental impact is highlighted by the fact that HDV represents only 11% of the motor vehicles in the world [17].

A study conducted by the International Council on Clean Transportation (ICCT) [18] focused on zero-emissions vehicles (ZEV) shown in Figure 2.6 predicts that CO_2

emissions from global road transport will increase by 32% in the next three decades in the case of absence of new policy action. Moreover, emissions must stabilise by 2030, decrease by 29% by 2040, and fall further, by 60%, by 2050, to avoid a global temperature increase above 2°C. Hewing to a 1.5°C compatible pathway is still tougher. In any scenario, HDVs account for about half of the emission reduction. Therefore, transitioning new HDV to ZEV is not, by itself, sufficient to align with the 1.5°C pathway, which for this, additional measures would be required, such as maximising fuel efficiency of existing internal combustion engine vehicles.

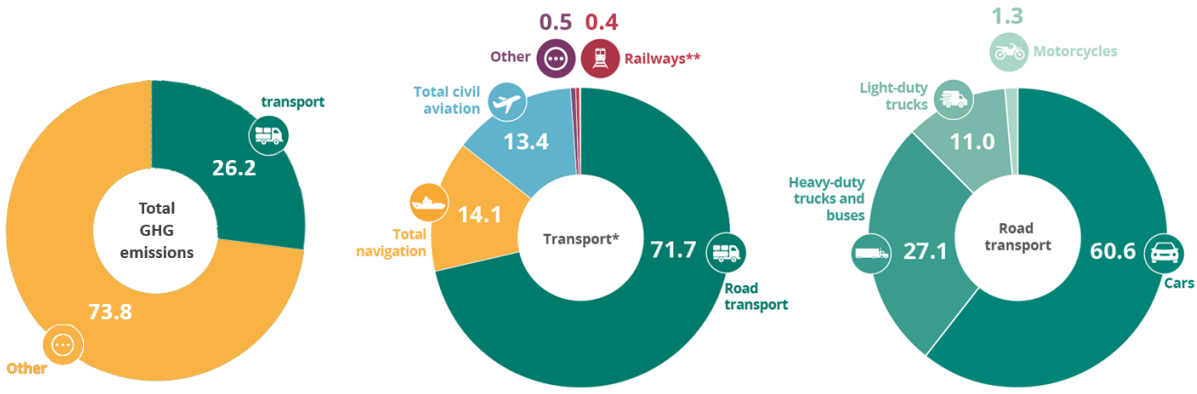

Figure 2.5 – GHG emissions from economic sectors in 2022. Adapted from [15]

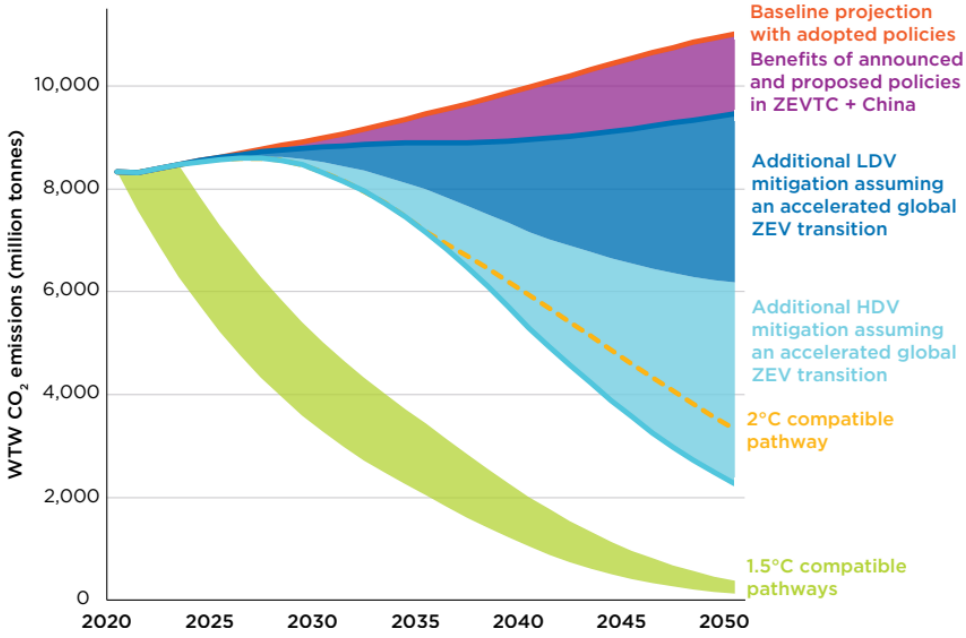

Figure 2.6 – Global Well-to-Wheel CO_2 emissions from road transport compared to a 1.5°C and 2°C compatible emissions pathways. Source: [18]

Thus, it is imperative to conduct further studies on emissions and fuel efficiency of HDV in order to mitigate GHG emissions and reduce the sector's disproportionate contribution to climate change. Advancing the use of renewable fuels alongside the development of novel engine technologies offers a viable pathway to lowering oil dependency while supporting the achievement of stringent emissions reduction goals.

2.2 Emission and fuel efficiency regulations

The aforementioned concerns about the environmental impacts have led in the implementation of stringent fuel efficiency and emission regulations. These regulations aim to mitigate the GHG emissions generation into the atmosphere as well as other pollutants. These pollutants can be carbon emissions, specifically carbon monoxide (CO) and hydrocarbons (HC), or other pollutants such as nitrogen oxides (NOx) and particulate matter (PM). The latter two are linked to millions of premature deaths caused by cardiovascular and respiratory diseases, and the loss of healthy years of life resulting in significant health care costs [19] as well as harmful effect on climate [20].

Regulating fuel consumption and emissions within the HD vehicle sector poses greater challenges compared to the light-duty segment, largely due to the wide variety of vehicles encompassed in this category. Emissions certification for heavy-duty vehicles (HDV) is typically carried out using an engine dynamometer on a test bench, with results expressed as the mass of pollutants emitted per unit of brake power output (g/kWh) [21, 22]]. This approach facilitates standardised comparisons across various engine types and operating conditions.

In the European Union, the governing emissions standard for on-road HDVs is the Euro VI regulation. This framework was initially established under Regulation (EC) No 595/2009 [23] and later implemented through Regulation (EU) No 582/2011 [24]. Since 2013, new engine types have been required to comply with Euro VI-A, with full compliance for all vehicles mandated from 2014 onward. The regulation has undergone several updates, with the current phase referred to as Euro VI-E. Specific provisions for dual-fuel (DF) engines were introduced under Regulation (EU) No

133/2014 [25], which outlined type-approval requirements for DF engines starting from the Euro VI-B phase.

Emission limits for both compression ignition (CI) and positive ignition (PI) engines must be demonstrated under two standardized testing procedures: the World Harmonised Transient Driving Cycle (WHTC) and the World Harmonised Stationary Cycle (WHSC), as defined in Regulation No. 49 [21]. Additionally, limits on ammonia (NH_3) emissions were introduced to prevent overuse of aqueous urea in SCR systems, which are commonly used to reduce NOx emissions.

Nevertheless, the European Parliament and the Council of the EU has approved the Regulation (EU) 2024/1257 [26]. This regulation enforces the implementation of the new Euro 7 standards, which will come into force in 2028 for new vehicles models and 2029 for all new vehicles. The Euro 7 regulation will replace the previously separate regulations for light- and heavy-duty vehicles. It sets new rules for passenger transport vehicles, namely categories M_2 and M_3 which apply to medium- and heavy-duty sizes, and for vehicles used for carrying goods, with categories N_2 and N_3 indicating medium- and heavy-duty specs. These new emission standards will impose more stringent tailpipe emission limits applied for the WHSC and WHTC, particularly targeting NOx and PM emissions, as seen in Figure 2.7, but also for non-methane hydrocarbons (NMHC) and CO.

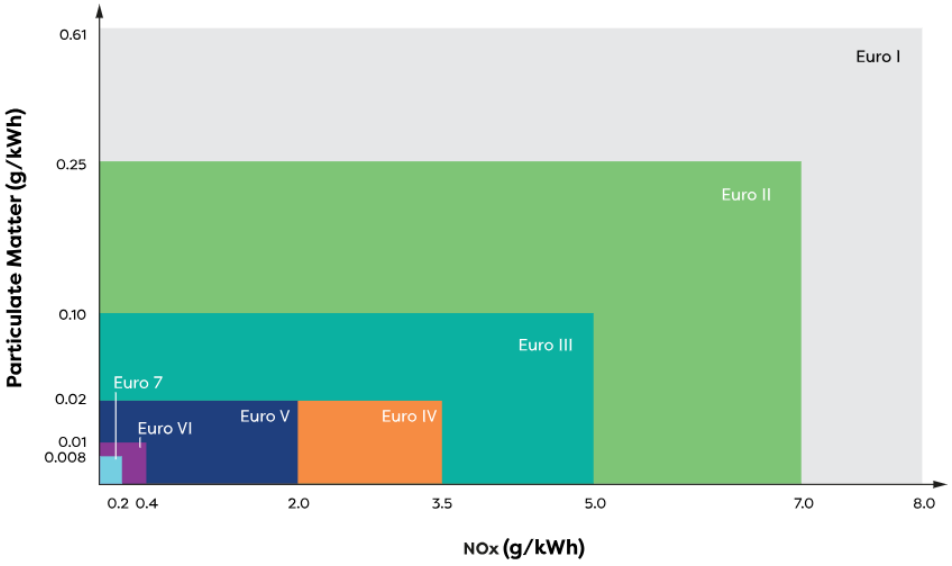

Figure 2.7 – Development of European HD legislated emissions limits for NOx and PM. Source [27]

Additionally, new limits on NH_3 as well as non-CO_2 GHG emissions such as N_2O and CH_4 will be introduced. This is a result of the high global warming potential (GWP) of CH_4 and N_2O, which are equivalent to 27 and 273 times that of CO_2 over a 100-year lifetime, respectively [28]. N_2O emissions can be produced in urea SCR systems during warm-up procedures [29] More information about Euro VI and Euro 7, and its test cycles – World Harmonised Stationary Cycle (WHSC) and World Harmonised Transient Cycle (WHTC) – can be found in Table 2.1. It is worth noting that Euro 7 is only focused on standard EU vehicle categories, such as passenger vehicles (M2), large passenger vehicles, buses and coaches (M3), medium goods vehicles (N2), and heavy goods vehicles (N3).

Table 2.1 – Euro VI for Type 2B HD DF engines [21, 25] and Euro 7 tailpipe emission limits for HDV of categories M2, M3, N2, and N3 [26].

Pollutant	WHSC			WHTC		
	Euro VI [mg/kWh]	Euro 7 [mg/kWh]	Change compared to Euro VI	Euro VI [mg/kWh]	Euro 7 [mg/kWh]	Change compared to Euro VI
NOx	400	200	-50%	460	200	-56%
PM	10	8	-20%	10	8	-20%
CO	1500	1500	No change	4000	1500	-62%
NMHC	130	80	-38%	160[a]	80	-50%
NH_3	-	60	New	-	60	New
CH_4	-	500	New	500[a]	500	No change
N_2O	-	200	New	-	200	New

[a] Only for gas engines

In terms of CO_2 emissions control, the EU issued Regulation (EU) 2019/1242 [30] in 2019, introducing the first-ever CO_2 emission standards for new HDVs. With the initial goal of lowering CO_2 levels by 15% in 2025 and 30% in 2030 compared to a 2019 baseline, the EU updated to align with the EU's climate objectives [12] for 2030 and beyond. The Regulation (EU) 2024/1610 [31] maintains the existing 2025 target of 15% emissions reduction, revised the 2030 target to 45% CO_2 reduction, and introduced new targets for 2035 and 2040 of 65% and 90% emission reduction,

respectively, based to a 2019 baseline. These targets will apply to medium- and heavy-duty trucks weighing over 7.5 tonnes and coaches.

Figure 2.8 briefly summarises the evolution of the EU's emission regulations over the years, which includes the multiple phases of Euro VI, the new Euro 7, and CO_2 reduction targets.

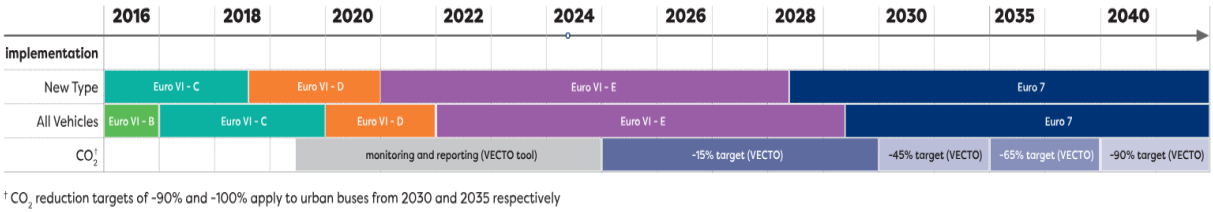

Figure 2.8 – Evolution of heavy-duty emissions standards in the EU. Source: [27]

2.3 Heavy-duty diesel engine emissions

Diesel engines have historically served as the dominant powertrain in the HD transport sector due to their ability to deliver high torque and achieve superior thermal efficiency [32]. In an ideal scenario, the conversion of diesel's chemical energy into mechanical work would yield only carbon dioxide (CO_2) and water vapour (H_2O) [33]. These products result from the combustion reaction, where carbon in the fuel reacts with oxygen (O_2) to form CO_2, and hydrogen atoms combine with oxygen to produce H_2O.

In practice, however, conventional diesel combustion – illustrated in Figure 2.9 – leads to the formation of several harmful emissions beyond CO_2 and H_2O, including carbon monoxide (CO), unburned hydrocarbons (such as CH_4 and NMHC), particulate matter (PM), and nitrogen oxides (NOx). CO, HC, and PM are primarily by-products of incomplete combustion and insufficient air-fuel mixing. In contrast, NOx emissions are mainly attributed to the presence of high-temperature zones and local fuel-rich regions resulting from the diffusion-controlled, non-premixed combustion process [34].

Mitigating these pollutants is critically important due to their impact on both environmental and human health [33, 35]. Therefore, it is essential to investigate the in-cylinder combustion behaviour and air-fuel interaction in greater detail to better understand and control the formation of these emissions.

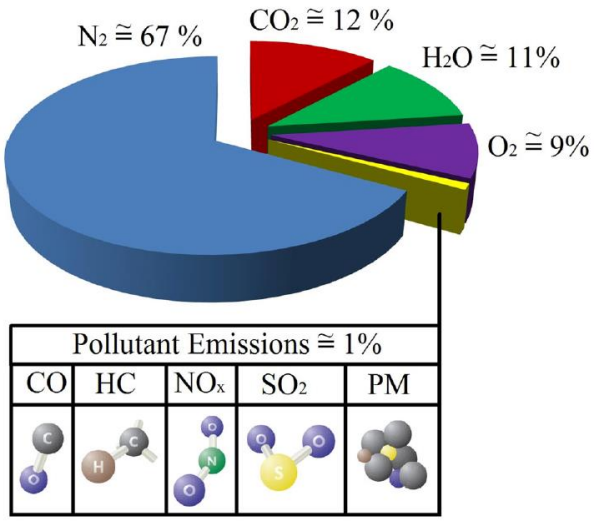

Figure 2.9 – The composition of diesel exhaust gas. Source: [36].

Carbon monoxide (CO) is primarily generated when combustion is incomplete, meaning the oxidation of carbon in the fuel does not fully convert to carbon dioxide (CO_2). The extent of CO formation is closely tied to the availability of oxygen in the intake charge [37], and its concentration increases significantly when the relative air-fuel ratio (λ) falls below 1.0, indicating a fuel-rich mixture [38]. Such conditions commonly occur during engine cold starts and sudden acceleration events, where richer mixtures are required. Under these oxygen-deficient conditions, not all carbon atoms are fully oxidised to CO_2, leading to increased CO formation. While CO is predominantly produced in rich conditions, a smaller amount may also be emitted under lean operation ($\lambda > 1$) due to specific chemical kinetic limitations [39].

Hydrocarbon (HC) emissions consist of unburned fuel resulting from regions within the combustion chamber that fail to reach sufficient temperatures, particularly near the cylinder walls where thermal gradients are significant [40]. Other contributors to HC emissions include lubricant oil combustion and flame quenching effects [41]. In diesel engines, these emissions are typically referred to as total hydrocarbons (THC), comprising both non-methane hydrocarbons (NMHC) and methane (CH_4), and are

more pronounced at low engine loads [36]. One of the main drivers of HC formation at low loads is lean combustion, where low flame propagation speeds may cause incomplete combustion during the expansion stroke—or in some cases, combustion may not occur at all – resulting in elevated HC levels [42]. However, if the exhaust temperature exceeds 600°C and sufficient oxygen is present, unburned hydrocarbons may undergo post-oxidation in the exhaust system, reducing the amount of HC emitted from the tailpipe [39].

Particulate matter (PM) in diesel exhaust is a byproduct of incomplete combustion, involving both the fuel and engine oil [36]. PM formation depends on various factors, including the combustion and expansion processes, the quality and quantity of fuel and oil used, combustion temperature, and the degree of exhaust gas cooling [43]. As shown in Figure 2.10, PM emissions primarily consist of dry carbon, commonly referred to as soot. In addition, they contain aggregates of fine particles formed from partially combusted fuel and lubricant, ash residues, sulfates, and condensed water vapour [44, 45].

Particulate matter (PM) in diesel exhaust is a by-product of incomplete combustion, involving both the fuel and engine oil [36]. PM formation depends on various factors, including the combustion and expansion processes, the quality and quantity of fuel and oil used, combustion temperature, and the degree of exhaust gas cooling [43]. As shown in Figure 2.10, PM emissions primarily consist of dry carbon, commonly referred to as soot. In addition, they contain aggregates of fine particles formed from partially combusted fuel and lubricant, ash residues, sulfates, and condensed water vapour [44, 45].

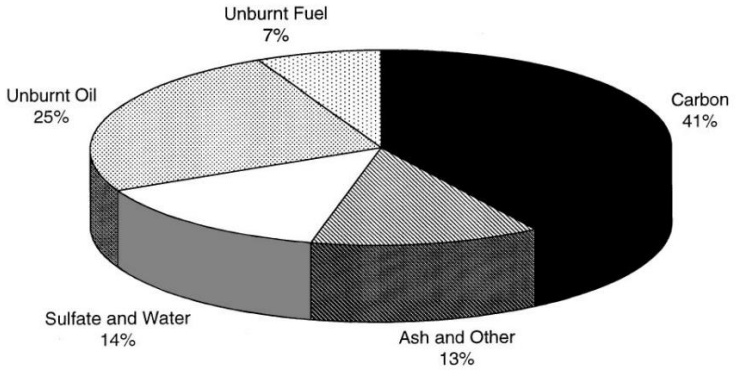

Figure 2.10 – Typical particular matter emissions composition from a heavy-duty diesel engine. Source: [45].

NOx emissions in the exhaust primarily consist of nitrogen monoxide (NO) and nitrogen dioxide (NO_2), with NO typically accounting for 85–95% of the total and NO_2 comprising the remaining 5–15% [36]. The formation of NOx is influenced by several key factors, including peak in-cylinder temperature and the availability of oxygen – known as Zeldovich mechanism – and the duration for which these conditions are sustained [46]. The majority of NOx generation occurs in the early phase of combustion, particularly when the piston is near top dead centre (TDC) at the end of the compression stroke. At this point, flame temperatures are at their highest, promoting NOx formation.

Under ideal combustion conditions, nitrogen (N_2) from the intake air remains inert and exits the engine unaltered. However, when combustion temperatures exceed approximately 1600°C, N_2 begins to react with O_2, resulting in the production of NOx compounds [36]. Understanding the mechanisms behind NOx formation is essential due to their considerable environmental and public health implications. These emissions are linked to several harmful effects, including acid rain, ground-level ozone (O_3) generation, nutrient pollution, and photochemical smog – issues commonly associated with air quality degradation in urban environments [47].

2.4 Heavy-duty diesel engine emissions control technologies

To meet GHG reduction goals and comply with increasingly stringent pollutant emission regulations, manufacturers have implemented a range of advanced engine design features and in-cylinder strategies. In HD diesel engines, notable examples include flexible diesel injection timing and pressure control for optimising combustion, high-efficiency turbocharging, cooled exhaust gas recirculation (EGR), variable valve actuation (VVA), and water injection. Alongside these internal measures, significant effort has also been directed toward developing effective ATS to minimise emissions.

When applied in combination, measures such as high-pressure fuel injection, enhanced air handling, and EGR can offer simultaneous benefits—reducing emissions

and increasing thermal efficiency by improving air-fuel mixing and moderating combustion temperatures. However, future HD engine efficiency targets raise concerns due to the persistent trade-off between reducing fuel consumption and controlling engine-out NOx emissions. For example, achieving just a 1% gain in fuel efficiency could result in a rise in NOx emissions from 10 to 14 g/kWh. Conversely, strategies aimed at aggressively minimising NOx may impair overall engine performance and increase PM emissions (such as soot), due to differing formation pathways.

2.4.1 Alternative combustion strategies

The development of alternative combustion strategies has become a crucial focus in response to increasingly stringent emissions regulations and rising fuel costs. Conventional diesel combustion (CDC) typically operates with excess air, resulting in a lean engine operation. However, this process leads to significant local variations in relative air-fuel ratios (λ) and temperatures within the combustion chamber [48], which can promote the formation of NOx in high-temperature regions near the diffusion flame [49] and soot in fuel-rich zones within the spray [32].

In light of these challenges, several innovative combustion technologies have been developed to optimise the combustion process while reducing the need for costly ATSs [50]. These strategies generally focus on lowering the local relative air-fuel ratios and reducing combustion temperatures to mitigate NOx and soot formation. This approach, often referred to as Low Temperature Combustion (LTC), aims to enhance fuel efficiency and reduce harmful emissions [51].

Among the various LTC strategies, Homogeneous Charge Compression Ignition (HCCI) stands out, characterised by early fuel injections that promote a fully premixed charge and longer ignition delays. While HCCI offers significant emissions benefits, such as reduced NOx and soot, it suffers from challenges such as difficulty in controlling ignition timing and combustion phasing, especially under transient conditions. Additionally, HCCI tends to result in higher combustion losses and noise [52, 53].

To overcome these limitations, other combustion concepts have been developed, including Premixed Charge Compression Ignition (PCCI) [54, 55], Partially Premixed Charge Compression Ignition (PPCI) [49], Modulated Kinetics (MK) [56], and the Uniform Bulky Combustion System (UNIBUS) [57]. These strategies provide a greater degree of control over combustion phasing at light and medium engine loads while keeping NOx and soot emissions low. However, they often result in lower engine efficiency, increased unburnt HC and CO emissions, and a limited operating range due to high EGR and boost requirements.

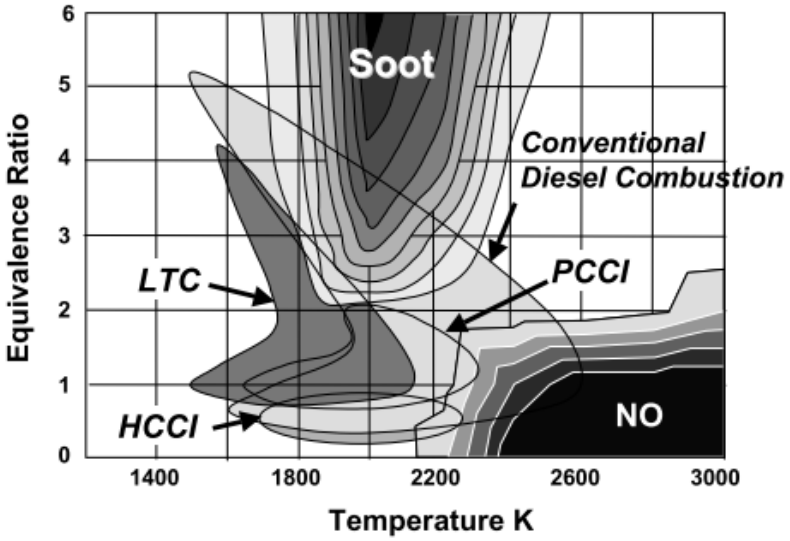

Figure 2.11. Local equivalence ratio versus temperature map for the classification of combustion strategies. Adapted from [58].

Gasoline Direct Injection Compression Ignition (GDCI) [59, 60] and Partially Premixed Combustion (PPC) [61, 62] are also considered as alternatives to diesel LTC. These strategies are capable of expanding the high-efficiency operating window and achieving very low NOx emissions even at full load. However, their reliance on gasoline rather than renewable fuels and the need for significant engine hardware modifications limit their application in reducing dependence on liquid fossil fuels [62].

Recent developments in PPC combustion with renewable fuels have demonstrated promising improvements in thermal efficiency and soot reduction [63, 64]. However, these approaches also face challenges such as increased acoustic noise and higher

peak heat release rates, requiring adjustments like lower intake air pressures and larger amounts of EGR, which can negatively impact combustion efficiency.

The dual-fuel combustion strategy has emerged as a promising solution to address the challenges posed by the aforementioned combustion concepts. It offers a more effective means of utilising low-carbon fuels, such as hydrogen and methane, in conventional diesel engines. By combining diesel with alternative fuels, dual-fuel combustion has the potential to mitigate the issues of high emissions and poor efficiency commonly associated with conventional diesel combustion [32].

2.4.2 Boosting technology

Turbocharger systems have an essential role of enhancing engine performance and combustion efficiency, which contributes to the mitigation of exhaust emissions. It permits to increase the amount of air (oxygen) entering the combustion chamber, which enables for a more complete combustion of the fuel, resulting in reduction of unburned THC, PM, and CO. The improvement of fuel efficiency also mitigates the CO_2 emission generation. Turbocharger systems can also help managing in-cylinder gas temperatures by optimising the air fuel ratio as well as the EGR systems, which can lead in minimising NOx formation.

A conventional turbocharger consists of a turbine section integrated into the engine's exhaust stream and a compressor section located in the intake system. This configuration increases intake pressure, thereby enhancing the in-cylinder air charge. The turbine generates power by expanding exhaust gases across a stator or nozzle ring and a rotating turbine wheel. The level of intake air compression achieved depends on specific characteristics of the turbine stage—primarily its swallowing capacity and isentropic efficiency. The swallowing capacity determines the degree of flow restriction across the turbine, while the isentropic efficiency indicates how effectively the turbine converts exhaust energy into mechanical power [65].

The fixed geometry turbocharger (FGT) was the first type widely adopted in diesel engine applications. It operates using a wastegate that controls boost pressure by allowing exhaust gases to bypass the turbine when necessary. At low engine speeds, closing the wastegate increases boost by directing more exhaust flow through the

turbine. At higher speeds, the wastegate opens to prevent over-boost conditions [66]. However, FGT systems face two main limitations: turbo-lag at low engine speeds and transient conditions, and limited EGR introduction capabilities across the full range of engine operation without compromising fuel efficiency [66].

To overcome these drawbacks, variable geometry turbochargers (VGTs) have been introduced. VGTs allow real-time adjustment of the turbine's flow characteristics without bypassing exhaust gases, thereby improving transient response and overall efficiency [65]. These systems serve multiple functions, including optimizing airflow for torque delivery and engine performance, controlling EGR flow, enabling Miller cycle operation, supporting engine braking, and assisting in exhaust aftertreatment system regeneration [67, 68].

2.4.3 Exhaust gas recirculation

One of the primary contributors to NOx formation in combustion engines is the peak temperature reached during the combustion process, often referred to as the flame temperature. Therefore, reducing this temperature is critical for effective NOx control, and several combustion control strategies have been developed to achieve this. Among them, exhaust gas recirculation (EGR) has proven particularly effective at lowering flame temperatures.

There are two main approaches to introducing exhaust gases back into the cylinder: external EGR (eEGR) and internal EGR (iEGR). The eEGR method is a well-established in-cylinder technique capable of significantly reducing NOx emissions—potentially eliminating them almost entirely when used at high rates. This system operates by extracting exhaust gases from the exhaust manifold and rerouting them into the intake system through a metering valve (EGR valve) and a heat exchanger (EGR cooler). The presence of exhaust gases in the intake mixture lowers the oxygen concentration and increases the inert content, thereby reducing combustion temperature and, as a result, NOx formation, as illustrated in Figure 2.12. Additionally, CO_2 and H_2O contribute to this reduction through their thermal properties, though their impact is secondary [69].

The EGR cooler plays a crucial role by lowering the temperature of the recirculated gases, helping to prevent excessive thermal stress on engine components, further reduce NOx, and support high engine power density. This configuration is typically referred to as high-pressure loop EGR.

To enable exhaust gases to flow from the exhaust manifold back into the intake system, the system must maintain a pressure differential – meaning the average exhaust pressure must exceed intake pressure. This is usually achieved with an exhaust throttle or a variable geometry turbocharger (VGT), as described earlier in Section 2.4.2. However, maintaining this pressure difference introduces additional challenges. It can reduce engine efficiency and, at high loads, demands significantly elevated intake pressure to preserve the air-fuel ratio and prevent excessive smoke or PM emissions. These demands place added stress on the turbocharging system and are constrained by limits on peak in-cylinder pressures.

Moreover, the use of high EGR rates – typically above 30% - introduces additional drawbacks. These include increased pumping losses and fuel consumption, greater heat rejection requirements, and the potential for condensation-related corrosion in engine components.

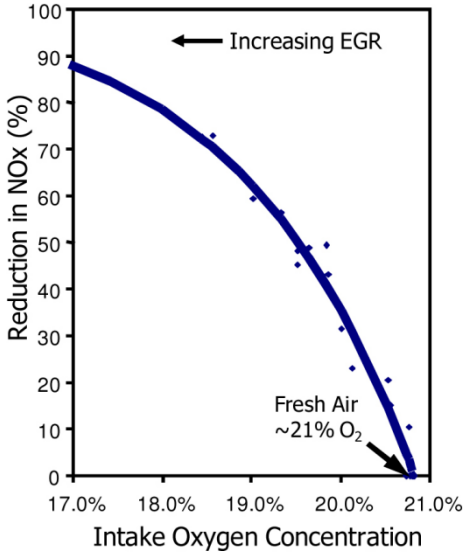

Figure 2.12 – Impact of intake oxygen concentration on NOx reduction. Source: [65]

The iEGR method utilises a VVA system to retain exhaust gases within the cylinder. This can be achieved by reopening the intake valve during the exhaust stroke (2IVO)

[70] or by reopening the exhaust valve during the intake stroke (2EVO) [71]. Among these options, 2IVO has demonstrated greater effectiveness in improving fuel efficiency and reducing smoke emissions [72, 73].

Compared to eEGR, iEGR offers multiple advantages, including a more compact design, reduced maintenance requirements, improved reliability, and enhanced cycle-by-cycle control of the retained exhaust gas fraction [74]. When implemented with increased exhaust back pressure, iEGR has also been shown to reduce THC and CO levels [71] and elevate EGT at low engine loads [75]. This rise in EGT is beneficial under low enthalpy conditions, supporting the effectiveness of ATS [76, 77].

However, iEGR does not allow for cooling of the recirculated gas due to the limited time available for temperature reduction. As a result, hot and low-density EGR gases are reintroduced into the cylinder, which increases in-cylinder temperatures. This can lead to elevated NOx emissions and reduced thermal efficiency, as the lower gas mass requires higher fuel input to maintain performance [70]. The drop in efficiency becomes especially apparent at high load, often causing a loss in engine power. For this reason, iEGR is usually disabled during high-load operation [74, 78].

2.4.4 Miller cycle

Engine processes are classified as over-expansion cycles when the effective expansion ratio (EER) exceeds the effective compression ratio (ECR). The Atkinson cycle, introduced by British engineer James Atkinson in the 1880s [79, 80], was the first engine concept to achieve this condition. It utilised a mechanically complex crank and linkage arrangement to produce a longer expansion than compression stroke.

On the other hand, Miller cycle engine, patented by an American engineer Ralph Miller in 1950s [81, 82, 83], is another type of over-expansion cycle engine. However, this one could achieve a differential between expansion and compression ratios by means of adjusting valve timing to control ECR, either by an early intake valve closing (EIVC) strategy or late intake valve closing (LIVC) strategy. Therefore, the usage of Miller

cycle in modern diesel engines are associated essentially to effectively improve the engine efficiency and exhaust emissions trade-off [84, 85].

By shortening the effective compression stroke while allowing a full expansion stroke, the Miller cycle reduces in-cylinder temperatures at the end of compression and during combustion, which directly lowers peak combustion temperatures. Since NOx formation is highly dependent on temperature, as discussed in Section 2.3, this approach can reduce NOx emissions. However, the drawback is a potential decrease in engine output and increased fuel consumption, which can result in higher CO_2 emissions [86].

Several studies [86, 87, 88] have shown that implementing the Miller cycle alone can reduce NOx emissions by 15-30%, but this often comes at the cost of reduced thermal efficiency. Moreover, the effectiveness of the Miller cycle for NOx control in diesel engines is limited under low-load conditions, as the reduction in peak in-cylinder temperature is relatively modest. Nevertheless, eEGR has proven highly effective for NOx mitigation, and when combined with the Miller cycle, the two approaches can yield more substantial reductions than either method alone. For instance, research by Verschaeren et al. [89] reported a 70% decrease in NOx emissions across various load conditions using a medium-speed HD diesel engine, alongside reductions in HC emissions – at the expense of increased CO and PM emissions and slightly reduced engine efficiency. The drop in HC was attributed to higher exhaust temperatures, which enhanced the oxidation of unburned hydrocarbons during the expansion phase.

The reduction in the volume of air during the compression stroke also results in lower peak in-cylinder pressure [90, 91]. Although this lower pressure delays the start of combustion, which can lead to a potentially penalty in engine performance and efficiency, it can also offer advantages in combustion control. A slower and more stable combustion process reduces the tendency for knocking or pre-ignition, as temperature and pressure spikes are less severe, particularly under varying load conditions. This, in turn, enables a more flexible engine operating window, allowing for more advanced diesel injection timings, higher fuel injection pressures, and increased boost pressures to recover or even enhance efficiency [90]. Additionally, the lower

peak in-cylinder pressure may lead to higher EGT [92], which can influence the performance and durability of ATSs.

2.4.5 Water injection

Injecting water into a CI engine has proven to be one of the most effective techniques for lowering in-cylinder temperatures in research context. This approach works by cooling potential ignition sources and decreasing the rate of chemical reactions during combustion [93, 94, 95]. Water's high heat absorption capacity – especially at elevated temperatures – allows it to extract significant thermal energy from the combustion process, thereby reducing the temperature of the combustion gases. This cooling effect can facilitate greater substitution of alternative fuels in CI engines by mitigating thermal limitations [96]. Additionally, water injection can decrease the likelihood of backfiring and reduce the engine’s tendency to knock [97].

2.4.6 Aftertreatment technologies

High-cost ATSs are widely implemented in modern HD engines to comply with strict emissions regulations while balancing pollutant control with fuel efficiency. These systems are typically integrated alongside in-cylinder combustion control strategies to effectively mitigate emissions present in the exhaust stream. However, the performance of ATS is highly sensitive to exhaust gas temperature (EGT). For effective activation – commonly referred to as catalyst light-off – a minimum EGT of around 200°C is necessary. Achieving this threshold becomes particularly difficult at low engine loads, where EGT tends to be insufficient for effective emissions treatment. As a result, it is essential to apply appropriate control strategies that can elevate EGT without compromising overall engine efficiency under such conditions [41].

Among the principal ATS technologies found in HD diesel engines are the diesel oxidation catalyst (DOC), diesel particulate filter (DPF), and selective catalytic reduction (SCR) system. Figure 2.13 provides a schematic overview of a typical ATS configuration used in current HDVs.

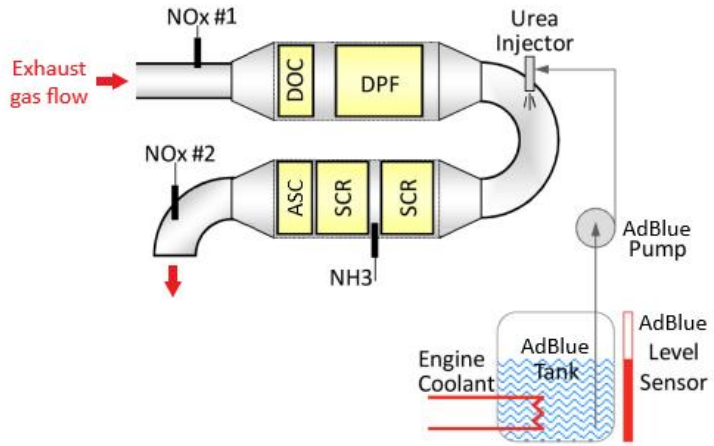

Figure 2.13 – Aftertreatment system configuration of a modern HD diesel engine. Adapted from [65].

The main function of the DOC, as illustrated in Figure 2.14, is to catalyse the oxidation of HCs, CO, and the volatile components of PM that result from incomplete combustion and from fuel intentionally injected during active DPF regeneration events [98, 99]. This catalyst system has been shown to reduce HC and CO emissions by approximately 60–90% [36]. Since the exhaust gas typically contains between 2% and 17% oxygen by volume [100], the DOC can also support additional oxidation processes beyond HC and CO removal. For example, it can convert NO into NO_2, thereby increasing the NO_2/NOx ratio, which is advantageous for passive DPF regeneration. An increased NO_2 concentration in the exhaust stream improves the performance of both DPF and SCR systems [101, 102].

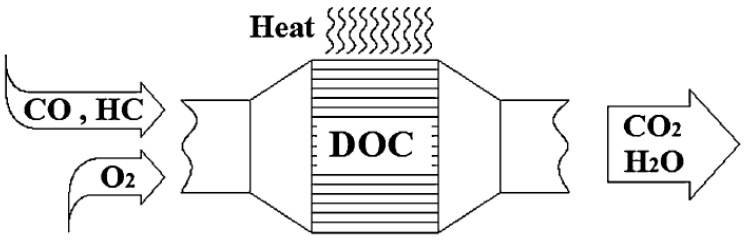

Figure 2.14 – Diesel oxidation catalyst. Source: [36].

Furthermore, the DOC can function as a catalytic heat source. The exothermic oxidation of HC and CO, along with post-injection of fuel into the exhaust stream, generates thermal energy that raises EGT downstream of the DOC. This temperature

increase is critical for achieving the light-off conditions required by the DPF and SCR units, especially under low-load operating conditions, ensuring optimal conversion efficiency [36].

The DPF reduces particulate matter in the exhaust by capturing soot particles through a wall-flow filtration process, where the soot is trapped within the porous structure of a ceramic honeycomb monolith. To prevent clogging, the filter must undergo either passive or active regeneration to remove the accumulated soot [103]. Passive regeneration occurs at relatively low temperatures – starting around 250°C – and relies on NO_2, which is typically produced in the DOC, to oxidise the soot. In contrast, active regeneration requires higher temperatures, generally above 500°C, and involves the oxidation of fuel that has been injected into the exhaust stream, reacting with available O_2 [65]. Inadequate or failed regeneration can result in various issues, including higher fuel consumption, potential engine damage, and excessive thermal and mechanical stress on the filter material [36].

The SCR system is composed of a SCR catalyst, a reduction agent injection system, NOx and NH_3 sensors, and an ammonia slip reduction (ASC) [104]. This is a technology used to reduce NOx emissions by using ammonia as the reductant. However, due to the toxic effects of NH_3 and to prevent its burning in the warm atmosphere before the reaction, NH_3 is directly injected into the exhaust stream by means of an aqueous urea solution. This reductant agent, also known as AdBlue in Europe or diesel exhaust fluid (DEF) in the US, is a 33% solution of high purity urea ($CO(NH_2)_2$) in deionised water. Through the processes of thermolysis and hydrolysis, the aqueous urea is decomposed into NH_3 and CO_2, upstream of the SCR catalyst at temperatures above 300°C [105] via Equation (2.1).

$$CO(NH_2)_2 \rightarrow 2NH_3 + CO_2 \quad (2.1)$$

Within the SCR catalyst, NH_3 reacts with NOx to produce harmless nitrogen (N_2) and water (H_2O). While this process is effective, the use of aqueous urea presents certain challenges, particularly the potential for deposit formation when exhaust temperatures fall below approximately 200°C [65]. For optimal performance, the injected amount of urea must correspond closely to the NH_3 required to match the NOx concentration and the catalyst's conversion efficiency under specific operating conditions.If the NH_3

supply is insufficient, some of the NOx will remain untreated, resulting in a drop in overall conversion efficiency. Conversely, excess NH_3 that exceeds the catalyst's capacity to convert it may lead to ammonia slip. In some cases, this excess NH_3 can be re-oxidised to NO, reducing the net NOx reduction achieved. To manage excess ammonia, an Ammonia Slip Catalyst (ASC) is employed downstream of the SCR. The ASC facilitates the oxidation of surplus NH_3 into NO, N_2O, and N_2, thereby minimising emissions of unreacted ammonia and supporting compliance with emission limits [65].

Therefore, the consumption of aqueous urea solution is an important aspect since it accounts for the total fuel consumption, often resulting in an increase ranging from 2% and 5% [65, 103, 106], thus affecting the total cost of ownership. SCR systems with open loop control of aqueous urea solution achieve a considerable NOx conversion efficiency, regularly exceeding 80% when the EGT is higher than 250°C, and reaching 94% between 250°C and 350°C [65, 103]. An optimised closed loop control of urea injection can obtain a higher efficiency of 97% [65].

Moreover, the balance between in-cylinder control of NOx using cooled EGR and aftertreatment control of NOx using SCR have been studied in order to reduce the engine running cost by minimising aqueous urea solution consumption and reduce the NOx conversion efficiency requirements [65, 107].

2.5 Dual-fuel combustion

Despite ongoing advancements in alternative powertrains, CI engines continue to play a central role in HD transportation due to their superior thermal efficiency and fuel economy. However, their reliance on diesel fuel poses a major challenge in the context of global efforts to reduce GHG emissions. With diesel combustion being a significant source of CO_2 and other pollutants, strategies to lower the carbon intensity of CI engines are increasingly being explored. Among these, dual-fuel operation has gained attention as a practical transitional solution, offering a way to partially substitute diesel with lower-carbon or carbon-neutral fuels – without the need for extensive modifications to the engine hardware [108, 109].

Dual-fuel operation is typically implemented by integrating a cost-effective port fuel injection (PFI) system into the intake manifold, enabling the introduction of a low-reactivity fuel – such as CNG, hydrogen, or ethanol – into the intake air stream [110, 111]. This setup allows for the preservation of the engine's original diesel injection and combustion systems. In this configuration, as shown in Figure 2.15, diesel fuel is directly injected and acts as the ignition source for the premixed air-fuel mixture [111]. Once sufficient in-cylinder pressure and temperature are reached during compression, the diesel ignites and initiates combustion, which then propagates through the charge, generally moving from higher to lower reactivity regions [32], as illustrated by Figure *2.16* The combustion process, emissions, and overall efficiency can be influenced by the fuel properties, the timing of diesel injection, and the energy fraction of each fuel (substitution ratio).

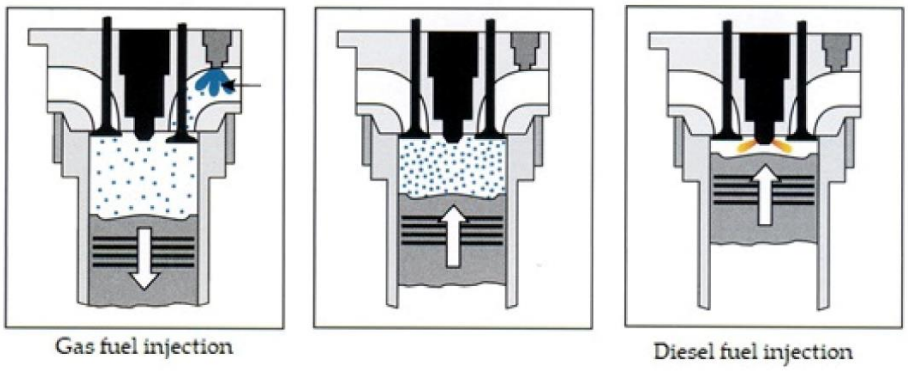

Figure 2.15. Use of diesel and gas fuels in a CI engine under dual-fuel technology. Adapted from [112].

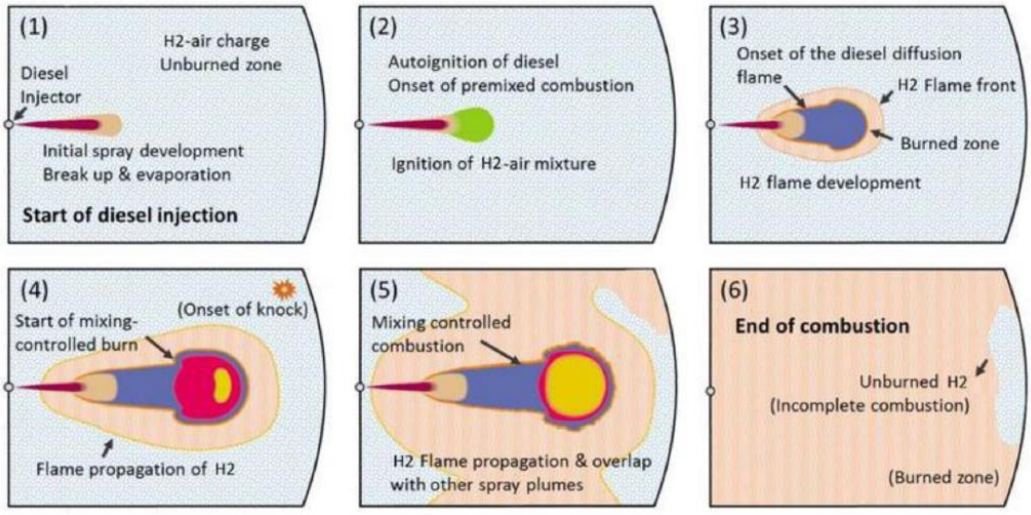

Figure 2.16. Progression of the combustion process of the hydrogen-fuelled diesel engine near TDC. Adapted from *[113]*.

2.5.1 Low- and zero-carbon fuels

In pursuit of decarbonising internal combustion engines, dual-fuel strategies increasingly rely on low- and zero-carbon fuels as partial replacements for diesel. Among these, methane and hydrogen have emerged as key candidates due to their potential to reduce CO_2 and overall GHG emissions. Methane, as the main component of natural gas (NG), is widely available and compatible with existing infrastructure. Hydrogen, in contrast, is carbon-free and offers superior combustion properties. Additionally, blending hydrogen with methane offers a compromise between availability, safety, and combustion enhancement. This section reviews the characteristics and implications of using methane, hydrogen, and their blends in dual-fuel diesel engines.

Natural gas (NG), primarily composed of methane, is a widely distributed fossil fuel extracted from underground reserves. Among all hydrocarbons, methane has the highest hydrogen-to-carbon ratio, making it a relatively low-carbon fuel [110]. It is commonly supplied in the form of compressed natural gas (CNG) or liquified natural gas (LNG). In dual-fuel diesel engines, methane achieves higher diesel replacement levels than other low-reactivity fuels such as liquified petroleum gas (LPG) due to its higher resistance to knock and the higher calorific value of CNG [114].

Methane readily forms homogeneous mixtures with air and has high autoignition resistance. However, its high activation energy leads to lower laminar flame speeds, particularly at low to medium engine loads, which can limit combustion efficiency [111].

Hydrogen, a carbon-free fuel, has gained attention in recent years for its potential to reduce GHG emissions in dual-fuel applications. Compared to hydrocarbon fuels, hydrogen exhibits a significantly faster burning rate – at least six times higher than methane under standard conditions and approximately eight times under the temperature and pressure ranges typical in internal combustion engines. Hydrogen also features a much wider flammability range and higher diffusivity, which enhances air–fuel mixing and promotes more complete combustion [115].

Blending hydrogen with methane can address the combustion limitations of methane by accelerating flame propagation and reducing combustion duration [114]. This

combination leads to faster heat release and sharper pressure rise rates (PRR), ultimately improving indicated thermal efficiency (ITE), as demonstrated in multiple studies [115, 116, 117]. Moreover, methane in the blend acts as a buffer, helping suppress abnormal combustion phenomena such as knock and flashback that are more common in pure hydrogen combustion.

Hydrogen's higher calorific value contributes further to performance improvements. Its wide flammability, together with its rapid combustion, can extend the lean burn capability of the mixture, reducing peak temperatures and associated heat transfer losses, thereby enhancing overall engine efficiency [116]. As a result, hydrogen-enriched methane fuels present a promising pathway to achieve both higher efficiency and lower GHG emissions in dual-fuel engines [118].

Despite its advantages, the widespread use of hydrogen is currently constrained by limited availability and distribution infrastructure. Unlike natural gas, which is accessible in most countries, hydrogen is available in only a few locations. A practical workaround to this issue is the use of premixed methane-hydrogen fuels, which can be distributed through existing natural gas networks [111]. These blends allow hydrogen to be co-distributed without requiring major changes to infrastructure.

In Europe and Asia, these mixtures are commonly referred to as HCNG, while in the USA, the term Hythane is more frequently used. Regulatory standards vary by region; in many European countries, hydrogen content in HCNG is limited to around 9% by energy—mirroring the allowable hydrogen content in transmission-grade natural gas. In contrast, Hythane in the USA typically contains approximately 20% hydrogen by volume. Distributing blends with higher hydrogen content remains technically challenging due to hydrogen's embrittlement effects on steel, which can compromise the integrity of pipelines, storage tanks, and engine components [111].

2.5.2 Potential and limitations of the dual-fuel combustion

An advanced low-temperature combustion (LTC) strategy known as Reactivity Controlled Compression Ignition (RCCI) has demonstrated strong potential for

significantly reducing NOx and soot emissions while enhancing engine efficiency [48, 110]. RCCI works by blending fuels of differing reactivities directly within the cylinder, creating a spatial gradient in fuel reactivity that enables precise control over combustion timing [119]. This is commonly implemented using early injection of the high-reactivity fuel – such as diesel – and high levels of EGR.

Despite its benefits, RCCI is highly sensitive to variations in intake air temperature and pressure due to its premixed and kinetics-driven combustion characteristics [79]. In the context of dual-fuel combustion, applying RCCI principles can offer a promising route to improving both performance and emissions.

For example, Pedrozo et al. [120] demonstrated that using RCCI mode in a diesel-CNG dual-fuel combustion with an 80% CNG energy fraction – combined with a Miller cycle via LIVC – enabled approximately 20% reduction in CO_2 emissions while maintaining diesel-equivalent thermal efficiency. This high substitution rate also provided a favourable balance among NOx emissions, peak in-cylinder pressure, PRR, and overall efficiency. Such findings suggest that adapting RCCI strategies in dual-fuel systems could be a key enabler for cleaner and more efficient heavy-duty engine technologies.

Extensive research has been conducted on diesel-natural gas dual-fuel combustion, particularly with CNG [109, 121, 122, 123, 124]. Natural gas, predominantly methane, enables significant carbon-based emissions reduction. However, natural gas dual-fuel operation faces challenges, such as increased CO and HC emissions, particularly under low-load conditions [125]. These are often attributed to incomplete combustion due to poor mixture reactivity. The pilot diesel amount plays a key role in ensuring stable ignition; insufficient pilot can lead to misfiring and combustion inefficiencies.

Although less studied than pure hydrogen or natural gas, hythane – typically a blend of 70–90% methane and 10–30% hydrogen – serves as an effective intermediate between natural gas and hydrogen. By combining the stable ignition properties of methane with the high flame speed of hydrogen, hythane offers a promising solution to address some of the limitations observed in natural gas dual-fuel systems. As the hydrogen fraction in hythane increases, the combustion characteristics start to

resemble those of hydrogen, providing a smooth transition toward higher hydrogen fractions in dual-fuel operations [126].

In comparative tests by Zhou et al. [125], diesel-hythane operation consistently reduced PM emissions compared to diesel-only operation. When assessing emission trends, higher hydrogen content (e.g., 70% hydrogen, 30% methane) was favorable for reducing CO and HC at low- and medium-loads. However, this same composition increased NOx emissions at higher loads. In contrast, a lower hydrogen fraction (e.g., H30-M70) was deemed more effective for reducing NOx and fuel consumption. Mansor et al. [127] also noted that NOx emissions rise with increasing hydrogen concentration in the hythane mixture, due to elevated in-cylinder temperatures, suggesting an optimal composition of H70-M30 for balancing performance and emissions.

However, due to incomplete or knocking combustion, this technology has a limited engine operation window, mostly at lower and higher loads [128]. Also, methane-based dual-fuel combustion may produce unburned CH_4 emissions [120], often known as methane slip, which can offset the GHG emissions.

On the other hand, conventional diesel engines to operate on a diesel-hydrogen dual-fuel mode typically allows for a hydrogen energy fraction of 30–40% under low- and medium-load conditions [129, 130], and between 6–25% at full-load without significant sacrifices in performance parameters such as power and efficiency [131, 132, 133]. These figures, however, are considerably lower compared to the substitution ratio achievable with methane-based dual-fuel operations. The introduction of high amounts of hydrogen into CI engines under dual-fuel operation introduces several challenges, including excessive PRR, which increases the risk of knocking [134, 130], and higher in-cylinder temperatures. This may lead to auto-ignition of the premixed hydrogen-air mixture, as well as a loss of available work due to advanced combustion timing [135, 136].

Research suggests that these challenges can be mitigated through LTC strategies, such as Homogeneous Charge Compression Ignition (HCCI) or Partial HCCI (PHCCI), water injection, reduced compression ratio, retarded diesel injection timing, intake air

cooling, and EGR [137, 138, 139]. These strategies enhance the hydrogen energy fraction while minimising NOx emissions.

When hydrogen is added to a CI engine, the in-cylinder pressure tends to rise at higher loads but decreases at lower loads. A reduction in diesel fuel, which serves as the ignition source, negatively impacts engine performance at low loads more than at high and medium loads. The findings of Santoso et al. [140] found that lower amounts of diesel fuel resulted in later combustion onset and lower in-cylinder pressure. As the hydrogen energy share increases from 50% to 97%, the in-cylinder pressure decreases substantially due to fewer ignition centres being formed by the smaller amount of diesel fuel, combined with poor spray characteristics and inefficient diesel fuel-air mixing.

At medium and high loads, however, these trends are reversed. The higher burning velocity of hydrogen contributes to a rapid and complete oxidation of the air-fuel charge, significantly increasing in-cylinder pressure [141, 137]. Liew et al. [141] reported that a substantial increase in peak cylinder pressure occurred when hydrogen was added at 70% load. It was also emphasised that, for safety and mechanical durability reasons, hydrogen should be limited at high loads to control the peak cylinder pressure [137].

From these studies, a clear pattern emerges: in a dual-fuel engine using hydrogen, in-cylinder pressure rises with increasing load but decreases at lower loads.

Regarding the combustion process, a diesel-hydrogen dual-fuel engine experiences poorer performance at low loads as the gaseous fuel fraction increases or the pilot diesel quantity decreases. The degree of performance degradation at low load depends significantly on the pilot fuel amount, the type of gaseous fuel, operating conditions, and the engine type [138]. At low load, both the ignition delay and incomplete combustion are exacerbated with the addition of gaseous fuels [138, 142], strongly affecting the combustion efficiency [141]. In contrast, at higher loads, the energy released mainly from the combustion of the gaseous fuel-air mixture reduces such issues, as the heat is predominantly derived from the gaseous fuel rather than the pilot diesel zones.

Studies have also shown that the addition of hydrogen at 70% load significantly shortens combustion duration and increases the peak heat release rate observed during diffusion combustion [141]. The fast-turbulent combustion of hydrogen, combined with diesel's diffusion combustion, leads to an increase in the heat release rate (HRR) [143].

In terms of overall performance, it has been reported that thermal efficiency improves at medium and high loads with increasing hydrogen fraction but decreases at low loads [144]. Likewise, NOx formation generally rises with the addition of hydrogen, while N_2O emissions are typically higher at lean conditions and significantly lower for rich mixtures [145]. However, research into the specific effects of hydrogen on N_2O emissions in dual-fuel engines remains limited. Additionally, carbon-based emissions such as soot, HC, CO, and CO_2 can be substantially reduced, usually by over 50% when the hydrogen substitution rate reaches 40% [146, 147, 130], owing to the enhanced homogeneity of the hydrogen-air mixture and faster combustion compared to CDC [134].

For instance, Monemian et al. [148] demonstrated that with a 35% hydrogen energy fraction in a 2.0 L single-cylinder heavy-duty diesel engine operating under medium load conditions (1.2 MPa IMEP), indicated efficiency increased by 2.4%, and CO_2, CO, and PM emissions were reduced by 27%, 45%, and 71%, respectively. However, NOx emissions increased by 56%, although the engine was still expected to meet Euro VI NOx limits with a 90% conversion rate after NOx aftertreatment. Under low-load conditions (0.3 MPa IMEP), a hydrogen energy fraction of 65% resulted in a 4.6% improvement in indicated efficiency, with CO_2, CO, and PM reductions of 58%, 83%, and 58%, respectively, while NOx emissions increased by 26%.

Contrary to some of the above studies, Saravanan et al. [149] reported that NOx emissions could be reduced if the hydrogen energy fraction exceeds 30%, attributing this to a reduction in peak combustion temperatures.

To tackle the NOx issue, Kumar et al. [2] proposed using EGR to dilute the air-fuel charge and reduce the oxygen concentration, thus lowering peak combustion temperatures. While EGR reduces volumetric efficiency by approximately 15%, it has

been shown to increase particulate emissions. The use of EGR also leads to an increase in unburned HC, CO, and CO_2 emissions.

Similarly, Karagoz et al. [150] conducted tests on a 0.8 L diesel engine under full-load conditions and found that, despite reductions in CO_2, CO, and PM emissions, and a consequent rise in NOx emissions, thermal efficiency dropped by 8.1% and 15.5% with 25% and 50% hydrogen energy fractions, respectively. This reduction can partly be explained by the decrease in volumetric efficiency of the naturally aspirated engine as hydrogen energy fraction increased, as well as a notable drop in output power.

Research exploring the influence of compression ratio on hydrogen substitution in diesel-hydrogen dual-fuel engines remains relatively limited. Nonetheless, existing studies indicate that a higher compression ratio can enhance engine performance under certain conditions [142, 151, 152]. On the other hand, lowering the compression ratio has been proposed as a method to increase the hydrogen energy fraction by reducing in-cylinder temperatures and improving the engine's resistance to knocking [152].

In a comparative study, Chintala et al. [153, 137] reported a substantial rise in hydrogen energy contribution – from approximately 19% at a compression ratio of 19.5 to 59% at a reduced ratio of 16.5. Meanwhile, Masood et al. [151] found that, at full engine load, higher compression ratios led to significant increases in peak in-cylinder pressure (by 42%), thermal efficiency (by 27%), and NOx emissions (by 38%), accompanied by reductions of around 20% in HC, CO, and PM emissions.

The combination of reduced compression ratios with water injection has also shown promise in further boosting hydrogen substitution levels in CI dual-fuel configurations. Chintala et al. [154] investigated this approach and observed a notable improvement in hydrogen energy fraction when water injection was applied in conjunction with a lower compression setting. The optimal configuration required a water consumption rate of about 340 g/kWh.

Water injection in CI engines has also been studied for its role in NOx mitigation through the reduction of localized high temperatures. Tesfa et al. [96] employed manifold water injection to address NOx emissions from a biodiesel-fuelled CI engine,

reporting a 50% NOx reduction with a water injection rate of 3 kg/h, without compromising engine efficiency—attributed to a decrease in premixed combustion temperature. However, increasing the water-to-air ratio was associated with elevated emissions of HC, CO, and soot [155, 153, 156]. Gonca [93] also documented a 34% reduction in NO emissions with the optimal steam injection rate, equivalent to 20% of the fuel mass, in a 13 kW direct injection diesel engine.

From the literature, it is emerged that water addition into a diesel engine could increase hydrogen energy fraction and decrease the NOx emission drastically due to occurrence of low temperature combustion [142].

Despite the promising characteristics of diesel-hythane and diesel-hydrogen dual-fuel combustion, several key research gaps remain.

In the case of diesel-hythane, most existing studies concentrate on combustion characteristics and emission metrics – particularly NOx, CO, and HC – while offering limited insights into overall CO_2 performance or the full GHG profile. In particular, there is a lack of comprehensive analyses that quantify methane slip alongside CO_2 emissions, which is critical for evaluating the true climate impact of methane-rich fuels. Furthermore, well-to-wheel (WTW) assessment that consider different hythane production pathways are virtually absent in the current literature, despite their importance in determining the long-term sustainability of this fuel. While studies often report the hydrogen-to-methane ratio within hythane, they rarely provide the total hythane energy fraction relative to the overall fuel input—an essential parameter for understanding energy substitution effectiveness and real-world scalability. Additionally, limited research is available on the application of RCCI strategies using hythane as a fuel, despite its potential to improve combustion efficiency and reduce emissions, which represents a key area for future exploration.

For diesel-hydrogen dual-fuel systems, inconsistencies in reported thermal efficiency trends, particularly at high hydrogen substitution levels and full-load operation, which calls for systematic experimental validation. Additionally, most studies to date have achieved relatively low hydrogen energy substitution across the entire load range, highlighting the need for improved engine strategies to enable higher and more stable

hydrogen integration. Likewise diesel-hythane, the current literature is primarily focused on combustion characteristics, with limited consideration of full-cycle environmental impacts. As a result, comprehensive analyses of GHG emissions are lacking – particularly with respect to N_2O – and there is a clear absence of WTW assessments that consider different hydrogen production pathways. A detailed evaluation of hydrogen's climate impact is essential to accurately quantify its potential in decarbonising the heavy-duty engine sector. Lastly, targeted engine optimisation for NOx reduction remains a priority, as increased hydrogen content typically elevates combustion temperatures and NOx formation.

As a result, addressing these gaps will be critical to advancing the viability of hythane and hydrogen as sustainable fuels in compression ignition engines.

2.6 Summary

This chapter highlights the need for a cleaner and more sustainable transport sector in response to climate change and increasing levels of air pollution. The transition to high-efficiency vehicles and the use of low- and zero-carbon fuels, such as methane-based mixtures like hythane, and hydrogen, represent significant steps towards achieving these goals. In this context, heavy-duty diesel engines and vehicle technologies are crucial to meeting stringent exhaust emission regulations. Various alternative combustion strategies that aim to simultaneously reduce exhaust emissions and improve fuel conversion efficiency have been presented.

The key advantages and challenges associated with dual-fuel engines have been explored. While diesel-hydrogen and diesel-hythane dual-fuel systems show promise for reducing carbon-based emissions from the transport sector and decreasing dependency on petroleum, further research is required to optimise engine control techniques and the combustion process. This is essential to address the unique challenges presented by these fuel types, such as increased NOx emissions and potential engine knocking issues. Future investigations should also focus on Well-to-Wheel assessments to quantify the climate impact of these fuels, offering a clearer understanding of their role in reducing the carbon footprint of heavy-duty engines.

Chapter 3
Experimental methodology

3.1 Introduction

This dual-fuel study was carried out using a single-cylinder HD diesel engine configured with separate port-fuel injection systems for hythane and hydrogen, coupled to an eddy current dynamometer. Section 3.2 provides a detailed overview of the engine setup and the test cell infrastructure used throughout the experiments. The procedures for data analysis are outlined in Section 3.3, and the engine testing methodology is described in Section 3.4.

3.2 Experimental setup

Figure 3.1 presents a schematic layout of the engine test bench used in this study, while Figure 3.2 shows a photograph of the test cell setup. The test bench incorporated a range of components, including a single-cylinder HD diesel engine fitted with a hydraulic lost-motion VVA system on the intake camshaft, a dynamometer, a closed-loop controlled external boosting system, a high-pressure loop (HPL) cooled EGR circuit, and separate port fuel injection systems for hythane and hydrogen, enabling dual-fuel operation. Emission analysers, along with data acquisition (DAQ) and control systems, were also integrated into the setup.

Engine coolant and lubrication oil were supplied from external sources, and their temperatures – along with those of the intake air and EGR – were regulated using water-cooled heat exchangers.

Prior to testing, all equipment within the test cell was calibrated. Additionally, daily system checks were performed before each test session. The detailed specifications of the measurement instruments are provided in Appendix A.

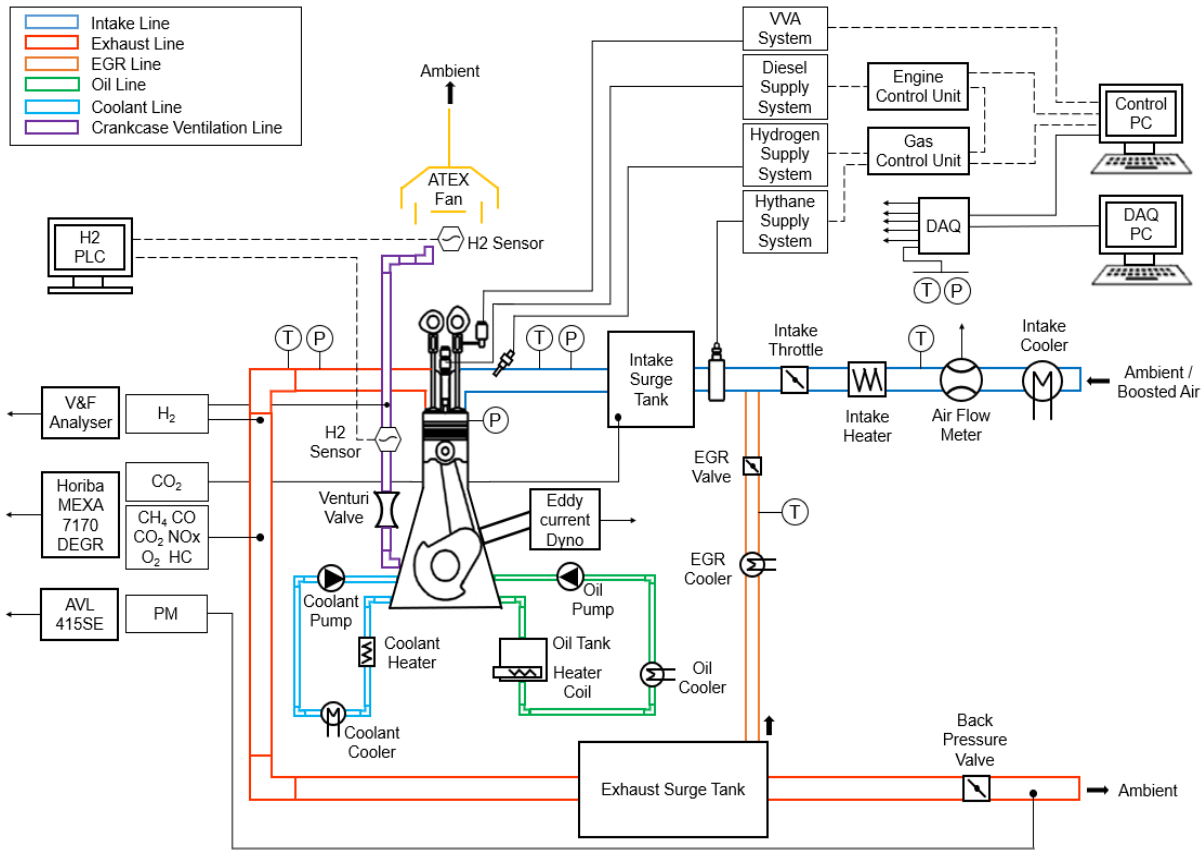

Figure 3.1 – Schematic diagram of the engine experimental setup.

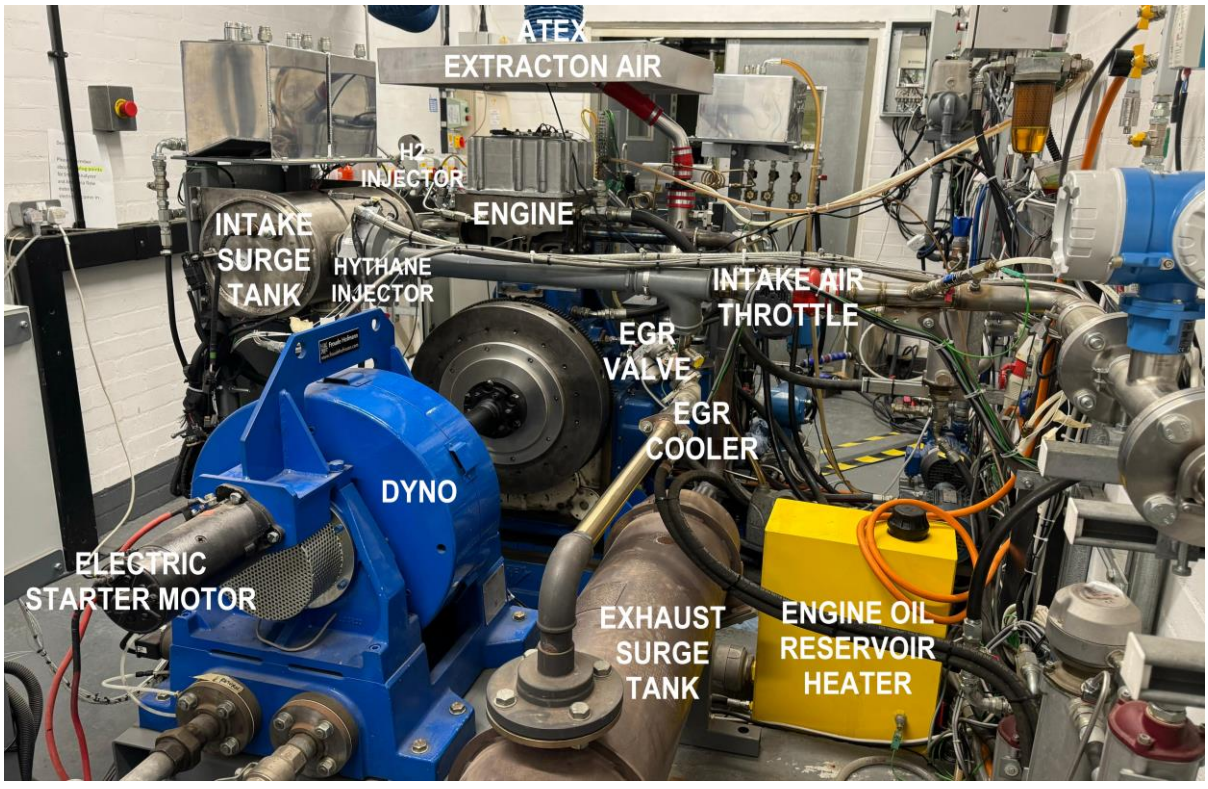

Figure 3.2 – Overview of the engine test bench.

3.2.1 Engine specifications

The experimental setup was based on a single-cylinder HD diesel engine, representative of modern heavy-duty vehicle powertrains. The combustion chamber featured a 4-valve swirl-enhancing cylinder head paired with a stepped-lip piston bowl, adapted from the Yuchai YC-6K six-cylinder engine architecture. The lower engine assembly was developed by AVL and included dual counter-rotating balance shafts to reduce vibration. Key specifications of the engine hardware are provided in Table 3.1.

Table 3.1 – Specification of the research engine.

Parameter	Value
Displaced volume	2026 cm^3
Clearance volume	128 cm^3
Bore x Stroke	129 x 155 mm
Connecting rod length	256 mm
Geometric compression ratio	16.8
Maximum in-cylinder pressure	18 MPa
Piston type	Stepped-lip bowl
Number of valves	4
Intake valve diameter	43.9 mm
Exhaust valve diameter	40.4 mm
Intake valve opening/closing (IVO/IVC)	Variable
Exhaust valve opening/closing (EVO/EVC)	144/360 CAD ATDC (0.5mm valve lift)
Maximum intake/exhaust valve lift	12/14 mm
Engine coolant	50% of water / 50% of ethylene-glycol
Engine oil	Comma TransFlow SD 15W-40
Maximum engine speed	1900 rpm

3.2.2 Variable valve actuation system

A prototype lost-motion variable valve actuation (VVA) system, developed by Jacobs Vehicle Systems, was implemented on the intake camshaft to enable hydraulic control of the intake valve lift profile. This control was achieved through a high-speed solenoid

valve assembly that remained normally open, paired with a specially designed camshaft profile. The mechanism featured a hydraulic collapsing tappet located on the valve side of the rocker arm [157], as illustrated in Figure 3.3. Actuation was managed using engine oil as the hydraulic medium and triggered by a calibrated TTL signal generated from an in-house control platform developed in MATLAB.

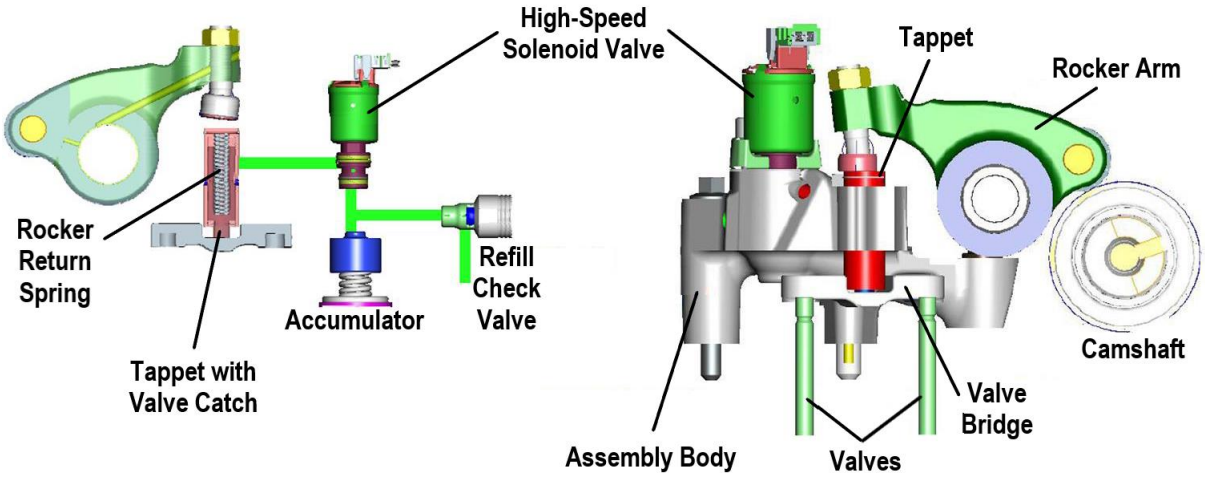

Figure 3.3 – Lost-motion intake VVA system with collapsing tappet on the valve side of the rocker arm [157].

Figure 3.4 illustrates the intake valve lift variability enabled by the VVA system, alongside the constant profile of the exhaust valve lift. By postponing the IVC, the system allows for control over the ECR. Furthermore, it provides the capability to implement a 2IVO strategy to enhance iEGR functionality.

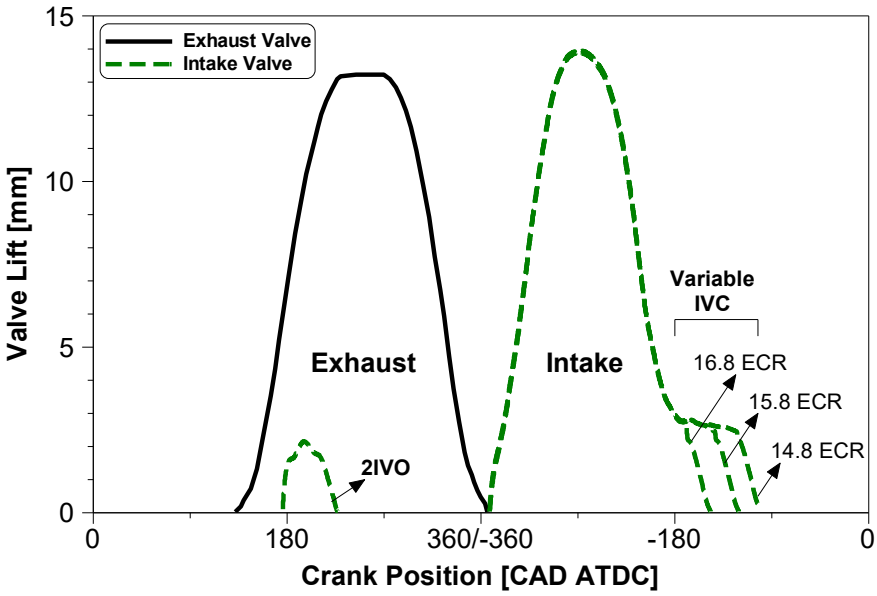

Figure 3.4 – Overview of variable intake valve lift and fixed exhaust valve lift curves.

The main intake valve opening (IVO) event was set at 369 CAD ATDC, as determined at 0.5 mm valve lift. This was essential to minimise the positive overlap period between the intake and exhaust processes in order to prevent any premixed fuel from bypassing the combustion chamber and being directly released through the exhaust. A LORD MicroStrain S-DVRT-24 displacement sensor was installed on the top of the intake valve spring retainer and was employed to measure the intake valve lift.

3.2.3 Dynamometer

A Froude Hofmann AG150 eddy current dynamometer was employed to absorb the engine's output power. This unit had a power rating of 150 kW and a maximum torque capacity of 500 Nm. Engine start-up was facilitated by an electric starter motor integrated into the dynamometer, powered by a 12V battery. Engine load, also known as indicated mean effective pressure (IMEP) was controlled using a Texcel V4-EC controller, which regulated the magnetic field strength within the coils. The induced eddy currents generated a resistive force against the engine's rotation, converting kinetic energy into heat, which was then dissipated through an external water-based cooling system.

3.2.4 Intake and exhaust systems

Fresh air supply to the test cell could be configured either through natural aspiration or boosted operation using an AVL 515 sliding vane compressor, which featured closed-loop control for maintaining the desired boost pressure. This compressor was capable of delivering air flow rates up to 300 m^3/h at an absolute pressure of 320 kPa, with pressure accuracy controlled within ±1.5 kPa. A throttle valve positioned upstream of a 24 dm^3 surge tank allowed precise regulation of intake manifold pressure. The intake air flow rate was measured using an Endress+Hauser Proline t-mass 65F thermal mass flow meter. This device operates based on the cooling effect exerted by the flowing air on a heated transducer. A PT100 temperature sensor provided a reference measurement of the gas temperature, while a second, heated sensor maintained a fixed temperature offset under zero flow conditions. As airflow increased, the resulting cooling effect required a greater electric current to maintain this differential, enabling accurate flow quantification.

In addition, a water (H_2O) injection system was coupled on the intake line downstream of the surge tank. It was composed of a Bosch gasoline injector. The H_2O mass flow rate ($\dot{m}_{water}$) was controlled by adjusting the SOI and the injection pulse width using an NI-9751 Injector Driver Module from National Instruments. Figure 3.5 represents the water injection system. The water was stored in a 24-litre tank, which is pressured by an external compressed air line to a pressure of 0.6 MPa. The water was fed into an Endress+Hauser Proline Promass 80A Coriolis flow meter using a flexible PVC hose, and then delivered to the injector.

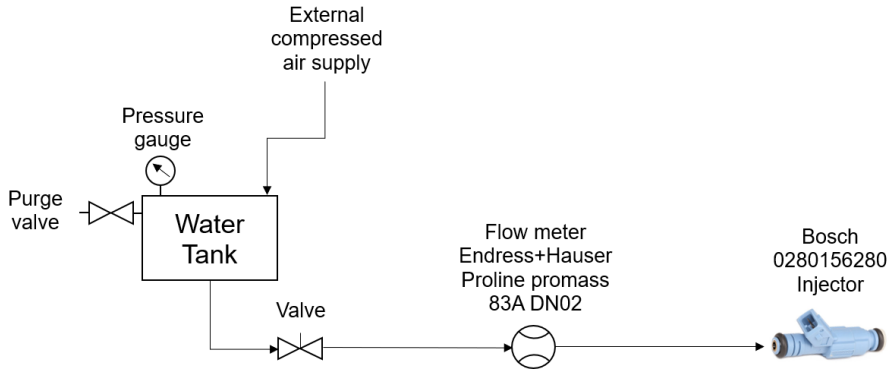

Figure 3.5 – Water injection system.

To regulate exhaust manifold pressure, the system incorporated an electronically controlled butterfly valve positioned downstream of a 54 dm³ surge tank. This surge tank acted as a pressure stabiliser, reducing fluctuations in the exhaust stream prior to EGR extraction. For exhaust gas recirculation, a high-pressure loop configuration was employed, in which cooled exhaust gases were redirected to the intake path. This flow was managed by a pulse-width-modulated EGR valve, which leveraged the pressure differential between the intake and exhaust manifolds to maintain controlled recirculation.

3.2.5 Fuel systems and proprieties

The main properties of the fuels used in this study – diesel, hythane, and hydrogen – are summarised in Table 3.2, with additional details provided in Appendices

The research engine was equipped with independent fuel systems for diesel, hythane, and hydrogen, allowing for flexible dual-fuel operation with adjustable ratios between

diesel and the gaseous fuels. In dual-fuel mode, the majority of the fuel energy was provided by port-injected hythane or hydrogen, which was ignited by a pilot injection of directly injected diesel. Full diesel operation remained possible, supported by appropriately sized diesel injectors. This indicates that the engine was not a dedicated dual-fuel design, which typically requires modified piston geometry and reduced-capacity diesel injectors. A detailed description of the fuel delivery systems is provided in the following sections.

Table 3.2 – Fuel proprieties.

Property	Diesel	Hythane	Hydrogen
Supplier	Speedy Fuels and Lubricants	BOC*	BOC*
Product specification	BS 2869 Class A2		
Liquid density STP	0.827 kg/dm^3	-	-
Gas density STP	-	0.562 kg/m^3	
Cetane number	> 45	< 5	< 5
Research octane number	30	120	130
Lower heating value (LHV)	42.9 MJ/kg	52.1 MJ/kg	120 MJ/kg
Mixture (mole fraction)	-	20% hydrogen 80% methane	100% hydrogen
Stoichiometric air-fuel ratio	14.5:1	17.1:1	34.3:1
Carbon mass fraction	86.6%	72.6%	-
Hydrogen mass fraction	13.2%	27.4%	100%
Oxygen mass fraction	0.2%	-	-
Normalised molecular composition	$CH_{1.825}O_{0.0014}$	$CH_{4.492}$	H_2

* British Oxygen Company

- Diesel

Diesel fuel was supplied to the engine through an 8-hole direct injection Bosch piezo-actuated injector connected to a high-pressure common rail system. Fuel pressurisation was handled by a Bosch CP4-S2 high-pressure pump driven by an ABB electric motor, delivering pressures ranging from 25 to 220 MPa. An independent low-

pressure circuit fed diesel to the high-pressure pump through a pressure regulator and a Bowman heat exchanger, which helped maintain stable fuel temperatures.

Injection parameters – including injection pressure, start of injection (SOI), and the number of injection events (up to three per cycle) – were managed by an engine control unit (ECU) provided by Engine Control Electronics (ECE) GmbH. Communication with the ECU was facilitated using ECE's AP 2.0 software and a USB-CAN interface.

Table 3.3 outlines the technical specifications of the diesel injector, while Figure 3.6 provides a schematic of the diesel injection system. Diesel mass flow rate $\dot{m}_{diesel}$ was measured using two Endress+Hauser Promass 83A Coriolis flow meters. These were placed to monitor the fuel supplied to and returned from the high-pressure pump and injector, a configuration that minimised suction line pressure drop and improved measurement stability.

Table 3.3 – Specifications of diesel injector.

Parameter	Value
Injector	Bosch CRIN3-22 (0446B00482)
Number of hole / Hole diameter	8 holes / 176 μm
Type	Solenoid, mini-sac hole, ks
Included spray angle	150 degrees
Operating rail pressure	25-220 MPa
Static flow meter	1600 cm^3/min at 10 MPa

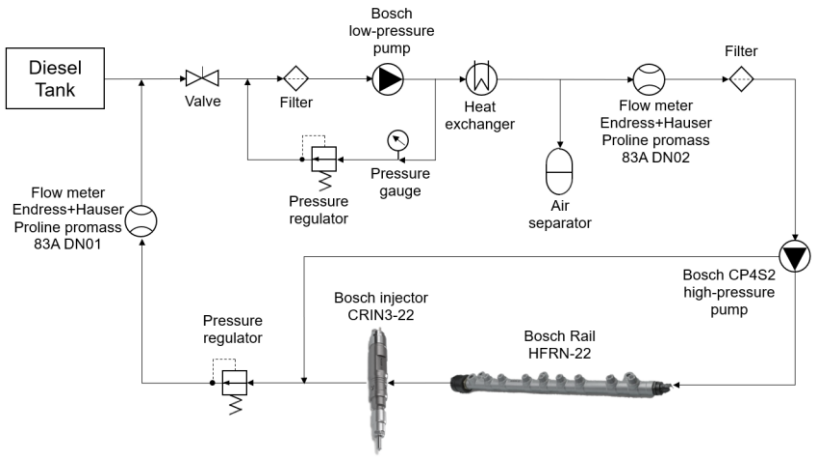

Figure 3.6 – Diesel fuel injection system.

- Hythane

Hythane was introduced upstream of the intake surge tank using an injector block assembly. Originally designed for natural gas applications, the assembly was machined from billet aluminium and featured mounting points for two Clean Air Power SP010 natural gas injectors, along with integrated temperature and pressure sensors. Injection timing and duration were managed by a dedicated gas ECU supplied by G-Volution, which enabled precise control of the hythane mass flow rate ($\dot{m}_{hythane}$). This setup allowed the engine to operate across a range of hythane energy fractions (EFs).

Figure 3.7 presents a schematic representation of the hythane fuel injection system. The hythane was stored externally to the engine test cell in a rack comprising six interconnected cylinders, each pressurised to 20 MPa. To ensure safe handling, the fuel was delivered through CNG-rated hoses featuring a conductive nylon core designed to dissipate static electricity. From the storage rack, the gas passed through two pneumatically actuated safety valves, a high-pressure filter, and a pressure regulator that reduced the supply pressure to 1 MPa. The regulator was thermally stabilised using heated engine coolant to counteract the cooling effect associated with gas expansion. After pressure reduction, the hythane entered the test cell and flowed through an Endress + Hauser Promass 80A Coriolis flow meter for accurate mass flow measurement. Downstream of the flow meter, the system included a low-pressure filter regulator, a purge/pressure regulator that set the final delivery pressure to 0.8 MPa, and an emergency solenoid valve. The gas was then routed to the injector block via a flexible hose for controlled delivery into the engine intake.

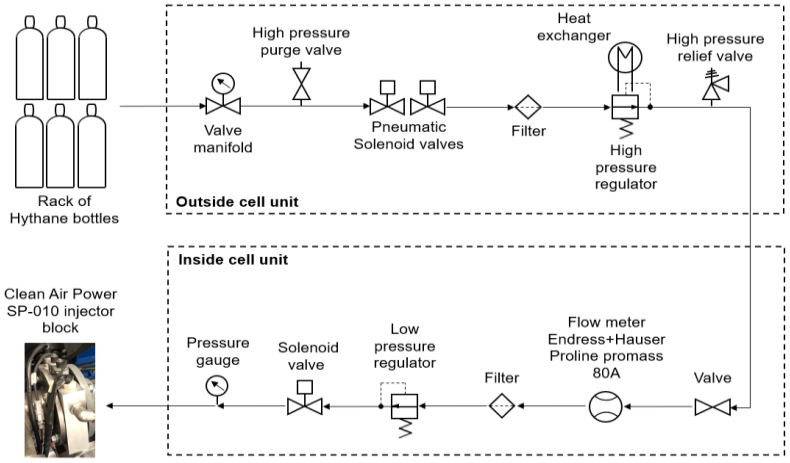

Figure 3.7 – Hythane fuel injection system.

- Hydrogen

Hydrogen fuel was supplied in the intake line immediately prior to the inlet manifold using a Clean Air Power prototype SP-010 hydrogen injector. Similarly to hythane fuel, the hydrogen mass flow rate ($\dot{m}_{hydrogen}$) was controlled by adjusting the injection pulse using the same dedicated gas ECU. This allowed the engine to operate at different hydrogen energy fractions.

Figure 3.8 illustrates a schematic diagram of the hydrogen fuel injection system. Due to safety reasons, all supply line accessories with the exception of the injector were located outside the test cell. This arrangement restricts the number of connections, mitigating the potential risk of hydrogen leakage within the test cell. Therefore, hydrogen fuel was stored outside the engine test cell in a rack of four interconnected 15 MPa bottles. From the interconnected manifold bottles, hydrogen was fed into a first-stage control panel. This panel contained a pressure regulator, which reduced hydrogen pressure to 4 MPa, a high-pressure sensor, a hydrogen flow meter and a solenoid valve. The flow meter was positioned downstream of the initial stage in order to mitigate any pressure drop that could potentially impact on the final pressure delivered to the injector. Hydrogen was then directed to a second stage control panel, where another pressure regulator was employed to reduce hydrogen pressure to the injection pressure of 0.8 MPa. This panel also included an additional pressure sensor and a safety solenoid valve, which serve the function of isolating the line and reducing the amount of hydrogen in the pipe line in case of event of a leak. After flowing through the second stage panel, hydrogen was fed into the test cell directly to the injector.

Furthermore, as depicted in Figure 3.1, the test cell was outfitted with an additional ATEX extraction system that featured a flexible hood and multiple air grilles in order to maximise air ventilation. A hydrogen sensor was installed under the hood extractor, and another was mounted in the crankcase ventilation system. The first sensor detected hydrogen concentration in the test cell's extracted air, while the second sensor measured the hydrogen concentration in the engine crankcase to prevent the potential accumulation of hydrogen. These sensors were connected to an automated shutdown programmable logic controller (PLC) system. This system was designed to automatically shut off the supply line by closing both solenoid valves if the hydrogen

level exceeded 3%. A thermal fuse was also installed in the intake manifold to activate the automated PLC when the intake temperature exceeded 130°C in case of severe backfire during hydrogen PFI operation.

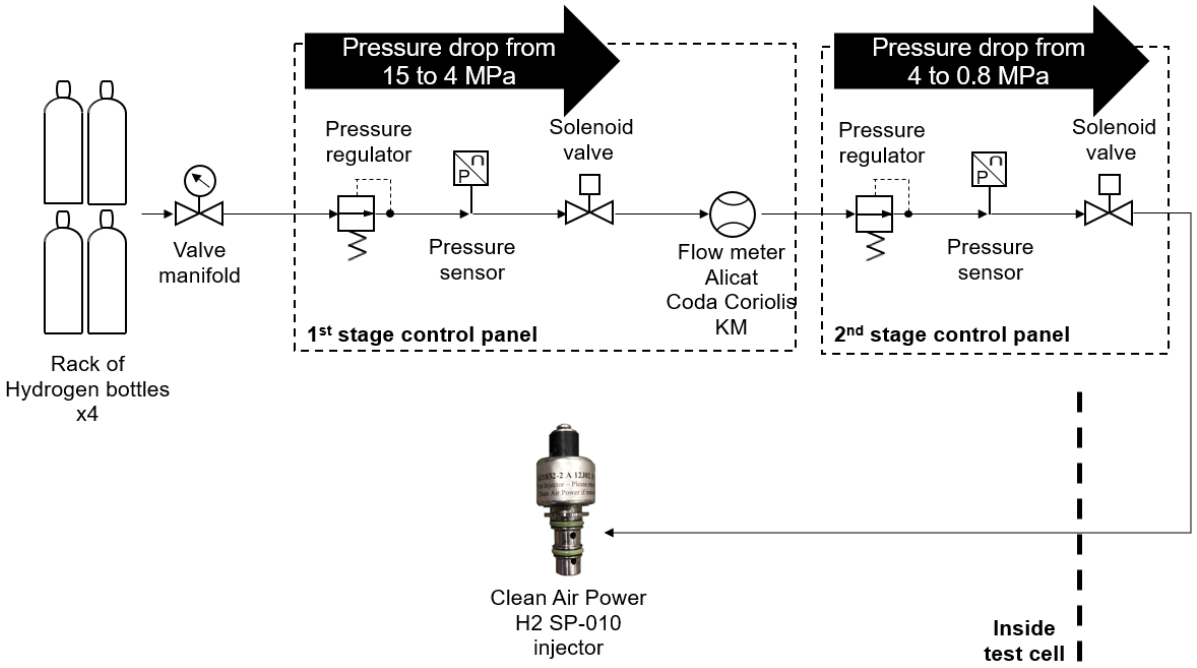

Figure 3.8 – Hydrogen fuel injection system.

3.2.6 Exhaust emissions measurement

The engine-out emissions – namely NOx, CO, CO_2, THC, CH_4, and O_2 – as well as the estimated eEGR rate, were monitored using a Horiba MEXA 7170-DEGR emissions analyser. A high-pressure sampling module enabled extraction of exhaust gases directly after the exhaust manifold, positioned upstream of the back-pressure valve. A heated line maintained the gas temperature at approximately 464 K to avoid condensation. Data transmission between the analyser and the data acquisition system was facilitated through Ethernet connectivity.

Carbon monoxide and carbon dioxide concentrations were quantified on a dry basis (excluding water vapour) using a non-dispersive infrared (NDIR) analyser. This technique operates by detecting the absorption of specific infrared wavelengths by the target gases [160]. The CO and CO_2 detection ranges were configured to 0–120,000 ppm and 0–200,000 ppm (v/v), respectively.

Total unburned hydrocarbons were measured on a wet basis (including water vapour) using a flame ionisation detector (FID) equipped with a heated sampling line. The detection range was set from 0 to 50,000 ppm (v/v). In this method, the gas sample is combusted with a hydrogen-helium mixture and purified air. The resulting combustion of hydrocarbons produces positively charged ions and electrons, which are detected as an electrical current. This current is directly proportional to the number of carbon atoms present in the exhaust gas.

NOx levels were determined by combining the concentrations of NO and NO_2, measured using a heated chemiluminescence detector (HCLD) operating on a dry basis with a range up to 10,000 ppm (v/v). As the device can only directly measure NO, a catalyst was employed to convert NO_2 into NO. The measurement principle involves a chemical reaction between NO and ozone (O_3), forming excited NO_2 molecules that emit red light. The intensity of this light correlates with the NO content in the sample.

Oxygen levels were assessed using a magneto-pneumatic analyser (MPA) operating within a 0–250,000 ppm (v/v) range on a dry basis. This method relies on a nonuniform magnetic field applied to a gas cell, where oxygen accumulates at one magnetic pole. A microphone detects the pressure difference caused by this accumulation.

To calculate the eEGR rate, the Horiba system was also connected to an AIA-722 NDIR analyser, which measured the CO_2 concentration in the intake manifold. The eEGR rate was then derived as the ratio of CO_2 concentration in the intake air to that in the exhaust gases.

$$eEGR\ rate = \frac{CO_{2_{intake}}}{CO_{2_{exhaust}}} \times 100\% \tag{3.1}$$

In addition, engine-out soot emissions were assessed using an AVL Smoke Meter 415SE. The sampling point was positioned downstream of the exhaust back-pressure valve, following the exhaust surge tank. This placement ensured a more uniform and stable exhaust gas flow. A 30-second sampling period was used to collect 5 dm^3 of exhaust gas, which was drawn through a filter paper. Soot presence was evaluated based on the degree of blackening on the paper, as measured by an optical

reflectometer. A Filter Smoke Number (FSN) of 10 indicated complete blackening (no light reflection), while an FSN of 0 corresponded to an unused, clean filter paper.

The concentration of unburned hydrogen was determined using a VF HSense emissions analyser. This analyser operates based on electron impact ionisation, wherein the gas sample is ionised, the ions are focused and subsequently separated by a magnetic field, allowing for accurate measurement of hydrogen content. A heated sampling line was employed to minimise condensation. As with the Horiba MEXA system, data transfer between the VF HSense analyser and the data acquisition system was facilitated via Ethernet communication.

3.2.7 Data acquisition and control

The data acquisition and control infrastructure consisted mainly of a dynamometer controller, two ECUs, a VVA control unit, two DAQ cards, and a pair of computers.

Engine loading and unloading were managed in real time by the TEXCEL V4 dynamometer controller. The diesel ECU governed key injection parameters, including injection pressure, SOI and the number of injection events. Fuel delivery at a given load condition was automatically regulated by the ECU based on a speed governor mechanism. If the engine speed dropped below the target value, additional fuel was injected to restore it; conversely, less fuel was supplied if the speed exceeded the setpoint.

Under dual-fuel operating mode, the supply of gaseous fuels – hythane and hydrogen – was managed by a separate gas ECU. This unit adjusted gas delivery based on input pulse width, which indirectly reduced diesel injection through the same speed-governing logic. Communication between the ECUs and the computer system was enabled using a USB-to-CAN interface along with dedicated software.

To capture signals from the various sensors and instruments, two National Instruments DAQ cards were employed alongside a host computer. High-speed data were handled by a USB-6251 DAQ card, capable of sampling at up to 1.25 mega samples per second (MS/s), while slower engine operating parameters were collected using a USB-

6210 DAQ card with a 0.25 MS/s capacity. These data streams were processed in real time using a transient combustion analysis application developed by Dr. Yan Zhang [158], and visualised through the software interface as shown in Figure 3.9. Each data set displayed represented 100 engine cycles.

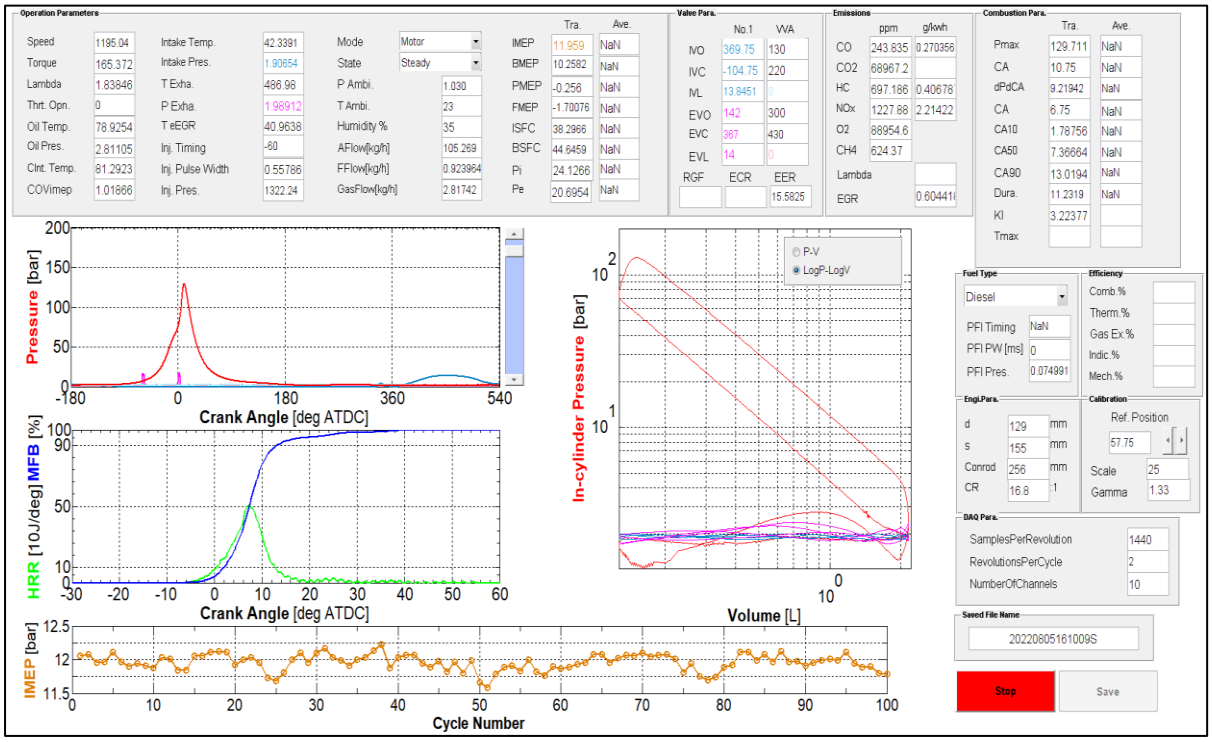

Figure 3.9 – DAQ transient combustion analyser software.

Engine speed was recorded using the dynamometer's electromagnetic pulse pickup system in conjunction with a toothed wheel mounted on the shaft half-coupling hub. Engine load measurements were performed using a Thames Side Sensor U4000 Universal tension load cell attached to the dynamometer. Crank angle position was determined by a high-resolution EB58 optical encoder installed on the engine crankshaft, featuring 1440 pulses per revolution and a resolution of 0.25 crank angle degrees (CAD).

In-cylinder pressure, used to calculate the indicated mean effective pressure (IMEP), was captured by a Kistler 6125C piezoelectric pressure sensor. This sensor was capable of measuring pressures up to 30 MPa, with a charge sensitivity of -0.3122 pC/kPa. The generated charge signal was converted into a voltage signal via an AVL FI Piezo charge amplifier. The amplifier was operated in cyclic drift compensation mode with a 100 kHz filter setting to minimise zero drift and phase shift errors. Since

the piezoelectric sensor measures only pressure fluctuations, absolute in-cylinder pressures were pegged to the average intake manifold pressure at bottom dead centre (BDC) during the intake stroke across all cycles. A reference (REF) trigger signal was used to synchronise the TDC position, ensuring that the motored peak cylinder pressure was phased between -1.0 and -0.5 CAD after TDC.

Intake and exhaust manifold pressures were recorded using Kistler 4049A water-cooled piezoresistive absolute pressure sensors, each connected to a Kistler 4622A signal amplifier. Engine oil pressure was measured by a GE UNIK 5000 pressure transducer. K-type thermocouples and pressure transducers were installed at key locations to monitor various temperatures and pressures throughout the system.

Intake valve timing was controlled through the DAQ software, which communicated with the VVA control unit via an analog output channel from the high-speed DAQ card. Real-time valve lift data was collected using an S-DVRT-24 displacement sensor connected to a LORD MicroStrain DEMOD-DVRT temperature-compensated signal conditioner. The intake valve lift curve was post-processed with a timing delay of 0.56 ms, corresponding to 4 CAD at 1200 rpm. IVO and IVC events were identified at a valve lift threshold of 0.5 mm.

Fuel injection pressure was monitored by a Bosch RDS4.5 high-pressure sensor mounted on the common rail. Additionally, diesel injector current signals were acquired using an LEM PR30 current probe.

3.3 Data analysis

For each engine operating condition, the DAQ software recorded two consecutive sets of 100 cycles, resulting in a total of 200 continuous cycles per test point. The recorded data were subsequently exported to an Excel spreadsheet for post-processing of parameters not calculated in real-time, including thermal efficiencies, fuel consumption, and specific emissions. Detailed descriptions of the relevant equations and data processing steps are provided within this section. To enhance readability, all variables and abbreviations are defined in the notation section, with values expressed in SI units unless otherwise indicated.

3.3.1 Heat release rate

Several key metrics, including the heat release rate (HRR), can be derived from the measured in-cylinder pressure and crankshaft position data. To estimate these values, a single-zone heat release model was applied, assuming homogeneous internal energy distribution between reactants and combustion products within the chamber. Under this assumption, the net chemical energy released by the fuel is directly related to the changes in in-cylinder pressure. Consequently, the combustion process was modelled using an energy balance equation, shown in Equation (3.2), which is based on an adaptation of the first law of thermodynamics.

$$dQ_{ch} = dW + dU_s + dQ_{ht} + \sum h_i dm_i \tag{3.2}$$

In this context, $\mathrm{Q_{ch}}$ denotes the chemical energy released by the fuel, W refers to the work performed by the combustion gases on the piston, and U_s represents the change in internal energy of the cylinder contents resulting from the combustion reaction. The term $\mathrm{Q_{ht}}$ accounts for heat transfer to the combustion chamber walls. The mass flux component $\mathrm{h_i dm_i}$ captures mass exchange across the system boundaries, such as fuel injection or gas movement from crevice volumes. It is assumed that the temperature within the cylinder charge remains spatially uniform, allowing the universal gas constant (R) in the ideal gas law $(\mathrm{pV = mRT})$ to remain constant. These simplifications lead to the derivation of Equation (3.3), following the approach described in [34].

$$dQ_{ch} = \left(\frac{C_v}{R}\right) V\, dp + \left(\frac{C_v}{R} + 1\right) p\, dV + dQ_{ht} + (h_{cr} - u + c_v T) dm_{cr} \tag{3.3}$$

Equation (3.3) can be further simplified by combining the chemical energy release term with the contributions from heat transfer and mass flux. This simplification leads to a focus solely on the work performed by the gases on the piston and the change in sensible internal energy, resulting in what is referred to as the apparent net heat release, (Q_{net}). Additionally, by differentiating Equation (3.3) with respect to crank angle position and assuming semi-perfect gas behaviour, the ratio $\left(\frac{\mathrm{C_v}}{\mathrm{R}}\right)$ can be expressed as $\left(\frac{\gamma}{\gamma-1}\right)$, yielding the simplified form presented in Equation (3.4).

$$HRR = \frac{dQ_{net}}{d\theta} = \frac{1}{\gamma - 1} V \frac{dp}{d\theta} + \frac{1}{\gamma - 1} p \frac{dV}{d\theta} \tag{3.4}$$

where $d\theta$ is the crank angle of 0.25 CAD as set by the encoder resolution, γ is the ratio of specific heats, while p and V are the in-cylinder pressure and volume at any crank angle position θ. The ratio of specific heats was assumed constant at 1.33 throughout the entire engine cycle as suggested by [159], although it is known that this value may change with the mixture composition and temperature. The in-cylinder V at any crank angle position was given by

$$V_i = V_c + \frac{V_d}{2}\left\{\left(\frac{l}{a}\right) + 1 - cos\,\theta - \left[\left(\frac{l}{a}\right)^2 - sin^2\,\theta\right]^{\frac{1}{2}}\right\} \tag{3.5}$$

The mass fraction burned (MFB) was calculated by integrating Equation (3.4) and referencing the maximum cumulative heat release. Combustion phasing (CA50) was defined as the crank angle at which 50% of the fuel mass had been burned. The combustion duration (CA10-CA90) was identified as the interval between the crank angles corresponding to 10% and 90% cumulative heat release. Ignition delay was measured as the time interval between the start of injection (SOI or SOI_2) and the start of combustion (SOC), which was defined as the crank angle at 2% MFB of the average cycle.

The pressure rise rate (PRR) serves as a key indicator of combustion-induced noise, as it reflects the rate at which heat release occurs. Expressed in MPa per crank angle degree (MPa/CAD), the PRR was determined by averaging the peak pressure gradients across 200 engine cycles and relating them to the corresponding crank angle positions, as shown in Equation (3.6).

$$PRR = \sum_{n=1}^{200} PRR_{max} \,/\, n = \sum_{n=1}^{200} \left(\frac{dp}{dt}_{max}\right) / \, n \tag{3.6}$$

The average in-cylinder pressure and HRR curves were post-processed using a third-order Savitzky-Golay filter with a five-point window to reduce signal noise.

3.3.2 Overall engine parameters

The net indicated work exerted on the piston throughout the complete engine cycle ($W_{c,ind}$) was calculated using Equation (3.7), with the zero crank angle position referenced to the firing TDC. This calculation involved integrating the in-cylinder pressure over the corresponding cylinder volume across the full four-stroke cycle.

$$W_{c,ind} = \int_{-180}^{540} p_i dV \tag{3.7}$$

The net indicated power (P_{ind}), given in kilowatts, was defined as the rate at which net indicated work is converted from the in-cylinder gas to the piston, as described in [34].

$$P_{ind} = \frac{W_{c,ind}\, N}{2 \times 60} \times 10^3 \tag{3.8}$$

At a given operating condition, engine load was characterised by the net indicated mean effective pressure (IMEP), expressed in MPa. IMEP serves as a useful comparative metric for engine performance, particularly across engines of varying displacement sizes. It was calculated as the ratio of $W_{c,ind}$ over the full four-stroke cycle to the engine's swept volume (V_d), as presented in Equation (3.9). It is worth noting that when the $W_{c,ind}$ is evaluated over only the compression and expansion strokes, the result is referred to as gross indicated mean effective pressure ($IMEP_{gross}$), as shown in Equation (3.10) [34].

$$IMEP = \frac{\int_{-180}^{540} p_i dV}{V_d} \tag{3.9}$$

$$IMEP_{gross} = \frac{\int_{-180}^{180} p_i dV}{V_d} \tag{3.10}$$

The pumping mean effective pressure (PMEP) represents the net work exchanged between the piston and the in-cylinder gas during the intake and exhaust strokes, as defined in Equation (3.11). PMEP is generally negative, indicating pumping losses associated with gas exchange. However, as intake and exhaust flow losses are reduced and the gas exchange process becomes more efficient, the magnitude of PMEP decreases (i.e., it becomes less negative, reflecting reduced pumping work.

$$PMEP = IMEP - IMEP_{gross} \tag{3.11}$$

Combustion and in-cylinder flow stability were assessed on a cycle-by-cycle basis using the coefficient of variation of IMEP (COV_{IMEP}), calculated over the 200 recorded cycles as follows:

$$COV_{IMEP} = \frac{IMEP_{std}}{IMEP_{avg}} \times 100\% \tag{3.12}$$

The net indicated thermal efficiency (ITE) was defined as the ratio of the net indicated work to the rate of fuel energy supplied to the engine. This metric is particularly valuable for comparing relative engine performance, as it excludes mechanical losses. It is important to note that in Equations (3.13), (3.14), and (3.15), the gas fuel component refers to either hythane or hydrogen, depending on the specific dual-fuel combustion mode examined in the corresponding chapters.

$$ITE = \left[\frac{3.6\ P_{ind}}{(\dot{m}_{diesel}\ LHV_{diesel}) + (\dot{m}_{gas\ fuel}\ LHV_{gas\ fuel})}\right] \tag{3.13}$$

In combustion systems utilising multiple fuels, the net indicated specific fuel consumption equivalent ($\mathrm{ISFC_{eq}}$) is defined by Equation (3.14), and expressed in grams per kilowatt-hour (g/kWh) [160, 161].

$$ISFC_{eq} = \frac{\dot{m}_{diesel} + \dot{m}_{gas\ fuel}\dfrac{LHV_{gas\ fuel}}{LHV_{diesel}}}{P_{ind}} \tag{3.14}$$

A key metric in dual-fuel operation was the energy fraction of hythane or hydrogen, defined as the ratio of the energy contribution from the gaseous fuel to the total fuel energy supplied to the engine.

$$EF = \frac{\dot{m}_{gas\ fuel}\ LHV_{gas\ fuel}}{(\dot{m}_{diesel}\ LHV_{diesel}) + (\dot{m}_{gas\ fuel}\ LHV_{gas\ fuel})} \tag{3.15}$$

Additionally, the mass fraction of hythane or hydrogen was defined as the ratio of the gas fuel mass to the total mass of fuel injected, as shown in Equation (3.16).

$$MF = \frac{\dot{m}_{gas\ fuel}}{\dot{m}_{diesel} + \dot{m}_{gas\ fuel}} \tag{3.16}$$

3.3.3 Mean in-cylinder gas temperature

The mean in-cylinder gas temperature at a specific crank angle position θ was estimated using the ideal gas law, as described in [34], and expressed as:

$$T_{cyl,i} = \frac{p_i \, V_i \, M_b}{m_{total} \, \tilde{R}} \tag{3.17}$$

where $\widetilde{\mathrm{R}}$ is the universal gas constant, valued at 8.31432 J/mol.K [34], and $\mathrm{M_b}$ represents the molecular weight of the burned gas in g/mol, which was determined using the following expression:

$$M_b = \frac{m_{RP}}{n_b} \tag{3.18}$$

where $\mathrm{m_{RP}}$ denotes the mass (including both burned and unburned components) per mole of O_2 in the mixture, and $\mathrm{n_b}$ represents the number of moles of burned gas. These parameters were calculated using Equations (3.19), (3.20), and (3.21), as outlined in Heywood [34].

$$m_{RP} = 32 + 4\,\Phi\,\zeta\left(1 + \frac{8}{4+y}\right) + 28.16 \times 3.773\,\zeta\left(1 - \frac{4\,z}{8+2y}\right) \tag{3.19}$$

$$n_b = \Phi\,\zeta\left(1 - \frac{4}{4+y}\right) + 1 + 3.773\,\zeta\left(1 - \frac{4\,z}{8+2y}\right) \tag{3.20}$$

$$\zeta = \frac{2}{2 - \frac{4\,z}{4+y}(1-\Phi)} \tag{3.21}$$

The term $\mathrm{m_{total}}$ in Equation (3.17) represents the total in-cylinder mass per cycle and is defined as:

$$m_{total} = m_{fuel} + m_{air} + m_{rg} \tag{3.22}$$

where $\mathrm{m_{fuel}}$ is the mass of injected fuel per cycle (e.g. diesel, hythane, hydrogen, etc.), and $\mathrm{m_{air}}$ is the mass of intake fresh air per cycle. $\mathrm{m_{rg}}$ is the mass of residual gas

trapped at IVC, which can be calculated using Equation (3.23) for cases without positive valve overlap.

$$m_{rg} = \frac{p_{EVC}\, V_{EVC}\, M_b}{EGT\, \tilde{R}} \tag{3.23}$$

where $\mathrm{p_{EVC}}$ is the in-cylinder gas pressure at exhaust valve closing (EVC), $\mathrm{V_{EVC}}$ is the corresponding in-cylinder volume, and EGT denotes the average exhaust gas temperature, measured using a K-type thermocouple.

It is important to note that for engine tests employing the 2IVO strategy, a correlated one-dimensional (1D) engine model was required to estimate $\mathrm{m_{rg}}$. This approach was necessary due to the complex gas flow dynamics in which residual gases are expelled into the intake port during the exhaust stroke and subsequently drawn back into the cylinder during the intake stroke.

3.3.4 Engine-out exhaust emissions

The exhaust emissions data obtained from the Horiba analyser were initially captured by the DAQ system in ppm. To enable performance-based comparisons, these values were converted into specific emissions, expressed in grams per kilowatt-hour (g/kWh). The conversion followed the procedure specified in Regulation No. 49 of the United Nations Economic Commission for Europe [21]. Using this methodology, Equations (3.24) to (3.29) were applied to determine the net indicated specific emissions for NOx, CO, CO_2, THC, CH_4, non-methane hydrocarbons (NMHC), H_2, and N_2O.

$$ISNOx = \frac{\dot{m}_{NOx}}{P_{ind}} = \frac{u_{NOx}\,[NOx]\,\dot{m}_{exh}\,k_w\,k_h}{P_{ind}} \tag{3.24}$$

$$ISCO = \frac{\dot{m}_{CO}}{P_{ind}} = \frac{u_{CO}\,[CO]\,\dot{m}_{exh}\,k_w}{P_{ind}} \tag{3.25}$$

$$ISCO_2 = \frac{\dot{m}_{CO2}}{P_{ind}} = \frac{u_{CO2}\,[CO_2]\,\dot{m}_{exh}}{P_{ind}} \tag{3.26}$$

$$ISTHC = \frac{\dot{m}_{THC}}{P_{ind}} = \frac{u_{HC}\,[THC]\,\dot{m}_{exh}}{P_{ind}} \tag{3.27}$$

$$ISCH_4 = \frac{\dot{m}_{CH4}}{P_{ind}} = \frac{u_{CH4}\,[CH_4]\,\dot{m}_{exh}}{P_{ind}} \tag{3.28}$$

$$ISNMHC = ISTHC - ISCH_4 \tag{3.29}$$

$$ISH_2 = \frac{\dot{m}_{UH2}}{P_{ind}} = \frac{[H_2]\,\dot{m}_{exh}}{P_{ind}} \tag{3.30}$$

$$ISN_2O = \frac{\dot{m}_{N2O}}{P_{ind}} = \frac{[N_2O]\,\dot{m}_{exh}}{P_{ind}} \tag{3.31}$$

where $\dot{m}_{gas}$ represents the mass flow rate of a given exhaust component in g/h, $[gas]$ s the concentration of that component in the exhaust, measured in ppm by the emissions analyser, and $\dot{m}_{exh}$ denotes the exhaust mass flow rate per cycle in kg/h, as defined by Equation (3.32).

$$\dot{m}_{exh} = \dot{m}_{air} + \dot{m}_{diesel} + \dot{m}_{gas\,fuel} \tag{3.32}$$

The term u_{gas} representing the raw exhaust gas quantity of a given component is defined as the ratio between the component concentration and the density of the exhaust gas, which varies depending on the type of fuel used, as outlined in Table 3.4.

Table 3.4 – Raw exhaust gas for diesel, hythane and hydrogen [21, 162].

Raw exhaust gas	$u_{gas,\ diesel}$	$u_{gas,\ hythane}$(*)	$u_{gas,\ hydrogen}$
u_{NOx}	0.001586	0.001624	0.001729
u_{CO}	0.000966	0.000989	0.001053
u_{CO2}	0.001517	0.001554	0.001654
u_{HC}	0.000482	0.000514	0.000075
u_{CH4}	0.000553	0.000566	0.000603

(*) The characteristics for hythane fuel were derived from CNG and adjusted for a 20% hydrogen 80% methane blend v/v.

In dual-fuel operation, the raw exhaust gas contribution was estimated based on the proportion of gas fuel in the total in-cylinder fuel mixture, as illustrated in Equation (3.33).

$$u_{gas\ DF} = \frac{\dot{m}_{diesel}\, u_{gas,\ diesel} + \dot{m}_{gas\ fuel}\, u_{gas,\ gas\ fuel}}{\dot{m}_{diesel} + \dot{m}_{gas\ fuel}} \tag{3.33}$$

As detailed in Subsection 3.2.6, the emissions analyser reported NOx and CO concentrations on a dry basis. To convert these values to a wet basis, a dry-to-wet correction factor was applied. This factor accounted for various influences, including ambient conditions – recorded daily using a laboratory barometer and thermometer – and changes in the composition of the in-cylinder fuel mixture. The correction method was adapted from [21] and is presented as follows:

$$k_w = 1.008 \left[1 - \frac{1.2442\ H_a + 111.19\ \%C \left(\frac{\dot{m}_{diesel} + \dot{m}_{gas\ fuel}}{\dot{m}_{dry\ air}} \right)}{773.4 + 1.2442\ H_a + 1000\ k_f \left(\frac{\dot{m}_{diesel} + \dot{m}_{gas\ fuel}}{\dot{m}_{dry\ air}} \right)} \right] \tag{3.34}$$

where $\mathrm{k_f}$ is a fuel specific factor of wet exhaust calculated by

$$k_f = 0.055594\ \%H + 0.0070046\ \%O \tag{3.35}$$

The estimation of the in-cylinder fuel mixture components were described in Equations (3.36), (3.37), and (3.38).

$$\%C_{DF} = \frac{(\dot{m}_{diesel}\ \%C_{diesel}) + (\dot{m}_{gas\ fuel}\ \%C_{gas\ fuel})}{\dot{m}_{diesel} + \dot{m}_{gas\ fuel}} \tag{3.36}$$

$$\%H_{DF} = \frac{(\dot{m}_{diesel}\ \%H_{diesel}) + (\dot{m}_{gas\ fuel}\ \%H_{gas\ fuel})}{\dot{m}_{diesel} + \dot{m}_{gas\ fuel}} \tag{3.37}$$

$$\%O_{DF} = \frac{(\dot{m}_{diesel}\ \%O_{diesel}) + (\dot{m}_{gas\ fuel}\ \%O_{gas\ fuel})}{\dot{m}_{diesel} + \dot{m}_{gas\ fuel}} \tag{3.38}$$

The term $\mathrm{H_a}$ in Equation (3.34) represents the air intake humidity, expressed in $g_{water}/kg_{dry\ air}$, as follow

$$H_a = \left(\frac{M_{H_2O}}{M_{dry\ air}}\right)\frac{p_{vapour}}{(p_{amb} - p_{vapour})} \times 10^3 \tag{3.39}$$

where $\mathrm{M_{H_2O}}$ is the molar mass of water equal to 18.01534 g/mol [21], $\mathrm{M_{dry\ air}}$ is the molar mass of dry air equal to 28.965 g/mol [21], and $\mathrm{p_{amb}}$ represents the ambient air pressure. $\mathrm{p_{vapour}}$ is the partial pressure of water vapour in the air derived from the relative humidity in ambient air (RH) and it is obtained by

$$p_{vapour} = p_{sat}\frac{RH}{100} \tag{3.40}$$

where $\mathrm{p_{sat}}$ is the saturation pressure of water vapour expressed in Pa and calculated from the formulation developed by Wexler [163].

$$p_{sat} = e^{F(7)\ ln(T_{amb}) + \sum_{j=0}^{6} F(j)(T_{amb})^{(j-2)}} \tag{3.41}$$

where $\mathrm{T_{amb}}$ is the ambient air temperature in K, and $\mathrm{F}(j)$ are constants and their values are given as follow:

Table 3.5 – Constant values for calculation of saturation pressure of water vapour [163].

Constant	Value
$\mathrm{F}(0)$	-0.29912729 x 10^4
$\mathrm{F}(1)$	-0.60170128 x 10^4
$\mathrm{F}(2)$	0.1887643854 x 10^2
$\mathrm{F}(3)$	-0.28354721 x 10^{-1}
$\mathrm{F}(4)$	0.17838301 x 10^{-4}
$\mathrm{F}(5)$	-0.84150417 x 10^{-9}
$\mathrm{F}(6)$	0.44412543 x 10^{-12}
$\mathrm{F}(7)$	0.28584870 x 10^1

The term $\mathrm{\dot{m}_{dry\ air}}$ in Equation (3.34) denotes the intake air mass flow rate on a dry basis. It was calculated by subtracting the moisture content from the total measured intake air flow rate, as shown below:

$$\dot{m}_{dry\ air} = \dot{m}_{air} - \dot{m}_{humidity} = \dot{m}_{air} - \left(\frac{\dot{m}_{dry\ air}\ H_a}{1000}\right) = \frac{\dot{m}_{air}}{(1 + H_a \times 10^{-3})} \tag{3.42}$$

Finally, the term k_h in Equation (3.24) refers to the humidity correction factor applied to NOx emissions for compression-ignition engines [21], and it is calculated as outlined in Equation (3.43)

$$k_h = \frac{15.698\ H_a}{1000} + 0.832 \tag{3.43}$$

On the other hand, the calculation of the net indicated specific emission of soot (ISsoot) was described as:

$$ISsoot = 1000 \times \frac{[soot]\ \dot{m}_{exh}}{\rho_{exh}\ P_{ind}} \tag{3.44}$$

where $[soot]$ is the concentration of soot, expressed in mg/m^3, was derived from the FSN-based smoke measurements and adjusted to a standard temperature of 237.15 K using the correlation provided by AVL [164].

$$[soot] = \frac{1}{0.405} \times 5.32\ [FSN]\ e^{0.3062\ [FSN]} \times \frac{298}{273.15} \tag{3.45}$$

The term ρ_{exh} present in Equation (3.44) corresponds to the exhaust gas density calculated using Equation (3.46) based on the Regulation number 49 [21].

$$\rho_{exh} = \frac{1000 + H_a + 1000\left(\frac{\dot{m}_{diesel} + \dot{m}_{gas\ fuel}}{\dot{m}_{dry\ air}}\right)}{773.4 + 1.2434\ H_a + 1000\ k_f\left(\frac{\dot{m}_{diesel} + \dot{m}_{gas\ fuel}}{\dot{m}_{dry\ air}}\right)} \tag{3.46}$$

Finally, combustion efficiency (CE) was evaluated after converting all measured exhaust gas species and soot emissions into net indicated specific emission values. The efficiency calculation was based on the presence of unburned combustion products in the exhaust. For CDC and diesel-hythane dual-fuel modes, the primary unburned components were THC and CO, as reflected in Equation (3.47). In the case of diesel-hydrogen dual-fuel operation, unburned hydrogen was also taken into account, as shown in Equation (3.48).

$$CE = \frac{Q_{ch}}{\dot{m}_{fuel} LHV_{fuel}} = 1 - \frac{\dot{m}_{THC} LHV_{DF} + \dot{m}_{CO} LHV_{CO}}{(\dot{m}_{diesel} LHV_{diesel}) + (\dot{m}_{hythane} LHV_{hythane})} \quad (3.47)$$

$$CE = 1 - \frac{\dot{m}_{THC} LHV_{DF} + \dot{m}_{CO} LHV_{CO} + \dot{m}_{UH2} LHV_{hydrogen}}{(\dot{m}_{diesel} LHV_{diesel}) + (\dot{m}_{hydrogen} LHV_{hydrogen})} \quad (3.48)$$

where $\mathrm{LHV_{CO}}$ is the lower heating value of CO, given by 10.1 MJ/kg [34], $\dot{\mathrm{m}}_{\mathrm{UH2}}$ is the mass flow rate of unburned hydrogen in the exhaust in kg/h, and $\mathrm{LHV_{DF}}$ is the lower heating value of the in-cylinder fuel mixture present in DF operation, which was estimated as

$$LHV_{DF} = \frac{(\dot{m}_{diesel} LHV_{diesel}) + (\dot{m}_{gas\ fuel} LHV_{gas\ fuel})}{\dot{m}_{diesel} + \dot{m}_{gas\ fuel}} \quad (3.49)$$

3.3.5 Combustion stoichiometry

The calculation of the molar carbon to carbon ratio (x), molar hydrogen to carbon ratio (y), and molar oxygen to carbon ratio (z) for a given gas fuel mass fraction. This was based on the conservation of mass of each chemical element in the reactants described in Equation (3.50) [34], and the normalised molecular composition of hythane ($C\mathrm{H}_{492}$), hydrogen (H_2), and diesel ($C\mathrm{H}_{1.825}\mathrm{O}_{0.0014}$).

$$C_x H_y O_z + \left(x + \frac{y}{4} - \frac{z}{2}\right)(O_2 + 3.773 N_2) \Rightarrow xCO_2 + \frac{y}{2} H_2O + 3.773 \left(x + \frac{y}{4} - \frac{z}{2}\right) N_2 \quad (3.50)$$

where $\mathrm{C_xH_yO_z}$ is the normalised molecular composition of the in-cylinder fuel mixture.

The obtention of x, y, and z for the in-cylinder fuel mixture enabled for the estimation of the stoichiometric air-fuel ratio (AFR_{stoich}).

$$AFR_{stoich} = \frac{\left(x + \frac{y}{4} - \frac{z}{2}\right)(M_{O_2} + 3.773 M_{N_2})}{12.011x + 1.008y + 15.999z} \quad (3.51)$$

where M_{O2} is the molar mass of oxygen of 31.9988 g/mol [21] and M_{N2} is the molar mass of nitrogen of 28.011 g/mol [21].

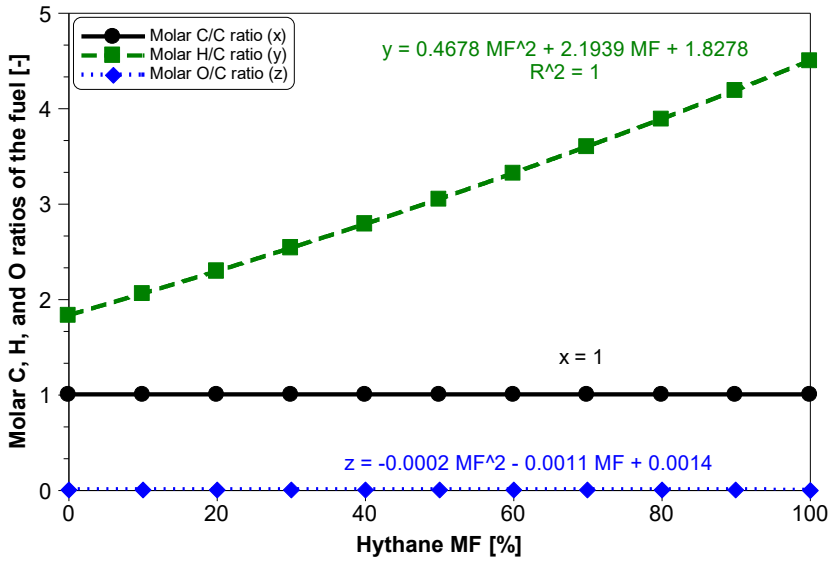

Figure 3.10 – Molar H/C and O/C ratios for the in-cylinder fuel mixture as a function of the hythane MF

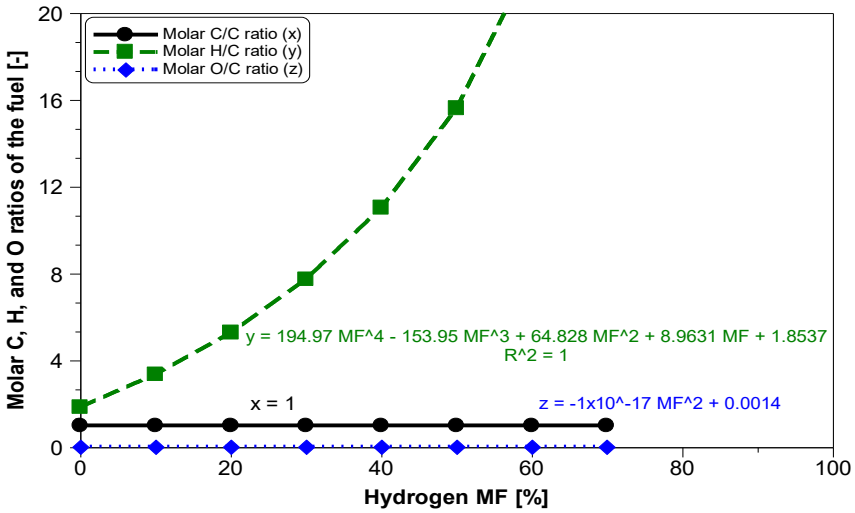

Figure 3.11 – Molar H/C and O/C ratios for the in-cylinder fuel mixture as a function of the hydrogen MF.

The AFR_{stoich} for diesel-hythane and diesel-hydrogen dual-fuel operations was validated using the AFR_{stoich} for diesel (14.5) and hythane (17.1) fuels in Equation (3.52), and diesel (14.5) and hydrogen (34.3) fuels in Equation (3.53).

$$AFR_{stoich} = 14.5\frac{\dot{m}_{diesel}}{\dot{m}_{diesel} + \dot{m}_{hythane}} + 17.1\frac{\dot{m}_{hythane}}{\dot{m}_{diesel} + \dot{m}_{hythane}} \quad (3.52)$$

$$AFR_{stoich} = 14.5\frac{\dot{m}_{diesel}}{\dot{m}_{diesel} + \dot{m}_{hydrogen}} + 34.3\frac{\dot{m}_{hydrogen}}{\dot{m}_{diesel} + \dot{m}_{hydrogen}} \quad (3.53)$$

The excess of fuel in the exhaust was given by the relative air-fuel ratio (λ).

$$\lambda = \frac{\frac{\dot{m}_{air}}{\dot{m}_{diesel} + \dot{m}_{gas\ fuel}}}{AFR_{stoich}} \quad (3.54)$$

Finally, the premixed gas fuel-air equivalence ratio (Φ) is given by

$$\Phi = \frac{AFR_{stoich}}{\frac{\dot{m}_{air}}{\dot{m}_{gas\ fuel}}} \quad (3.555)$$

3.4 Engine testing

The experiments were conducted at a constant engine speed of 1200 rpm and three load conditions corresponding to 0.6, 1.2, and 1.8 MPa IMEP, representing approximately 25%, 50%, and 75% of the engine's full load capacity.

These operating points reflect high residency regions typical of a heavy-duty vehicle drive cycle, such as the WHSC cycle [21], as illustrated in Figure 3.12. The selected speed was aligned with the characteristic speed at which maximum power is achieved, based on the engine's full load curve [21, 165].

In the figure, the size of each circle denotes the weighting factor, with larger circles indicating a greater contribution of that operating condition to the overall cycle.

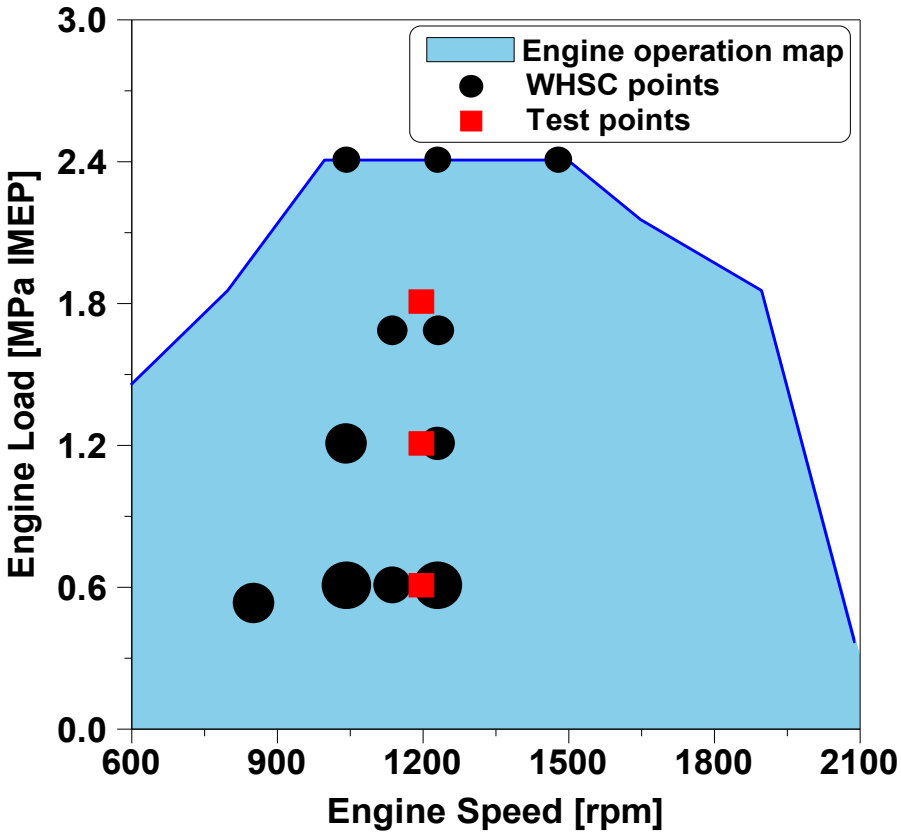

Figure 3.12 - The selected test points and the WHSC [21] test cycle points over the experimental HD engine speed-load map.

3.5 Summary

This chapter provides a description of the research engine and test cell facilities that were utilised, as well as the specifications of the measurement devices. An overview was given on the hythane and hydrogen port fuel injection systems. Moreover, it presented the methodology employed for collecting, processing, and analysing data. This included the description of the data acquisition system and explanation of both real-time and post-processing analysis, namely the combustion heat release, engine performance, and exhaust emissions. Finally, the selected engine speed and loads for the dual-fuel investigations were described and compared with one of the primary modern heavy-duty engine test cycles.

Chapter 4
Characterisation of diesel-hythane dual-fuel combustion

4.1 Introduction

This chapter experimentally investigates the performance and emissions of a diesel-hythane dual-fuel combustion system across three engine loads, from low to high. Various diesel injection strategies were examined to optimise engine efficiency and minimise emissions at each load condition. The study encompasses a detailed analysis on the quantification of engine-out emissions with a particular focus on the reduction of greenhouse gas (GHG) emissions. A well-to-wheel analysis is also presented to evaluate the overall environmental impact of the dual-fuel system, along with a comprehensive cost-benefit analysis that includes qualitatively evaluating operational costs associated with dual-fuel engine operation.

Moreover, at low engine loads, strategies such as the combination of internal and external exhaust gas recirculation (iEGR and eEGR) were explored to improve exhaust gas temperature (EGT), combustion efficiency, and reduce carbon monoxide (CO) and unburnt methane emissions. The potential benefits of these strategies were carefully assessed to enhance fuel conversion efficiency while maintaining emission standards. At medium and high engine loads, the introduction of external eEGR was investigated to further optimise combustion characteristics and reduce NOx emissions under more demanding operating conditions.

Finally, an optimal dual-fuel engine map is provided, outlining the highest energy fraction for various dual-fuel combustion strategies (conventional and advanced) across different engine loads. A matrix will be provided in order to guide the selection of the most suitable combustion strategies to achieve the desired performance and emission targets.

4.2 Evaluation of the optimum diesel injection strategy

Experiments were conducted to demonstrate the effect of different diesel injection strategies on the dual-fuel operations at low, medium, and high engine loads. The effective compression ratio (ECR) was optimised for the dual-fuel combustion process.

4.2.1 Experimental test procedure

Engine tests were carried out at engine loads of 0.6, 1.2, and 1.8 MPa IMEP at a constant speed of 1200 rpm. The limits of the peak in-cylinder pressure and the maximum PRR were set to 18 MPa and 2.0 MPa/CAD, respectively, while COV_{IMEP} lower than 3% was used to determine stable engine operation. Table 4.1 summarises the overall engine operating conditions used for this study.

Table 4.1. Engine operating conditions for optimum diesel injection experiment.

Parameter	Unit	Low load	Medium load	High load
Engine load (IMEP)	MPa	0.6	1.2	1.8
Engine speed	rpm	1200	1200	1200
Hythane energy fraction (HEF)	%	76 ± 1	76 ± 1	76 ± 1
ECR	-	Sweep	Sweep	Sweep
Intake air temperature	°C	41	42	43
Intake air pressure	kPa	125	190	260
Exhaust air pressure	kPa	135	200	270
eEGR	%	0	0	0
iEGR	%	0	0	0
Diesel injection pressure	MPa	100	130	160

The intake and exhaust air pressure set-points from Euro V compliant multi-cylinder HD diesel engine were used in order to provide a sensible starting point, since an external boosting system was used in place of a turbocharger. The exhaust pressures were adjusted to provide a constant pressure differential across the cylinder of 10 kPa. This differential between intake and exhaust pressures was used to simulate the pumping losses typically related to turbocharger. Intake air temperatures were maintained constant at 41°C, 42°C and 43°C throughout the experiments at low,

medium and high loads, respectively, by using an air-to-water cooler and intake air heater. The study was performed without external exhaust gas recirculation (EGR) in order to simplify the experimental investigation.

The selected diesel injection strategies are depicted in Table 4.2. Conventional diesel combustion (CDC) and conventional dual-fuel combustion (CDF) operations at the baseline ECR of 16.8 were compared against an advanced dual-fuel combustion (ADF) at a lower ECR of 14.8 using alternative diesel injection strategy.

Table 4.2. Diesel injection strategies for different combustion modes.

Mode	Type	ECR	Low load	Medium load	High load
CDC	Non-premixed combustion	16.8	*Late split (pilot and main injection): 1/99* SOI_1 @ -17 CAD ATDC SOI_2 @ -10 CAD ATDC	*Late split (pilot and main injection): 1/99* SOI_1 @ -15 CAD ATDC SOI_2 @ -8 CAD ATDC	*Late split (pilot and main injection): 1/99* SOI_1 @ -9 CAD ATDC SOI_2 @ -2 CAD ATDC
CDF	Non-premixed combustion	16.8	*Late split (pilot and main injection): 3/97* SOI_1 @ -17 CAD ATDC SOI_2 @ -10 CAD ATDC	*Late split (pilot and main injection): 3/97* SOI_1 @ -15 CAD ATDC SOI_2 @ -8 CAD ATDC	*Late split (pilot and main injection): 5/97* SOI_1 @ -9 CAD ATDC SOI_2 @ -2 CAD ATDC
ADF	Premixed combustion	14.8	*Early single: 100/0* SOI_1 @ -42 CAD ATDC	*Split (early and late injection): 50/50* SOI_1 @ -60 CAD ATDC SOI_2 @ +4 CAD ATDC	*Split (early and late injection): 20/80* SOI_1 @ -60 CAD ATDC SOI_2 @ +10 CAD ATDC

Regarding CDC and CDF, both operations were categorised as non-premixed combustion due to a late split injection near TDC. A diesel first/pilot injection (SOI_1) was set to be between 1% and 3% of the total diesel injected at CDC and CDF,

respectively, with a constant delay time of 1ms (7.2 CAD at 1200 rpm) before diesel second/main injection (SOI_2). The pilot injection was employed in order to reduce the level of PRR. Such a split injection procedure has been generally adopted to commercial diesel engines [166].

The ADF operations were combined with a LIVC strategy in order to adjust the in-cylinder lambda and the charge reactivity, with the goal of increasing combustion efficiency and EGT. The ECR of 14.8 represented the latest LIVC that could be used without compromising the combustion stability. The ADF has been characterised as fully or partially premixed combustion, depending on the engine load operation. At low engine load, an early single injection was employed, resulting in fully premixed combustion, also known as RCCI, whereas at medium and high load conditions, a split injection (early SOI_1 and late SOI_2) was applied, leading to partially premixed combustion. The diesel fuel supplied to the engine during SOI_1 had to be lowered as the engine load increased, in the case of split injection strategy. This was essential in order to keep the combustion process within the engine hardware limitations (PRR and P_{max}). As a result, the maximum percentage diesel split ratio obtained between SOIs for medium and high loads was 50/50 and 20/80, respectively.

The engine calibrations were achieved via a long optimisation process that focused on diesel SOI and diesel split ratio, targeting to lowest CO_{2eq} emissions. It should be noted, however, that throughout this optimisation, the hythane supply was kept constant for each engine load while diesel SOI_2 was automatically adjusted by the ECU to maintain IMEP constant, resulting in a small hythane energy fraction (HEF) variation (around 2%).

Taking combustion stability (PRR and COV_{IMEP}) into consideration, the HEF was limited at 76% for all operation modes because that was the highest possible value at CDF at low load, resulting in an overall combustion mixture of 23% diesel, 16% hydrogen, and 61% methane. In order to provide a fair comparison at different engine loads between combustion strategies.

Additionally, to avoid uncontrollable combustion (e.g. exponential rise of PRR and COV_{IMEP}) when switching from CDF to ADF mode, extra attention is required. The

hythane injector pulse width, which controls $\dot{m}_{hythane}$, and the resulting HEF must be reduced before adding diesel fuel via an early single/split injection.

4.2.2 Overview of the dual-fuel operation and combustion characteristics

For the investigated dual-fuel combustion operations at a constant HEF of 76% for 25%, 50% and 75% of full engine load, Figure 4.2 compares the measured in-cylinder average pressure and temperature, heat release rate and diesel SOI, while combustion characteristics, such as SOC, ignition delay (SOC-SOI_1), CA50, combustion duration and some more additional combustion parameters are depicted in Figure 4.1.

The employment of the Miller cycle via a LIVC strategy reduced compression pressures in ADF mode at all engine loads, as illustrated in the in-cylinder pressure graphs in Figure 4.2, which may decrease the amount of hythane fuel pushed into these crevice volumes. This reduction in pressures and temperatures enabled more stable and flexible combustion control (lower COV_{IMEP}) compared to CDF, allowing for a larger diesel percentage amount at SOI_1 in the case of medium and high load conditions. Furthermore, adopting a lower ECR increased the global fuel-air equivalence ratio, that is lower λ due to a reduction in the intake air mass flow rate. Nevertheless, it also decreases in-cylinder heat capacity during the combustion event, which resulted in higher average in-cylinder combustion temperatures [167, 168], as shown in Figure 4.2.

As discussed in previous investigation [169], ADF regime is dependent on premixed charge reactivity and homogeneity. And at low engine load, the single early diesel injection allowed ADF mode to increase the reactivity of the mixture, since the longer ignition delay allowed for more significant dilution of the high reactivity fuel (diesel) into the well-premixed charge (air + hythane). As a result, more advanced SOC and CA50 were obtained, as displayed in Figure 4.1, leading to a shorter combustion duration around TDC, and thus, significantly higher HRR peak than CDF, similar to CDC mode. The main drawback of this operation mode, however, is associated to increased maximum in-cylinder pressure verified in Figure 4.2, which was controlled by the lower ECR via LIVC strategy.

At medium engine load, ADF demonstrated to be the best combustion regime. The split diesel injection with an early SOI helped to enhance reactivity, in which 50% of the diesel quantity controlled the ignition of the premixed charge and the other 50% controlled the main heat release process (CA50). As a result, the combustion duration was significantly shorter than any other combustion mode, as observed in Figure 4.1. More premixed injection, however, was not possible since it would increase the reactivity of the mixture, resulting in fast combustion and premature advance of the CA50, resulting in excessive PRR. In the case of ADF, lower ECR led to slightly longer ignition delay, in other words, more time for mixture preparation before autoignition, due to worse thermodynamic conditions (lower in-cylinder temperature and pressure), and hence higher degree of premixed mixture [76] than CDF. On the other hand, the richer fuel-air ratio (lower lambda) noticed in Figure 4.1 caused by lower mass air flow rate for the same fuel injected (diesel and hythane) generated a slightly more advanced CA50, resulting in shorter combustion duration and higher peak HRR when compared to CDF mode, as seen in Figure 4.2.

At high engine load, however, although early injection of ADF increased the reactivity of the premixed charge, it was less effective when compared to other engine loads because only 20% of the total diesel was used in first injection. Therefore, it only improved the initial combustion, resulting in significantly more advanced SOC and CA50 than any other operation mode, as displayed in Figure 4.1. As a result, the peak in-cylinder pressure was obtained earlier (approximately 3 CAD), as depicted in Figure 4.2, making the pressure rise event more sensitive and limiting the flexibility of this combustion mode. Nonetheless, the reduced diesel quantity of SOI_1 led to a smaller release of thermal energy closer to TDC, resulting in lower peak HRR and in-cylinder temperature as can be seen in Figure 4.2. In addition, because 80% of the total diesel was still injected in the SOI_2, the combustion process was similarly characterised as CDC, mainly driven by the main injection. Due to the fact that this SOI occurred after CA50, a second and later peak HRR was created, as displayed in Figure 4.2, resulting in an extended combustion duration noticed in Figure 4.1. The limitation of diesel split ratio between injection events by the reactivity of the mixture was more evident than at medium load, because the thermodynamic conditions at 75% of full engine load are closer to the engine hardware limits, making this combustion mode extremely challenging, and a small change in the mixture reactivity could contribute to a

significant rise in the peak in-cylinder pressure and PRR, generating knocking combustion. Similar to the medium load operation, the utilisation of reduced ECR via LIVC strategy was essential for controlling combustion stability, resulting in an improvement of the premixed charge reactivity (higher diesel split ratio).

Additionally, it can be observed in Figure 4.2 a small peak of heat release rate before SOC, in all dual-fuel regimes at all engine loads. This can be further explained by the increased reactivity of the fuel mixture on enhance the low temperature reaction of the diesel fuel [169]. Therefore, ADF displayed a faster and shorter combustion process at low and medium loads, resulting in a more efficient heat release process around TDC.

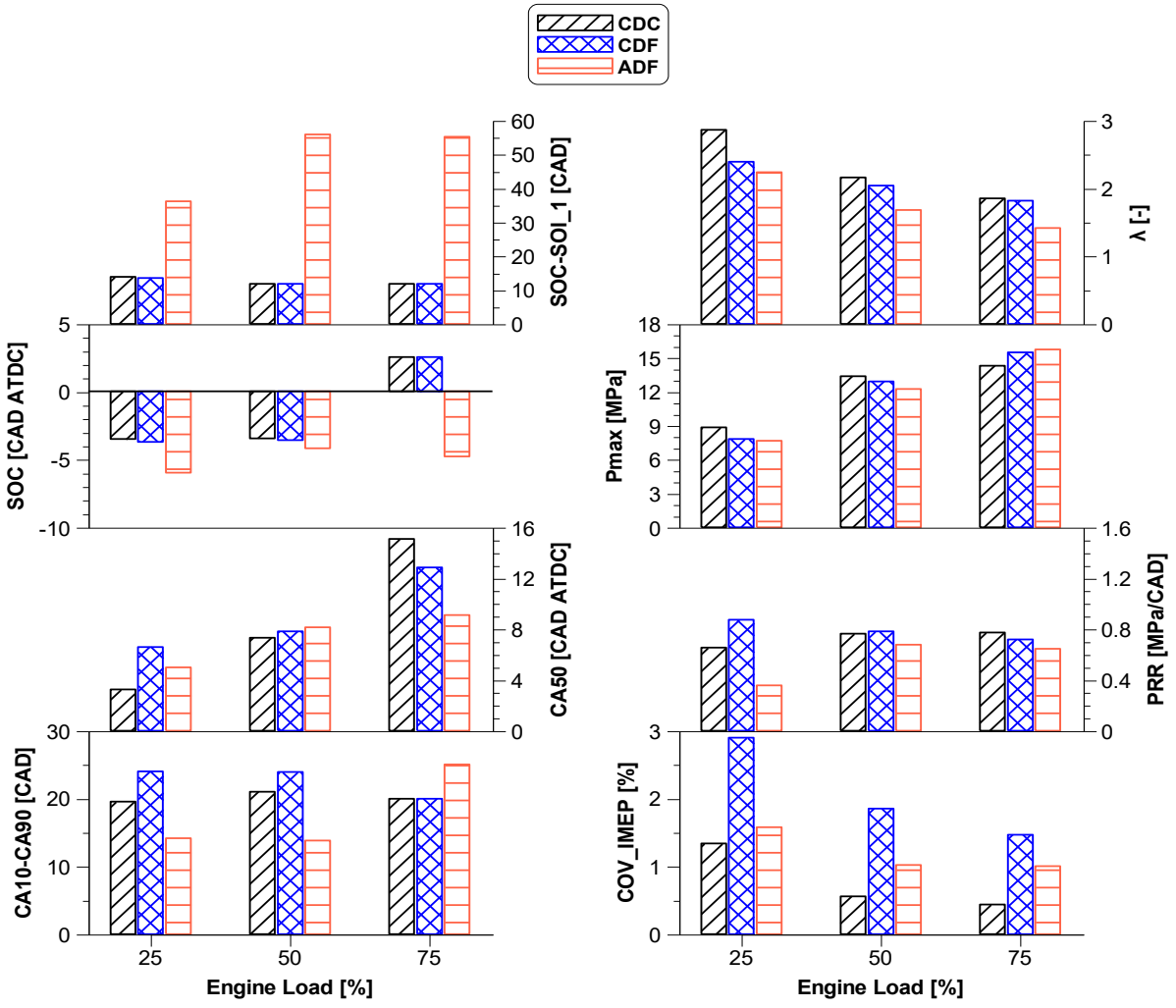

Figure 4.1. The effect of combustion mode on combustion characteristics and stability.

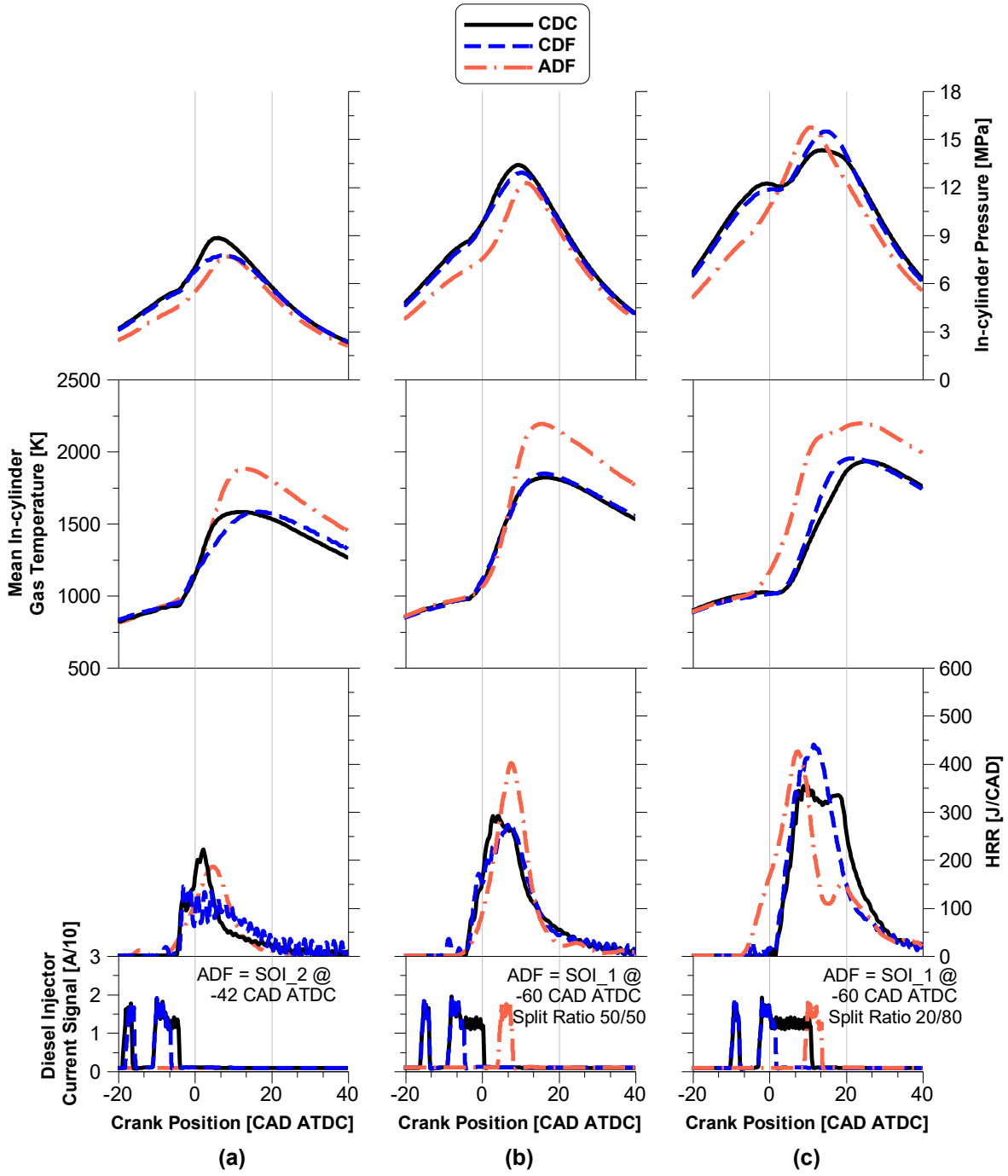

Figure 4.2. The effect of combustion mode on in-cylinder pressure, mean in-cylinder gas temperature, HRR and diesel injection at: (a) low engine load, (b) medium engine load, and (c) high engine load.

4.2.3 Engine performance

The impact of the different combustion mode on combustion and indicated thermal efficiencies, exhaust gas temperature (EGT) and indicated equivalent specific fuel consumption are depicted in Figure 4.3.

It can be seen from Figure 4.3 that EGT increased linearly with the increase in engine load, independently on the combustion mode. Moreover, all dual-fuel modes depicted higher EGT than CDC, which can be explained in part by the presence of hydrogen and methane, which have a higher flame temperature [170]. However, at each load, the EGT increased similarly for the ADF operation, when comparing to CDF, as observed in Figure 4.3. This is related to the decrease in the relative air-fuel ratio due to the lower ECR. Therefore, the effect of combustion mode on EGT is mainly related to the difference in ECR via the application of LIVC. In addition, it is worth noticing in Figure 4.3 that although ADF increased by approximately 40°C the EGT when comparing to CDF regime, the level of temperature reached (about 366°C) is still below the methane oxidation catalyst (MOC) light-off temperature of 400°C for high CH_4 conversion efficiency [171]. Thus, the combination of LIVC with internal exhaust gas recirculation (iEGR), which is an effective strategy to improve exhaust thermal management as a result of hot residuals trapped from previous cycle [76, 172], has the potential to generate even higher EGTs and improve CH_4 conversion efficiency in MOCs at low engine loads.

As described in the 4.2.2, the ADF mode displayed in Figure 4.1 the fastest and shortest combustion processes at 0.6 and 1.2 MPa IMEP, respectively, providing the thermodynamic advantage of releasing thermal energy closer to TDC and thus improving work during the expansion stroke [173]. This resulted in a 15% savings in the indicated equivalent specific fuel consumption when compared to CDF at low load, and a 3% and 1% savings when compared to CDF, at medium load, as observed in Figure 4.3. As a consequence, the ADF operation produced an ITE of 46.4% at 0.6 MPa IMEP and 46.6% at 1.2 MPa IMEP, respectively. This is equivalent to a 17% increase at low engine load and 2.5% and 0.7% increases when compared to CDF mode at medium load, respectively. Nonetheless, the ADF combustion limitations at 1.8 MPa IMEP described in the previous subsection, result in a 0.6% increase in $ISFC_{eq}$ and as a consequence, a 0.6% decrease in ITE when compared to CDF and ADF operations.

The combustion efficiency of dual-fuel operations demonstrated in Figure 4.3 a trend of linear overall increase with the increase of engine load. This can be explained by the natural improvement of thermodynamic conditions present at higher engine load

conditions. The significant difference on combustion efficiency noticed in Figure 4.3 between ADF and CDF operations is mainly related to the enhance reactivity of the premixed charge provided by the injection strategy of ADF, contributing to a more complete combustion, as it improved fuel conversion efficiency with lower levels of unburned CH_4 and CO emissions, as discussed further in the following section. In contrast to medium load operation, the CE of ADF regime depicted in Figure 4.3 identical results at high load. This was a result of limited reactivity improvement provided by the SOI_1 of ADF, limited by hardware constrains, as discussed previously.

When compared to other dual-fuel operations, ADF combustion displayed significant performance improvement. However, at 75% of full engine load, advanced dual-fuel combustion operations maintained a similar ITE to CDC, with ADF mode indicating a 3.6% improvement at low engine load.

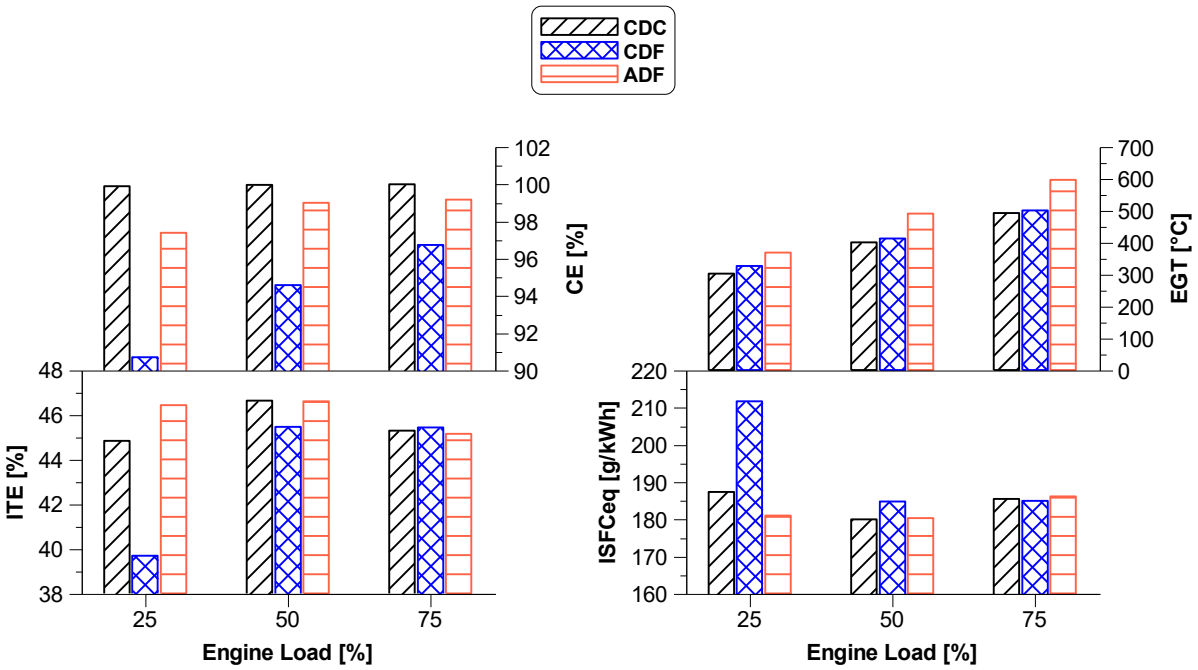

Figure 4.3. The effect of combustion mode on engine performance.

4.2.4 Engine-out emissions

Exhaust emissions in the form of net indicated specific values for the 3 combustion modes are depicted in Figure 4.4.

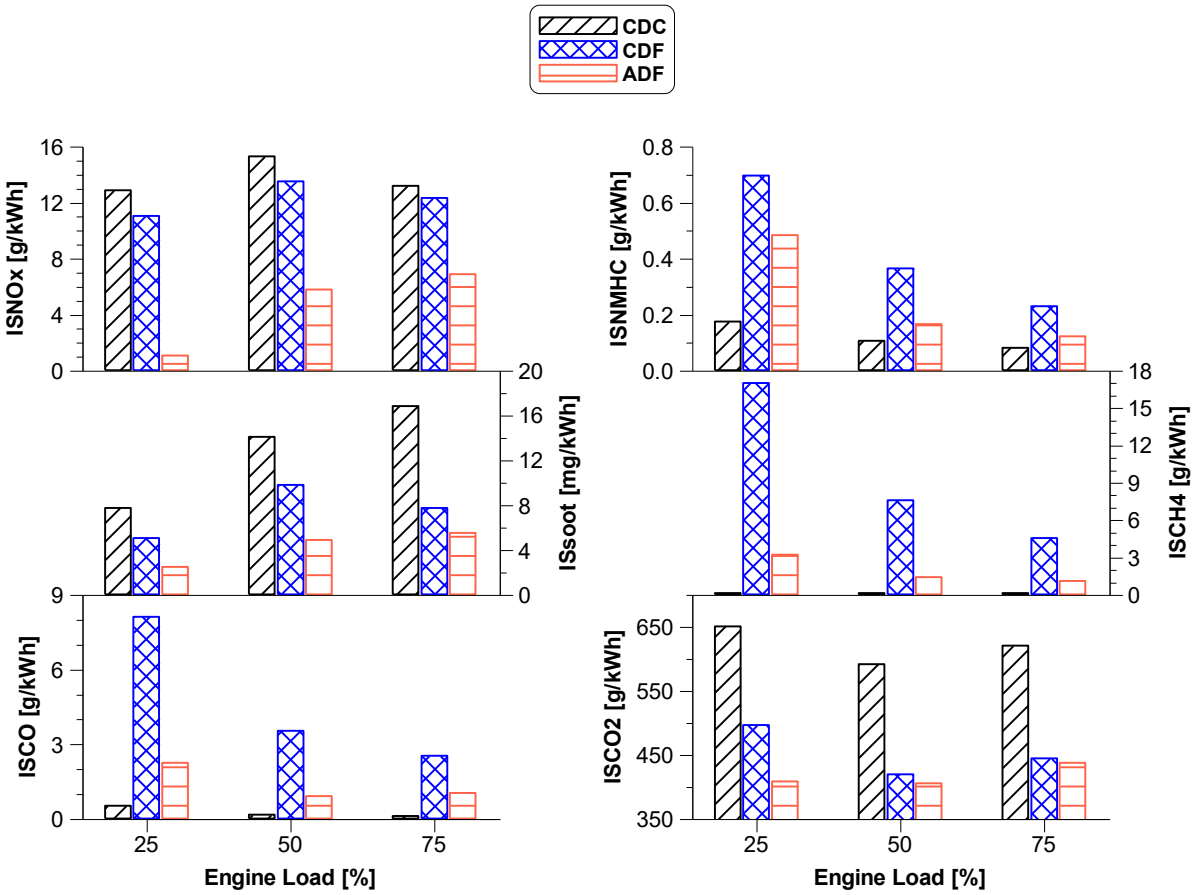

Figure 4.4. The effect of combustion mode on engine-out emissions.

- NOx emissions

NOx is formed in larger amount with high peak in-cylinder combustion temperatures, high oxygen concentrations and long residence time [174]. ADF mode is, as displayed in Figure 4.4, the combustion mode with the lowest NOx emissions, although having achieved significantly higher in-cylinder temperatures than CDC and CDF, as seen in Figure 4.2. This phenomenon is most likely explained by the fact that the majority of the fuel is burned under lean premixed conditions as a consequence of early diesel injection, resulting in reduced local temperature [169, 174]. As engine load increases, the diesel SOI_1 quantity injected on ADF mode gradually decreased, causing a decrease in fuel amount burned under lean premixed conditions, consequently increasing NOx emissions. However, these NOx levels remain considerably lower than those observed under non-premixed combustion regimes (CDC and CDF), as demonstrated in Figure 4.4. In comparison to CDC and CDF operations, ADF can

reduce NOx levels by 89% and 87% at low load, 62% and 57% at medium load, and 48% and 44% at high load, respectively. However, it is feasible to obtain even greater reductions by using: more advanced diesel SOI_1, which promotes leaner and more homogenous premixed conditions; and more retarded SOI_2, which reduces temperature peaks. Furthermore, alternative combustion strategies, such as EGR dilution could also be considered to further reduce NOx levels, particularly at higher engine loads by decreasing combustion temperature and in-cylinder oxygen concentration.

- soot emissions

Soot is primarily formed in rich fuel-air equivalence ratio regions of the combustion chamber at elevated temperatures. When compared to conventional diesel mode, dual-fuel operations significantly decreased soot emissions, as shown in Figure 4.4. One reason for this is that diesel fuel only accounts for 23% of the total mixture, with hythane fuel being the major compound of all dual-fuel combustions, which is composed of hydrogen and methane, having no carbon-carbon bond, a lower C/H, and lower soot tendencies [175]. Moreover, the port injected hythane fuel has sufficient time to form a well-premixed charge before combustion. Despite this, the utilisation of higher boost pressures and more retarded diesel SOIs results in a slight reduction in the ignition delay duration at higher engine loads, as can be seen in Figure 4.1. As a result, more fuel participates in the diffusion combustion process, leading to the increase in soot emissions.

During ADF operation, the use of diesel early single injection at low load enhanced the mixing time, thereby improving the premixed charge and contributing to a substantial decrease in soot levels, namely 69% when compared to CDC and 36% more decrease than CDF mode. However, at higher loads, this reduction gradually decreased, particularly when compared to CDF mode as observed in Figure 4.4, because the diesel split ratio had to be adjusted, as previously described, leading in more diesel fuel amount being injected later in the cycle, resulting in reduced mixing timing. Ultimately, under high engine load, ADF produced 68% lower soot than CDC and 15% lower than CDF mode, as shown in Figure 4.4. It is worth to note that ADF operation fully met Euro VI and Euro VII standards at all engine conditions.

- CO emissions

The rate of CO formation is a function of the unburned gaseous fuel availability and mixture temperature, both of which control the rate of fuel decomposition and oxidation [34, 176]. It can be clearly noticed that CO emission with dual-fuel operations is always higher than with CDC. This is because dual-fuel mode suffers from a poor fuel conversion that leads to incomplete combustion, as reflected by the CE in Figure 4.3, and high unburned fuel (NMHC and CH_4 emissions). As engine load is increased, the combustion process improves, resulting in lower CO emissions due to increased fuel conversion efficiency.

With regards to ADF mode, it displayed reduced CO levels compared to CDF combustion. This is explained by the previously reported improvement in the combustion process with Miller cycle utilisation. Furthermore, when compared to CDF, ADF has more complete combustion, as demonstrated by the CE in Figure 4.3, resulting in higher CO oxidation. As a result, as compared to CDF, ADF can reduce CO levels by 72% at low load, 75% and 48% at medium load, and 59% and 29% at high load. Therefore, it can be stated with a degree of confidence that ADF can fully meet Euro VI standards at medium and high engine loads without the use of an ATS. At low load condition, however, an optimisation should be undertaken to further minimise CO levels, such as the employing of iEGR combined with LIVC strategy, which has the potential to improve in-cylinder temperatures at part-load conditions, as demonstrated by Guan et al. [76].

- Unburned total hydrocarbons emissions

The variation in the amount of total hydrocarbons in exhaust, which corresponds to the sum of NMHC and CH_4 emissions, complies with the combustion process quality [34, 176]. It is evident in Figure 4.4 that dual-fuel modes suffer from significant methane slip, especially at low load conditions. This is explained by the high HEF used, as hythane fuel is mainly composed of methane, resulting in an inevitable increase in unburned CH_4 levels in the exhaust pipe when poor fuel utilisation efficiency is attained, especially during part load conditions, as shown in the $ISFC_{eq}$ graph in Figure 4.3. The increase in mixture reactivity and improvement in fuel

conversion efficiency induce an important decrease observed in Figure 4.4 in both unburned NMHC and CH_4 at higher load conditions, although its value remains higher than that of CDC.

As previously reported for CO emissions, the improved reactivity of the mixture enabled ADF to lower fuel consumption even further, particularly at low load, as seen previously in Figure 4.3, results in a nearly 80% reduction in methane slip compared to CDF mode at all engine loads. The best ADF mode results, however, are still above the 0.50 and 0.35 g/kWh imposed by Euro VI and Euro VII, respectively, forcing the use of a MOC to oxidise the remaining unburned methane. In-cylinder CH_4 control, such as the use of iEGR combined with the LIVC strategy, is another way to reduce methane slip, particularly at low engine load, for the same reasons as discussed for CO emission.

- CO_2 emissions

It can be seen in Figure 4.4 that dual-fuel modes generate considerably lower CO_2 emission, compared with conventional diesel mode. This can be explained in part by the addition of hydrogen into the combustion, because hythane fuel has a lower C/H in comparison to diesel fuel, as depicted in Table 3.2. The other reason can be the THC emission of dual-fuel regimes and the incomplete combustion, as revealed by the high CO emission, particularly at low load. At higher loads, however, the improvement in the combustion process causes CO_2 emissions to increase, although its values remain considerably lower than to that of conventional diesel combustion, as displayed in Figure 4.4. Thus, when analysed alongside CDC, ADF mode was able to cut CO_2 emissions by 242, 186, and 183 g/kWh at low, medium, and high load conditions, corresponding to reductions of 37%, 31%, and 30%, respectively. When comparing to CDF combustion, ADF indicated an improvement in 13%, 2% and 1% over CDF combustion at low, medium and high engine loads. The gradually decreasing CO2 reduction benefit of ADF over CDF mode is owed to the improvement in fuel conversion efficiency displayed by CDF operation, as illustrated in Figure 4.3.

4.2.5 GHG emissions estimation

Hythane is considered a lower carbon fuel for ICEs, since it is composed of hydrogen, a potential carbon-free fuel, and methane, which has a lower carbon content than diesel. And as discussed previously, hythane fuel can considerably reduce CO_2 emissions, independent of the combustion mode selected. However, hythane combustion in dual-fuel mode generates unburned methane, which is one of the challenges of hythane- or CNG-fuelled engines. Furthermore, CH_4 is recognised have higher Global Warming Potential (GWP) of 27 that of CO_2 over a 100-year lifetime [28]. Hence, a small amount of CH_4 emission can offset the benefits of reduced CO_2 in the diesel-hythane DF engine.

On the other hand, although hydrogen is not a GHG itself, hydrogen leakage may influence the atmospheric concentrations of other GHGs, such as methane and ozone, and thus may be associated to a GWP [177, 178, 179]. Nevertheless, hydrogen GWP will not be considered in this section because hydrogen emissions were not measured at the exhaust line of diesel-hythane dual-fuel combustion experiments.

Therefore, it is essential to estimate the total CO_2-equivalent (CO_{2eq}) of both GHGs investigated. In order to find a single value of CO_{2eq}, the level of emissions of a GHG have to be multiplied by its GWP and combine all GHG together, as shown below.

$$ISCO_{2_{eq}} = ISCO_2 * 1 + ISCH_4 * 27 \quad (4.1)$$

Figure 4.5 depicts the GHG emissions for the combustion modes investigated at low, medium, and high engine loads. GHG levels are expressed in grams of CO_{2eq} emissions per kWh of power generated. When CO_2 and CH_4 levels are taken into account, ADF mode was the combustion strategy that revealed the lowest CO_{2eq} levels, suggesting an average reduction in GHG emissions of 25% across all engine operation conditions when compared to the conventional diesel baseline. Despite this, methane slip affected the GHG reduction, especially at low load, where the achieved 37% CO_2 drop was offset by unburned CH_4 (reflected by light blue bar in Figure 4.5), resulting in a still considerable 24% GHG emission reduction. As a result, there is still potential for higher GHG reduction on ADF regime, particularly by methane control at low engine conditions. However, that offset was more pronounced in the

non-premixed dual-fuel combustion modes, mainly CDF, as shown in Figure 4.5, where methane slip resulted in a considerable rise in GHG emissions compared to the CDC baseline under part- and mid-load conditions, highlighting the importance of unburned methane control in diesel-hythane dual-fuel combustion.

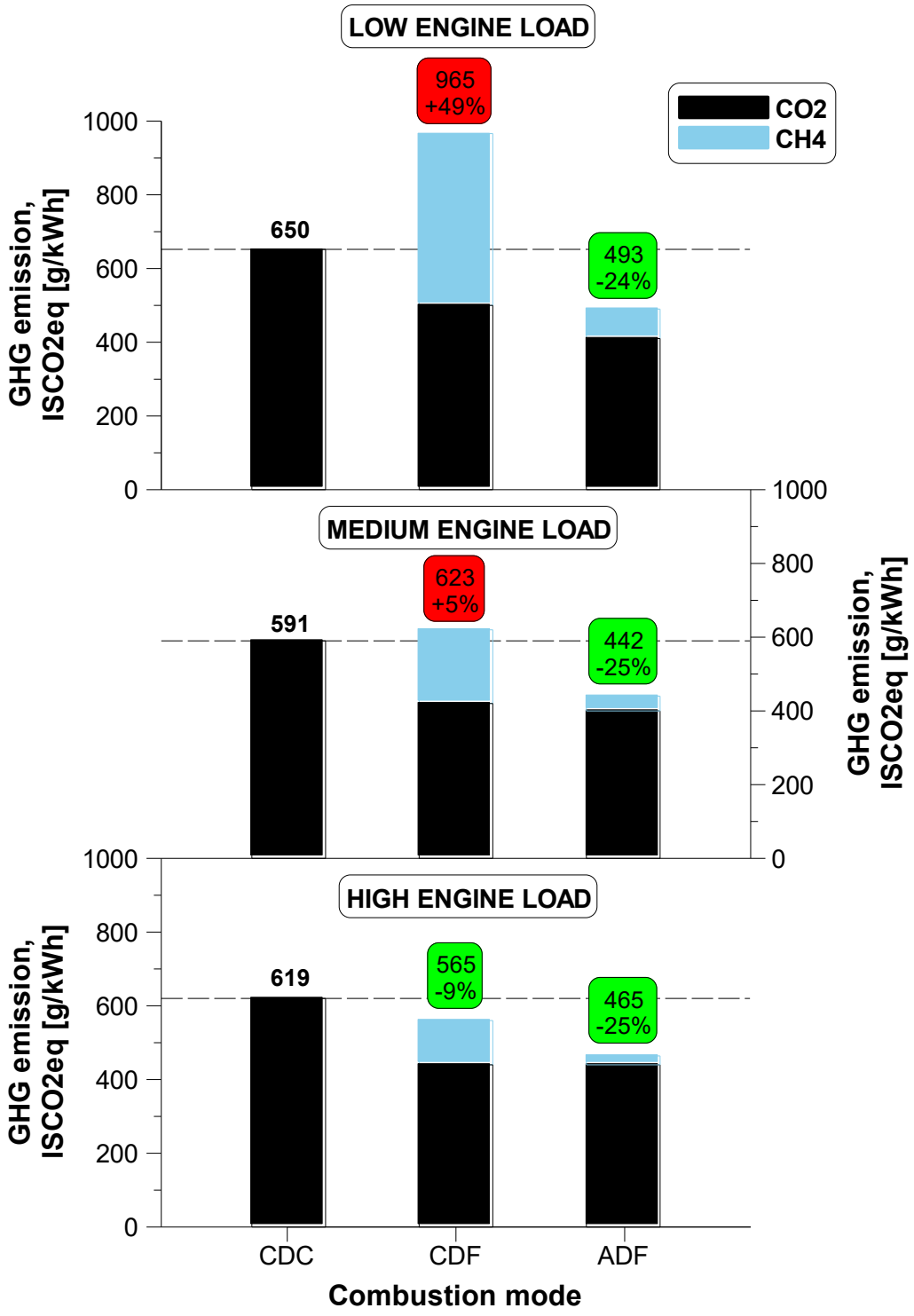

Figure 4.5. The effect of combustion mode on combined GHG emissions.

As a result of this analysis, one key conclusion is that reducing GHG emissions is dependent not only on fuel type, but also on the combustion process, where diesel injection strategy and ECR play critical roles.

4.2.6 NOx emissions mitigation and additional practical considerations

Additional practical aspects for diesel-hythane dual-fuel operation were assessed in order to evaluate whether these combustion modes can be a viable alternative and successfully utilised in the most recent Euro VII emission standard.

As previously concluded, the in-cylinder measures studied in this work did not entirely meet the emissions requirements limits. Although the majority of the emissions produced by the dual-fuel combustion, such as CO and NMHC emissions can be removed by a diesel oxidation catalyst [36], extremely high CH_4 conversion efficiency in the methane oxidation catalyst will be necessary to comply the stringent tailpipe unburnt CH_4 emission of 0.5 g/kWh. CH_4 can be significantly minimised by optimising dual-fuel operation, such as the case of ADF mode with a lower ECR in order to increase the EGT, which leads to an improvement in methane conversion in an ATS.

Similarly, despite soot levels were below the standard limits, they can be further reduced with higher diesel injection pressures. With the generation of very low levels of soot via ADF mode, typical particulate filters employed in HD diesel applications for smoke control purposes can be avoided. This will enable this application to avoid traditional fuel consumption penalty from associated higher backpressure and periodic regenerations issue caused by this ATS [180].

Considering that NOx emissions remain to be a significant concern, since Euro VII will set even tighter limits, NOx control will play a critical part in total cost of ownership. That being said, NOx levels are controlled through in-cylinder control (e.g. ADF mode, EGR utilisation) and aftertreatment control by use of a SCR. The latter is dependent on the engine calibration due to limited conversion efficiency of the SCR and/or high aqueous urea solution usage (e.g. increased engine operational cost). The NOx conversion efficiency of SCR ATS (SCR Conv.Eff) typically ranges between 80% and 90% [181, 182].

Figure 4.6 compares the estimated SCR-out NOx levels obtained with various SCR conversion efficiencies when the engine is operated in CDC, CDF, and ADF regimes. ISNOx levels downstream of the SCR system were calculated as

$$SCR_{-out}\ ISNOx = ISNOx - (ISNOx * SCR\ Conv.Eff) \quad (4.2)$$

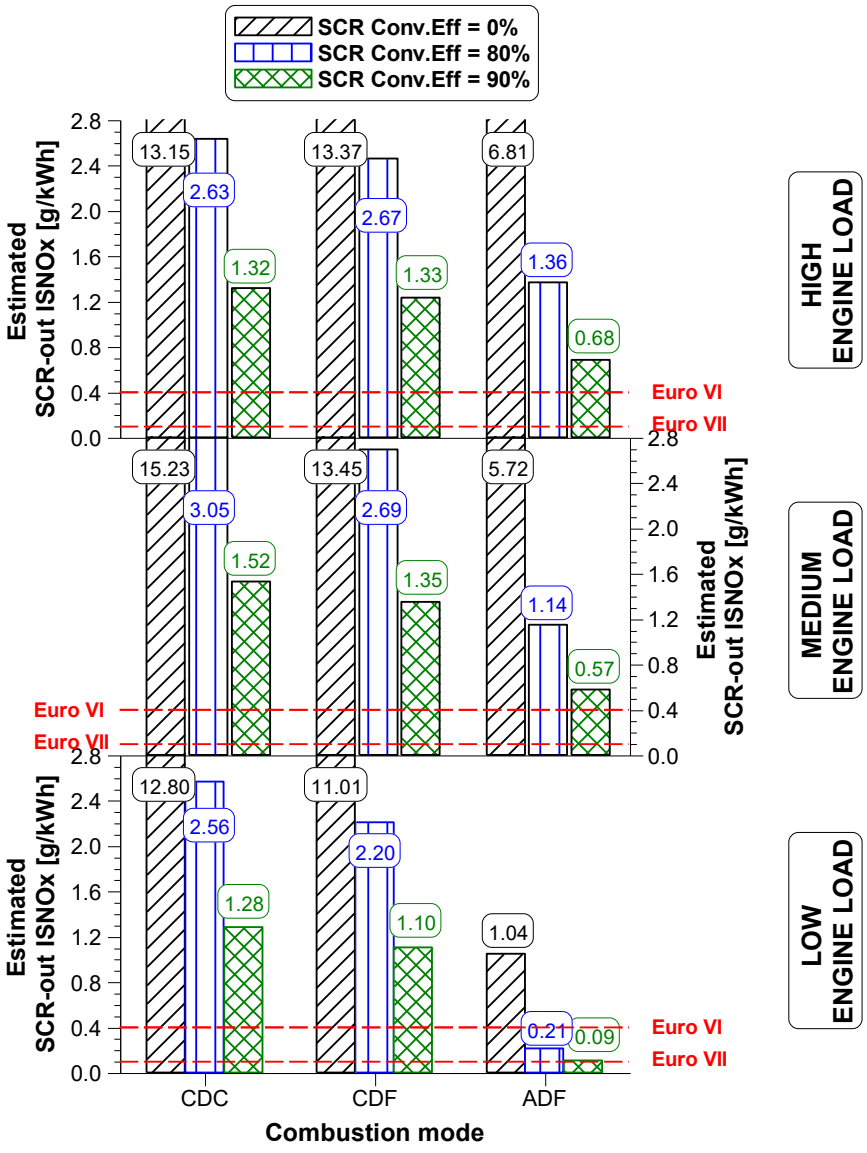

Figure 4.6. Estimated ISNOx levels for different SCR conversion efficiencies.

The use of high HEF in CDF mode, as conventional diesel combustion, resulted in estimated SCR-out ISNOx higher than the less stringent emission standard limit of 0.4 g/kWh, regardless of NOx conversion efficiency. Later diesel injection timings are likely to be required, which would negatively affect soot emissions and ITE. Also, the addition of EGR can allow for NOx emissions compliance. Using a high hythane

percentage in an ADF regime with a NOx conversion efficiency of 90%, on the other hand, can achieve an estimated SCR-out ISNOx of 0.09 g/kWh at low engine load, which is in line with both the Euro VI and Euro VII, without any ATS usage. Nevertheless, none of the dual-fuel combustion mode could meet NOx requirement, even with an SCR conversion efficiency of 90%.

A reduction in NOx levels provided by ADF mode enables for operational cost savings due to lower aqueous urea solution consumption ($\dot{m}_{urea}$) in the SCR system in order to meet Euro VII limits. Furthermore, optimising the ADF operation by means of more advanced diesel SOI (in-cylinder NOx control) may have the ability to further reduce NOx levels, thus potentially eliminating the need for an SCR system at low engine loads, as can be seen in Figure 4.7.

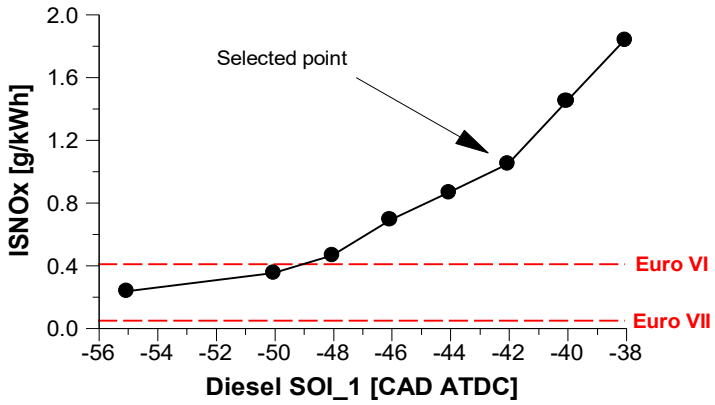

Figure 4.7. Diesel SOI as a NOx generation control at low engine load.

As a result, significant total cost of ownership savings, including SCR operational running costs, can be achieved. Even so, it is worth mentioning that other engine in-cylinder NOx control such as EGR can also further improve NOx reduction, including at higher engine loads.

To determine the effectiveness of the ADF combustion in terms of running costs, the $\dot{m}_{urea}$ required to reduce the NOx levels to the Euro VII emissions standard limit was calculated as

$$\dot{m}_{urea} = 0.01(ISNOx - ISNOx_{EuroVII})\left(\dot{m}_{diesel} + \dot{m}_{hythane}\frac{LHV_{hythane}}{LHV_{diesel}}\right) \quad (4.3)$$

where $\dot{m}_{urea}$ is estimated at 1% of the diesel equivalent fuel flow rate per g/kWh reduction in NOx emissions [183, 107, 184]. By adding the estimated $\dot{m}_{urea}$ to the measured diesel fuel flow rate allowed for the calculation of the SCR corrected indicated thermal efficiency (ITE SCR_{corr}), which was defined as

$$ITE\ SCR_{corr} = \frac{P_i}{\dot{m}_{hythane} LHV_{hythane} + (\dot{m}_{diesel} + \dot{m}_{urea}) LHV_{diesel}} \quad (4.4)$$

Figure 4.8 depicts the difference between the ITE with and without SCR correction for the three investigated combustion modes. Due to increasing urea use, CDC and CDF operations resulted in a significant fall in SCR corrected indicated thermal efficiency. The ADF mode with a high hythane percentage reduced NOx emissions and consequently the $\dot{m}_{urea}$ required. This enabled higher ITE SCR_{corr}, which effectively translates into lower operational costs. The ADF mode with high hythane percentage significantly decreased NOx emissions and thus the $\dot{m}_{urea}$ required.

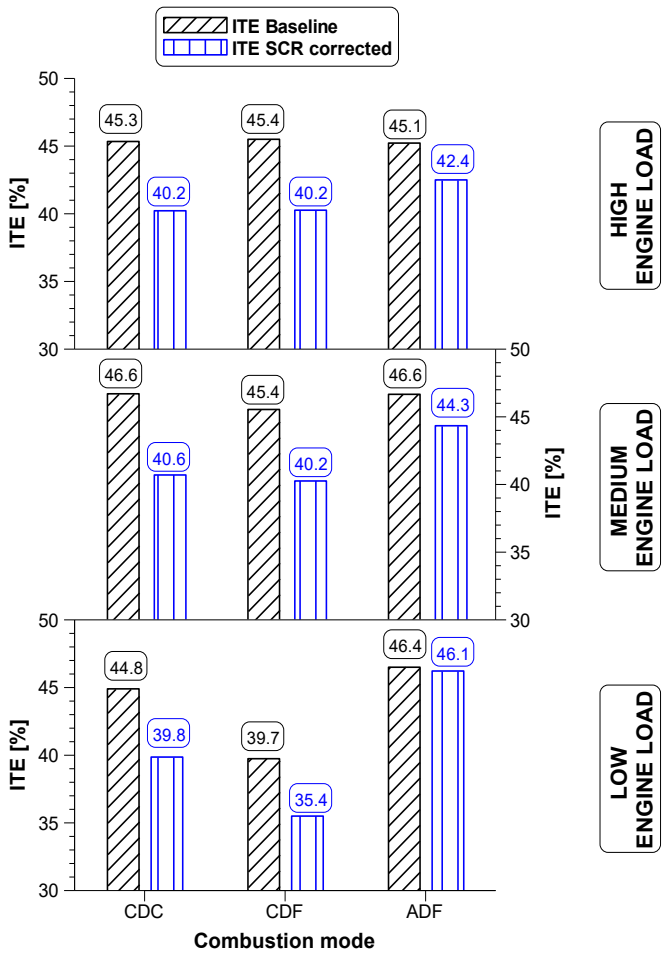

Figure 4.8. Difference between baseline ITE and SCR corrected ITE.

The estimated $\dot{m}_{urea}$ combined with $\dot{m}_{diesel}$ and $\dot{m}_{hythane}$ generated the total fluid consumption in kg/h, as shown in Figure 4.9. ADF regime demonstrated potential reduction of up to 25%, 20% and 16% of total fluid consumption for low-, mid-, and high-loads, respectively, when compared to the conventional diesel combustion, which is significantly higher than what the conventional dual-fuel mode can achieve, particularly at low engine load. Given the global variability in the pricing of diesel and aqueous urea solution, it is common in simulations to assume that the cost and properties of urea are equivalent to those of diesel fuel [107]. Under the assumption that hythane is priced similarly to diesel, the ADF combustion mode would offer the lowest operational cost due to its reduced overall fluid consumption. Consequently, the long-term sustainability of this strategy is closely linked to the market price – or more precisely, the demand – of hythane.

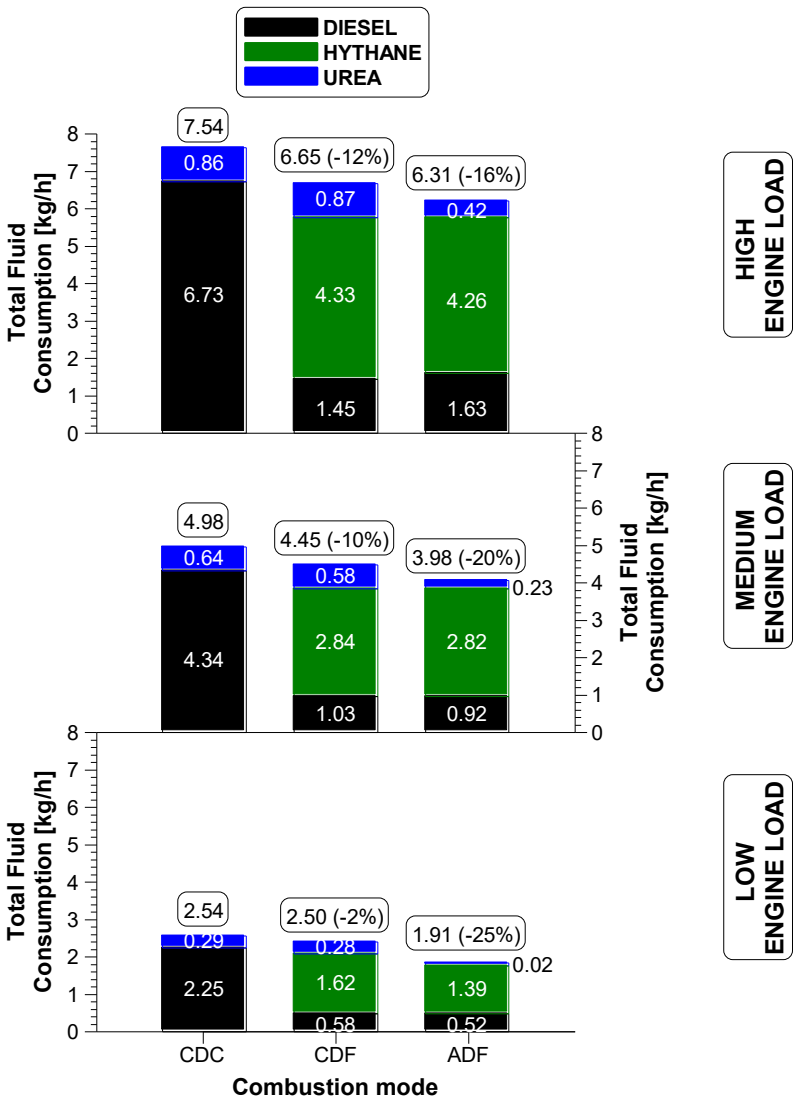

Figure 4.9. Total fluid consumption for CDC, CDF and ADF operations.

Therefore, the ADF combustion has the potential to substantially reduce engine-out NOx emissions while delivering the lowest total fluid consumption and, as a direct consequence, the highest SCR corrected indicated thermal efficiency, resulting in significantly lower operational costs. In addition, ADF regime at low engine load with no ATS may be able to meet NOx emissions limits, taking into account of the Euro VI regulation.

4.3 The combination of internal EGR and external EGR at low engine load

The impact of internal exhaust gas recirculation (iEGR) on combustion characteristics, engine efficiency, and emissions was investigated under dual-fuel operation at a fixed engine speed of 1200 rpm and a low-load condition of 0.6 MPa IMEP. iEGR was implemented through intake valve re-opening (2IVO) using the variable valve actuation (VVA) system. The strategy involved retaining hot residual gases within the cylinder to enhance fuel-air mixing and promote earlier autoignition in regions of higher reactivity. A one-dimensional (1D) engine simulation was used to predict both the residual gas fraction (RGF) and the average in-cylinder gas temperature.

It is important to note that this experiment was limited to low engine loads, as iEGR led to a decrease in ITE and increased knock tendency at higher engine loads.

4.3.1 Experimental test procedure

Table 4.3 summarises the engine operating condition. In this experiment, the diesel SOI was swept at a constant injection pressure of 100 MPa in order to determine the CA50 which achieved the highest ITE. The $\dot{m}_{hythane}$ was adjusted in function of the diesel SOI in order to maintain a HEF of 84% constant throughout the entire experiment. PRR and COV_{IMEP} were limited to 2.0 MPa/CAD and 3%, respectively.

The intake valve events were defined with an opening (IVO) at 369 CAD ATDC and a closing (IVC) at -105 CAD ATDC, using the 0.5 mm valve lif. The maximum lift of the intake valve reached 14 mm. For the implementation of the 2IVO strategy, the intake

valve was reopened during the exhaust phase, with its peak lift occurring around 195 CAD ATDC. When this strategy was employed, the earliest and latest valve re-opening positions were set at 145 and 230 CAD ATDC, respectively. This configuration enabled a peak secondary lift of 2 mm and achieved the highest RGF attainable based on the geometry of the intake cam profile.

Table 4.3. Engine operating conditions for the iEGR evaluation.

Parameter	Unit	ADF
IMEP	MPa	0.6
Engine speed	rpm	1200
HEF	%	84 ± 1
ECR	-	14.8
Intake air temperature	°C	41 ± 1
Intake air pressure	kPa	125
Exhaust air pressure	kPa	135
Diesel injection strategy	-	Early single injection
Diesel SOI_1	CAD ATDC	Sweep [-46 to -36]
Diesel injection pressure	MPa	100

Table 4.4 describes the three advanced dual-fuel testing modes explored: baseline (case 1), iEGR (case 2), and iEGR combined with eEGR (case 3). The baseline represents the same ADF mode studied in Section 4.2. The iEGR consists in the baseline advanced dual-fuel combustion combined with the 2IVO strategy to achieve internal exhaust gas recirculation. The case 3 is the combination of ADF with iEGR strategy and external EGR operated with 20% recirculation. The intake manifold air pressure was held constant at 125 kPa. Similarly, the exhaust pressure was maintained constantly 10 kPa higher than the intake in order to generate back pressure, allowing to deploy eEGR and achieve higher RGF.

Table 4.4. The testing modes matrix.

Testing modes	Case number	iEGR	eEGR
Baseline	1	NO	NO
iEGR	2	YES	NO
iEGR + eEGR	3	YES	YES (20%)

4.3.2 Engine modelling

To predict residual gas fraction (RGF) and average in-cylinder gas temperature under various intake camshaft configurations, a one-dimensional engine model was constructed using Ricardo WaveBuild simulation software. This tool applies the finite difference method to solve transient compressible flow equations based on conservation laws for mass, momentum, and energy. The model incorporates detailed thermodynamic properties, including equilibrium calculations for combustion products, and accurately represents the unsteady flow dynamics typical in internal combustion engines. Through this approach, the RGF can be estimated by analysing valve mass flow behaviour in conjunction with fuel injection dynamics.

Figure 4.10 provides a representation of the single-cylinder engine model. The inlet and exhaust pipelines were precisely measured from the engine test cell and simulated accordingly. Oscilloscopes were positioned in the corresponding locations as the experimental in-cylinder, intake, and exhaust pressure transducers. The geometric data of the cylinder head was acquired from the computer-aided design model supplied by Yuchai. Experimental data, including temperatures, initial intake and exhaust pressures, fuel flow rates, injection locations and timings, and heat release profiles, were incorporated into the model. Hythane was introduced homogeneously at the boosted air, whereas diesel was directly injected into the cylinder.

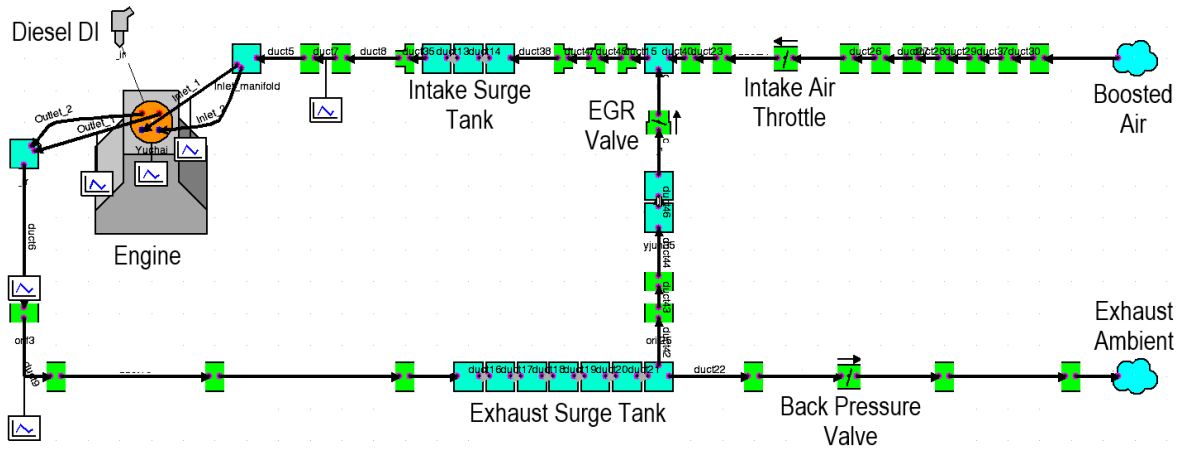

Figure 4.10. 1D model of the single cylinder HD engine

The coefficients evaluate the real airflow rate via the poppet valves in relation to the performance of theoretical ports free of constraints. The calculation of the CFs employs the ideal gas velocity and the cross-sectional area of the valve throat. The reference diameters (D), which were taken from [185], were measured from the inner seats of the valves, yielding 39.2 mm for the intake side and 35.8 mm for the exhaust side.

The engine heat transfer sub-model employed a detailed thermal network, incorporating components such as the piston, cylinder liner, cylinder head, intake and exhaust valves, valve seats, and associated ports. Initial surface temperatures on the gas side were set at default values – 385 K on the intake side and 500 K on the exhaust side. A coolant temperature of 380 K was applied to key regions including the piston, liner, and head, using heat transfer coefficients adapted from a multi-cylinder diesel engine case provided within the simulation software's library.

The combustion modelling was based on empirical approaches embedded within the 1D simulation platform and corresponded to empirical relationships developed in [186]. For dual-fuel operation, a specialized Wiebe-based sub-model was applied, allowing for the use of multiple fuel types and components. This configuration employed up to four overlapping Wiebe functions to better replicate the mass fraction burned (MFB) profiles observed in experimental pressure data.

Figure 4.11 presents the result of combining three Wiebe curves, calibrated to match the experimentally measured burn rate under dual-fuel conditions. Each curve was defined by parameters including the crank angle at which 50% of the mass was burned, burn duration, curve shape exponent, and the proportional fuel mass associated with it. The aggregate burn rate was adjusted based on experimentally determined combustion efficiency to account for incomplete combustion phenomena.

For heat transfer calculations, the Woschni correlation was implemented to estimate heat exchange between the working gas and the cylinder walls. The model assumed a consistent convective heat transfer coefficient and uniform flow velocity over all combustion chamber surfaces. A correction factor was included to compensate for engine load, which influenced the characteristic gas velocity and, consequently, the

calculated heat transfer coefficient. This factor accounted for both the mean piston speed and combustion-induced velocity changes, which were tied to in-cylinder pressure.

To simplify dual-fuel modelling, diesel was assumed to be fully premixed at the start of combustion, with timing and quantity set according to the injection schedule. This simplification influenced the calculated post-combustion gas temperatures, which were excluded from the scope of this study.

The simulation was configured to run for 80 engine cycles or until a convergence threshold of 0.1% was met. If the model met this convergence requirement before completing all cycles, an additional cycle would be simulated to ensure stability.

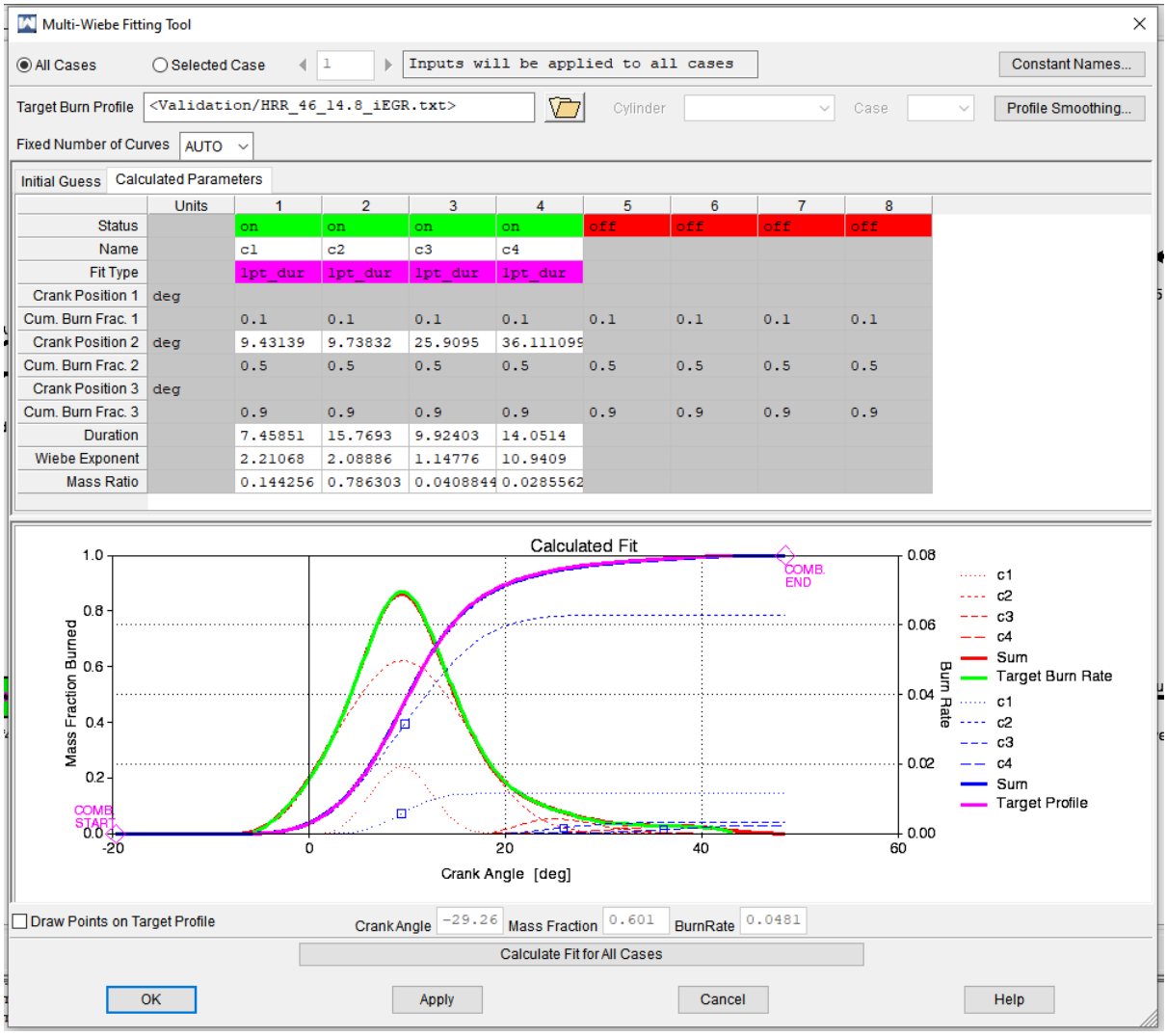

Figure 4.11. Multi-Wiebe fitting tool panel

4.3.3 Validation of the 1D engine model

The intake air mass flow and the maximum in-cylinder gas pressure (P_{max}) were validated to within 1% of the experimental data. Figure 4.12 shows a strong correlation between experimental and numerical intake average mass air flow rate ($\dot{m}_{air}$), while Figure 4.13 shows excellent alignment in in-cylinder pressure during compression and expansion strokes, permitting the 1D model to estimate RGF and mean in-cylinder gas temperature.

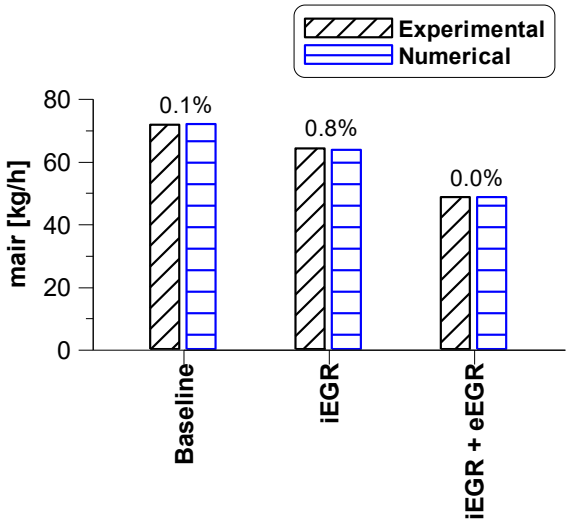

Figure 4.12. Validation of intake mass flow rate for multiple cases applying iEGR.

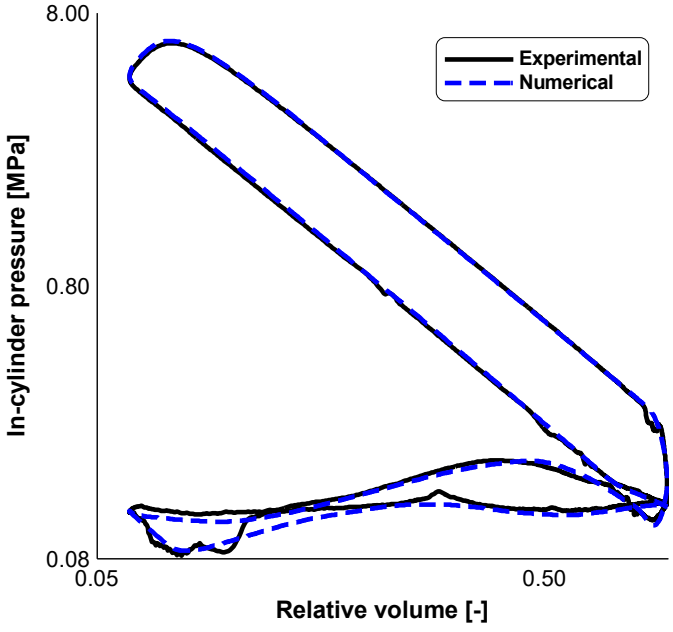

Figure 4.13. Experimental and numerical log P-V diagram of Case Miller + iEGR.

4.3.4 Overview of the iEGR and combustion characteristics

Figure 4.14 compares the measured in-cylinder average pressure, heat release rate for a constant diesel SOI. Combustion characteristics, including SOC, ignition delay (SOC-SOI_1), combustion duration, and other combustion parameters, are illustrated versus CA50 in Figure 4.15, enabling the identification of the optimal CA50 for the studied cases. Figure 4.16 depicts the simulated mean in-cylinder gas temperature and residual gas fraction.

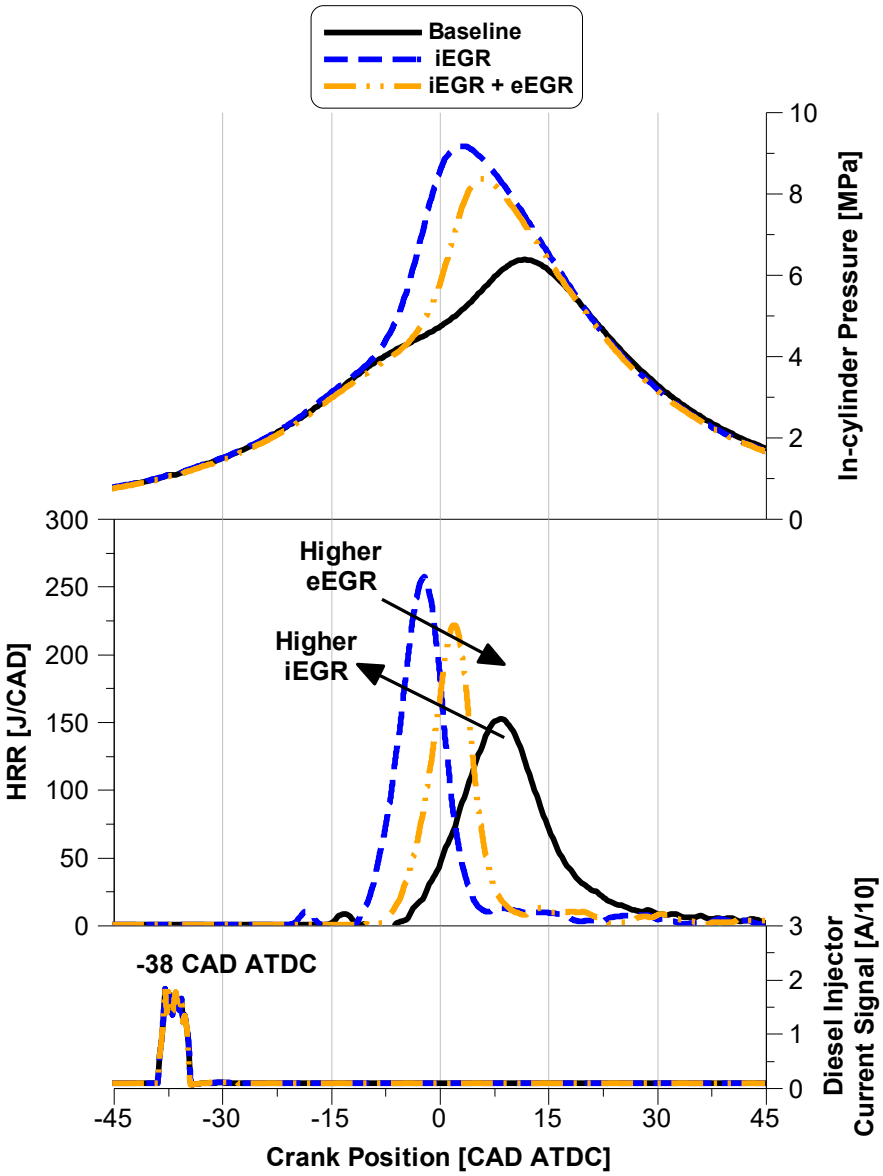

Figure 4.14. The effect of iEGR on in-cylinder pressure, mean in-cylinder gas temperature and HRR for constant diesel injection.

Relatively later diesel injections resulted in the production of slightly lower λ regions in the piston bowl [187]. This higher degree of stratification increased local in-cylinder temperatures, advancing the CA50 positions and reducing the COV_{IMEP}. In comparison, advanced SOI allowed for more uniform equivalence ratio and ignition delay distribution [187], yielding opposite effects to later SOI.

The early single diesel injection strategy ensured sufficient mixing time and allowed an almost linear combustion phasing control with low overall COV_{IMEP}. A low COV_{IMEP} is important to minimise the combustion instability associated with misfiring cycles and partial burning of the fuel [188].

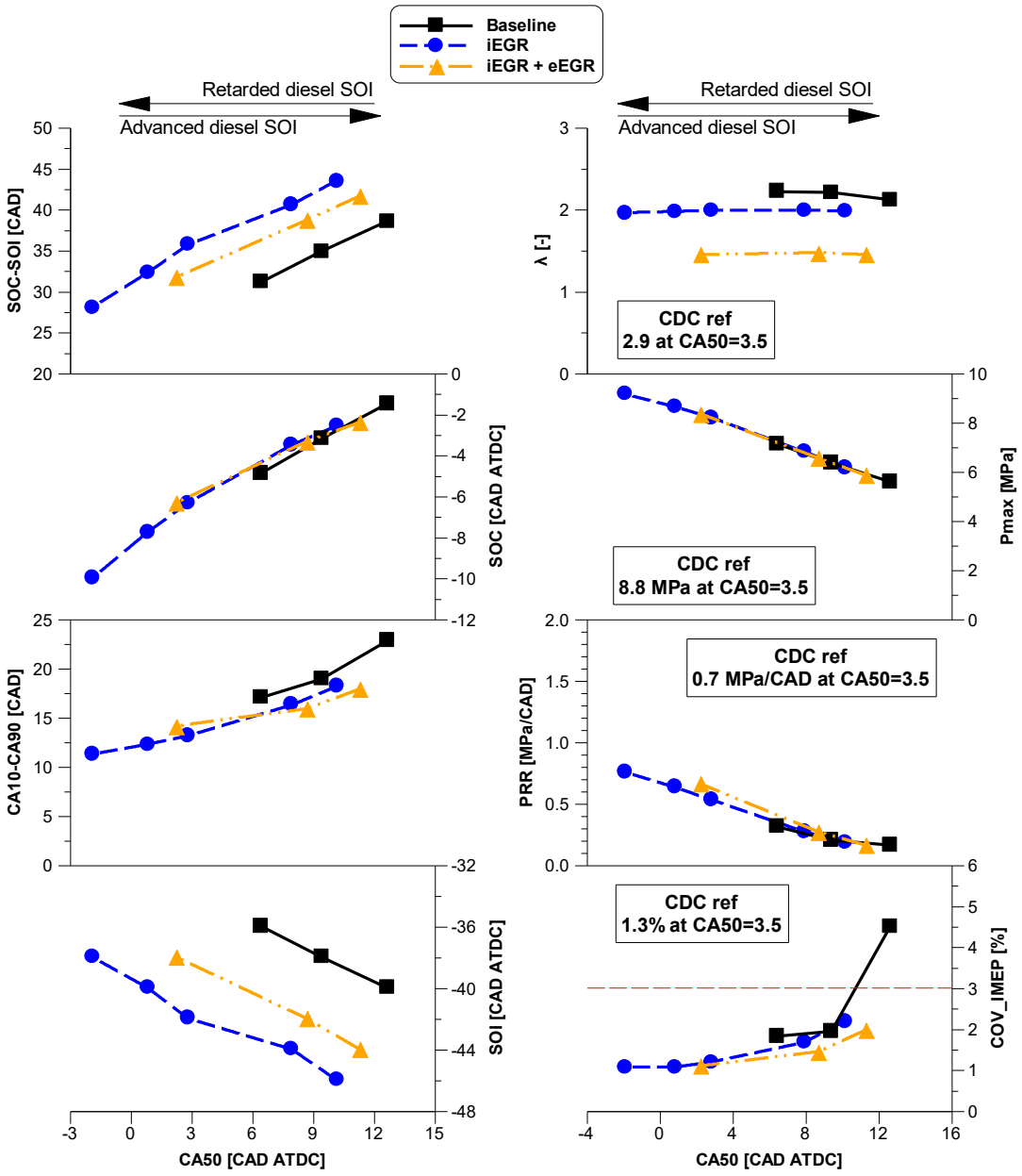

Figure 4.15. The effect of iEGR on combustion characteristics at low engine load.

The introduction of the 2IVO strategy in the iEGR mode increased the RGF to 12.7%, while the combined iEGR + eEGR strategy in case 3 resulted in an RGF of 10%. Higher amounts of hot residuals augmented the mean in-cylinder gas temperature depicted in Figure 4.16, consequently accelerating the evaporation and combustion processes and diminishing the cycle-to-cycle variability (COV_{IMEP}) relative to the baseline, as shown in Figure 4.15. As a result, advanced SOIs were required to control charge reactivity. The use of a constant SOI would lead to over-advanced burn rates triggered by the more reactive mixture with iEGR.

According to Caton [189], shorter burning rates and relatively lower heat losses allow for more advanced CA50 and considerably higher maximum in-cylinder pressure (Pmax), as evidenced in Case 2. This is the case of the iEGR mode, where peak combustion temperatures (i.e. burnt zone) and heat transfer are likely to be reduced by the dilution and higher heat capacity introduced by higher RGFs [190]. The more advanced and faster combustion process resulted in higher Pmax.

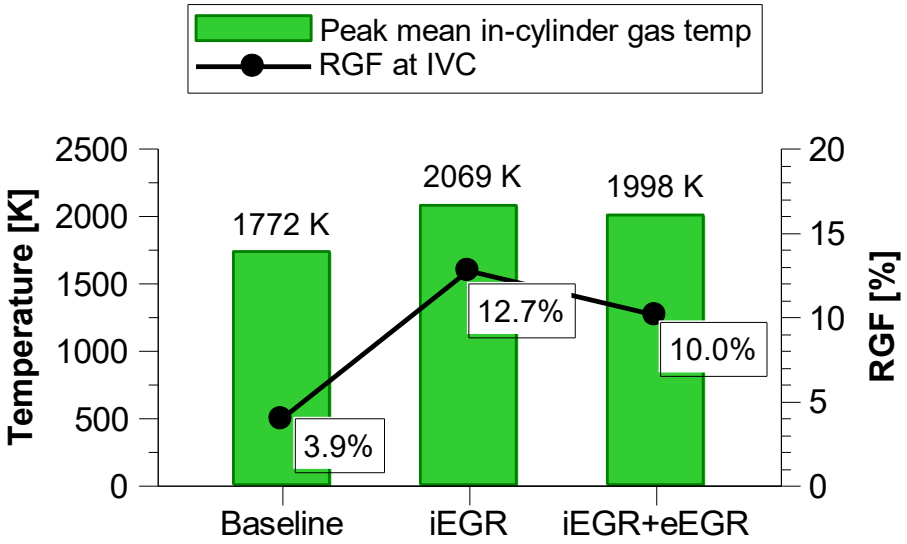

Figure 4.16. In-cylinder gas temperatures and RGF for the three dual-fuel cases obtained from the 1D engine model.

On the other hand, when combined with iEGR, eEGR acts as an additional mechanism that further reduces the oxygen content in the intake charge, improving combustion stability, reducing peak mean gas temperatures, and allowing for a higher fraction of

exhaust gases in the cylinder. This results in lower effective intake oxygen level and subsequently lowers the RGF when compared to case 2, as observed in Figure *4.16*.

The decrease in oxygen content provided by the addition of eEGR helps explaining the reduction in λ noted in Figure 4.15 when compared to other two cases. Nevertheless, this also contributed to longer ignition delay, consequently leading the SOC to take place after TDC. As a result, both peak in-cylinder pressure and HRR decreased when compared with Case 2 (only iEGR), as observed in Figure 4.14.

4.3.5 Engine performance

The impact of the iEGR on combustion and indicated thermal efficiencies, EGT and indicated equivalent specific fuel consumption are depicted in Figure 4.17. Earlier combustion processes resulted in higher compression work and possibly higher heat losses. Later combustion events lowered the engine efficiency due to higher combustion losses and decreased expansion work.

The hotter combustion processes provided by the combination of iEGR and eEGR elevated the EGT to above 400°C, which is sufficiently high to initiate the catalyst light-off enhance conversion efficiency of the DOC [191] and MOC [171]. Nonetheless, although yielding higher exhaust gas temperatures than the baseline, dilution of the in-cylinder charge with residual gases and reduced local in-cylinder gas temperatures limited the exhaust gas temperatures in the iEGR mode.

The relatively higher mean combustion temperatures with richer air-fuel mixture enhanced the oxidation process of NMHC and CO. As a result, combustion efficiencies increased from 95% in the baseline dual-fuel case to 96% in the iEGR. The combination of iEGR with eEGR leads to an improvement to approximately 97.5%, largely because to the considerable decrease in unburned CH_4.

The iEGR mode provided a similar ITE when compared to the ADF baseline, as the diesel SOI remained above -40 CAD ATDC, which produced a comparable ISFCeq.

However, when adding eEGR, this resulted in a more retarded diesel SOI, increasing the ISFCeq and consequently lowering ITE by 1 percentage point.

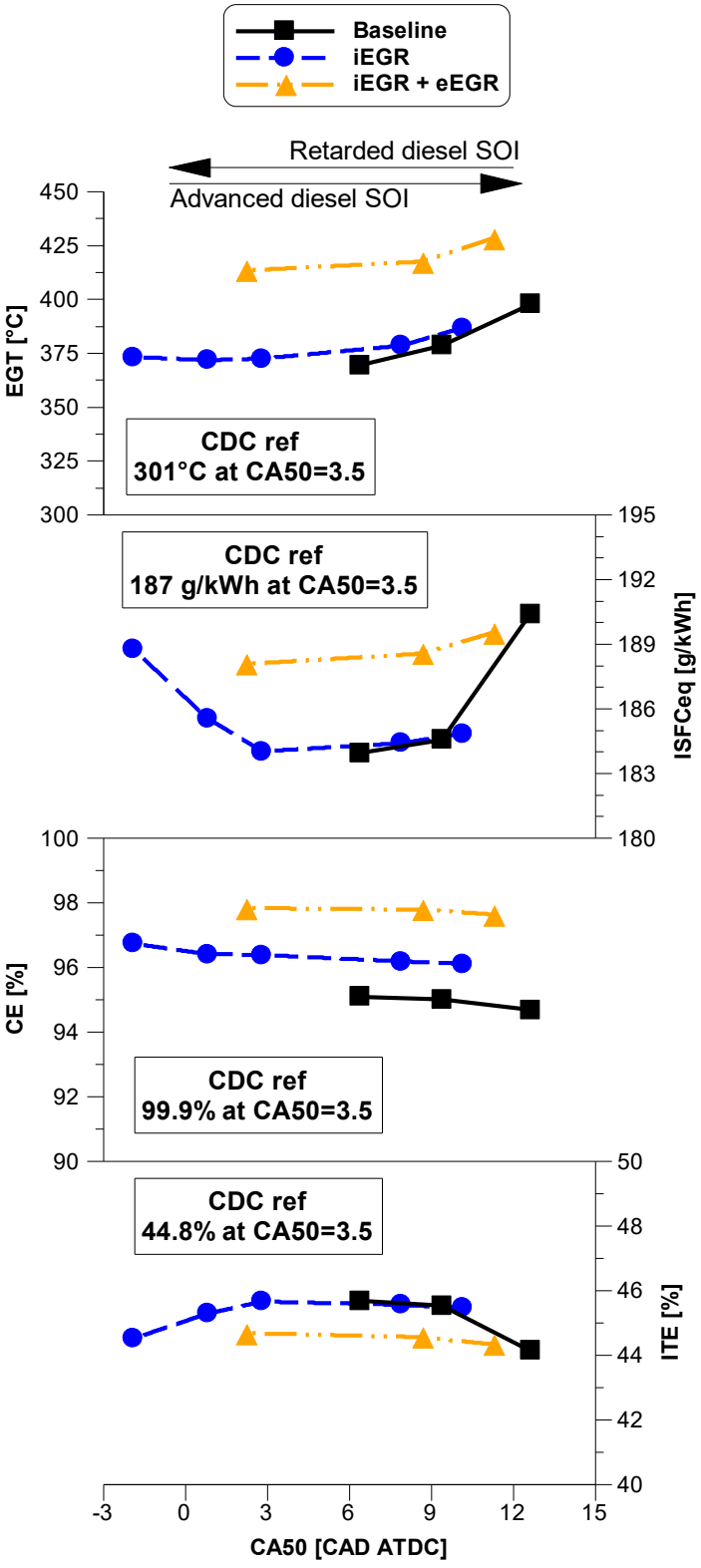

Figure 4.17. The effect of iEGR on engine performance at low engine load.

4.3.6 Engine-out emissions

Exhaust emissions in the form of net indicated specific values for the three cases modes are depicted in Figure 4.18. The use of the iEGR modes to achieve lower λ was shown effective in reducing unburnt NMHC and CH_4, as well as CO emissions.

The higher RGF demonstrated by the iEGR mode elevated the in-cylinder charge temperature. The hotter charge and lower relative air-fuel ratio led to peak mean in-cylinder gas temperature by around 300K when compared to the baseline. Thus, this warmer combustion process enhanced the oxidation of CO, enabling to reduce it to under the Euro VI limit of 1.5 g/kWh at more retarded diesel SOI. However, as a drawback, this led to a higher CO_2 generation, particularly at diesel SOI where CO oxidation were more noticeable. Similarly to CO, NMHC was considerably decreased.

Considering CO2eq, although its negative impact on CO_2, the iEGR mode can substantially decrease unburned methane, as shown in Figure 4.18, leading to a 7% reduction in GHG emissions. The combination of iEGR with eEGR can yield to an even higher reduction up to 11%, as eEGR further maximises the recirculation of unburned methane.

Within the same CA50 range as the baseline, NOx emissions were comparably low with the introduction of the iEGR strategy, nearing Euro VI standards. This demonstrates that iEGR mode has no negative impact on NOx levels. Nevertheless, the addition of eEGR seems to marginally elevate NOx formation, indicating an unexpected result. The utilisation of eEGR reduces the advantages of fuel combustion under lean premixed conditions, as promoted by the early diesel injection strategy of ADF combustion, due to eEGR's enhancement of in-cylinder charge reactivity, which requires the retardation of the diesel SOI.

Soot emissions were found to be considerably reduced with the use of iEGR. This is likely due to the longer ignition delay, resulting in improved diesel mixing, as iEGR enables a more advanced diesel SOI compared to the baseline. The addition of eEGR apparently did not affect soot emissions, maintaining them at levels similar to the iEGR mode.

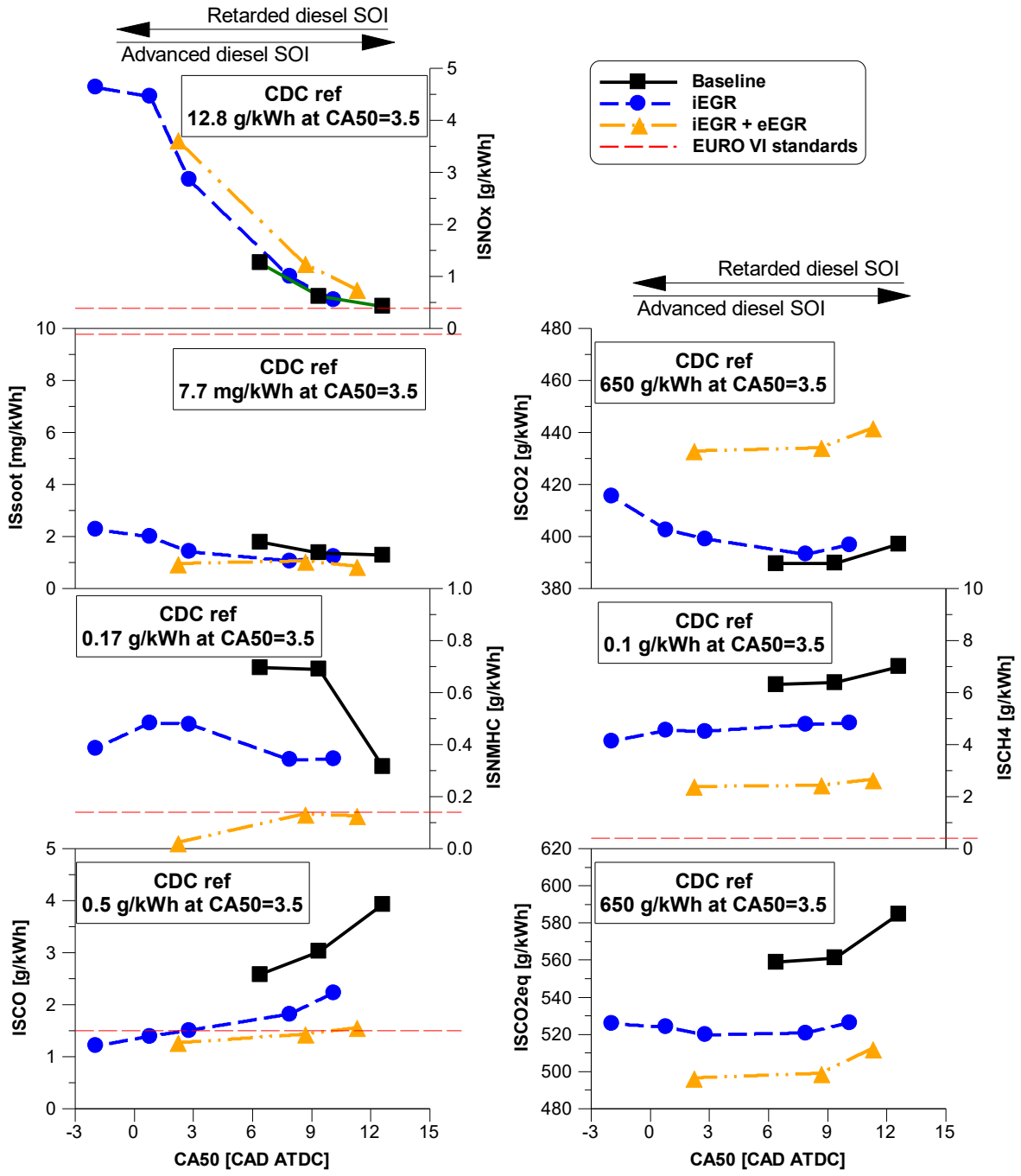

Figure 4.18. The effect of iEGR on engine-out emissions at low engine load.

Overall, the combination of internal and external EGR has a greater potential to maintain NOx emissions under Euro VI standards while achieving higher EGTs, which is especially important at low engine loads for achieving the minimum light-off temperature for ATSs such as SCR and MOC for NOx and CH_4 reduction, respectively.

4.4 The effect of external EGR at medium and high engine loads

In Section 4.2, although ADF indicated a significant reduction in NOx emissions when compared to CDF and CDC, particularly at low engine loads, medium and high loads revealed that NOx levels remained significant. As a result, experiments were conducted to evaluate whether external EGR has the capacity to reduce NOx emissions at medium and high engine loads without sacrificing efficiency and GHG levels. The investigation was carried out for medium and high engine loads of 1.2 and 1.8 MPa IMEP, respectively.

4.4.1 Experimental test procedure

Table 4.5 summarises the engine operating conditions. The diesel injection strategy used was the same as that described in Section 4.2: split injection, with 50% of the diesel injected during a fixed early injection (SOI_1) at -60 CAD ATDC and 50% during a late injection (SOI_2). The SOI_2 was swept across multiple timings. The $\dot{m}_{hythane}$ was adjusted in function of the diesel SOI in order to maintain a HEF of 76% constant throughout the entire experiment.

Table 4.5. Engine operating conditions for the investigation of eEGR.

Parameter	Unit	Medium load	High load
IMEP	MPa	1.2	1.8
Engine speed	rpm	1200	1200
HEF	%	76 ± 1	76 ± 1
ECR	-	14.8	14.8
Intake air temperature	°C	43	44
Intake air pressure	kPa	190	260
Exhaust air pressure	kPa	200	270
eEGR	%	Sweep [0, 10]	Sweep [0, 10]
iEGR	%	0	0
Diesel SOI_1	CAD ATDC	-60	-60
Diesel SOI_2	CAD ATDC	Sweep [0 to 8]	Sweep [3 to 10]
Diesel injection pressure	MPa	130	160

The use of external EGR rate of 10% was compared to a baseline ADF without EGR. The intake and exhaust manifold pressures were held constant. PRR and COV_{IMEP} were limited to 2.0 MPa/CAD and 3%, respectively.

4.4.2 Overview of the eEGR and combustion characteristics

Figure 4.19 and Figure 4.20 show the effect of eEGR on the combustion with constant diesel SOI_1 and SOI_2. Figure 4.21 depicts combustion indicators such as relative air-fuel ratio, peak in-cylinder pressure, PRR, and combustion stability versus CA50, allowing for a direct comparison of ADF with and without eEGR at a constant CA50.

The introduction of an EGR rate of 10% with constant diesel SOIs shows a similar trend at medium and high engine loads. It was observed an increased ignition delay, which resulted in longer combustion duration. This was attributed to lower in-cylinder gas temperatures introduced by increased specific heat capacity of the in-cylinder charge (e.g. presence of CO_2 in the recycled gases) and reduced oxygen availability - dilution effect [192, 190]. Consequently, the peak in-cylinder pressure is also decreased, especially at high engine load. And this can be a positive aspect to note, since as described in 4.2, the excessive in-cylinder pressure rise rates caused by the autoignition of the premixed charge can be mitigated with the application of eEGR.

The lower oxygen available in the in-cylinder charge results in lower relative air-fuel ratio. This is evident in Figure 4.21 in which the ADF with 10% eEGR tends to present lower λ in both medium and high engine loads at constant CA50.

Nevertheless, unlike at constant diesel SOI, Figure 4.21 demonstrates comparable Pmax and COV_{IMEP} with and without 10% eEGR at constant CA50. For that, SOI was retarded with 10% eEGR in order to increase the charge reactivity and phase the burn rate closer to the combustion phasing of the 0% eEGR case.

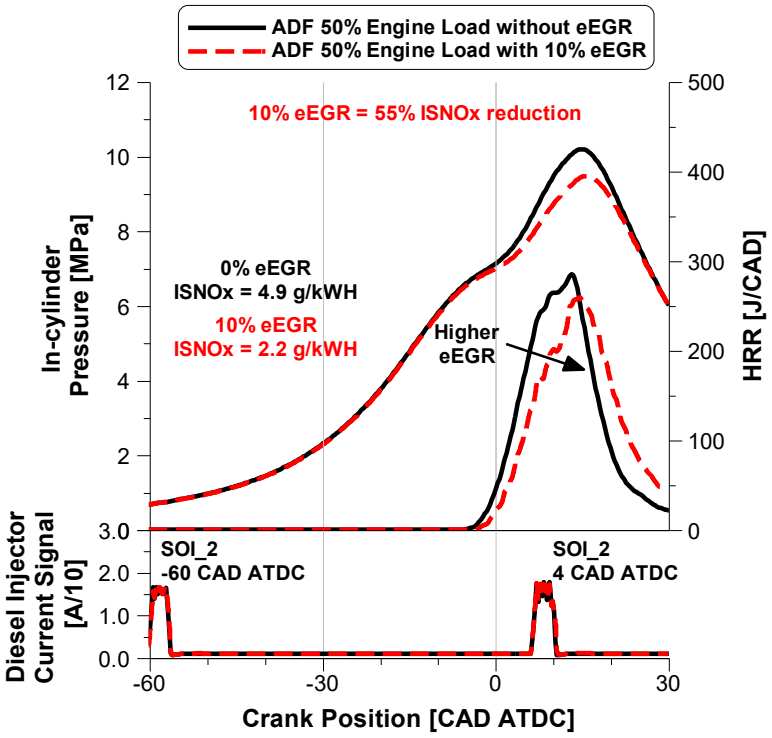

Figure 4.19. The effect of eEGR on in-cylinder pressure and HRR for constant diesel injection at medium engine load.

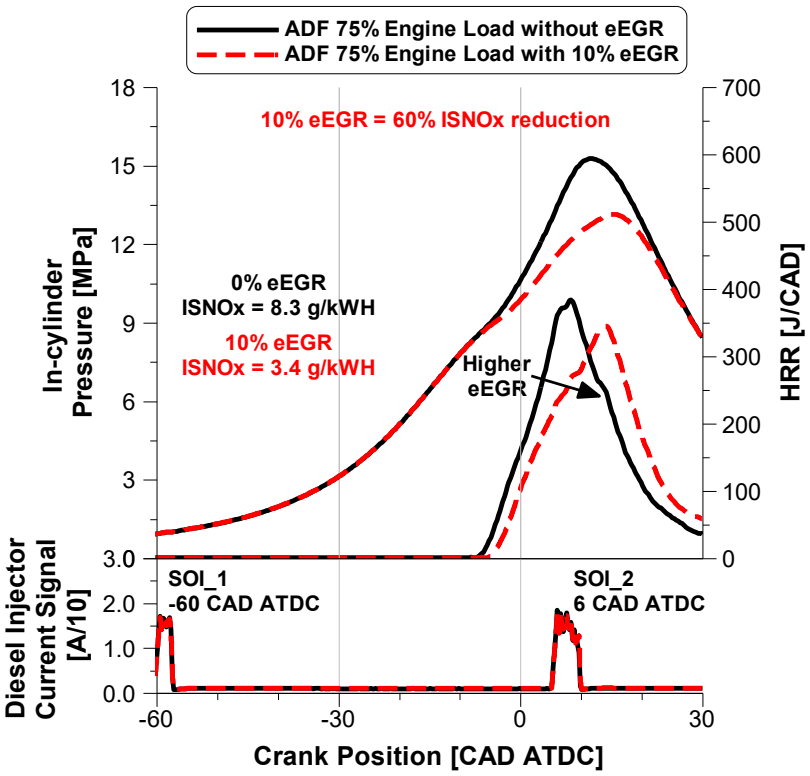

Figure 4.20. The effect of eEGR on in-cylinder pressure and HRR for constant diesel injection at high engine load.

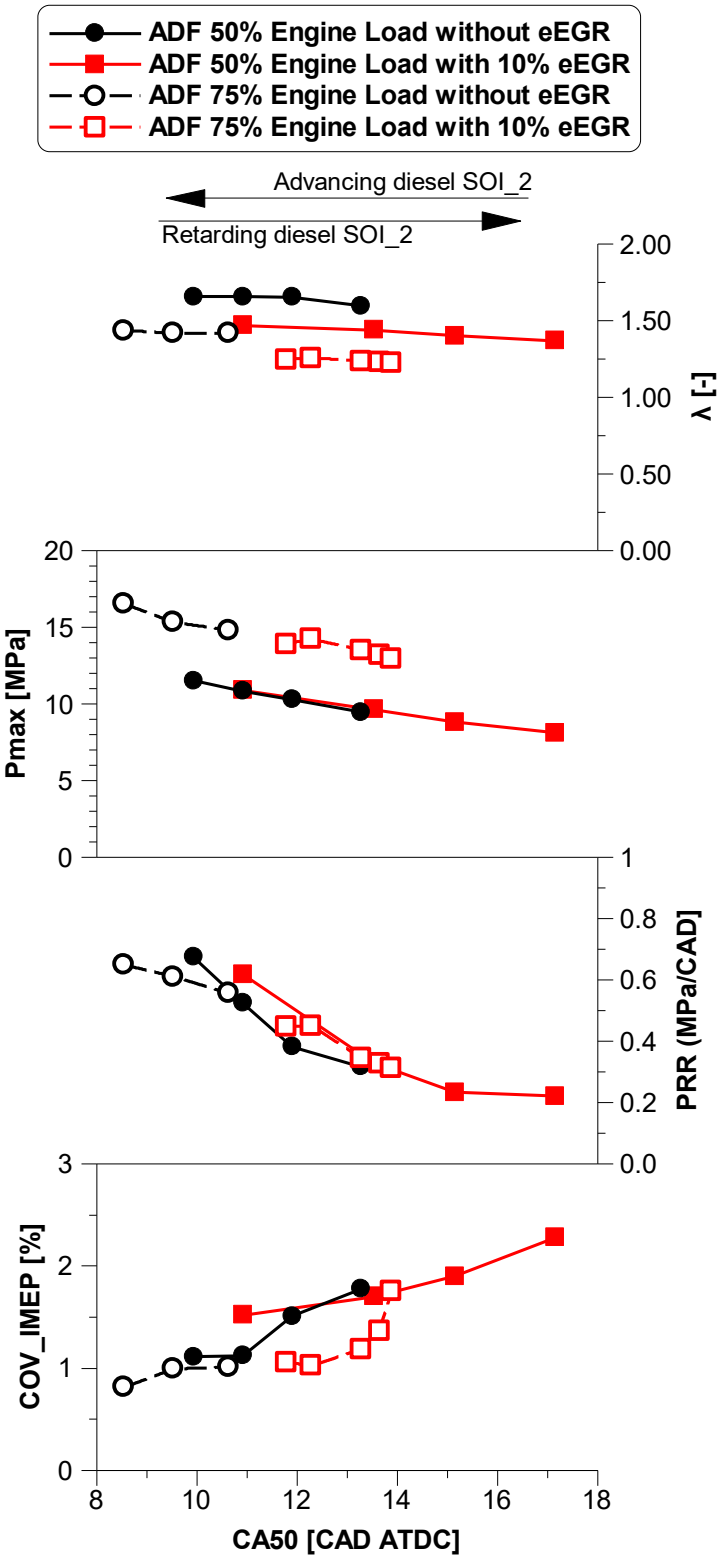

Figure 4.21. The effect of eEGR on combustion parameters at medium and high engine loads.

4.4.3 Engine-out emissions and performance

The impact of the eEGR on combustion and indicated thermal efficiencies, EGT and indicated equivalent specific fuel consumption are depicted in Figure 4.22. Exhaust emissions in the form of net indicated specific values with and without the use of eEGR are depicted in Figure 4.23.

As seen previously, the addition of eEGR generates a longer ignition delay, resulting in a delay of the combustion process. This therefore allows the ADF combustion to run with more retarded CA50, achieving higher EGTs. The external EGR increased fuel consumption slightly, likely due to the lower oxygen content in the in-cylinder charge, leading the engine to inject more fuel to maintain the IMEP output.

The results highlight the CO and NOx emissions' strong dependence on CA50 position. At a given combustion phasing, the introduction of EGR required relatively shorter ignition delays via later diesel injection timings. Retarded SOIs likely increased local temperatures, improving the oxidation of CO emissions. In addition, a lower relative air-fuel ratio achieved with EGR possibly helped minimise overly lean regions, curbing CO and unburnt HC emissions. However, the increased local rich mixture contributes to increased soot generation, potentially causing emissions to exceed the emission standard limits.

On the other hand, lower λ can help maintain the air-fuel ratio within a more optimal range for complete combustion, resulting in a decrease of unburned hydrocarbons (both NMHC and CH_4) and thus enhancing combustion efficiency, as illustrated in Figure 4.22. Conversely, more complete combustion resulted in an undesirable increase in CO_2 emissions, leading to an approximate 4% increase in GHG due to the greater quantity of fuel burned.

This experiment shows that the combination of external EGR with the advanced dual-fuel strategy can mitigate the excessive in-cylinder pressure of the ADF mode at high engine load, and can potentially improve the total cost of ownership at medium and high engine loads via reduction of the aqueous urea solution consumption in the SCR system, but at the expense of higher GHG emissions.

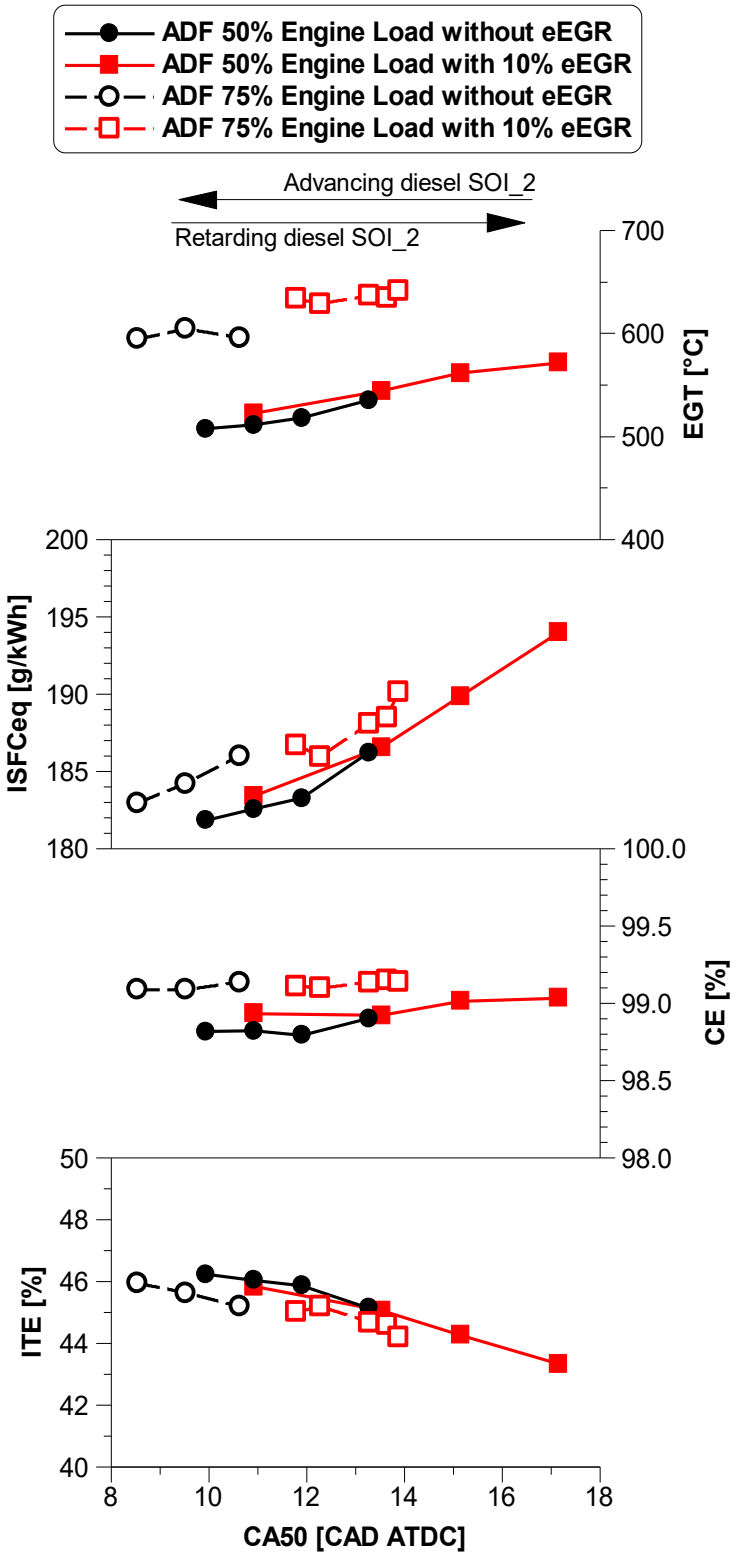

Figure 4.22. The effect of eEGR on engine performance at medium and high engine loads.

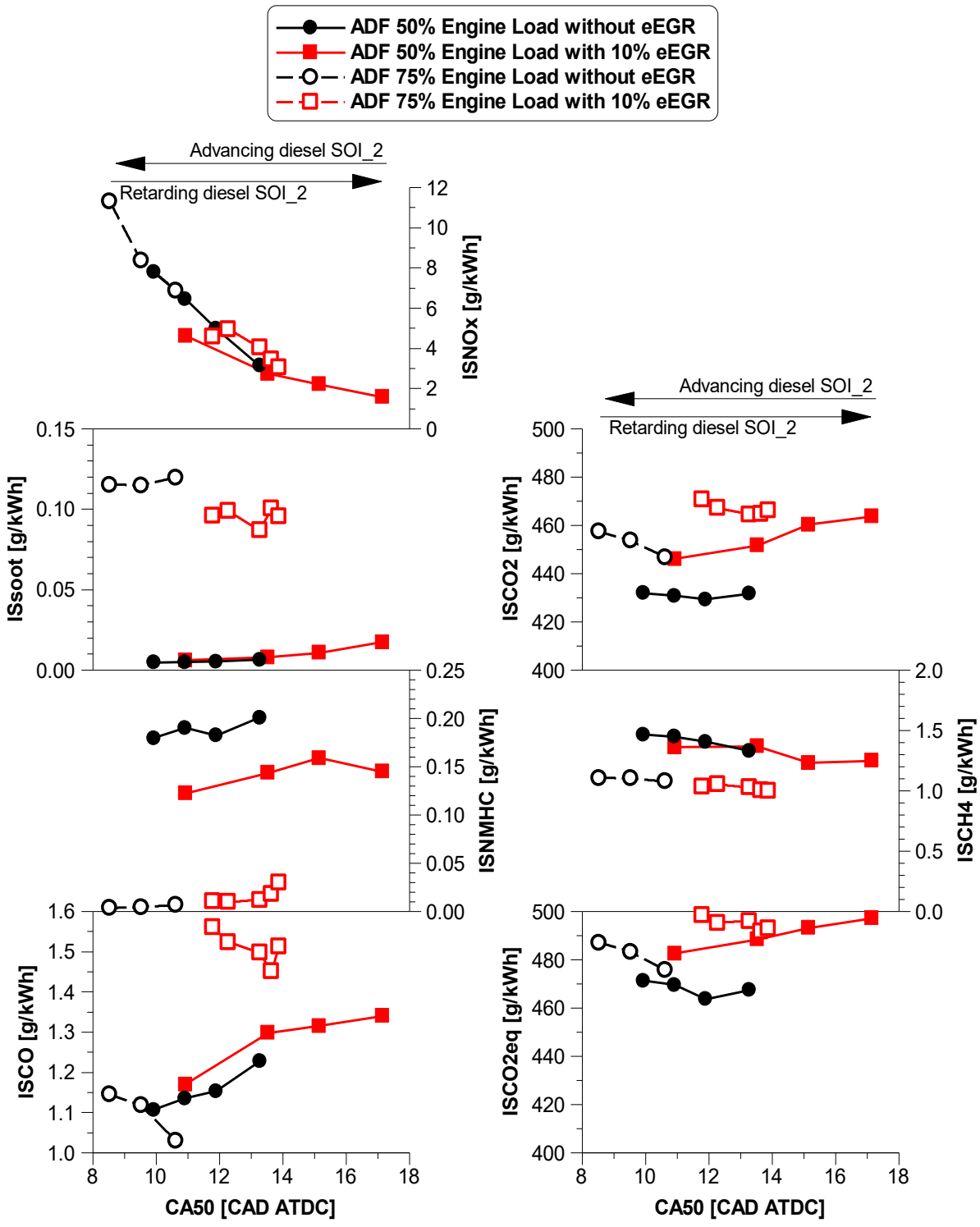

Figure 4.23. The effect of eEGR on engine-out emissions at medium and high engine loads.

4.5 Overview of optimal dual-fuel engine operation

This section presents an overview of optimal engine operation tailored to various performance and emissions targets. The analysis focuses on maximising the hydrogen energy fraction achievable in the two dual-fuel modes studied, comparing combustion strategies based on their GHG reduction potential, and providing a Well-to-Wheel (WTW) analysis for different hythane fuel sources. Additionally, a performance matrix is introduced to summarise the key findings and support the selection of the most suitable strategy for specific objectives.

The investigation was conducted for CDF and ADF combustion modes at a constant engine speed of 1200 rpm, under low, medium, and high engine loads of 0.6, 1.2, and 1.8 MPa IMEP, respectively. The diesel SOIs were optimised for every data point.

4.5.1 Maximisation of hythane energy fraction

Figure 4.24 illustrates the maximum HEF achieved for each dual-fuel combustion mode across the engine map. The red annotations represent ADF results, while the blue annotations indicate CDF outcomes.

A clear contrast between the two combustion modes is evident. The ADF regime achieves the highest HEF at low engine loads, reaching up to 87% diesel replacement on an energy basis. However, this percentage decreases with increasing load, reaching 83% at high engine load. This reduction is attributed to the limitations of early diesel injection at higher loads, where the diesel quantity in the SOI_1 must be reduced from 100% at low load to approximately 20% at high load, as discussed in Section 4.2.

Conversely, the CDF mode allows for greater diesel replacement at higher loads. At low loads, the maximum HEF achieved was 78% with 20% eEGR, while at high loads, the HEF increased to 87%, which is four percentage points higher than ADF.

As a result, the optimal strategy for maximising HEF is to utilise the ADF mode at low and medium loads and CDF combustion at high engine loads.

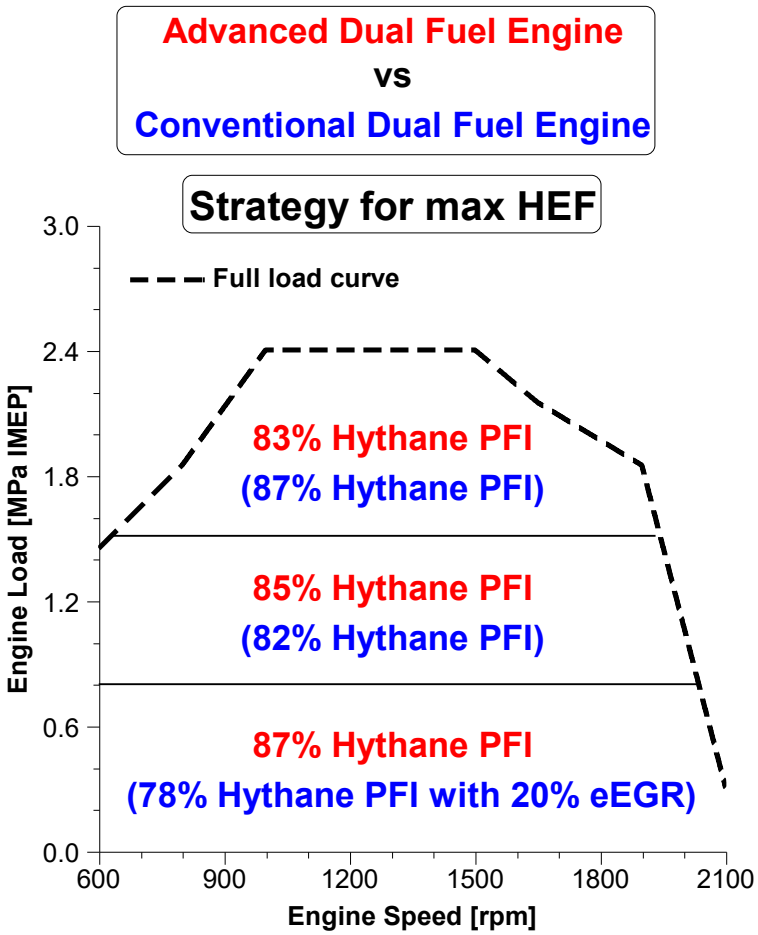

Figure 4.24. Comparison of dual-fuel strategies for HEF maximisation across low, medium and high engine loads.

4.5.2 Maximisation of GHG reduction potential

Figure 4.25 shows the highest reduction of GHG emissions achieved for each dual-fuel combustion mode across the engine map. The red annotations indicate ADF results, whereas the blue annotations represent CDF outcomes.

Overall, the advanced dual-fuel strategy consistently achieved the highest GHG reduction across all engine loads. It provided a maximum 25% reduction at low load and 26% at medium and high loads, significantly outperforming the CDF mode. The underlying reasons for these results were discussed in Section 4.2.

Notably, for both dual-fuel modes at all engine loads, the optimum HEF for maximum GHG reduction does not correspond to the maximum HEF shown in Figure 4.24. This

discrepancy arises because, although a higher HEF leads to greater CO_2 reduction, it also increases unburned CH_4 emissions, which negatively impacts overall GHG performance. Therefore, the HEF values in Figure 4.25 represent the optimal balance for lowering GHG emissions in diesel-hythane dual-fuel combustion.

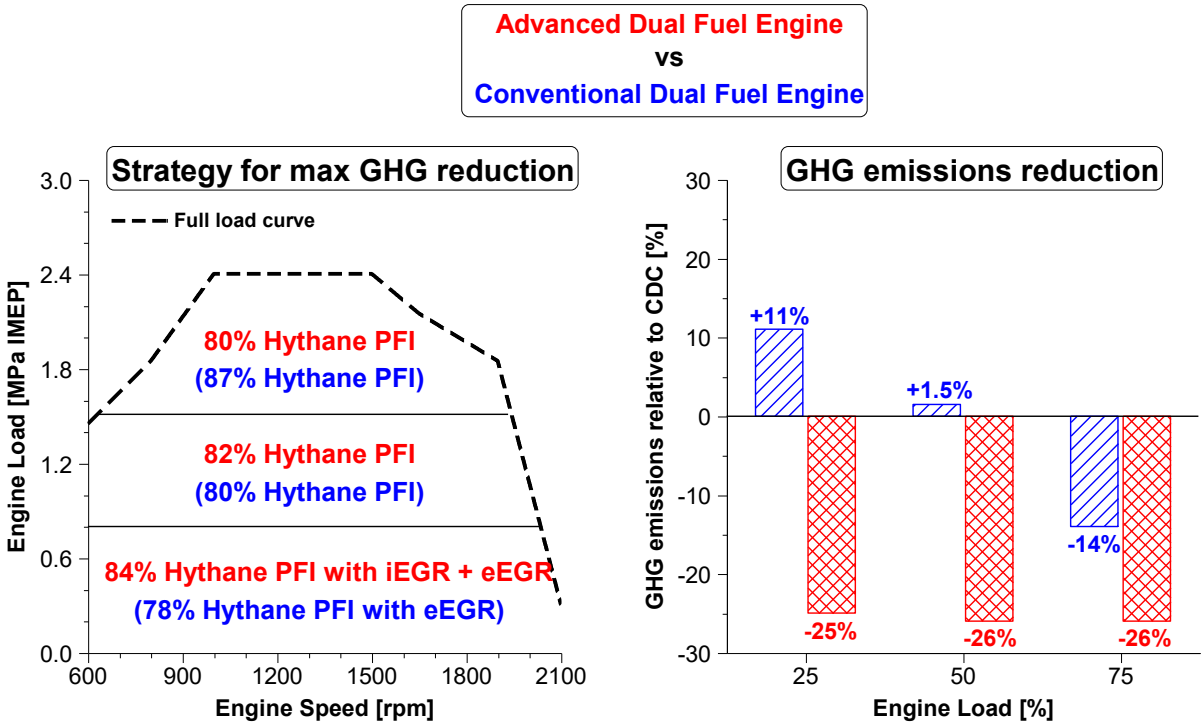

Figure 4.25. Comparison of dual-fuel strategies for maximum GHG emissions reduction across low, medium and high engine loads.

4.5.3 Well-to-Wheel analysis

A Well-to-Wheel (WTW) analysis was conducted to evaluate the real impact of using hythane fuel in advanced combustion modes on GHG emissions in the transportation sector. This holistic approach combines Well-to-Tank (WTT) and Tank-to-Wheel (TTW) data to estimate the total GHG emissions associated with both the production and use of a given fuel [193, 194]. The WTT phase accounts for emissions generated during the extraction or cultivation of raw materials, processing, transportation, and delivery to the fuel tank, while TTW reflects the emissions during the actual engine operation. GHG levels were quantified in grams of CO_2 equivalent (CO_{2eq}) emissions per MJ of fuel injected.

The first part of the methodology was to obtain the TTW CO_{2eq}, which consisted in calculating the ratio of the estimated mass of CO_{2eq} emissions to the total fuel energy supplied to the engine as

$$TTW\ CO_{2_{eq}} = \frac{ISCO_{2_{eq}}\ P_{ind}}{\dot{m}_{diesel}\ LHV_{diesel} + \dot{m}_{hythane}\ LHV_{hythane}} \tag{4.5}$$

The WTW CO_{2eq} emissions were given by

$$WTW\ CO_{2_{eq}} = \left[WTT_{diesel}(1 - HEF) + WTT_{hythane}(HEF)\right] + TTW\ CO_{2_{eq}} \tag{4.6}$$

where WTT_{diesel} is the WTT CO_{2eq} emissions for fossil diesel fuel of 18.9 g/MJ [195]; and $WTT_{hythane}$ is the WTT CO_{2eq} emissions for hythane, which varies with the fuel production process and was obtained by Equation (4.7).

$$WTT_{hythane}\ CO_{2_{eq}} = \left[WTT_{hydrogen} * \frac{\dot{m}_{hydrogen}\ LHV_{hydrogen}}{\dot{m}_{hythane}\ LHV_{hythane}}\right] + \left[WTT_{methane} * \frac{\dot{m}_{methane}\ LHV_{methane}}{\dot{m}_{hythane}\ LHV_{hythane}}\right] \tag{4.7}$$

WTW CO_{2eq} emissions from the dual-fuel operation were calculated for grey hythane ($WTT_{hythane}$ of 21.9 g/MJ), representing the majority of the current production, generated by the combination of grey hydrogen produced from steam methane reforming (SMR) ($WTT_{hydrogen}$ of 113.0 g/MJ [195]) and compressed methane filtered from CNG coming from South West Asian locations with transport distance of 4000 km ($WTT_{methane}$ of 15.1 g/MJ [195]); and green hythane ($WTT_{hythane}$ of 2.9 g/MJ), generated from renewable sources, which was produced by the mixture of green hydrogen generated by electrolysis using renewable energy from wind and solar sources ($WTT_{hydrogen}$ of 9.5 g/MJ [195]) and synthetic compressed biomethane (CBM) obtained from renewable electricity ($WTT_{methane}$ of 2.4 g/MJ [195]).

Figure 4.26 shows the real TTW CO_{2eq} and WTW CO_{2eq} emissions for both conventional diesel combustion and dual-fuel operation. For the sake of clarity and understanding the effect of hythane production pathways, only ADF was used in this

evaluation, since it was the dual-fuel operation that demonstrated the highest GHG emission reduction. The advanced premixed dual-fuel combustion with green hythane provided the best results, cutting WTW CO_{2eq} emissions by up to 32.1 g/MJ in comparison to a conventional diesel baseline operation, a 34% reduction. Likewise, the use of grey hythane can still generate a decrease of roughly 17 g/MJ, resulting in a reduction of up to 18%, when compared to CDC operation.

It can be stated with a degree of confidence that the proposed ADF combustion strategy with hythane fuel can help combat climate change and achieve a more sustainable energy source for the transportation sector, regardless of whether hythane is derived from renewable or fossil sources.

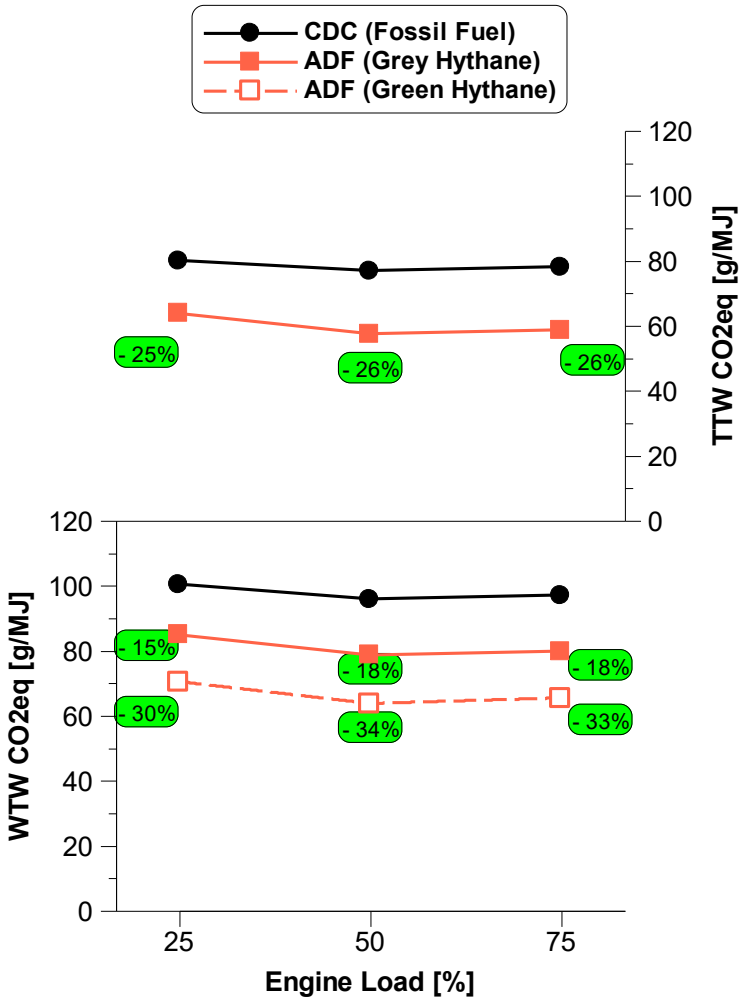

Figure 4.26. Theoretical TTW and WTW CO2eq emissions for CDC and ADF modes, simulating different hythane production sources.

4.5.4 Summary matrix of strategies for optimal engine efficiency and emissions

After conducting extensive experiments on hythane dual-fuel combustion and implementing emissions control technologies, the matrix in Table 4.6 was developed to illustrate the influence of different strategies on efficiency and emissions optimisation. Red circles indicate a negative effect on the analysed parameters, while other circles represent varying degrees of positive impact – with white indicating no/negligible impact, and dark green, light green and yellow signifying high, moderate, and low positive effects, respectively.

Table 4.6. Matrix representative of optimal strategy for efficiency and emissions.

Parameter	Premixed combustion	ECR		Diesel SOI		EGR	
		Higher	Lower	Advancing	Retarding	external	internal
ITE							
CO_2							
CH_4							
NOx							
soot							
CO							
NMHC							

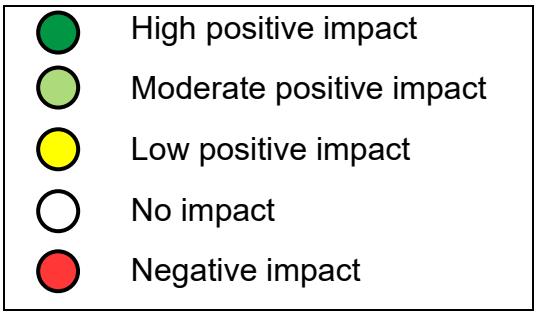

Advancing SOI emerged as the most effective strategy for improving indicated thermal efficiency, leading to lower CO_2 emissions. Additionally, the premixed combustion obtained by ADF mode, combined with a lower ECR, proved to be another efficient

approach for increasing ITE and reducing CO_2 emissions. Conversely, eEGR above 20% significantly compromised both CO_2 emissions and efficiency.

Unburned methane emissions were primarily mitigated through premixed combustion with lower ECR. Both internal and external EGR strategies also contributed to CH_4 reduction by recirculating unburned fuel. Unlike other emissions metrics, retarding diesel SOI was found to help reduce CH_4, though it was less effective than premixed combustion and EGR strategies.

NOx emissions were dramatically reduced through ADF-mode premixed combustion and eEGR implementation, consistent with findings from previous studies. However, lowering ECR slightly increased NOx emissions.

The iEGR demonstrated to be an effective tool for significantly reducing CO and NMHC, especially when combined with premixed combustion. eEGR also had the potential to lower these emissions, though its effectiveness varied with engine load.

Lastly, soot emissions were minimised through premixed combustion, lower ECR, and advanced diesel SOI timing during diesel injection optimisation. However, eEGR negatively impacted soot emissions under certain conditions.

4.6 Summary

In this chapter, advanced engine control and fuel injection strategies were investigated in order to reduce overall GHG emissions and improve the fuel conversion efficiency. Experiments were performed at a constant engine speed of 1200 rpm, with loads varying from 0.6 to 1.8 MPa IMEP, representing a sweep from low to high loads. A 1D engine model was used to estimate the in-cylinder residual gas fraction and the mean in-cylinder gas temperature in order to understand how internal EGR influences dual-fuel combustion optimisation at low load. At medium and high engine loads, the addition of external cooled EGR was evaluated.

The main findings of the diesel-hythane dual-fuel operation with different diesel injection strategies can be summarised as follow:

- The maximum hythane percentage changes according to the diesel injection strategy selected. Hence, the highest diesel replacement with hythane for full combustion optimisation is 87% at low and high engine loads, and 85% at medium load.

- Dual-fuel combustion with a single diesel injection near TDC (CDF mode) has a limited operating range due to high PRRs and low net indicated efficiency.

- The use of an early single diesel injection strategy combined with Miller cycle (lower ECR), also called as ADF, is an effective strategy for low load dual-fuel operation. It ensured sufficient air-fuel mixing time while enabling linear combustion phasing control. At higher loads, excessive PRRs and knock tendency limit the early injection quantity, necessitating split diesel injection.

- The ADF mode can significantly reduce CO_2 emissions by up to 40% and GHG emissions by 25%. Using green hythane in this combustion strategy could achieve a global GHG emissions reduction of up to 34% over a WTW cycle. Additionally, indicated thermal efficiency is optimised, particularly at low loads.

- ADF combustion burns most of the fuel under lean premixed conditions, thanks to early diesel injection, which lowers local combustion temperatures and results in a significant NOx reduction. At low loads, ADF mode can achieve ultra-low NOx emissions, potentially meeting regulatory standards without requiring ATSs.

The key findings regarding dual-fuel operation with iEGR and eEGR were as follow:

- Combining external EGR with ADF mode can mitigate excessive in-cylinder pressure at high engine loads. This approach may also improve the total cost of ownership at medium and high loads by reducing aqueous urea solution consumption in the SCR system, though it comes at the cost of higher GHG emissions.

- The iEGR mode resulted in a hotter combustion process, leading to lower CO, NMHC, and unburned methane emissions, as well as higher exhaust gas temperatures. However, iEGR needed to be deactivated at higher loads to prevent a drop in net indicated efficiency and increased knock risk.

Chapter 5
Characterisation of diesel-hydrogen dual-fuel combustion

5.1 Introduction

This chapter presents and discusses the performance and emissions of a diesel-hydrogen dual-fuel combustion system across a range of engine loads. Unlike the diesel-hythane dual-fuel study discussed in the previous chapter, this study focuses on a single diesel injection strategy to optimise engine efficiency and minimise emissions at each load condition. This approach was dictated by project timeline constraints and safety concerns associated with premixed hydrogen combustion.

The study provides a detailed analysis of engine performance and engine-out emissions, with particular emphasis on GHG emissions across two different combustion modes based on effective compression ratio – conventional and advanced – throughout a broad range of hydrogen energy fractions.

Moreover, further optimisation on the advanced mode focused on efficiency and emissions at low, medium, and high engine loads were carried out using various alternative emission control strategies. These included a wide relative air-fuel ratio sweep, achieved by varying intake air pressure; the employment of eEGR; and the addition water injection in the intake line to improve combustion stability and mitigate emissions at high load. The potential benefits of these strategies were carefully assessed to enhance fuel conversion efficiency while maintaining emission standards.

Finally, an overview on the optimal dual-fuel engine operation is provided, highlighting: the highest achievable energy fraction for both dual-fuel combustion modes (conventional and advanced), the strategy for greatest reduction in GHG emissions across engine loads, a Well-to-Wheel assessment to evaluate the environmental impact of this dual-fuel solution in both engine operation and fuel production pathways, and finally a summary of the advanced mode optimisation for NOx mitigation.

5.2 Evaluation of effective compression ratio

Experiments were conducted to demonstrate the effect of lower effective compression ratio (ECR) by implementing the Miller cycle via LIVC events on the diesel-hydrogen dual-fuel operations.

5.2.1 Experimental test procedure

The study was performed at a constant engine speed of 1200 rpm and three engine loads – 0.6, 1.2 and 1.8 MPa IMEP, representing low, medium, and high loads, respectively. The limits of the peak in-cylinder pressure and the maximum PRR were set to 18 MPa and 2.0 MPa/CAD, respectively, while COV_{IMEP} of 3% was used to determine stable engine operation. Table 5.3 summarises the overall engine operating conditions used for this study.

Table 5.1. Engine operating conditions for the ECR sweep.

Parameter	Unit	Low load	Medium load	High load
IMEP	MPa	0.6	1.2	1.8
Engine speed	rpm	1200	1200	1200
Hydrogen energy fraction target	%	30	20	20
ECR	-	16.8, 14.8	16.8, 14.8	16.8, 14.8
Intake air temperature	°C	40	42	43
Intake air pressure	kPa	125	190	260
Exhaust pressure	kPa	135	200	270
eEGR	%	0	0	0
iEGR	%	0	0	0
Diesel injection pressure	MPa	100	130	160
Hydrogen injection pressure	MPa	0.8	0.8	0.8

Similar to Section 4.2.1, The intake and exhaust air pressure set-points from Euro V compliant multi-cylinder HD diesel engine were used in order to provide a sensible starting point, since an external boosting system was used in place of a turbocharger. The exhaust pressures were adjusted to maintain a constant 10 kPa pressure difference over intake pressure, simulating pumping losses typically associated with a turbocharger. Intake air temperatures were maintained constant at 40°C, 42°C and

43°C for low, medium and high loads, respectively, using an air-to-water cooler and intake air heater. To simplify the experimental investigation, eEGR was not used.

Unlike the previous chapter, where multiple diesel injection strategies were explored, only one diesel injection strategy was used across all combustion modes in this section, due to safety and time constrain reasons. The details of this strategy are provided in Table 5.2. All combustion modes – conventional diesel combustion (CDC), conventional dual-fuel combustion (CDF), and advanced dual-fuel combustion (ADF) – were categorised as non-premixed combustion due to a late split injection near TDC.

Table 5.2. Diesel injection strategy employed for conventional diesel and both dual-fuel combustions.

Mode	Type	ECR	Low load	Medium load	High load
CDC	Non-premixed combustion	16.8	*Late split (pilot and main injection): 1/99*		
CDF	Non-premixed combustion	16.8	SOI_1 @ -15 CAD ATDC	SOI_1 @ -9 CAD ATDC	SOI_1 @ -9 CAD ATDC
ADF	Non-premixed combustion	14.8	SOI_2 @ -8 CAD ATDC	SOI_2 @ -2 CAD ATDC	SOI_2 @ -2 CAD ATDC

The diesel injection strategy consisted of a first (pilot) injection (SOI_1) and a second (main) injection (SOI_2). The pilot injection accounted for 1% of the total diesel injected in CDC and CDF modes, respectively, and was set 1ms (7.2 CAD at 1200 rpm) before SOI_2. This split injection approach was implemented to reduce PRRs and is a common practice in commercial diesel engines [166]. The SOI_2 for both dual-fuel modes was selected following an injection timing optimisation process, with the primary goal of achieving the highest ITE. This optimisation ensured the timing was set to improve engine efficiency while maintaining combustion stability.

For ADF mode, the LIVC strategy was applied to adjust the in-cylinder pressure and charge reactivity, aiming to increase combustion efficiency and reduce peak in-cylinder pressure. The ECR was reduced to 14.8, representing the latest LIVC setting that could be used without compromising combustion stability. In contrast, CDC and CDF modes operated at a baseline ECR of 16.8.

It is important to note that, in this experiment, the hydrogen energy fraction (H2EF) was constrained by the maximum percentage achieved in the CDF and maintained at the same level in the ADF to ensure a fair and consistent comparison between dual-fuel modes.

5.2.2 Overview of the dual-fuel operation and combustion characteristics

Figure 5.1, Figure 5.2, and Figure 5.3 compare the measured in-cylinder average pressure and heat release rate at constant diesel SOI for CDC, CDF, and ADF modes at low, medium, and high engine loads, respectively. Figure 5.4 presents combustion characteristics, including ignition delay (CA10-SOI_2), CA10, CA50, combustion duration, and additional combustion stability metrics as a function of engine load, also at constant diesel SOI.

In Figure 5.1, Figure 5.2, and Figure 5.3, an initial heat release peak is observed while the in-cylinder pressure is still increasing, which aligns with the findings from [166]. This pattern is consistent across all engine loads and can be attributed to the autoignition of the hydrogen-premixed charge triggered by the diesel pilot injection (SOI_1). The resulting heat release occurs around the diesel jet flame, which entrains the surrounding air-hydrogen mixture, leading to localised hydrogen combustion. While hydrogen burns alongside diesel, only the portion near the diesel jet flame ignites initially. This ignition front then propagates through the hydrogen-air mixture. As this flame propagation progresses, the SOI_2 is introduced into the burnt gases of diesel fuel and hydrogen, further influencing the combustion process.

The influence of hydrogen addition on peak in-cylinder pressure is highly dependent on the selected effective compression ratio. Although the diesel replacement percentage achieved in this experiment was relatively low, in CDF mode – where the

ECR remains the same as in CDC – the addition of hydrogen consistently increased peak in-cylinder pressure across all engine load conditions, also leading to higher peak HRR. Specifically, CDF mode increased peak in-cylinder pressure by 1-3% across the engine loads analysed; nonetheless, this increase would likely have been more pronounced in case higher H2EF percentages had been reached. This enhancement can be attributed to the unique properties of hydrogen, including its high flame temperature, rapid burn propagation, and superior diffusion rate, all of which contribute to faster and more intense combustion. This effect is particularly evident in the more advanced combustion phasing than CDC, especially at medium and high engine loads.

However, this also introduced a significant drawback in CDF mode: poor combustion stability, as indicated by the elevated COV_{IMEP} values in Figure 5.4. At low engine load, COV_{IMEP} reached approximately 8% when achieving 32% H2EF, while at medium and high loads, it remained consistently above 3% for H2EF levels exceeding 20%. This instability severely limited the potential for higher diesel replacement through increased hydrogen addition.

Conversely, in ADF mode, where a lower ECR was applied via the Miller cycle strategy using LIVC approach, a different trend was observed. The lower ECR delayed hydrogen autoignition and slowed reaction rates at equivalent H2EF levels across all engine loads. This was particularly noticeable in the CA50 trends shown in Figure 5.4, which indicates a retardation in combustion phasing compared to CDF, particularly at medium and high loads. This effect primarily stemmed from the reduced in-cylinder pressure during the compression stroke, as depicted in Figure 5.1, Figure 5.2, and Figure 5.3. Additionally, the lower ECR led to a slight extension in diesel injection duration, suggesting a drop in indicated thermal efficiency. This was likely due to richer dual-fuel mixtures (lower λ) and increased heat transfer losses [196] associated with the Miller cycle strategy at constant boost pressure.

Another advantage of the Miller cycle observed during the tests – though not reflected in the data shown in the figures – is its potential to optimise the combustion process further. In particular, the Miller cycle strategy enabled the use of more advanced diesel

SOI, which can improve overall engine efficiency by ensuring better combustion phasing and reduced fuel consumption.

The impact of the Miller cycle on combustion characteristics is further reflected in the peak pressure trends shown in Figure 5.4. At all engine loads, ADF mode exhibited lower peak compression pressures for a given H2EF compared to CDF, with peak in-cylinder pressure reduced by 10-15%. This reduction in peak in-cylinder pressure and temperature influenced the air-fuel ratio, increased the combustion duration, and consequently improved combustion stability, as indicated by lower COV_{IMEP} values.

Thus, considering combustion stability, the CDF mode with a higher ECR, while producing higher peak in-cylinder pressures, was limited to a maximum H2EF of 32% at low load and 20% at higher engine loads. In contrast, the ADF combustion, with lower ECR, demonstrated the potential for considerably higher hydrogen energy fractions when compared to CDF, regardless of the engine load. This will therefore be explored in more detail in Section 5.3. These conclusions are consistent with findings from previous studies [153, 137].

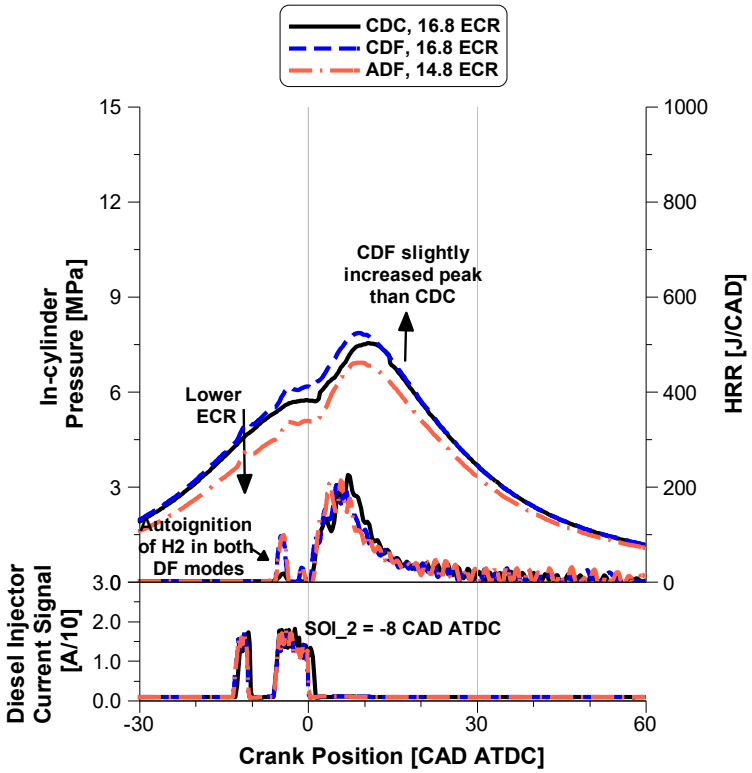

Figure 5.1. The effect of ECR on in-cylinder pressure and HRR for constant diesel injection at low engine load.

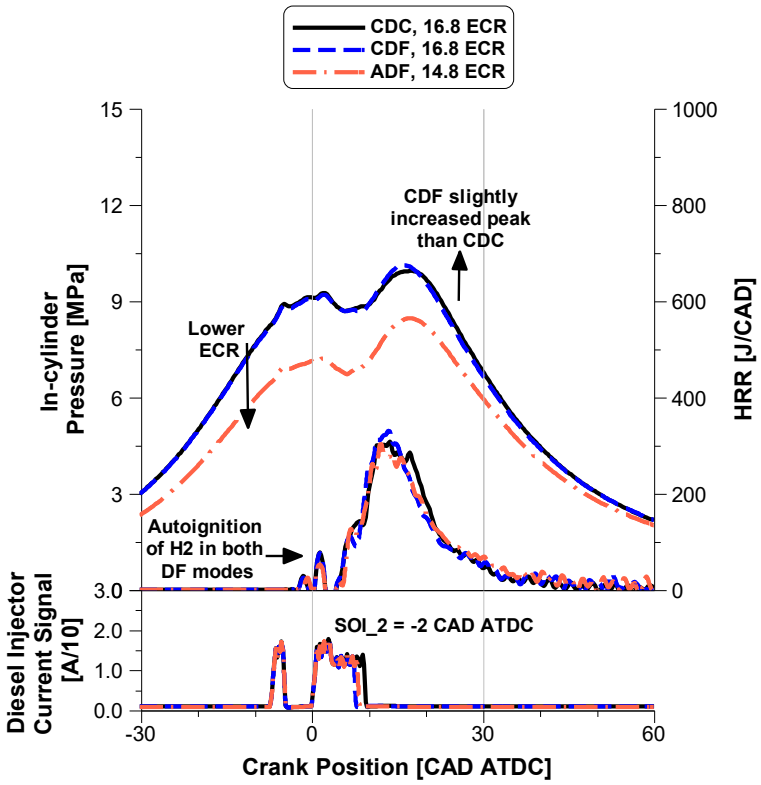

Figure 5.2. The effect of ECR on in-cylinder pressure and HRR for constant diesel injection at medium engine load.

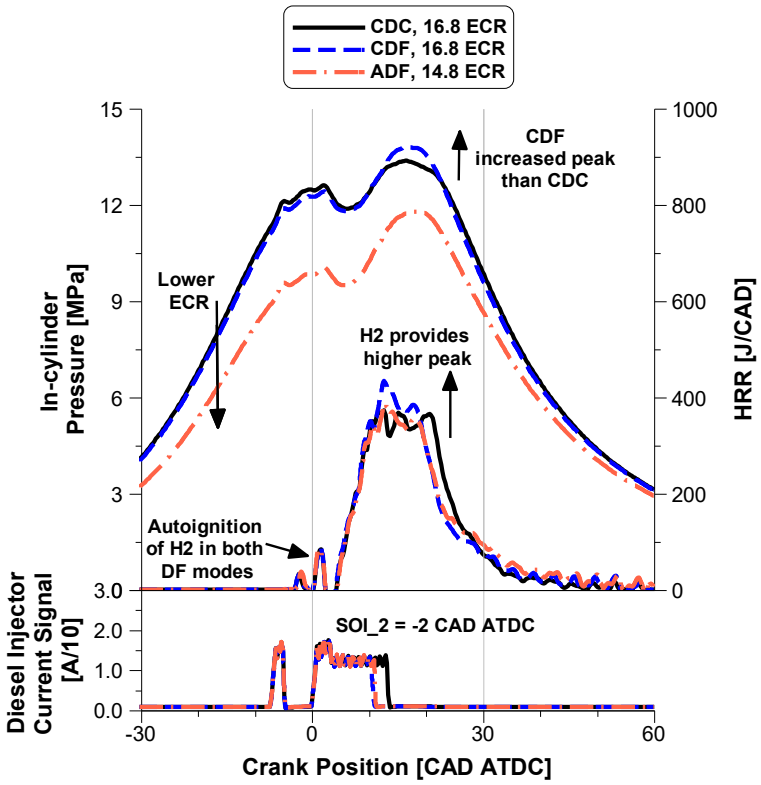

Figure 5.3. The effect of ECR on in-cylinder pressure and HRR for constant diesel injection at high engine load.

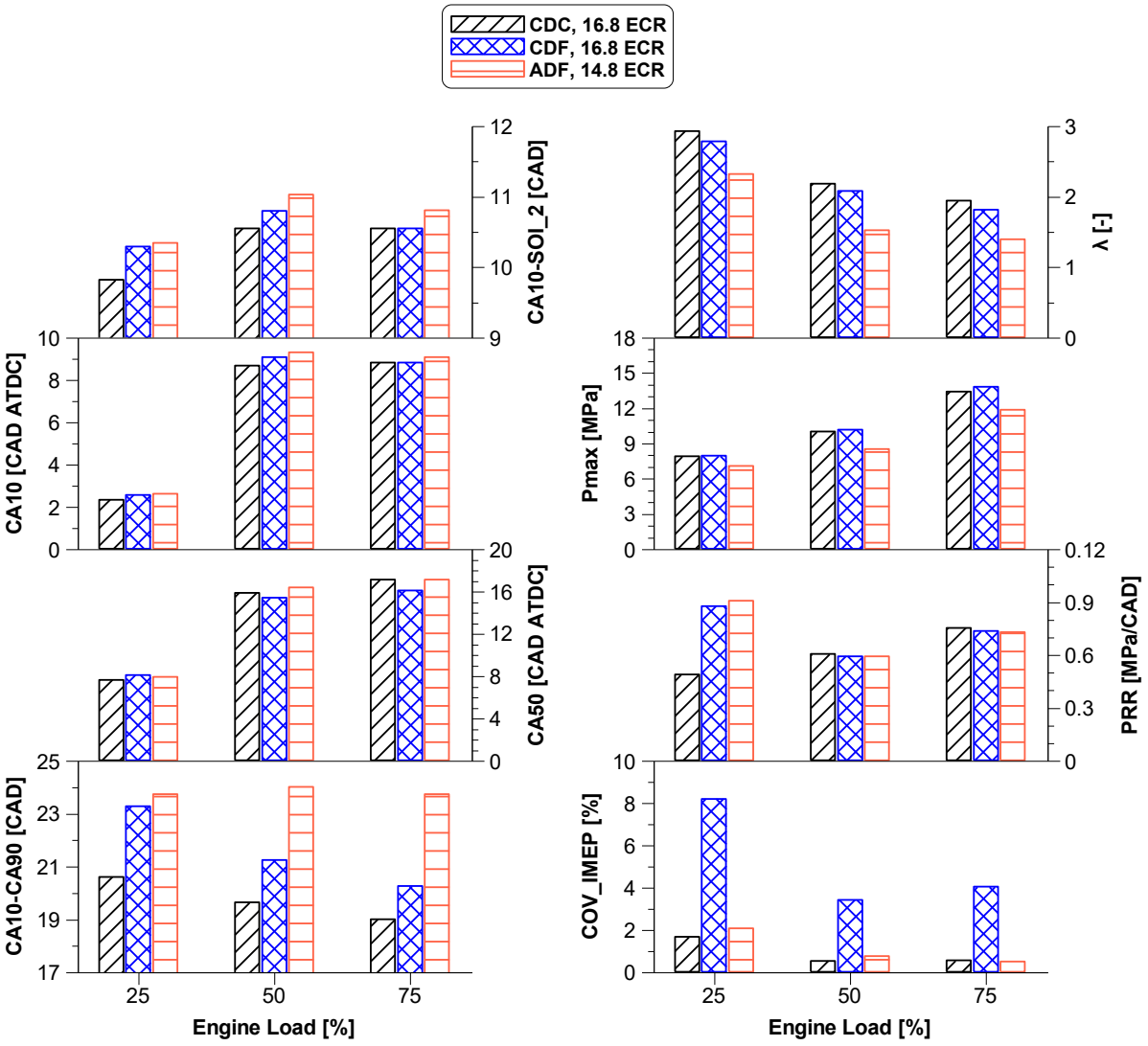

Figure 5.4. The effect of ECR on combustion characteristics and stability.

5.2.3 Engine performance

The effect of ECR on combustion and indicated thermal efficiencies, EGT and indicated equivalent specific fuel consumption are depicted in Figure 5.5, while Figure 5.6 presents the hydrogen slip in the crankcase and exhaust line.

It can be seen from Figure 5.5 that EGT increased linearly with the increase in engine load, regardless of the combustion mode. Moreover, both dual-fuel modes depicted higher EGT than CDC, which can be explained in part by the presence of hydrogen, which has higher flame temperature than diesel fuel [170, 197]. Additionally, this

increase in EGT can also be related to a decrease in the relative air-fuel ratio due to the lower ECR resulting from the application of LIVC.

Further analysis in Figure 5.5 reveals that to achieve the same indicated output power as CDC, both dual-fuel modes required higher ISFCeq. This indicates that dual-fuel modes generally exhibit poorer fuel conversion efficiency compared to CDC, leading to more incomplete combustion and lower indicated thermal efficiency. Despite hydrogen fuel's higher energy content per mass unit, its low density in gaseous form requires a greater overall energy input to match the engine conditions of CDC.

On the other hand, when comparing the dual-fuel modes, the mode with the higher ECR (CDF) provided better overall engine performance in most of the conditions analysed. In particular, although CDF exhibited lower ITE at low engine load (a 3% decrease relative to CDC) due to substantially higher unburned hydrogen in the exhaust (as shown in Figure 5.6) – resulting in poorer fuel conversion efficiency – its ITE reduction was 3% at medium and higher loads, when compared to CDC. This was still better than ADF with lower ECR, where the reduction in thermal efficiency was approximately 10% at medium load and 4% at high load, relative to CDC. This difference is mainly due to higher in-cylinder pressures in CDF, which aligns with findings from the literature review.

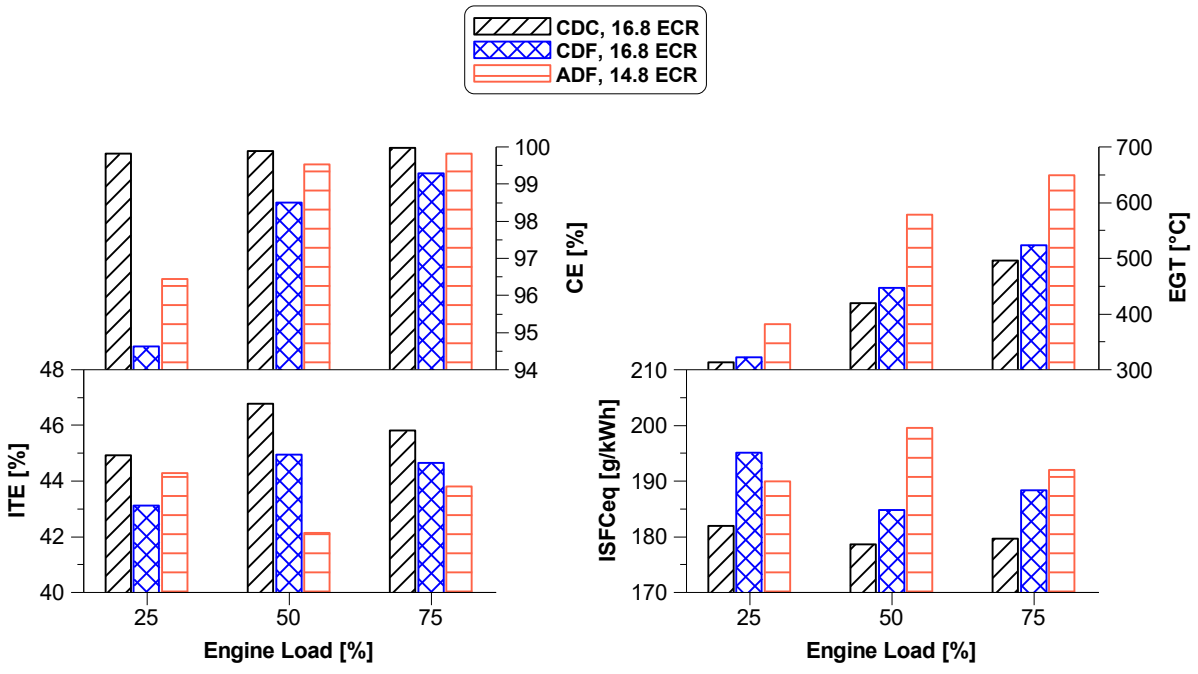

Figure 5.5. The effect of ECR on engine performance.

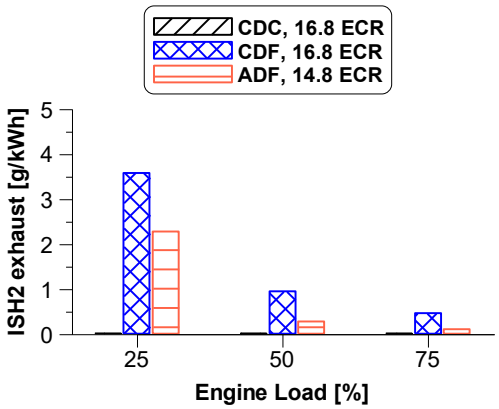

Figure 5.6. The effect of ECR on hydrogen slip in the exhaust line.

Overall, dual-fuel combustion with a higher ECR resulted in a smaller loss of thermal efficiency at medium and high loads. However, the lower ECR provided better fuel conversion efficiency (higher combustion efficiency) across all engine loads, which resulted in considerably lower hydrogen slip.

5.2.4 Engine-out emissions

The effect of ECR on exhaust emissions for the different combustion modes are depicted in Figure 5.7 in the form of net indicated specific values. It is important to note that, unlike diesel-hythane dual-fuel operation, this chapter will focus on total unburned hydrocarbons (THC) rather than separate NMHC and CH_4 emissions, since methane emissions are negligible in diesel-hydrogen dual-fuel combustion. On the other hand, nitrous oxides (N_2O) will be presented and discussed on every experimental study presented across this chapter.

The expected CO_2 reduction achieved by both dual-fuel strategies is evident in Figure 5.7 across all engine load conditions. However, the dual-fuel mode with a higher ECR exhibited a greater reduction, achieving a 21% decrease at low load and 15% at higher loads. While ADF also attained a 21% CO_2 reduction at low load, its reduction was limited to 6% at medium load and 11% at high load. This discrepancy may be attributed to ADF's higher combustion efficiency, especially at medium and high loads, where it exceeded 95% (Figure 5.5). This higher combustion efficiency resulted in more fuel

being burned, which led to more complete oxidation of carbon to CO_2, thus increasing the overall CO_2 emissions despite improved fuel conversion efficiency.

Other carbon emissions also showed an overall reduction across different engine loads with the employment of both dual-fuel combustion modes. Although dual-fuel operation generally resulted in more incomplete combustion – and therefore more unburned fuel – the total unburned hydrocarbons were consistently reduced across all load conditions. This is due to the replacement of diesel with a zero-carbon fuel, leading to a decrease in the total carbon content of the fuel mixture. Notably, ADF provided the greatest reduction in unburned hydrocarbons, ranging from 16% to 23%, while CDF achieved reductions between 7% and 21%.

NOx emissions increased by 2–8% in dual-fuel operation with a higher ECR, likely due to the rise in peak in-cylinder pressure and temperature caused by hydrogen's chemical properties, which favour NOx formation. In contrast, the lower ECR mitigated NOx emissions by 16–21% relative to CDC, primarily due to the reduced in-cylinder pressure and lower gas temperature at the end of the compression stroke [91]. However, at higher H2EF percentages in ADF mode, NOx emissions may increase.

CO and soot emissions were notably reduced, particularly at low engine loads, for both dual-fuel combustion modes. That reduction reached up to 47% for CO and 60% for soot emissions. This can be attributed to the lower diesel injection, which reduces carbon content and promotes a more homogeneous mixture. Regarding N_2O emissions, no consistent trend was observed across engine loads to establish a clear conclusion, at least at this specific H2EF percentage.

That being said, dual-fuel combustion reduced CO_2 emissions across all loads, with higher ECR achieving the greatest reduction – up to 21% at low load and 15% at higher loads. Although ADF was slightly less effective in CO_2 reduction, it improved combustion efficiency, which in turn led to a greater reduction in unburned hydrocarbons. Both combustion modes also resulted in significant reductions in carbon monoxide and soot emissions, particularly at low engine load. On a final note, while NOx emissions increased by 2–8% with higher ECR, ADF mitigated this increase by up to 21%.

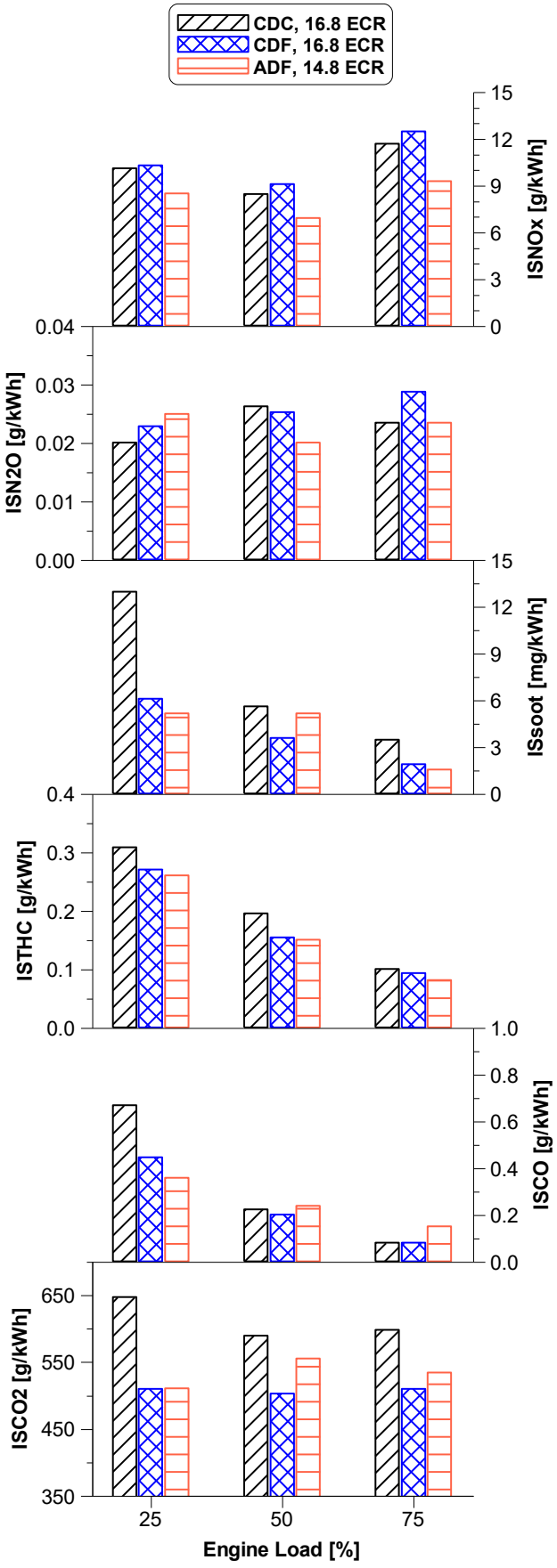

Figure 5.7. The effect of ECR on engine-out emissions.

5.3 The exploration of hydrogen energy fraction

Experiments were conducted to demonstrate the effect of increasing hydrogen energy fraction for different engine loads. In this section, only advanced dual-fuel combustion is explored, since Section 5.2 demonstrated that CDF has limited operation range for good stability.

5.3.1 Experimental test procedure

The experimental setup and test methodology for this section were identical to those described in Section 5.2, including engine speed, load conditions, and combustion strategies. However, this study focused solely on advanced ADF, as Section 5.2 demonstrated the operational limitations of CDF.

Unlike Section 5.2, where a fixed H2EF was used, this section explores the effect of increasing H2EF in ADF mode across different engine loads. The H2EF was systematically swept, reaching a maximum of 70% at low and medium loads and 36% at high load. These upper limits were constrained by combustion stability criteria, ensuring safe and reliable operation. Specifically, the peak in-cylinder pressure and maximum PRR were limited to 18 MPa and 2.0 MPa/CAD, respectively, while a COV_{IMEP} threshold of 3% was used to determine stable engine operation. Table 5.3 summarises the engine operating conditions used in this analysis.

Table 5.3. Engine operating conditions for the energy fraction sweep.

Parameter	Unit	Low load	Medium load	High load
IMEP	MPa	0.6	1.2	1.8
Engine speed	rpm	1200	1200	1200
H2EF	%	0 - 70	0 - 70	0 - 36
ECR	-	14.8	14.8	14.8
Intake air temperature	°C	40	42	43
Intake air pressure	kPa	125	190	260
Exhaust pressure	kPa	135	200	270
eEGR	%	0	0	0
Diesel injection pressure	MPa	100	130	160
Hydrogen injection pressure	MPa	0.8	0.8	0.8

The intake and exhaust conditions were controlled as described in Section 5.2, with exhaust pressures adjusted to maintain a 10 kPa difference to the intake pressure. The same late split-injection strategy was used for diesel fuel delivery. The reduced ECR (14.8) remained unchanged from Section 5.2 to enhance combustion stability and efficiency in ADF mode.

By allowing higher H2EF values in ADF while adhering to combustion stability constraints, this study aims to investigate the impact of hydrogen enrichment on combustion performance, efficiency, and emissions at different loads.

5.3.2 Overview of the dual-fuel operation and combustion characteristics

Figure 5.8, Figure 5.9, and Figure 5.10 compare the measured in-cylinder average pressure and heat release rate at constant diesel SOI for CDC and the highest H2EF achieved in the advanced dual-fuel mode at low, medium, and high engine loads, respectively. Figure 5.11 presents combustion characteristics, including ignition delay, CA10, CA50, combustion duration, and additional combustion stability metrics as a function of hydrogen energy fraction, also at constant diesel SOI.

The increase in hydrogen energy fraction leads to slightly lower peak in-cylinder pressure and heat released at low engine loads, as engine performance in this operating condition depends largely on the quantity of diesel fuel supplied [138]. The premixed hydrogen-air ratio (Φ) is relatively lower at low engine load, as can be seen in Figure 5.11, which results in significantly slower burning and thus contributes to the lower peak in-cylinder pressure. As a result, the ignition delay increases considerably with the addition of hydrogen when compared to CDC, as shown in Figure 5.11. This delay can also result in a significant portion of the fuel not burning completely. Additionally, another potential explanation for the lower peak in-cylinder pressure is the use of lower ECR, as discussed in Section 5.2.

In contrast, at medium and high engine loads, these trends differ significantly from those observed at lower loads. The high burning velocity of hydrogen facilitates the rapid and complete oxidation of the air-fuel mixture, which considerably advances

combustion phasing, enhancing in-cylinder pressure. This aligns with findings from the literature [141, 137].

At higher engine loads, the addition of a relatively large amount of hydrogen notably reduces combustion duration (Figure 5.11) and increases the peak HRR, particularly during the middle phase of diffusion combustion. As seen in Figure 5.9 and Figure 5.10, the high peak HRR results from combined effect of rapid turbulent combustion of hydrogen and the diffusion combustion of diesel at overall rich conditions.

From Figure 5.11, it is also visible a linear increase in the PRR was observed across all engine loads as the H2EF increased, revealing that combustion became progressively stronger with higher hydrogen fractions.

Thus, considering combustion stability, the highest achievable H2EF was 70% at low and medium loads, and 36% at high load. In all cases, further increases were prevented by rising peak in-cylinder pressure and PRR, which could not be recorded due to safety and mechanical durability constraints. The lower threshold at high load reflects a reduced margin before reaching these constraints.

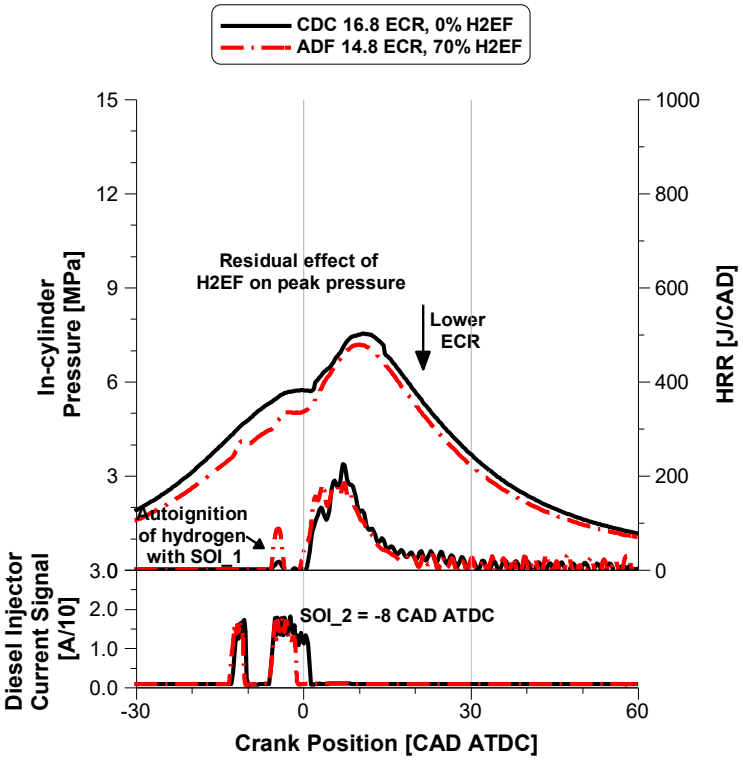

Figure 5.8. The effect of H2EF on in-cylinder pressure and HRR for constant diesel injection at low engine load.

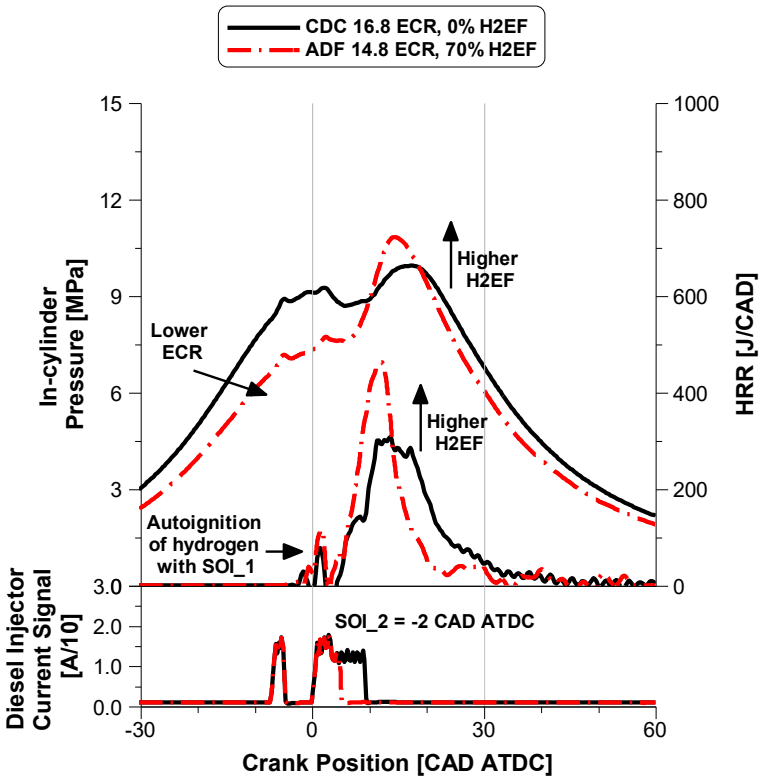

Figure 5.9. The effect of H2EF on in-cylinder pressure and HRR for constant diesel injection at medium engine load.

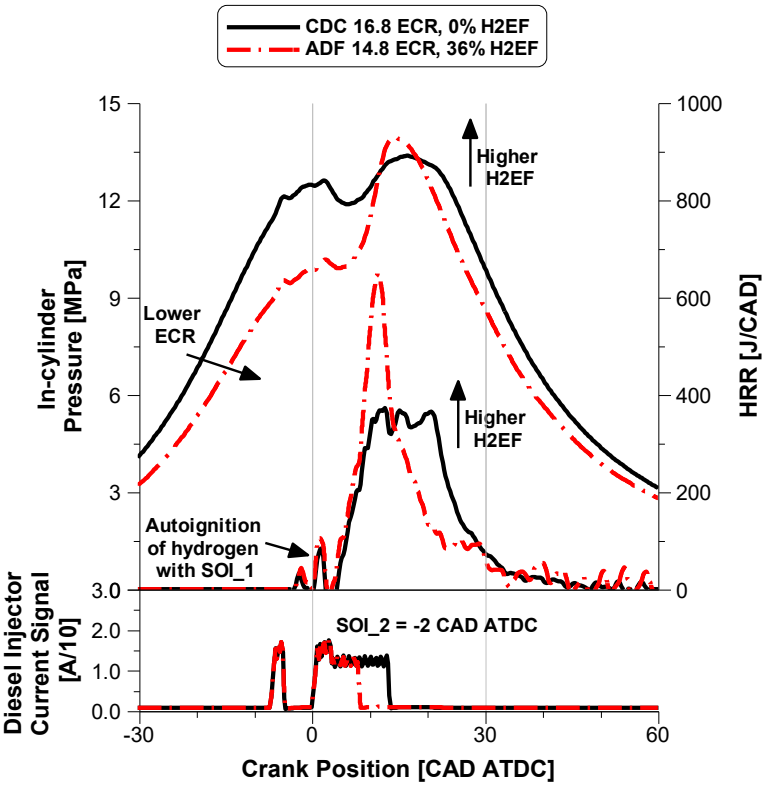

Figure 5.10. The effect of H2EF on in-cylinder pressure and HRR for constant diesel injection at high engine load.

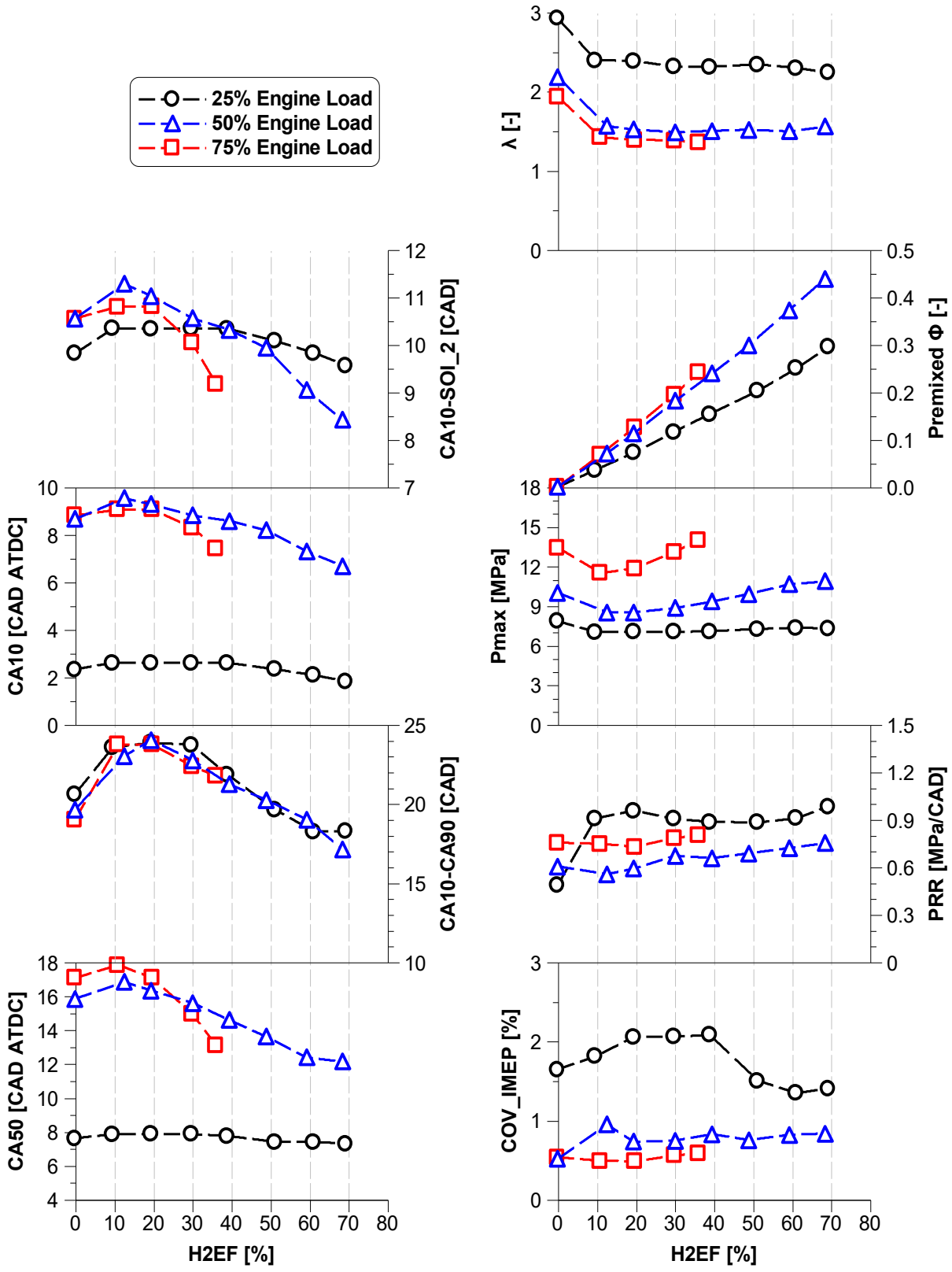

Figure 5.11. The effect of H2EF on combustion characteristics and stability.

5.3.3 Engine performance

The effect of hydrogen energy fraction on combustion and indicated thermal efficiencies, EGT and indicated equivalent specific fuel consumption are depicted in Figure 5.13, while Figure 5.12 presents the hydrogen slip in the crankcase and exhaust line.

As concluded in Section 5.2.3, the use of ADF (lower ECR) with hydrogen consistently resulted in higher EGT compared to CDC. However, in this section, it is observed that while hydrogen addition increases EGT across all engine loads, the sensitivity of EGT to changes in H2EF is relatively low. In other words, while ADF mode leads to an increase in EGT, further increases in the H2EF percentage do not lead to a significant or proportionate rise in EGT.

Combustion efficiency, especially at low engine condition, decreased considerably with the increase in H2EF compared to CDC. This is primarily explained by the high amount of unburned hydrogen measured in the exhaust, as shown in Figure 5.12. Hydrogen slip was more predominant at low engine load likely due to the lower premixed hydrogen-air fuel ratio observed in Figure 5.11, which limited the oxidation of the fuel mixture.

However, hydrogen slip tended to decrease substantially for energy fraction above 40%. A possible explanation for this is the shorter combustion duration observed at H2EF above this range, as depicted in Figure 5.11, which may have improved the burn conditions of the in-cylinder mixture.

On the other hand, per Arrhenius equation [198], fuel oxidation rate is directly proportional to combustion temperature. This reaction rate increases exponentially with increasing in-cylinder temperature and pressure during combustion. As thermodynamics conditions improve with increasing hydrogen energy fraction, reaction rate increases exponentially resulting to significant improvement in combustion efficiency at higher H2EF.

It is important to note that, as presented in Equation (3.48) from Chapter 3, only unburned hydrogen measured in the exhaust was considered in the combustion

efficiency calculation, as it is the only unburned fuel effectively lost from the combustion process. The hydrogen slip detected in the crankcase was not measured for efficiency purposes, but rather for safety reasons. However, this measurement still provides a linear indication that hydrogen slip increases as the H2EF is raised.

The addition of hydrogen resulted in an overall decrease in thermal efficiency. More specifically, the highest H2EF led to a 5% reduction in ITE at low and medium engine loads, and a 4% reduction at high loads, with absolute values ranging between 42.4% and 44.4%. The low load results are consistent with the literature presented in Chapter 2, and can be attributed to a lower charge temperature at the end of the compression process, the low flame velocity of the lean gaseous fuel-air mixture, and the sufficient time available for heat transfer to the cylinder walls. Nonetheless, both medium and high engine loads also showed a decrease in ITE with the addition of hydrogen, which in not aligned with other studies [197, 199]. Potential explanations for this discrepancy could include the lower ECR strategy in the ADF mode, which decreases the volumetric efficiency, as well as the lower energy density associated with hydrogen fuel.

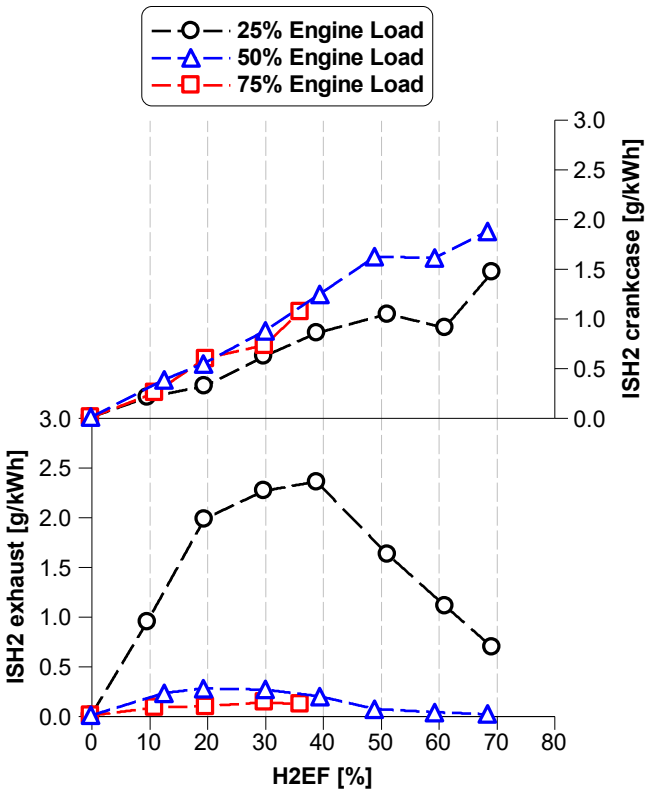

Figure 5.12. The effect of H2EF on hydrogen slip in the exhaust line and crankcase.

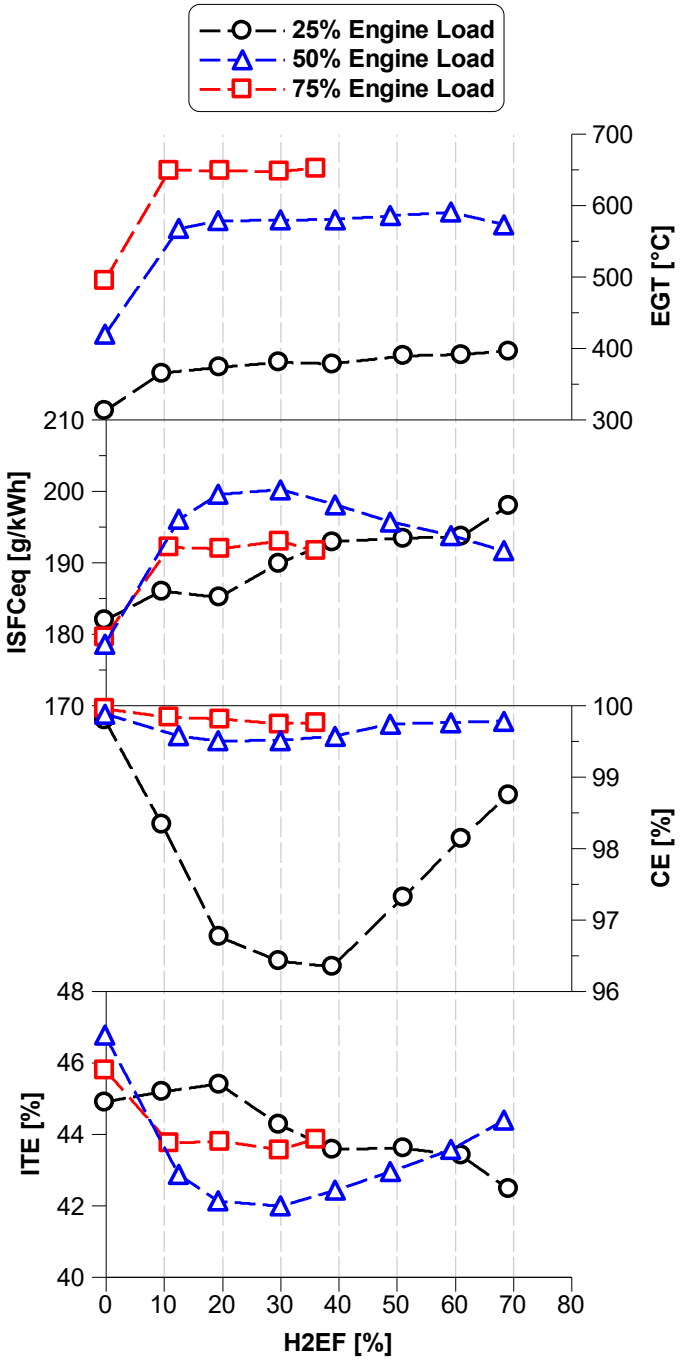

Figure 5.13. The effect of H2EF on engine performance.

Overall, hydrogen addition reduced thermal efficiency compared to CDC, with the highest H2EF causing a 5% drop at low and medium loads and 4% at high loads. However, combustion efficiency improved above 40% H2EF due to shorter combustion duration. While ADF mode consistently increased EGT, further H2EF increases had little impact on exhaust temperature.

5.3.4 Engine-out emissions

Exhaust emissions in the form of net indicated specific values for ADF mode adding hydrogen at different engine load conditions are depicted in Figure 5.14.

As expected, a gradual reduction in CO_2 emissions was observed as the H2EF increased. At low and medium engine loads, a 70% diesel replacement enabled a cut in CO_2 emissions by 363.2 g/kWh and 330.4 g/kWh, respectively, representing a reduction of approximately 56-57%. However, due to the limitation of hydrogen energy fraction of 36% at high load operation, the CO_2 reduction was less pronounced, reaching a total cut of 168.8 g/kWh, which corresponds to a 28% decrease compared to CDC.

Similarly, other carbon emissions, such as CO and THC, also demonstrated significant reductions, particularly at low and medium loads, where the diesel replacement was higher. At these engine loads, a 70% H2EF resulted in reductions of 80% and 59% in CO emissions, with absolute values ranging from 0.09–0.13 g/kWh, and reduction of 47% and 31% in THC emissions, with absolute values comprises between 0.08-0.16 g/kWh. In contrast, high load conditions showed low sensitivity to changes in CO and HC emissions, primarily due to the limited diesel replacement percentage.

Although NOx emissions initially drop with the addition of up to 10% H2EF, they progressively increase as the hydrogen content rises further, regardless of the engine load. This initial decrease can be attributed to the reduction in peak in-cylinder pressure observed between 10% and 20% H2EF, as shown in Figure 5.11. However, as the hydrogen fraction increases, the combustion characteristics of hydrogen – such as its high flame speed and shorter combustion duration – become more pronounced. These characteristics lead to higher in-cylinder temperatures and pressures, creating ideal conditions for NOx formation. At low and medium engine loads, a 70% H2EF resulted in a 1.6-1.7 g/kWh increase in NOx emissions, representing a 16% rise. A similar trend was observed at 75% engine load: while NOx emissions at 36% H2EF were comparable to the CDC, higher H2EF percentages would have led to significantly higher NOx emissions. As a result, NOx emissions ranged between 11.1–13.1 g/kWh across the different operating conditions.

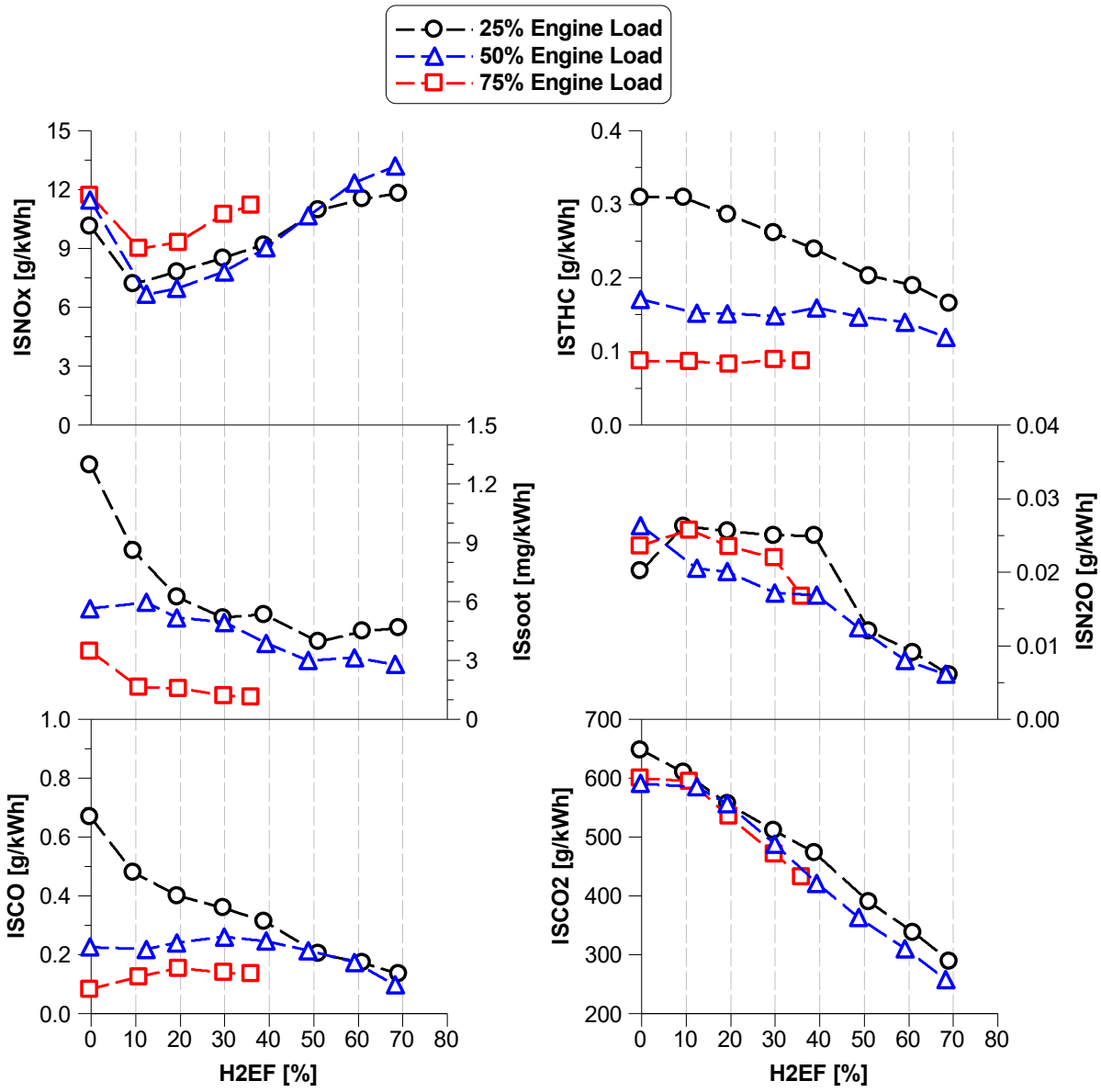

Figure 5.14. The effect of H2EF on engine-out emissions.

Another benefit of the diesel-hydrogen dual-fuel operation is the overall reduction in soot emissions, regardless of engine load conditions. Soot levels were observed to decrease by 65%, 51%, and 68% at low, medium, and high loads, respectively, with absolute values ranging between 1.1–4.6 mg/kWh. This reduction can be attributed to the decrease in diesel fuel usage, which lowers the carbon-to-hydrogen ratio. Additionally, hydrogen's low density and high diffusivity, combined with its injection into the intake, create ideal conditions and provide sufficient time for a well-premixed charge to form before combustion.

Finally, N_2O emissions showed a clear reduction trend with the addition of hydrogen at all engine loads analysed, reaching 6 mg/kWh representing a 75% reduction at both low and medium loads. Nonetheless, at high engine load, the reduction was lower, only 30%, reaching approximately 16 mg/kWh.

This decrease can likely be attributed to the decrease in the relative air-fuel ratio observed in Figure 5.11, as N_2O tends to be lower for richer mixtures [145]. Additionally, this trend can be linked to the formation of NOx, since the oxidation of N_2O is inversely proportional to NOx oxidation. In other words, as NOx levels increase, the oxidation of N_2O decreases, contributing to the observed reduction in N_2O levels.

In summary, the maximum hydrogen energy fraction in ADF mode reduced CO_2 emissions by up to 56% at low and medium loads, surpassing the 45% reduction target set for 2030 in the updated EU CO_2 regulation, allowing this solution to operate until end of 2034. However, at high engine loads, the CO_2 reduction was limited to 28%, falling short of the 2030 target, indicating the need for further improvement. It also lowered THC, CO, N_2O, and soot emissions, with the latter three meeting the new Euro 7 emission standards. However, NOx emissions increased with higher hydrogen fractions due to higher in-cylinder temperatures, which remains the main challenge of this solution. Overall, diesel-hydrogen dual-fuel operation offers significant reductions in carbon-based pollutants, highlighting its short-term potential.

5.3.5 GHG emissions estimation

Hydrogen is considered a zero-carbon fuel for ICEs, since it contains no carbon in its chemical composition. As discussed previously, hydrogen can significantly reduce CO_2 emissions, with the reduction directly dependent on the hydrogen energy fraction added to the combustion process. Nevertheless, although hydrogen is not a GHG itself, some research [177, 178, 179] consider that hydrogen leakage may influence the atmospheric concentrations of other GHGs, such as methane and ozone. In particular, higher hydrogen emissions lead to a longer lifetime and higher abundance of methane. As a result, hydrogen may be assigned a GWP to account for these indirect effects. However, there is currently no clear consensus on the appropriate

GWP value: some studies suggest a value around 3-5 times [178, 179] that of CO_2 over a 100-year lifetime, whereas a policy paper published in the United Kingdom Government official online platform [177] shows an estimation around 11 times that of CO_2 over a 100-year lifetime. In light of this uncertainty regarding hydrogen's GWP, this thesis considered a hydrogen GWP equal to 11.

On the other hand, it is important to note that hydrogen combustion also generates N_2O emissions. Furthermore, N_2O is recognised have high GWP of 273 that of CO_2 over a 100-year lifetime [28]. Hence, a small amount of nitrous oxides emission could offset the benefits of reduced CO_2 in the diesel-hydrogen DF engine.

Therefore, it is essential to estimate the total CO_2-equivalent (CO_{2eq}) of both GHGs investigated. In order to find a single value of CO_{2eq}, the level of emissions of a GHG have to be multiplied by its GWP and combine all GHG together, as shown below.

$$ISCO_{2_{eq}} = ISCO_2 * 1 + ISH_2 * 11 + ISN_2O * 273 \quad (5.1)$$

Figure 5.15 depicts the comparison of GHG emissions between CDC and ADF at low, medium, and high engine loads, expressed in grams of CO_{2eq} per kWh of power generated.

The addition of hydrogen results in a substantial GHG reduction of 55-57% at low and medium engine load operation when compared to the conventional diesel baseline. That reduction is less effective at high load, with a GHG emission reduction of 28%, limited by the restriction on diesel replacement, as discussed earlier. This indicates remaining potential for further GHG mitigation under the ADF regime, particularly through enhanced combustion stability at higher engine loads.

It is also worth noting that H_2 and N_2O emissions were found to have a marginal influence on the total GHG estimation, contributing less than 1% of the overall GHG – ranging from 1.5 to 4.5 g/kWh when converted to CO_{2eq}. Furthermore, N_2O levels were observed to decrease with increasing H2EF, generating thus less N_2O than CDC, as seen earlier. Hence, the impact of N_2O on the GHG remains negligible in the context of this analysis.

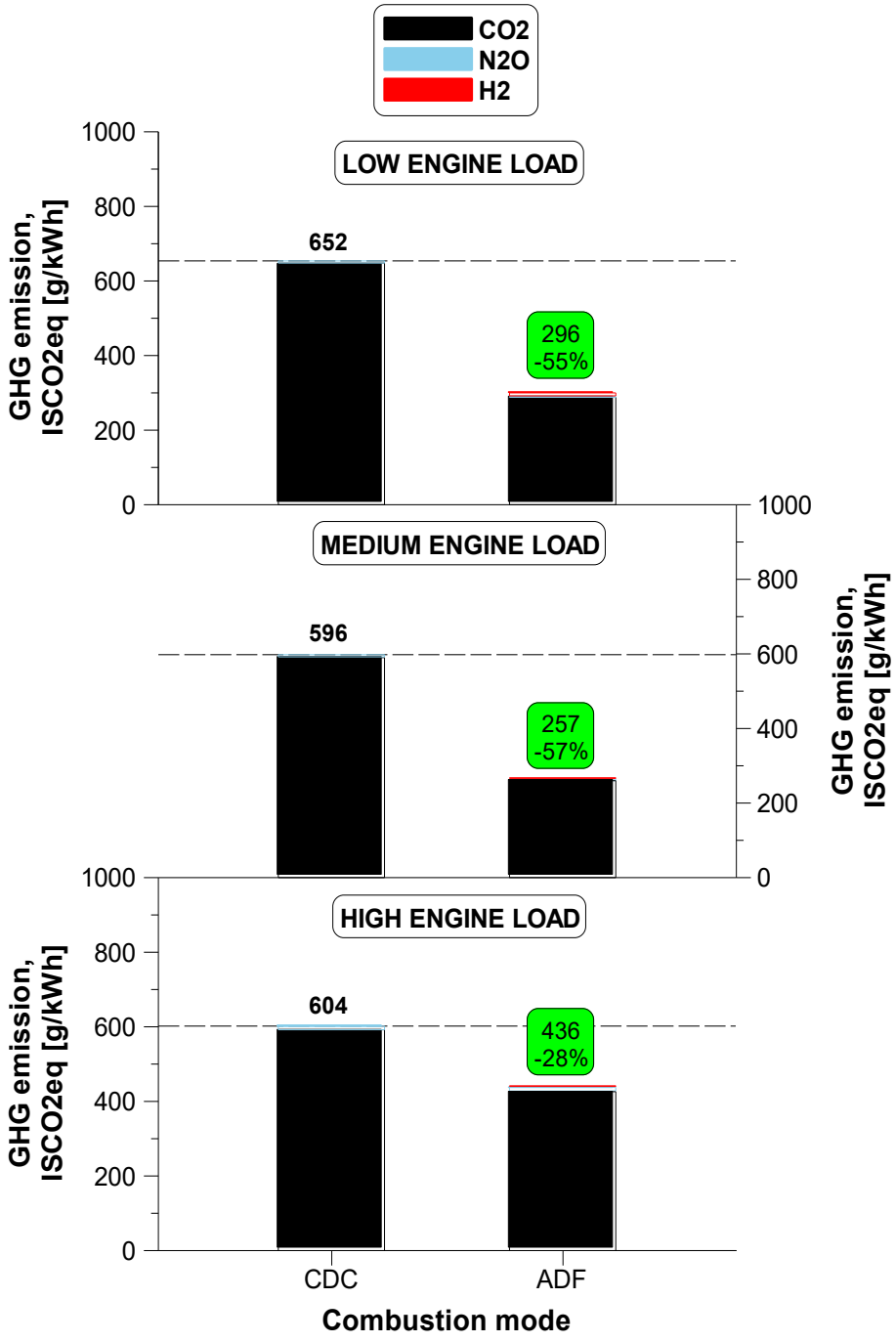

Figure 5.15. The effect of H2EF on combined GHG emissions.

As a result of this section, one key conclusion is that reducing GHG emissions is highly dependent on the control and stability of the combustion process. Effectively managing combustion allows for an increase in hydrogen fraction, which can reduce CO_2 emissions, while the impact of N_2O remains relatively low.

5.4 The effect of relative air-fuel ratio

Building on the challenges identified in Section 5.3, namely the need for more effective NOx control at high H2EF and the challenge of increasing the H2EF percentage at high engine loads, further optimisation was conducted. This includes experiments designed to explore the impact of increasing the relative air-fuel ratio across different engine loads. This section focuses exclusively on advanced dual-fuel combustion with the maximum H2EF obtained in Section 5.3.

5.4.1 Experimental test procedure

The experimental setup for this section were identical to those described in Section 5.2, including engine speed, load conditions, and combustion strategies. However, this study specifically focused on ADF with highest H2EF percentage, which was set to 70% at low and medium loads, and 36% at high load condition.

Relative air-fuel ratios were increased by gradually raising intake air pressures from the baseline values used in previous sections, which were 125, 190, and 260 kPa for low, medium, and high engine loads, respectively. Exhaust pressures were adjusted to maintain a 10 kPa difference to the intake pressure. The same late split-injection strategy was used for diesel fuel delivery. The reduced ECR of 14.8 remained unchanged to enhance combustion stability and efficiency in ADF mode.

Combustion stability criteria followed the same parameters as in previous sections: peak in-cylinder pressure and maximum PRR were limited to 18 MPa and 2.0 MPa/CAD, respectively, while a COV_{IMEP} threshold of 3% was used to determine stable engine operation. Table 5.4 summarises the engine operating conditions used in this analysis.

By allowing higher relative air-fuel ratios in ADF mode, while maintaining to combustion stability constraints, this study seeks to mitigate NOx emissions and improve the diesel replacement percentage at high engine loads.

Table 5.4. Engine operating conditions for the relative air-fuel ratio sweep.

Parameter	Unit	Low load	Medium load	High load
IMEP	MPa	0.6	1.2	1.8
Engine speed	rpm	1200	1200	1200
H2EF	%	70	70	36
ECR	-	14.8	14.8	14.8
Intake air temperature	°C	40	42	43
Intake air pressure	kPa	125 – 145	190 – 290	260 – 290
Exhaust pressure	kPa	135 – 155	200 – 300	270 – 300
eEGR	%	0	0	0
iEGR	%	0	0	0
Diesel injection pressure	MPa	100	130	160
Hydrogen injection pressure	MPa	0.8	0.8	0.8

5.4.2 Overview of the dual-fuel operation and combustion characteristics

Figure 5.16, Figure 5.17, and Figure 5.18 compare the measured in-cylinder pressure and heat release rate at constant diesel SOI for different relative air-fuel ratios in the advanced dual-fuel mode across low, medium, and high engine loads, respectively. Figure 5.19 presents combustion characteristics, including ignition delay, CA10, CA50, combustion duration, and additional combustion stability metrics as a function of relative air-fuel ratio, also at constant diesel SOI.

Increasing the relative air-fuel ratio by boosting the intake pressure leads to a greater mass of the air-fuel mixture within the cylinder. This results in higher initial in-cylinder pressure and temperature, particularly near TDC, as well as an increase in peak in-cylinder pressure, as observed in Figure 5.16, Figure 5.17, and Figure 5.18.

In contrast, HRR shows an opposite trend – higher λ values result in lower and delayed peak HRR, especially at medium and high loads. This is attributed to the reduced reactivity of the mixture at higher λ, which delays ignition despite the increased initial in-cylinder pressure and slows down the combustion process. This effect is reflected in the retarded CA50 and longer combustion duration shown in Figure 5.19.

The slower combustion also leads to a lower maximum PRR, which could potentially provide a margin for an increase in H2EF at high engine load. This can be seen in Figure 5.19, and is further evidenced by the less steep slope of the pressure trace just before peak pressure, consistently observed across all loads.

It is important to mention that at medium and high loads, the relative air-fuel ratio could not be increased further due to the limitation imposed by the maximum pressure capability of the boosting system used in this experiment.

Overall, increasing λ by boosting intake pressure raises in-cylinder pressure and temperature. However, higher λ values lead to lower PRR, resulting in delayed and lower peak HRR, especially at higher loads. This could potentially provide a margin for higher H2EF. Additionally, at medium and high loads, λ could not be further increased due to the limitations of the boosting system's maximum pressure capability

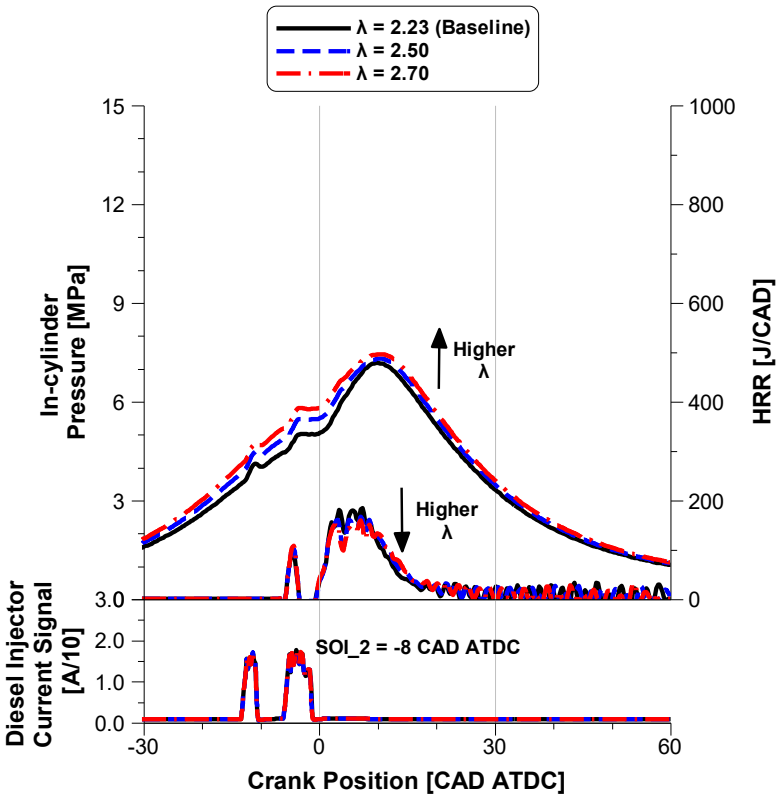

Figure 5.16. The effect of relative air-fuel ratio on in-cylinder pressure and HRR for constant diesel injection at low engine load.

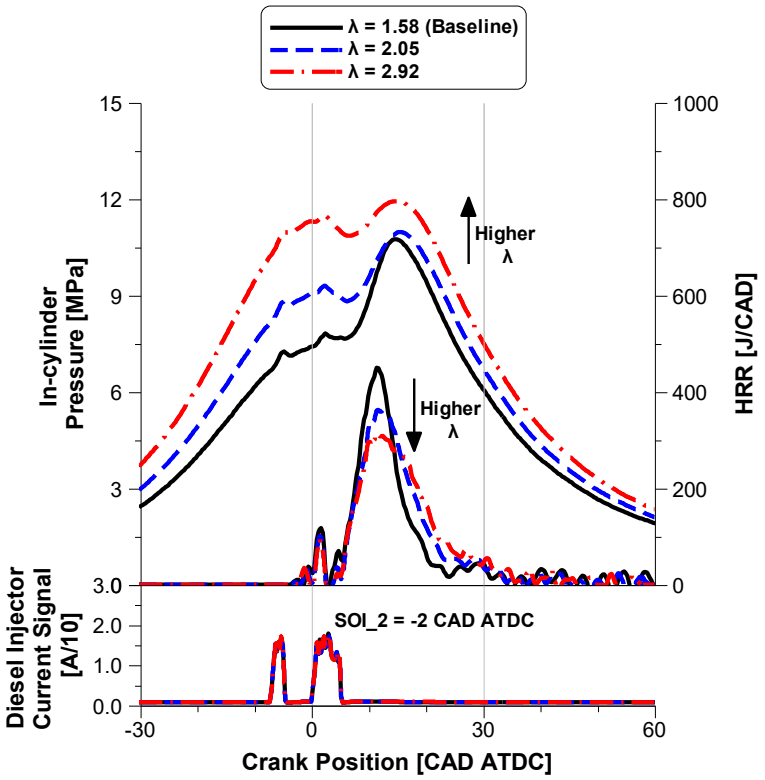

Figure 5.17. The effect of relative air-fuel ratio on in-cylinder pressure and HRR for constant diesel injection at medium engine load.

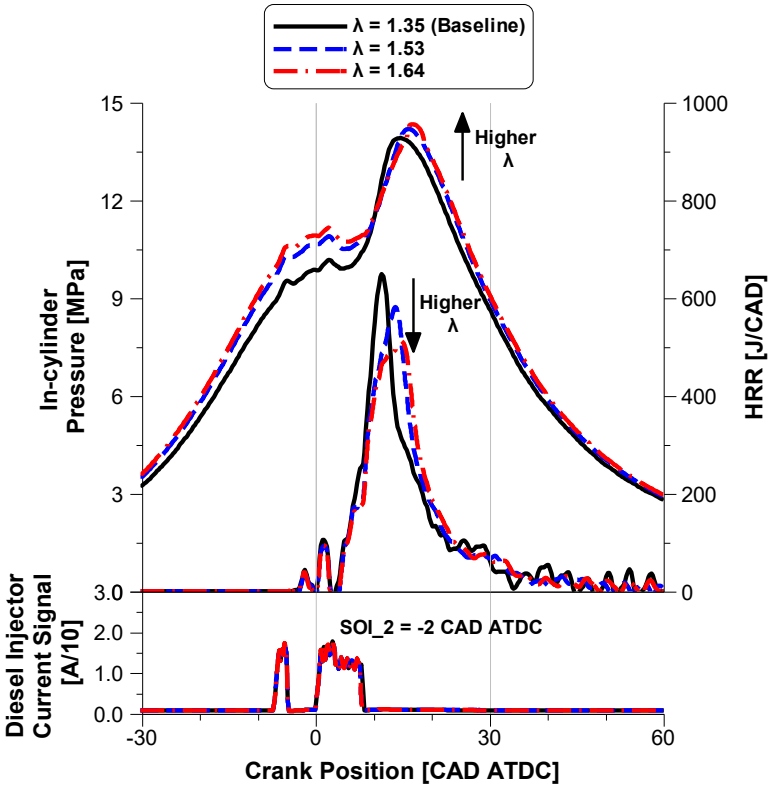

Figure 5.18. The effect of relative air-fuel ratio on in-cylinder pressure and HRR for constant diesel injection at high engine load.

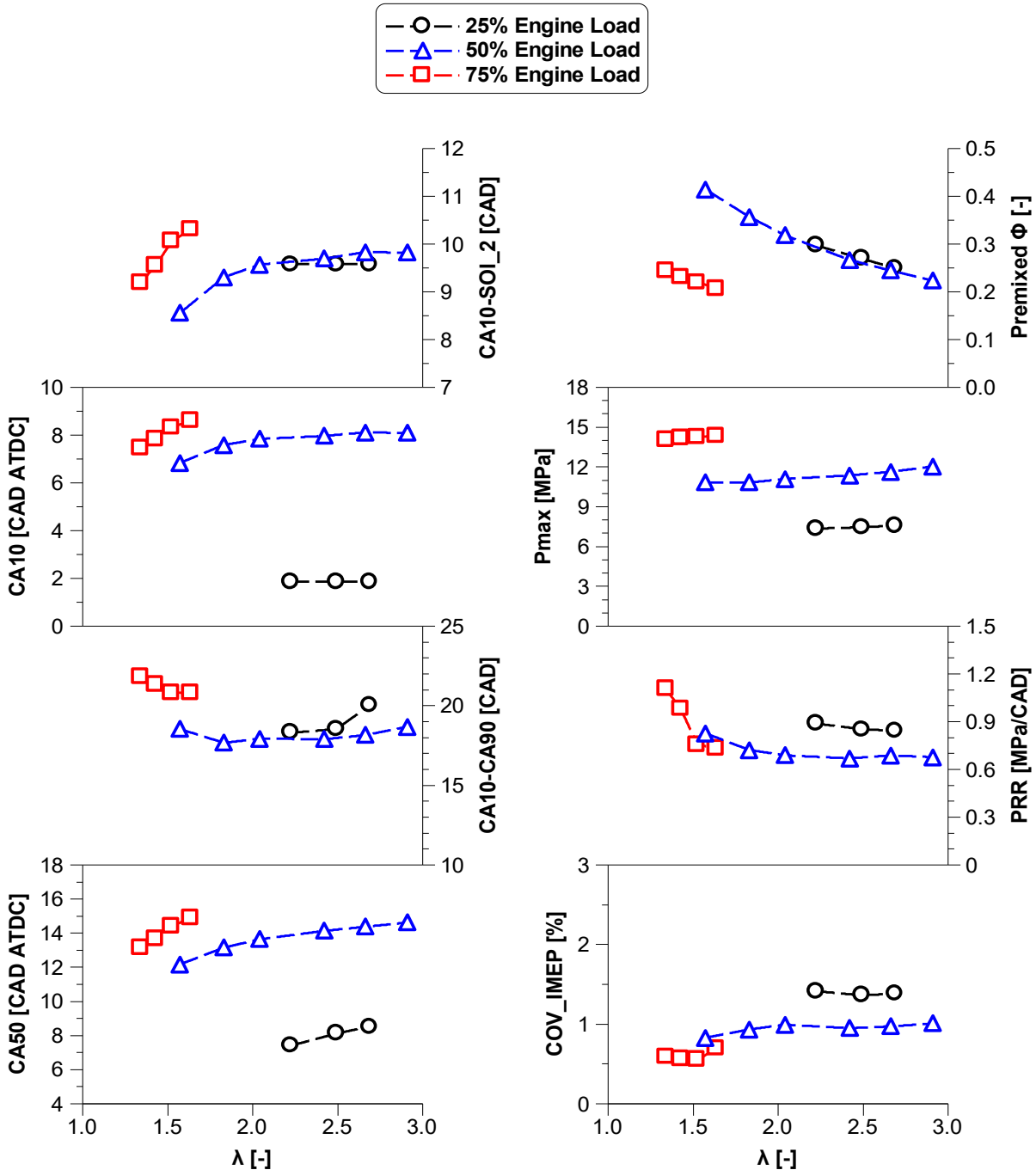

Figure 5.19. The effect of relative air-fuel ratio on combustion characteristics and stability.

5.4.3 Engine-out emissions and performance

The effect of relative air-fuel ratio on combustion and indicated thermal efficiencies, EGT and indicated equivalent specific fuel consumption are depicted in Figure 5.20.

Exhaust emissions in the form of net indicated specific values for ADF mode with increased λ values at different engine load conditions are depicted in Figure 5.21.

The decrease in EGTs with an increase in relative air-fuel ratio can be attributed to several factors. As λ increases, the mixture becomes leaner, leading to a reduced adiabatic flame temperature because the excess air dilutes the combustion process, absorbing heat without contributing to the chemical reaction. Additionally, the lower PRR, resulting from reduced mixture reactivity, causes a decrease in peak HRR, further reducing combustion intensity.

These factors collectively contribute to the observed decrease in EGTs. Specifically, at low and high loads, EGTs decreased by approximately 11%, while at medium load, the decrease was more pronounced at 27%. As a result, at low load, EGTs reduced to 352°C, still remaining within the range that supports high SCR conversion efficiency [65, 103].

The increase in relative air-fuel ratio also leads to a considerable decrease in combustion efficiency, particularly at λ above 2, as can be seen in Figure 5.20. With higher λ, the leaner mixture reduces the available fuel for combustion, causing the remaining air to have a less optimal ratio for complete combustion. Consequently, there is a slight increase in unburned hydrocarbons across all loads, and a significant rise in hydrogen slip observed in Figure 5.21 – particularly at low and medium engine loads, where λ values exceeded 2. At high engine load, however, this λ region was not reached, and hydrogen slip remained considerably lower.

ITE exhibited varying trends with an increase in relative air-fuel ratio (λ), dependent on the engine load. At low load, ITE showed a 1% increase within the λ range of 2.23–2.70. In contrast, at medium load, ITE consistently decreased as λ increased from 1.58 to 2.92, resulting in a 2% reduction. At high load, ITE notably increased by 3.4% within the λ range of 1.35–1.64.

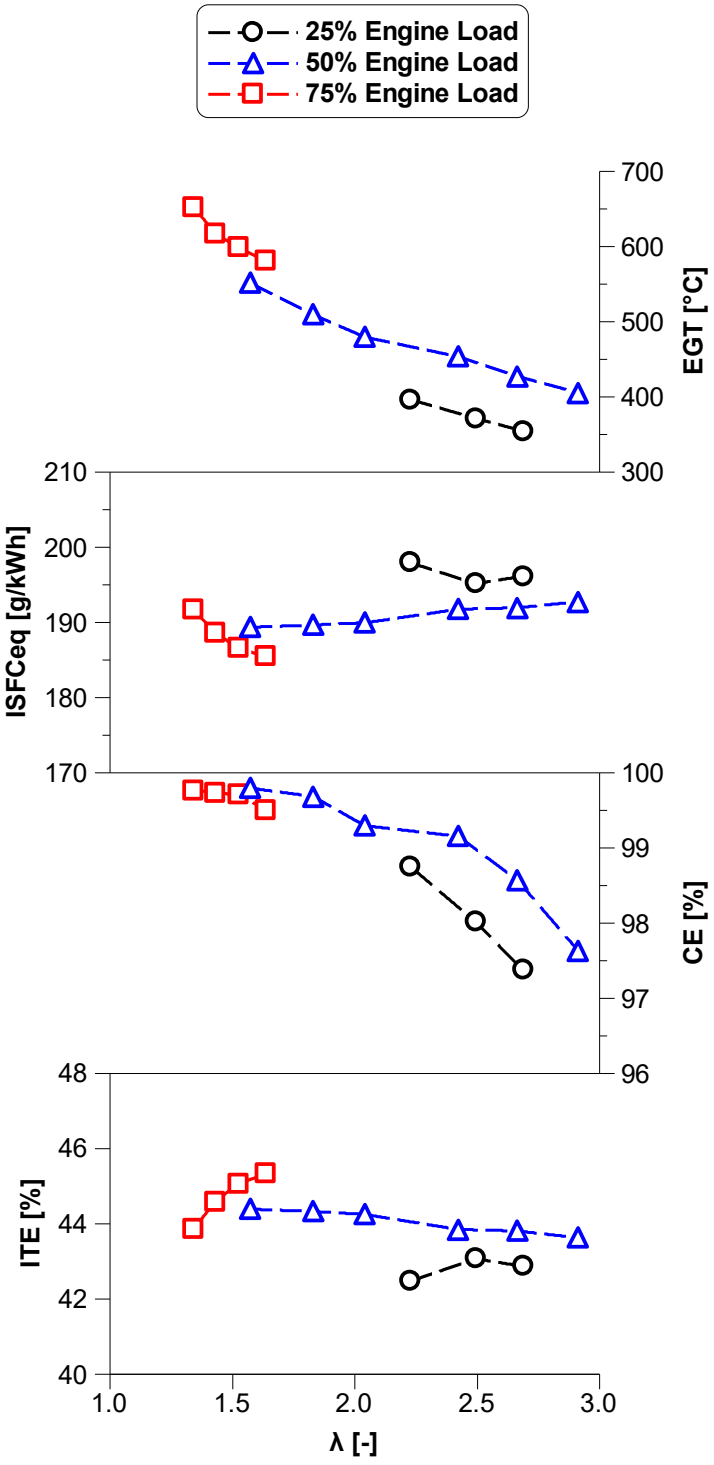

Figure 5.20. The effect of relative air-fuel ratio on engine performance.

These differing trends suggest that the effect of λ on ITE is not only nonlinear, primarily due to increased combustion duration at low and medium loads when λ exceeds 2, while at high load, where λ remains well below 2, combustion becomes shorter with

increasing λ. This indicates the need for load-specific optimisation rather than applying a fixed λ target across all operating conditions.

The increase in relative air-fuel ratio demonstrated low sensitivity on most emissions. However, there were notable exceptions – particularly unburned hydrogen and unburned hydrocarbons, as discussed earlier, as well as NOx emissions.

NOx emission generally reduced at low and medium loads with increasing λ, with reductions in the range of 15-17%. This is attributed to the leaner mixture lowering combustion temperature, which limits thermal NOx formation. In contrast, at high load, increasing λ from the baseline (λ = 1.35) to λ = 1.65 led to a 10% increase in NOx emissions. This unexpected behaviour can be explained by two factors:

- The increase in in-cylinder pressure and temperature due to higher intake charge mass and shorter combustion duration at higher λ promotes NOx formation, even under leaner conditions.

- The overall mixture remained within the high-sensitivity region for NOx formation. When λ is below 2, NOx emissions appear to be less sensitive to further increases in λ. Thus, moving from 1.35 to 1.65 does not substantially reduce NOx and may in fact enhance it due to the elevated combustion temperature.

These effects help explain why increased λ reduces NOx at lower loads but increases it at higher loads. Generally, high engine load demonstrated different trends in emissions, which is associated at the different λ operational range, as already explained.

Similarly to the ITE trends, CO_2 emissions did not exhibit a consistent pattern across the evaluated engine loads. A slight reduction of 1% was observed at low and high loads, while medium load showed a gradual increase.

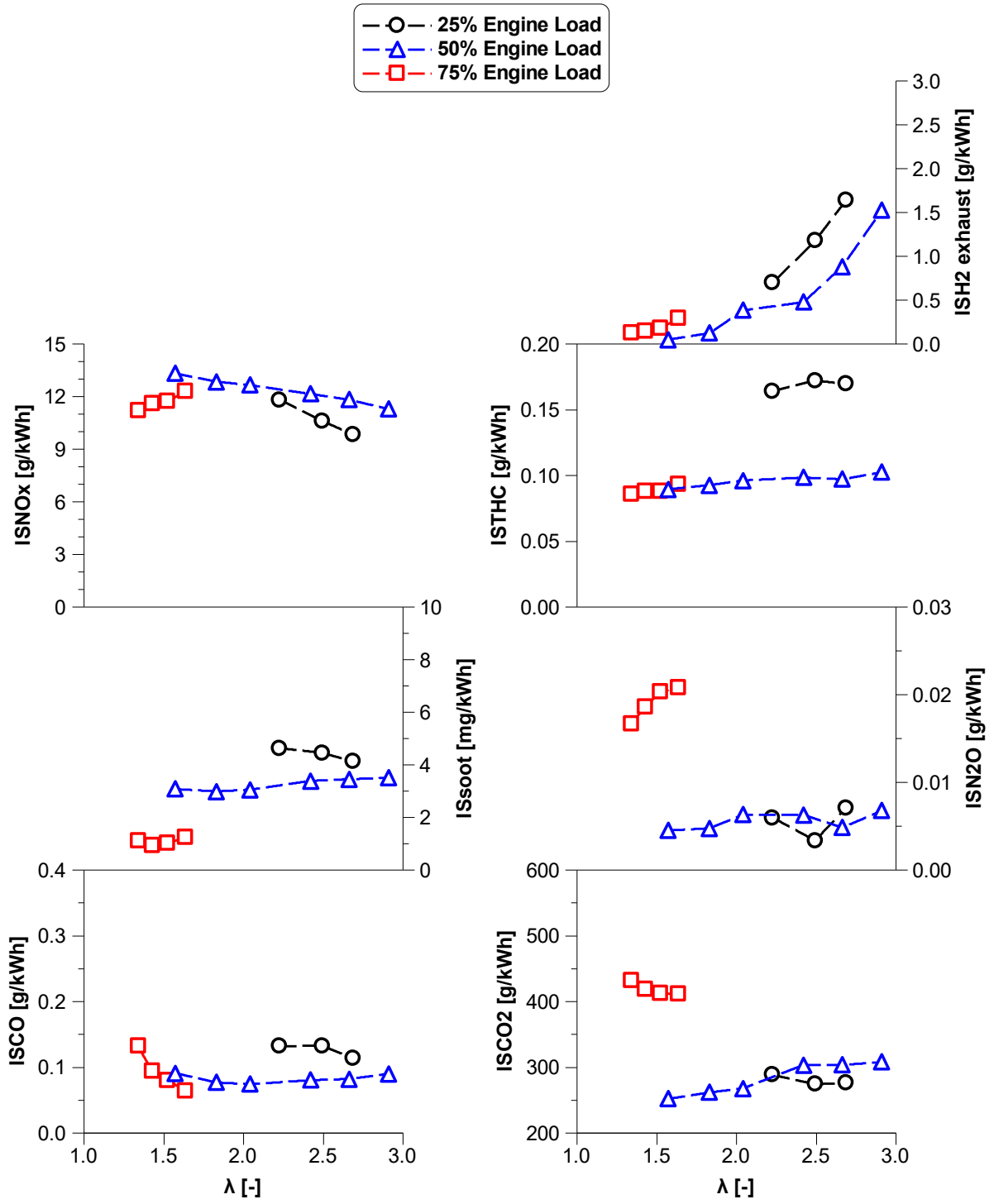

Figure 5.21. The effect of relative air-fuel ratio on engine-out emissions.

Overall, increasing the relative air-fuel ratio revealed load-dependent effects on efficiency and emissions. ITE improved slightly at low and high loads but decreased at medium load, highlighting the need for load-specific λ optimisation to maximise efficiency. Emissions were generally insensitive to λ variation, with some exceptions:

NOx decreased at low and medium loads by 15-17% (compared to ADF baseline) but increased at high load due to elevated in-cylinder temperatures and the operating λ range – indicating that relative air-fuel ratio is not a consistently effective strategy for NOx control below a certain λ threshold. Additionally, a slight increase in unburned THC and a substantial rise in hydrogen slip were observed at λ values above 2. CO_2 emissions followed no consistent trend across loads. Lastly, EGTs consistently decreased with increasing λ.

5.4.4 Enhancement of H2EF at high engine load

The lower PRR observed in Figure 5.19 with increased λ provided a margin for optimising H2EF, especially at high engine load, where only 36% had been previously achieved. Therefore, additional experiments were conducted at high engine load with an intake air pressure of 2.90 kPa (λ = 1.65), optimising H2EF up to the peak in-cylinder pressure and PRR constraints.

Figure 5.22 compares the highest relative air-fuel ratio achieved at high engine load, baseline H2EF (36%), and maximum H2EF (43%) for engine performance and combustion stability metrics. Figure 5.23 illustrate the impact of this comparison on exhaust emissions, while Figure 5.24 shows the GHG emissions comparison between CDC and ADF using highest λ and maximum 43% H2EF at high engine load only.

The further optimisation increased the H2EF to 43%, a 7-percentage point improvement over the previous 36%. This led to a reduction in CO_2 emissions to 382 g/kWh, representing an additional 48 g/kWh decrease. When considering total GHG emissions (CO_2, H_2, N_2O), the overall reduction reached 35% compared to the CDC, which is 7% greater than the 28% reduction achieved with a baseline intake air pressure of 2.60 kPa (λ = 1.35) as presented in Section 5.3.5. It was also noted a slightly improvement on combustion efficiency.

On the other hand, the increase in H2EF led to a 5% increase in NOx emissions. This rise is explained by the higher PRR and peak in-cylinder pressure observed in Figure 5.22.

In conclusion, increasing intake air pressure to create a leaner mixture (higher λ) effectively enhanced diesel replacement with another 7% at high engine load, further reducing GHG emissions, albeit with a trade-off in higher NOx levels.

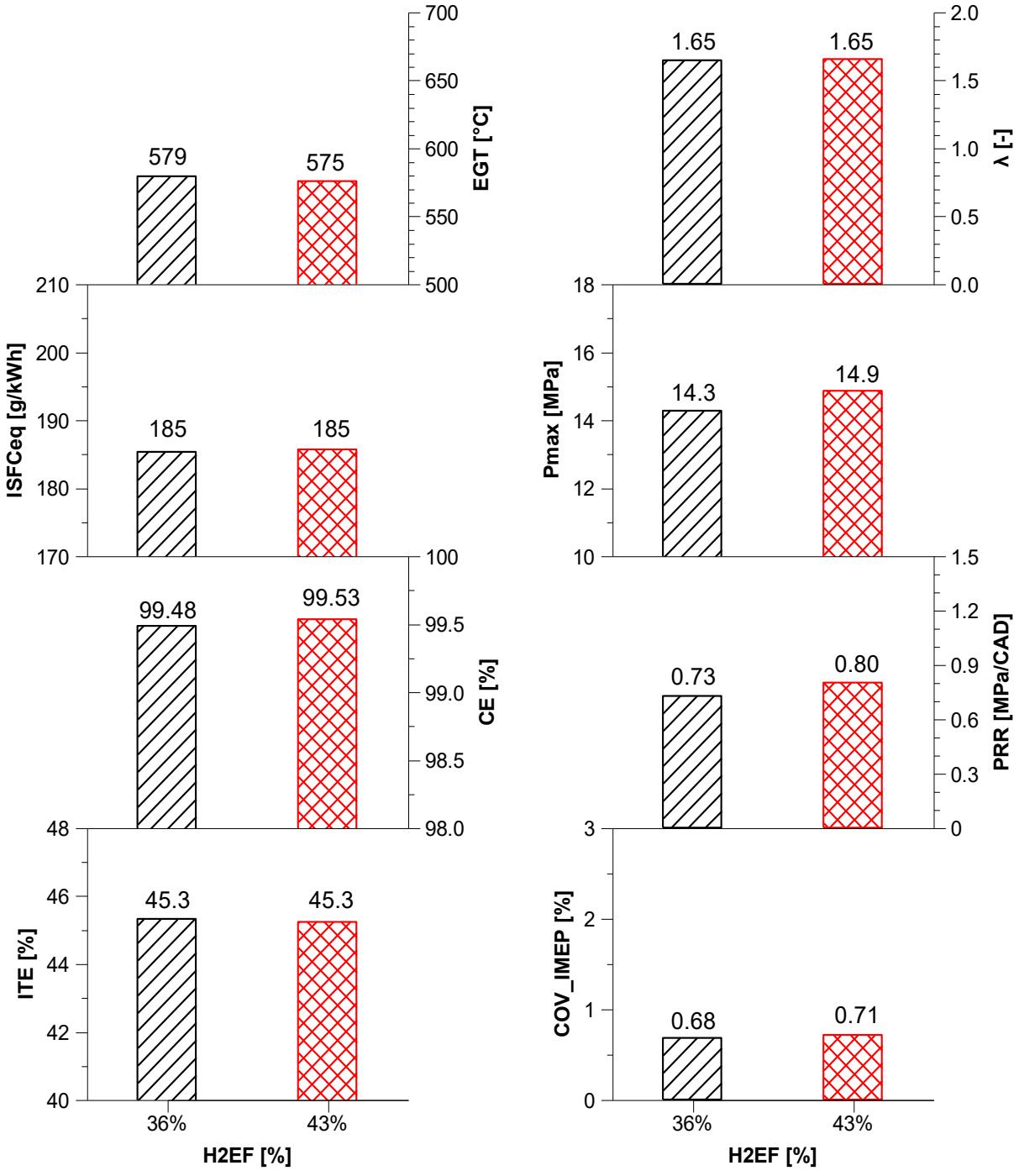

Figure 5.22. The effect of increased H2EF at leaner mixture on engine performance and combustion stability.

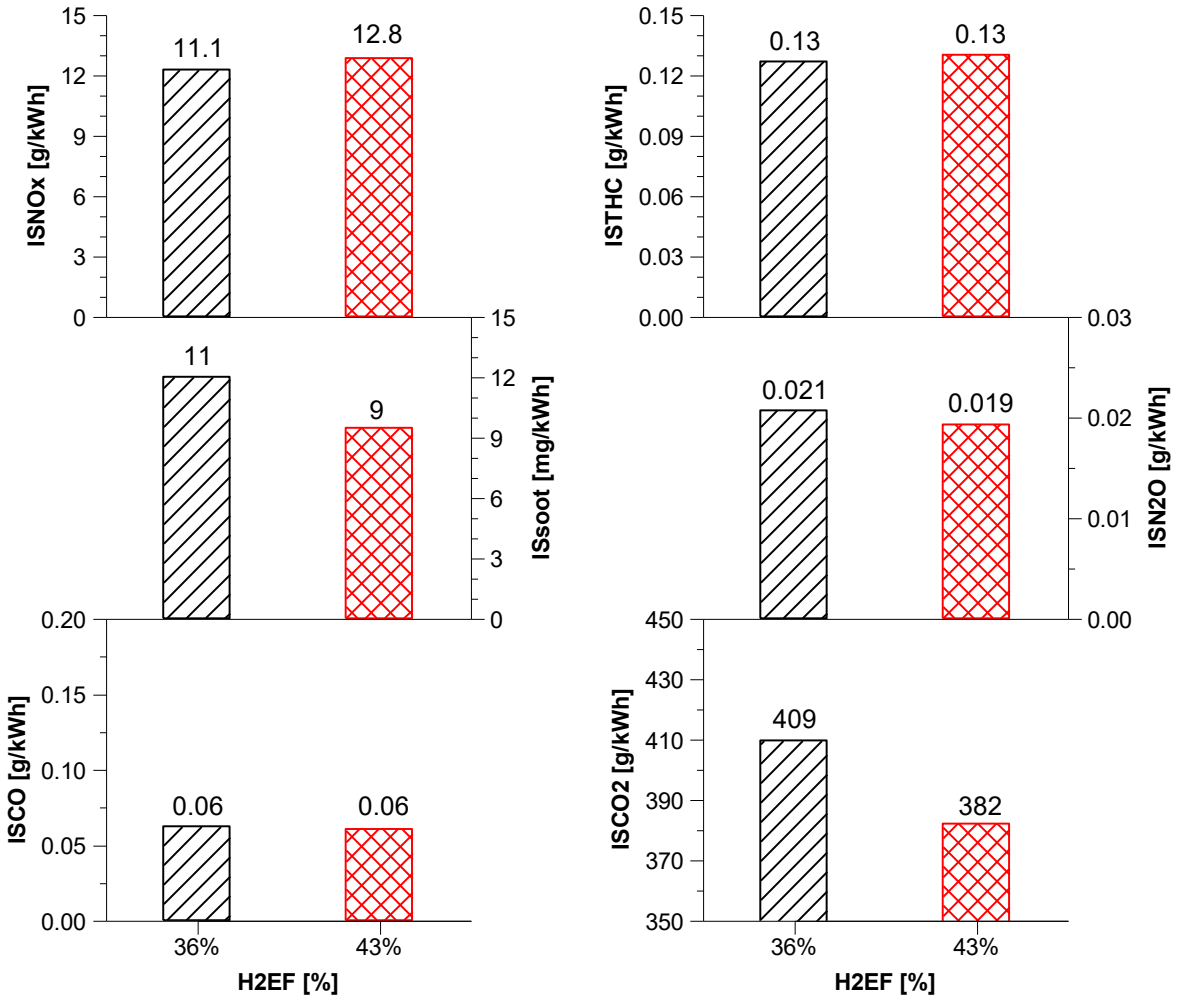

Figure 5.23. The effect of increased H2EF at leaner mixture on exhaust emissions.

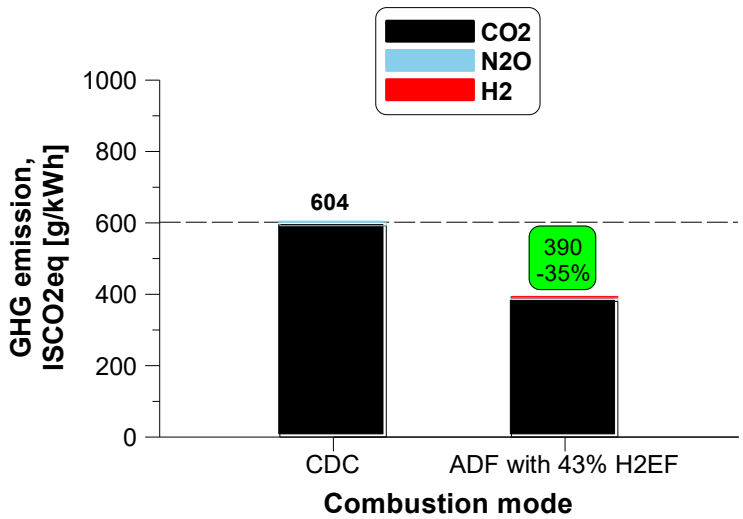

Figure 5.24. The impact of the H2EF enhancement with highest relative air-fuel ratio on combined GHG emissions at high engine load.

5.5 The employment of external EGR at low and medium engine loads

Following the analysis of relative air-fuel ratio as a NOx control strategy in Section 5.4, external exhaust gas recirculation (eEGR) was also investigated to further mitigate NOx emissions. This set of experiments was conducted at various engine loads using ADF mode with the maximum H2EF obtained in Section 5.3 as a baseline.

5.5.1 Experimental test procedure

In line with the previous sections, most of the conditions remain the same. The methodology of this experiment was focused on an eEGR sweep from 0 to 20% at 0.6 and 1.2 MPa IMEP, representing low and medium loads, respectively. The ADF regime with 70% H2EF, as established in Section 5.3, was used as the baseline. To determine stable engine operation, maximum PRR was set to 2.0 MPa/CAD, while COV_{IMEP} was set to 3%. Table 5.3 summarises the overall engine operating conditions used for this study.

Table 5.5. Engine operating conditions for the eEGR sweep.

Parameter	Unit	Low load	Medium load
IMEP	MPa	0.6	1.2
Engine speed	rpm	1200	1200
H2EF	%	70	70
ECR	-	14.8	14.8
Intake air temperature	°C	40	42
Intake air pressure	kPa	125	190
Exhaust pressure	kPa	135	200
eEGR	%	0 - 20	0 - 20
iEGR	%	0	0
Diesel injection pressure	MPa	100	130

To maintain consistency between results and allow for valid comparisons, intake and exhaust pressures, as well as diesel injection timing and pressure, were kept the same as in Section 5.3. This approach enabled the isolation of the effect of eEGR addition.

5.5.2 Operation overview and combustion characteristics

Figure 5.25 and Figure 5.26 compare the measured in-cylinder pressure and heat release rate at constant diesel SOI for different eEGR percentages in the advanced dual-fuel mode for low and medium engine loads, respectively. Figure 5.27 presents combustion characteristics, including ignition delay, CA10, CA50, combustion duration, and additional combustion stability metrics as a function of eEGR percentage, also at constant diesel SOI.

The employment of eEGR up to 20% showed a marginal impact on peak in-cylinder pressure and HRR at low engine load, and no measurable effect at medium load. Typically, eEGR is expected to retard the combustion ignition and reduce and delay the peak heat release rate due to lower combustion temperatures, thus lowering both peak pressure and PRR [192, 190]. However, in this experiment, a slight increase in HRR was observed at low load despite a minor reduction in peak in-cylinder pressure.

This behaviour may be attributed to the significant amount of unburned hydrogen recirculated into the intake system via the EGR loop, which primarily enhanced the combustion process after the ignition phase. The start of combustion (CA10) was still retarded due to the expected dilution effect of eEGR on in-cylinder temperature. As a result, combustion phasing was only slightly delayed – by 0.2 CAD at 20% eEGR, and the total combustion duration was shorter by 0.25 CAD. The reduction in hydrogen slip, as will be discussed in more detail in Section 5.5.3, supports this explanation. However, the reintroduction of unburned fuel also led to an increase in maximum PRR, which ultimately limited the potential for further increases in H2EF.

In contrast, this unexpected HRR trend was not observed at medium load, as the baseline ADF with 70% H2EF produced minimal unburned hydrogen, leading to a negligible impact from its recirculation via the EGR system. Therefore, while the EGR dilution effect did not affect the in-cylinder pressure trace, the expected retardation in CA50 and a longer combustion duration were still observed.

Additionally, the reduction in λ for higher eEGR percentage observed in Figure 5.27 is mainly caused by the lower oxygen available in the in-cylinder charge. The resulting decrease in relative air-fuel ratio also promotes faster combustion.

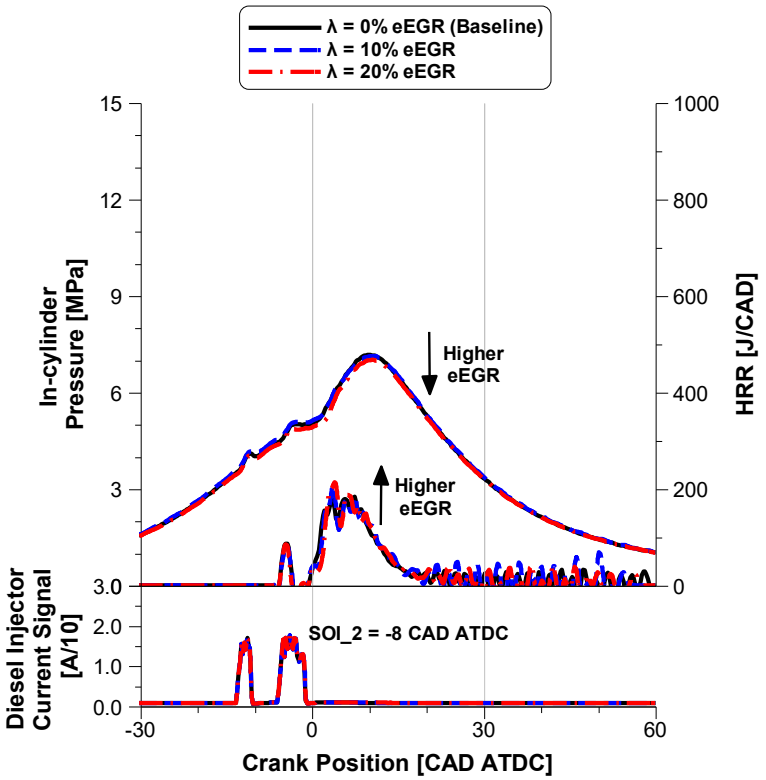

Figure 5.25. The effect of external EGR on in-cylinder pressure and HRR for constant diesel injection at low engine load.

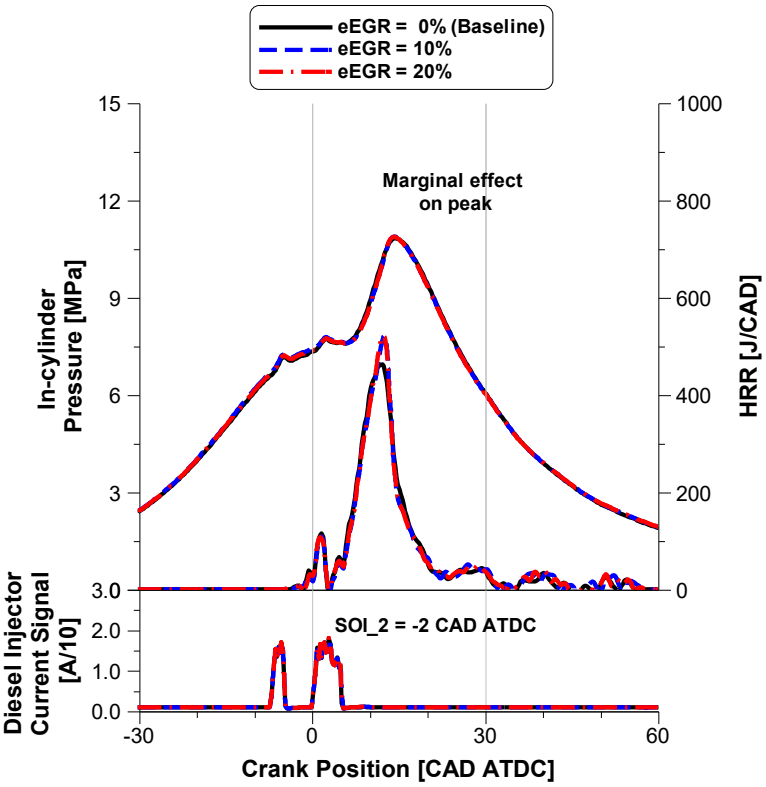

Figure 5.26. The effect of external EGR on in-cylinder pressure and HRR for constant diesel injection at medium engine load.

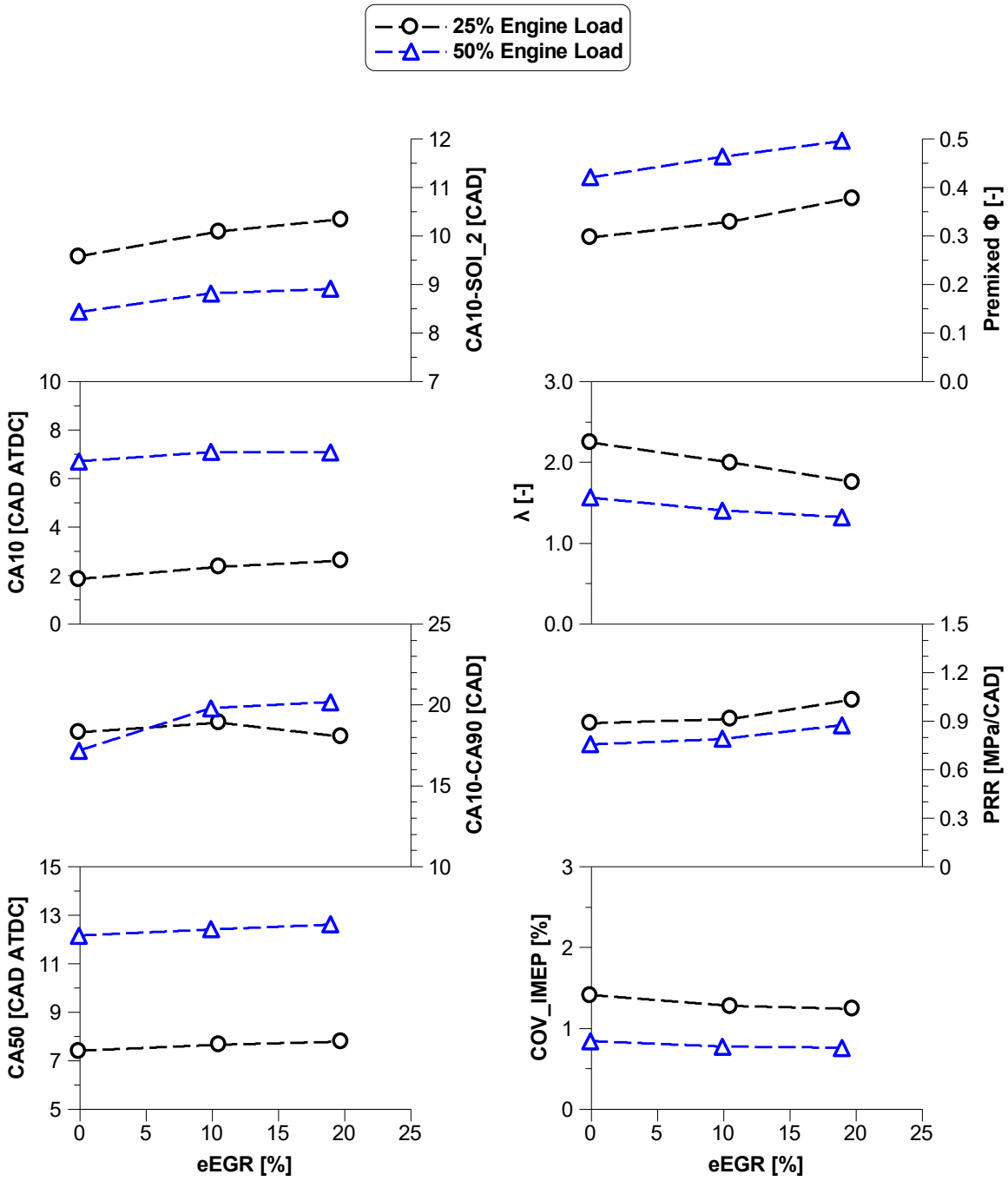

Figure 5.27. The effect of external EGR on combustion characteristics and stability.

5.5.3 Engine-out emissions and performance

The impact of the eEGR on combustion and indicated thermal efficiencies, EGT and indicated equivalent specific fuel consumption are depicted in Figure 5.28. Exhaust emissions in the form of net indicated specific values with and without the use of eEGR are depicted in Figure 5.29.

The introduction of eEGR did not negatively affect engine performance. A slight increase in ITE of 0.7% was observed at low load, primarily attributed to a 0.2 percentage points improvement in combustion efficiency, resulting from a 21% reduction in hydrogen slip with 20% eEGR. At medium load, ITE was insensitive to the increase eEGR percentage increase, mainly due to the fact that hydrogen slip was already nearly zero at the baseline.

EGTs were minimally impacted by the increase in eEGR, with only a slight increase observed at medium load due to the combustion occurring later and lasting longer in the cycle.

Regarding emissions, a significant reduction in NOx emissions, around 57-62% at 20% eEGR, was observed at both engine loads when compared to the baseline ADF. This reduction aligns with the range reported in the literature [200, 201, 91]. However, this reduction came at the expense of an increase in soot and CO emissions, following a similar trend to that observed by Verschaeren et al. [89]. Specifically, the increase in soot, reaching up to 9 and 14 mg/kWh at low and medium loads, respectively, is relevant, as it exceeds the limits set by Euro 7 regulation at both loads.

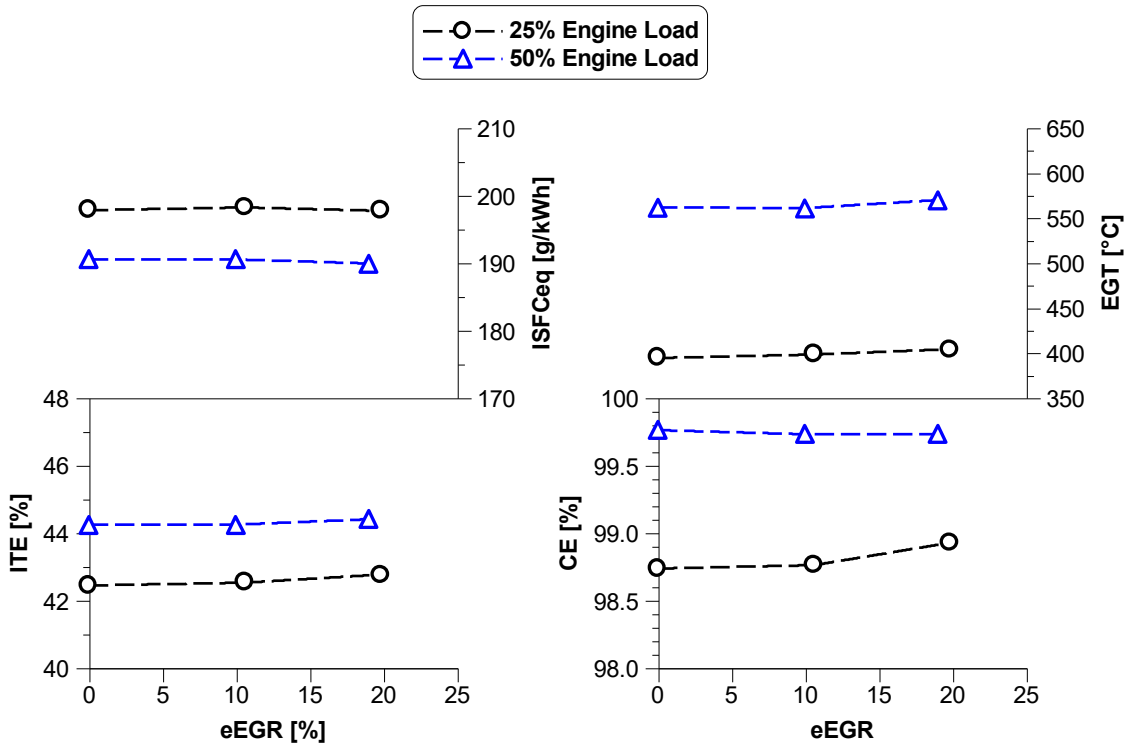

Figure 5.28. The effect of external EGR on engine performance.

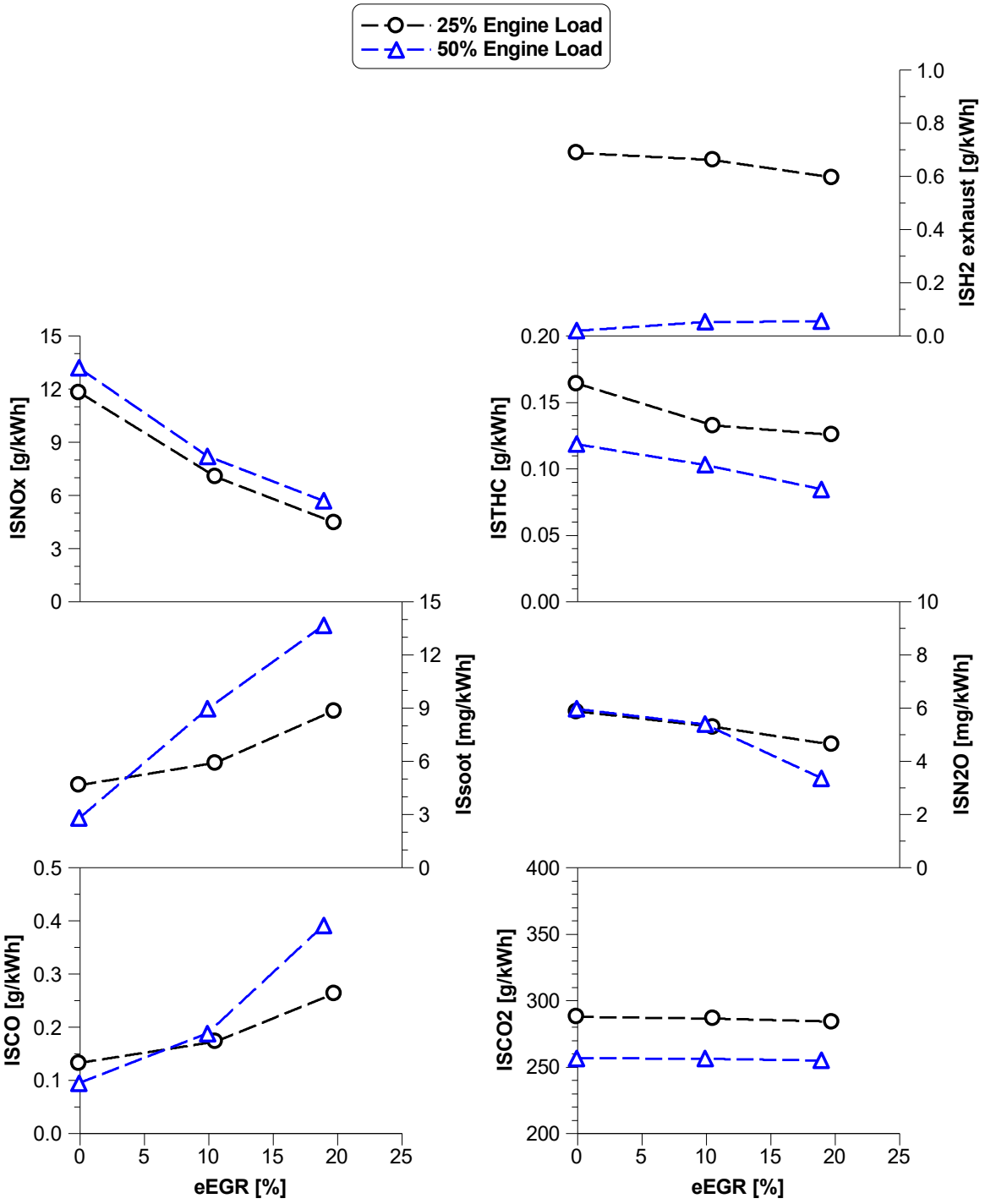

Figure 5.29. The effect of external EGR on engine-out emissions.

Overall, the use of eEGR combined with a high hydrogen energy fraction proves to be an effective solution for NOx control (around 60% reduction when compared to 70% H2EF baseline) without compromising engine performance, in contrast to the findings in Section 4.4, where eEGR in diesel-hythane dual-fuel operation led to performance compromises. Nonetheless, there is a deterioration in soot and CO emissions.

5.6 The impact of water injection at high engine load

Given the limited research on the effect of water (H_2O) injection combined with hydrogen dual-fuel engines and its potential benefits for NOx reduction, the final step in the optimisation of diesel–hydrogen dual-fuel combustion involved introducing water injection into the intake manifold.

5.6.1 Experimental test procedure

The methodology of this experiment involved a water injection flow rate ($\dot{m}_{H2O}$) sweep from 0 to 0.6 kg/h at 1.8 MPa IMEP, representing high engine load. The ADF combustion with 36% H2EF, as established in Section 5.3, was used as the baseline. Table 5.6 summarises the overall engine operating conditions used for this study.

Table 5.6. Engine operating conditions for the water injection sweep.

Parameter	Unit	High load
IMEP	MPa	1.8
Engine speed	rpm	1200
H2EF	%	36
ECR	-	14.8
Intake air temperature	°C	43
Intake air pressure	kPa	260
Exhaust pressure	kPa	270
eEGR	%	0
iEGR	%	0
Diesel SOI_2	CAD ATDC	+1
Diesel injection pressure	MPa	160
Hydrogen injection pressure	MPa	0.8
H_2O injection pressure	MPa	0.6
$\dot{m}_{H2O}$	kg/h	0 – 0.6

To ensure stable engine operation, the maximum PRR was limited to 2.0 MPa/CAD, while COV_{IMEP} threshold was set to 3%. In-cylinder pressure was constrained to a

peak below 18 MPa to preserve engine reliability. In order to comply with these boundary conditions throughout the sweep and ensure consistent comparisons, the diesel main injection timing was retarded to 1 CAD ATDC – corresponding to a 3 CAD delay relative to previous experiments.

To preserve consistency between results and allow for valid comparisons, intake and exhaust pressures, as well as diesel injection pressure, were kept the same as in Section 5.3. This approach enabled the isolation of the effect of water injection.

5.6.2 Overview of the dual-fuel operation

The comparison of measured in-cylinder pressure and heat release rate at constant diesel SOI with and without water injection is depicted in Figure 5.30. On the other hand, Figure 5.31 displays combustion characteristics, combustion stability metrics, and indicated thermal efficiency as a function of water injection flow rate, also at constant diesel SOI. Finally, Figure 5.32 illustrates the variation in engine-out emissions with increasing water injection flow rates.

As can be seen in Figure 5.30, the injection of 0.6 kg/h of water generated a significant impact on the combustion process. Contrary to findings in the literature [155], the peak in-cylinder pressure increased by 9% (0.12 MPa) and occurred approximately 7 CAD earlier. Although the absolute peak of the heat release rate was reduced, it occurred much closer to TDC compared to the baseline, indicating an earlier start of combustion. This observation is confirmed by the more advanced CA10 and shorter ignition delay shown in Figure 5.31.

The increased reactivity during the initial stage of combustion is likely explained by the dissociation of water molecules during evaporation, which releases hydrogen and oxygen atoms. These contribute to enhanced fuel reactivity and increased oxygen availability, effectively resulting in leaner premixed charge. This is supported by the observed increase in the relative air-fuel ratio depicted also in Figure 5.31.

At the same time, water injection reduces combustion temperature due to the cooling effect of evaporation, which absorbs thermal energy from the in-cylinder gases. This cooling effect is evident from the 35°C reduction in EGT and the progressive slowdown in combustion, as seen in the more modest CA50 advancement (only 3 CAD) and the increase in combustion duration from 24 to 28 CAD. The combination of an aggressive initial combustion phase and an overall more controlled burn rate contributes to improved combustion stability, as shown by COV_{IMEP} values remaining well below 1%.

As a result, indicated thermal efficiency improved by more than 2% relative to the ADF baseline, indicating that this strategy enables greater flexibility in engine operation. Specifically, it allows further diesel SOI retardation without compromising performance.

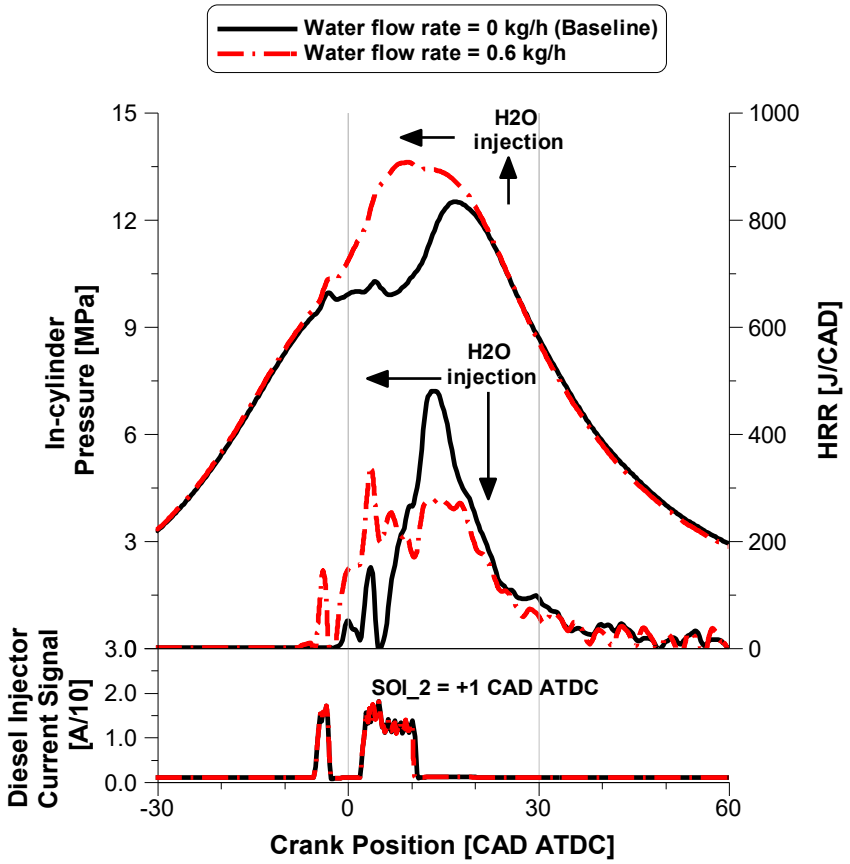

Figure 5.30. The impact of water injection on in-cylinder pressure and heat release rate for constant diesel injection timing at high engine load.

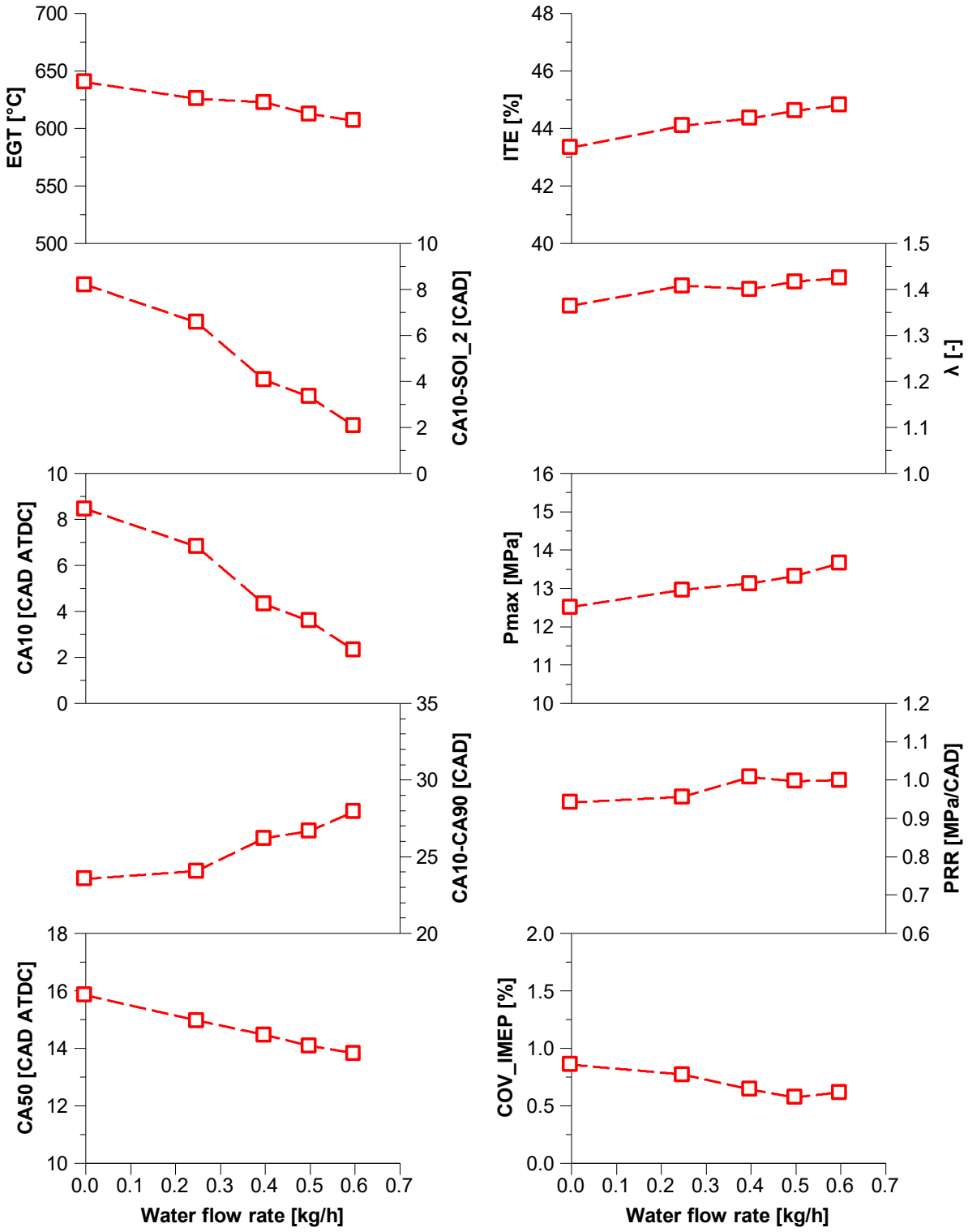

Figure 5.31. The impact of water injection on combustion characteristics and stability.

Another advantage of the reduced combustion temperature achieved through the addition of water at high load is the effective reduction in NOx emissions as seen in

Figure 5.32. A decrease of 22% was observed with only 0.6 kg/h of water – significantly lower than injection rates commonly reported in the literature.

Carbon emissions also benefited, with CO_2 reduced by 5% and CO by 21%. This reduction in CO_2 can be partially attributed to the slight decrease in diesel fuel quantity as water injection increased. Notably, this suggests that if the same amount of diesel had been maintained, the additional energy made available through water-enhanced combustion would have resulted in higher torque output. Therefore, water injection not only improves combustion characteristics but also opens the potential for increased power without additional fuel input. However, THC appeared largely unaffected by water injection.

It is important to note that further increases in water injection at a constant diesel SOI of 1 CAD ATDC were limited by a sharp rise in peak in-cylinder pressure and PRR, exceeding acceptable operational limits. This is attributed to the combustion process initiating near TDC. To allow for higher water content without violating boundary conditions, strategies such as further retarding diesel SOI or reducing diesel injection pressure could be considered.

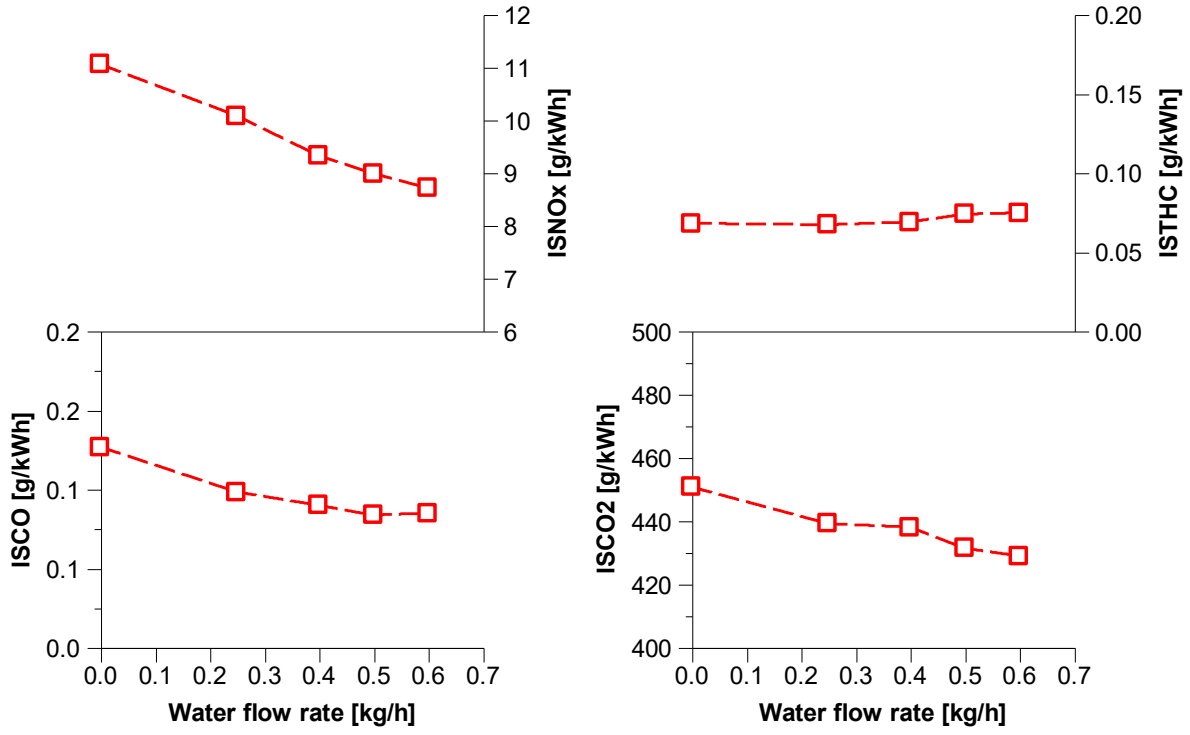

Figure 5.32. The impact of water injection on exhaust emissions.

Overall, water injection at high load increased peak in-cylinder pressure and advanced the heat release, indicating earlier combustion phasing. The resulting lower combustion temperatures slowed the burn rate as combustion progressed, which contributed to improved combustion stability. ITE improved by over 2% compared to the ADF baseline. Emission-wise, NOx was reduced by 22%, while CO_2 and CO decreased by 5% and 21%, respectively.

5.7 Overview of optimal dual-fuel engine operation

This last section presents an overview of optimal engine operation for diesel-hydrogen dual-fuel combustion, structured according to key performance and emissions objectives. The assessment was focused on both conventional and advanced dual-fuel modes at a constant engine speed of 1200 rpm, across three engine loads: 25%, 50%, and 75% of the full load. The section begins by summarising the strategy used to maximise the hydrogen energy fraction in both dual-fuel modes. This is followed by an evaluation of the approach that delivers the greatest GHG reduction potential. A Well-to-Wheel analysis is then introduced to quantify the environmental impact of hydrogen fuel derived from both grey and green production pathways. Finally, the section concludes with a summary of the ADF optimisation work carried out on this chapter focused on NOx mitigation.

5.7.1 Maximisation of hydrogen energy fraction

The maximisation of hydrogen in the dual-fuel operation plays a critical role in achieving greater carbon reduction and ensuring compliance with CO_2 emissions regulations. Figure 5.33 illustrates the maximum H2EF achieved for each dual-fuel combustion mode across the engine map. The red annotations represent ADF results, while the blue annotations indicate CDF outcomes.

It is evident that ADF combustion enables significantly higher diesel replacement on an energy basis compared to the conventional dual-fuel mode, as combustion stability issues prevented CDF to reach higher H2EF percentages. This advantage is

particularly pronounced at low and medium loads, where the baseline advanced mode obtained in Section 5.3 achieved up to 70% H2EF – representing a 38% and 50% higher than the mode CDF at low and mid loads, respectively. At high load, hydrogen substitution was limited by engine boundary conditions, yet ADF with increased relative air-fuel ratio still reached 43% H2EF, more than twice the level achieved by CDF.

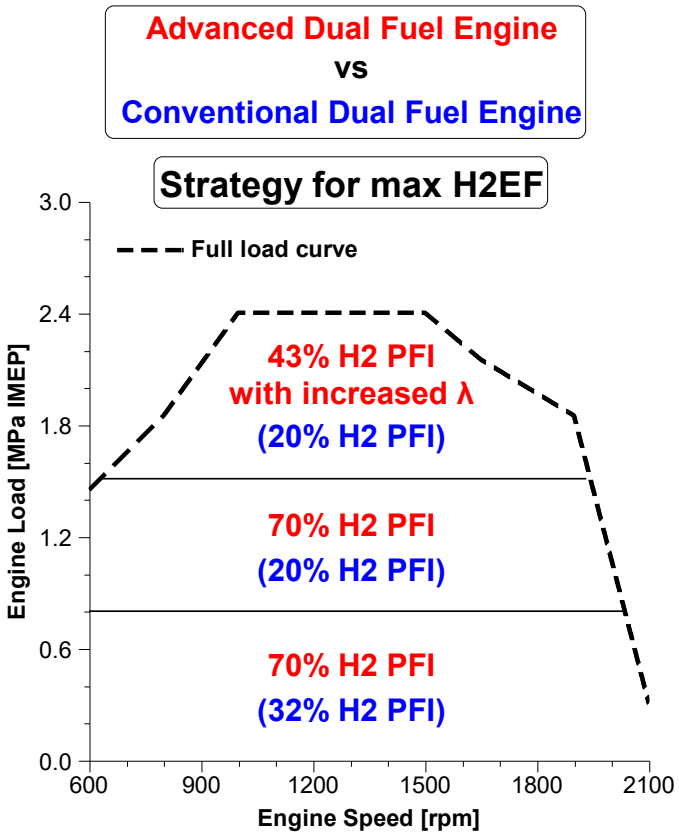

Figure 5.33. Comparison of dual-fuel strategies for H2EF maximisation across low, medium and high engine loads.

5.7.2 Maximisation of GHG reduction potential

The quantification of GHG emissions from the dual-fuel engine operations is essential to understanding the environmental impact of each combustion mode. This analysis includes the summation of greenhouse gases measured at the exhaust line, namely carbon dioxide, nitrous oxide, and methane.

In diesel-hydrogen dual-fuel combustion, methane has no significant influence, as there is no direct CH_4 involvement in the process, and the amount formed during premixed charge combustion was negligible. Nitrous oxide is a relevant greenhouse gas to consider due to its high GWP – 273 times that of CO_2 over a 100-year period [28] – which could, in theory, substantially increase CO_2 equivalent emissions. However, as discussed in Section 5.3.5, N_2O was not included in this analysis due to its negligible concentration in the exhaust. Consequently, CO_2 remains the dominant contributor to GHG emissions in diesel–hydrogen operation.

Figure 5.34 shows the highest reduction of GHG emissions achieved for each dual-fuel combustion mode across the engine map, along with their respective strategy. Red annotations indicate ADF results, while blue annotations represent CDF outcome.

Overall, the advanced dual-fuel strategy consistently delivered the greatest GHG reductions across all engine loads, significantly outperforming the CDF mode. At low and high loads, ADF combined with an increased relative air–fuel ratio achieved maximum reductions of 58% and 36%, respectively. At medium load, ADF with 20% eEGR let to a 58% reduction. The underlying reasons for these trends were discussed in Section 5.3.

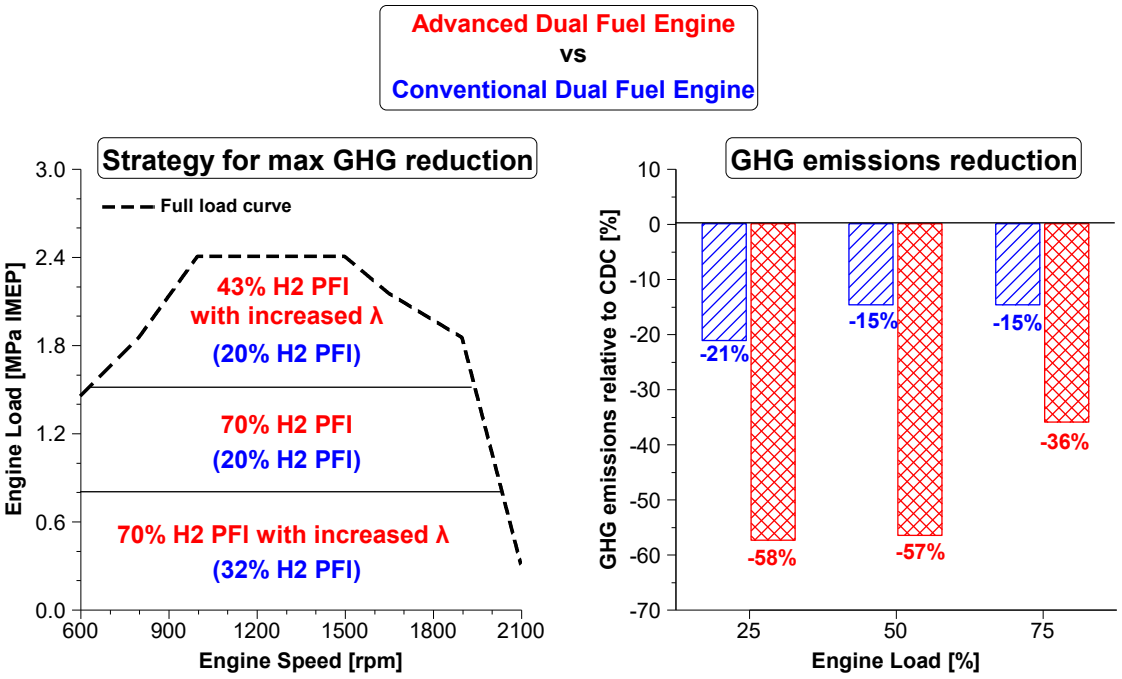

Figure 5.34. Comparison of dual-fuel modes in terms of maximum GHG emissions reduction across low, medium and high engine loads, relative to CDC, with identification of the most effective strategy for each case.

5.7.3 Well-to-Wheel analysis

The WTW analysis of diesel-hydrogen dual-fuel operation, was conducted to assess the actual impact of hydrogen use in advanced dual-fuel combustion mode on GHG emissions within the transportation sector. This comprehensive approach integrates both Well-to-Tank and Tank-to-Wheel components to quantify the total GHG emissions associated with the production and utilisation of a specific fuel [193, 194].

The WTT phase accounts for emissions generated during raw material extraction or cultivation, processing, transportation, and delivery to the vehicle's fuel tank. In contrast, the TTW phase accounts for emissions released during engine operation. GHG emissions were expressed in grams of CO_{2eq} per MJ of fuel energy injected.

The same methodology used in the WTW assessment of diesel–hythane dual-fuel combustion in Chapter 4 was adopted here. Specifically, Equations (4.5) and (4.7) were applied to calculate the TTW and WTT contributions, respectively, while Equation (4.6) was used to estimate the overall WTW values. Table 5.7 summarises the estimated WTT CO_{2eq} values gathered from the literature.

Table 5.7. Estimated Well-to-Tank CO_{2eq} emissions for diesel and various hydrogen production pathways.

Fuel	Unit	WTT	Source
Diesel	gCO_{2eq}/MJ	18.9	Current fossil fuel [195]
Grey hydrogen	gCO_{2eq}/MJ	113.0	SMR, natural gas feedstock [195]
Blue hydrogen	gCO_{2eq}/MJ	50.0	SMR with retrofit CCS, natural gas feedstock [202]
Green hydrogen	gCO_{2eq}/MJ	9.5	Electrolysis using renewable energy from wind and solar sources [195]

Figure 5.35 presents the theoretical CO_{2eq} emissions for both conventional diesel and advanced dual-fuel operations as a function of engine load. The upper graph illustrates the Tank-to-Wheel CO_{2eq} emissions, while the lower graph displays the Well-to-Wheel values. To isolate the influence of hydrogen production pathways, only the ADF mode was considered for this evaluation, as it consistently demonstrated the greatest potential for GHG emissions reduction. Furthermore, the TTW analysis shows

overlapped data points for ADF at each engine load, representing all three hydrogen sources, since emissions from this phase are independent of the fuel production route.

The TTW CO_{2eq} emissions, representing the GHG released during engine operation, are consistent with the results discussed in the previous section.

In terms of WTW performance, the use of green hydrogen produced via electrolysis using renewable energy sources led to the most favourable outcome – reducing WTW CO_{2eq} emissions by up to 57 g/MJ compared to the CDC baseline, which corresponds to a 56% reduction. Blue hydrogen, derived from steam methane reforming (SMR) with integrated carbon capture and storage (CCS), also contributed to a considerable reduction of 29 g/MJ, equivalent to a 28% decrease. In contrast, grey hydrogen produced from conventional SMR without CCS resulted in a 19% increase in WTW GHG emissions, despite the reduction achieved during engine operation.

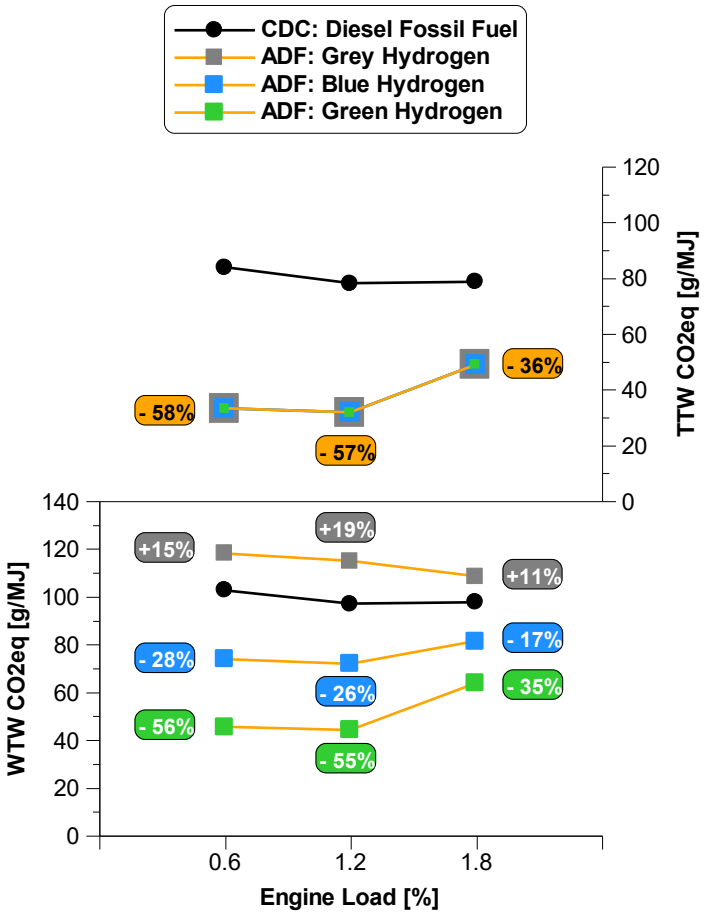

Figure 5.35. Theoretical TTW and WTW CO_{2eq} emissions for CDC and ADF modes, simulating different hydrogen production pathways.

Overall, this analysis highlights that, while engine operation optimisation plays a significant role in reducing GHG emissions, the fuel production pathway remains a critical factor in determining the overall environmental impact. Consequently, it can be concluded with a reasonable degree of confidence that the proposed ADF combustion strategy, when applied with blue or green hydrogen, presents a viable pathway to support climate change mitigation efforts and promote a more sustainable energy solution for the transportation sector.

5.7.4 Advanced dual-fuel optimisation for NOx reduction

The mitigation of NOx emissions is another key factor in the viability of diesel-hydrogen dual-fuel combustion. This section provides a summary of the ADF optimisation work presented in Sections 5.4 to 5.6, building upon the baseline ADF results introduced in Section 5.3. Further technical details concerning combustion characteristics, performance, and emissions associated with each strategy can be found in the corresponding sections referenced above.

Figure 5.36 provides a comparative summary of the impact of each NOx control optimisation strategy – namely increased λ, eEGR, and water injection – relative to the ADF baseline. The results are expressed as percentage changes in NOx emissions (bottom graph) and ITE (top graph). Each strategy is represented by three bars corresponding to the engine loads tested: black for low load, blue for medium load, and red for high load. It is worth noting that some data points are absent – specifically, eEGR at high load, and water injection at low and medium loads – as these conditions were not evaluated in this experimental optimisation due to the lack of time available to complete such tests during the PhD project.

Therefore, it can be observed that the employment of eEGR was the most effective strategy for reducing NOx emissions from the ADF baseline, while also providing a small ITE enhancement (0.1–0.7%). This approach resulted in NOx reductions well above 50% at low and medium loads – substantially greater than the 15-17% reductions achieved through increased relative air-fuel ratio. The latter did not show a

consistent effect on ITE: a 0.9% improvement at low load contrasted with a 1.7% reduction at medium load. Nonetheless, there is a deterioration in soot and CO levels.

At high load, water injection was proved to be the more effective of the two strategies evaluated under this condition, demonstrating potential for simultaneous NOx reduction and ITE improvement. A relatively modest water injection rate of 0.6 kg/h – low by comparison with literature benchmarks – yielded a 22% reduction in NOx and a 2.2% increase in thermal efficiency. Conversely, although increasing the relative air-fuel ratio led to a notable ITE improvement of 3.3%, it also caused a 10% rise in NOx emissions.

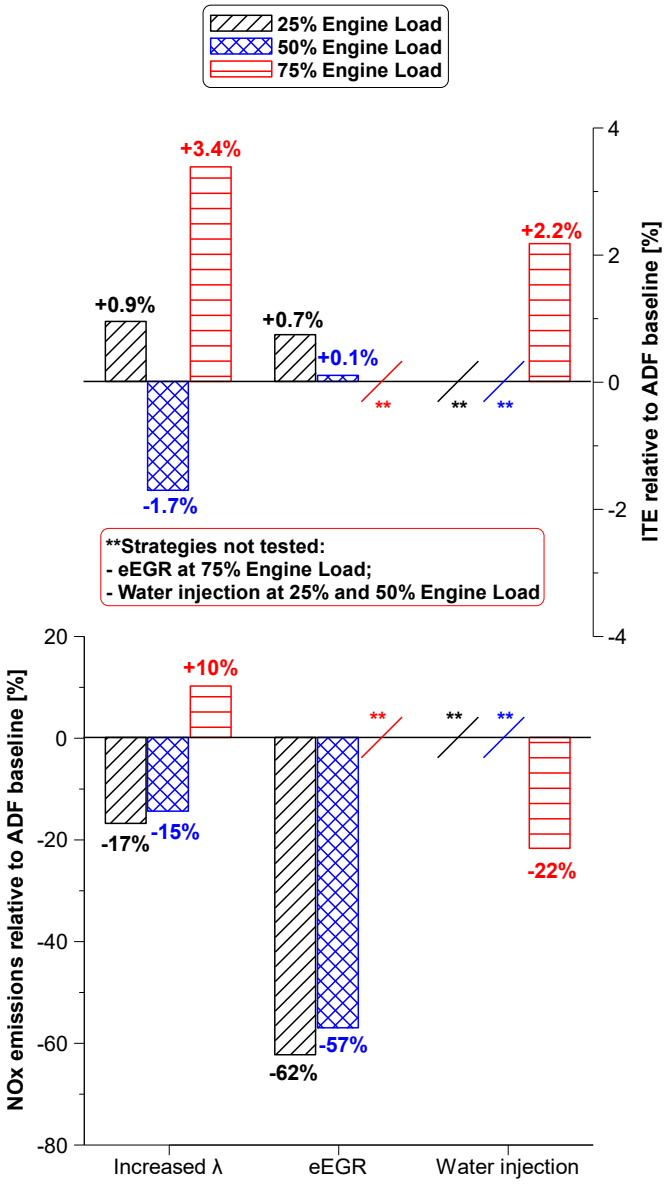

Figure 5.36. Relative changes in NOx emissions (bottom graph) and ITE (top graph) for each NOx control strategy tested compared to the ADF baseline.

In conclusion, the most effective strategies identified through this optimisation process were the application of 20% eEGR at low and medium engine loads, and the use of water injection at high engine load.

To place this optimisation in context with conventional diesel combustion, Figure 5.37 depicts the achieved ADF optimised setup for maximum NOx reduction in the left-hand graph, while the right-hand graph provides a comparative analysis of NOx emissions per engine load between the ADF baseline and the optimised ADF configuration, both shown relative to the CDC operation. The results are presented as percentage changes in NOx emissions.

As discussed in Section 5.3, the ADF baseline – defined by increasing the H2EF up to 70% at low and medium engine loads and 36% at high load – led to a 15–17% rise in NOx emissions at low and medium loads. At high load, however, NOx emissions decreased slightly (by about 5%), likely due to the lower hydrogen substitution achievable under those conditions. Figure 5.37 reinforces the need for further optimisation of the ADF baseline to effectively control NOx emissions. In this context, the optimised configuration of ADF demonstrates significant potential relative to CDC, achieving NOx reductions exceeding 50% at low and medium loads, and approximately 25% at high load.

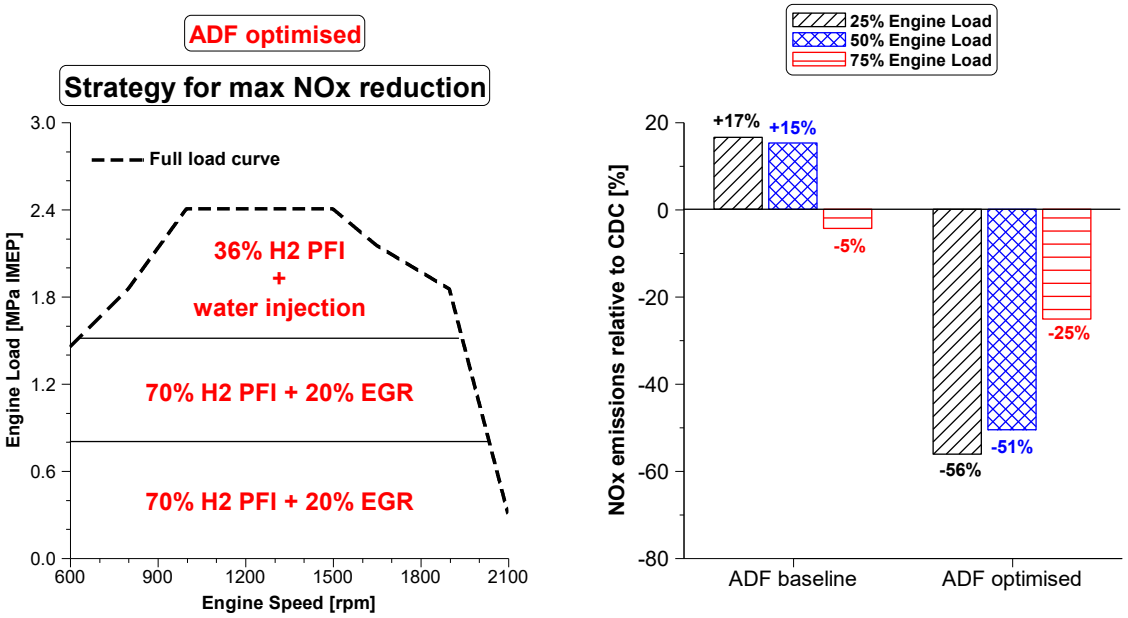

Figure 5.37. Comparison of NOx emissions between the ADF baseline and ADF optimised relative to CDC, and identification of the most effective ADF optimised strategy for NOx mitigation.

Overall, controlling NOx emissions is a critical aspect of diesel-hydrogen dual-fuel operation, as increasing the hydrogen content in the mixture has been demonstrated to elevate NOx formation. Therefore, implementing mitigation strategies – such as external EGR at low and medium engine loads, and water injection at high load – proved to be effective in optimising combustion. These approaches enabled NOx reductions of up to 56% compared to conventional diesel operation, highlighting their potential for improving the environmental viability of this advanced dual-fuel system.

5.8 Summary

In this chapter, experiments were conducted to characterise and optimise diesel-hydrogen dual-fuel combustion at a constant engine speed of 1200 rpm, with loads varying from 0.6 to 1.8 MPa IMEP, covering low to high load conditions. The primary objective of this study was to reduce overall GHG emissions while maintaining high engine efficiency. A comparative evaluation between conventional (CDF) and advanced dual-fuel (ADF) combustion strategies – based on effective compression ratio variation – was undertaken to assess the influence on hydrogen energy fraction. The focus then shifted to exploring the ADF baseline's potential for maximising the use of hydrogen. Further optimisation targeting both increased hydrogen substitution and NOx emissions reduction was carried out through three strategies: increasing the relative air–fuel ratio, employing external EGR, and introducing water injection in the intake line. Finally, an overview assessment of optimal dual-fuel operation relative to conventional diesel combustion was presented, highlighting strategies for maximising hydrogen use, minimising NOx formation, and reducing GHG emissions. The latter included a Well-to-Wheel analysis to evaluate the broader environmental viability of the proposed solution under various hydrogen production pathways.

The primary findings of the diesel-hydrogen dual-fuel operation using different ECRs and exploring hydrogen substitution are as follow:

- CDF (Conventional Dual Fuel) mode at a higher ECR produced 1-3% higher peak in-cylinder pressures than CDC (Conventional Diesel Combustion), and

considerably higher ADF (Advanced Dual Fuel) operation with a similar H2EF, which resulted in smaller loss of thermal efficiency than ADF relative to CDC. The maximum H2EF was limited 32% at low load and 20% at higher engine loads. This limitation was caused by the poor combustion stability. At low engine load, COV_{IMEP} reached approximately 8% when achieving 32% H2EF, while at medium and high loads, it remained consistently above 3% for H2EF levels exceeding 20%. This instability severely limited the potential for higher diesel replacement, which resulted in limited CO_2 reduction.

- ADF combustion achieved with a lower ECR via the Miller cycle strategy using LIVC approach, demonstrated the potential for considerably higher hydrogen energy fractions than CDF, regardless of the engine load. Thus, the highest achievable H2EF was 70% at low and medium loads, and 36% at high load. The lower threshold at high load reflects a reduced margin before reaching safety and mechanical durability constraints.

- ADF provided better hydrogen fuel conversion efficiency across all engine loads than CDF, due to considerably lower hydrogen slip. However, the high hydrogen substitution reduced ITE compared to CDC, with the highest H2EF causing a 5% drop in ITE at low and medium loads and 4% at high loads. While ADF mode consistently increased EGT compared to CDF, further H2EF increases had little impact on exhaust temperature.

- When compared to CDC, ADF reduced CO_2 emissions by up to 56% at low and medium loads. At high load, the CO_2 reduction was limited to 28%. At low and medium loads, CO emissions were cut by 80% and 59%, while THC were lowered by 47% and 31%, due to higher diesel substitution. In contrast, high load conditions showed low sensitivity to changes in CO and HC emissions.

- Another benefit of ADF is the overall reduction in soot emissions relative to CDC, regardless of engine load conditions. Soot levels were observed to decrease by 65%, 51%, and 68% at low, medium, and high loads, respectively, with absolute values ranging between 1.1–4.6 mg/kWh.

- N_2O emissions showed a clear reduction trend with the addition of hydrogen at all engine loads analysed, reaching 6 mg/kWh representing a 75% reduction at both low and medium loads. Nonetheless, at high engine load, the reduction was lower, only 30%, reaching approximately 16 mg/kWh.

- Reducing GHG emissions is primarily determined by CO_2 mitigation, as the contribution of N_2O remains relatively low. Therefore, effective combustion control enables higher H2EF, which in turn enhances CO_2 emissions reduction.

- On the other hand, NOx emissions increased by 1.6-1.7 g/kWh, representing a 16% rise. As a result, NOx emissions ranged between 11.1–13.1 g/kWh across the different operating conditions

The primary findings of the optimisation of ADF using increased relative-air fuel ratio, external EGR, and water injection were as follow:

- Increasing λ by boosting intake pressure led to higher in-cylinder pressure and temperature during the compression stroke. However, the increase cylinder mass and heat capacity resulted in lower PRR, delaying and reducing peak HRR, particularly at high loads. This provided a margin to increase the H2EF by an additional 7% at high load – reaching 43% diesel replacement, resulting in a total CO_2 reduction of 36%, 8% more than the ADF baseline offered.

- The impact of λ variation was found to be load-dependent, with ITE slightly improving at low and high loads but decreasing at medium load. NOx decreased at low and medium loads (by 15–17% relative to the ADF baseline) but rose at high load. CO_2 emissions showed no consistent trend across the load range. Furthermore, higher λ values (above 2) led to a slight increase in unburned THC and a substantial rise in hydrogen slip, while EGTs consistently declined with increasing λ.

- The use of eEGR combined with a high hydrogen energy fraction proved to be an effective solution for NOx control – above 50% reduction when compared to CDC – without compromising engine performance. Nonetheless, there is a deterioration in soot and CO emissions.

- Water injection at high load increased peak in-cylinder pressure and advanced the heat release, indicating earlier combustion phasing. The resulting lower combustion temperatures slowed the burn rate as combustion progressed, which contributed to improved combustion stability. ITE was improved by over 2% compared to the ADF baseline. Emission-wise, NOx was reduced by 22%, while CO_2 and CO decreased by 5% and 21%, respectively.

Overall, the advanced diesel-hydrogen dual-fuel combustion demonstrated that it can effectively reduce CO_2 emissions by up to 58%, exceeding the 45% reduction target of CO_2 set for 2030 in the updated EU CO_2 regulation [31] – potentially enabling this solution to operate until end of 2034. It also offers significant reductions in other carbon-based pollutants, highlighting its short-term potential. Furthermore, the WTW analysis revealed that when fuelled with blue or green hydrogen, the ADF strategy presents a viable pathway to support climate change mitigation efforts and promote a more sustainable energy solution for the transportation sector.

Chapter 6
Multi-fuel comparison in dual-fuel operation from low to high engine load

This chapter presents a comparative assessment of various dual-fuel strategies tested on the same single-cylinder heavy-duty research engine across a wide range of engine loads – 0.6, 1.2, and 1.8 MPa IMEP – corresponding to 25%, 50%, and 75% of the total engine load, respectively. The analysis focuses on four combustion systems configurations: diesel-only, diesel-CNG, diesel-hythane, and diesel-hydrogen, thereby enabling a clear evaluation of the influence of each gaseous fuel.

The dual-fuel configurations using hythane and hydrogen were experimentally investigated as part of this research project, and their detailed analysis was presented in the preceding chapters. In contrast, the CNG data were sourced from a separate study conducted by another researcher using the same experimental engine setup. Although not part of the current project's test campaign, the CNG results, which were published in a peer-reviewed study [120], and are incorporated here to enable a broader and more complete fuel comparison under consistent engine hardware and test boundary conditions.

The objective is to evaluate and contrast the performance and emissions characteristics of each fuel – specifically indicated thermal efficiency, CO_2 and total GHG emissions, and NOx emissions – when used as the gaseous component in diesel-based dual-fuel operation. This comparison aims to assess the viability of these low-carbon alternatives in replacing conventional diesel systems for future heavy-duty applications, particularly in terms of their GHG mitigation potential. The sequence of this analysis intentionally follows a progression from lower-carbon to zero-carbon fuels, enabling a systematic evaluation of how incremental shifts toward decarbonised gaseous fuels influence engine performance and environmental outcomes in dual-fuel operation.

To complement the GHG emissions data, a Well-to-Wheel (WTW) analysis is included to evaluate the environmental impact of each fuel, taking into account not only engine operation but also upstream emissions associated with fuel production and delivery. This provides a more holistic view of the GHG reduction potential for each fuel pathway. The WTW results presented in this chapter are a consolidated comparison, combining the analyses previously discussed in Chapter 4 for hythane and Chapter 5 for hydrogen, along with data compiled for CNG fuel [120].

The first key aspect when assessing dual-fuel performance is determining the maximum diesel replacement that can be achieved, as this directly impacts the range of GHG emissions reductions. Figure 6.1 illustrates the maximum energy fraction achievable by each dual-fuel system operating in advanced dual-fuel mode with lower ECR via the LIVC strategy.

It is clear that increasing the hydrogen content in the dual-fuel combustion leads to a reduction in total energy substitution rate by the port injected gaseous fuel. This trend is tied to the faster combustion of hydrogen and hence greater heat release rate, causing engine hardware limitations to be reached sooner as more energy is supplied by the premixed fuel in place of the directly injected diesel. This effect becomes more pronounced at higher engine loads, where the energy fraction decreases further.

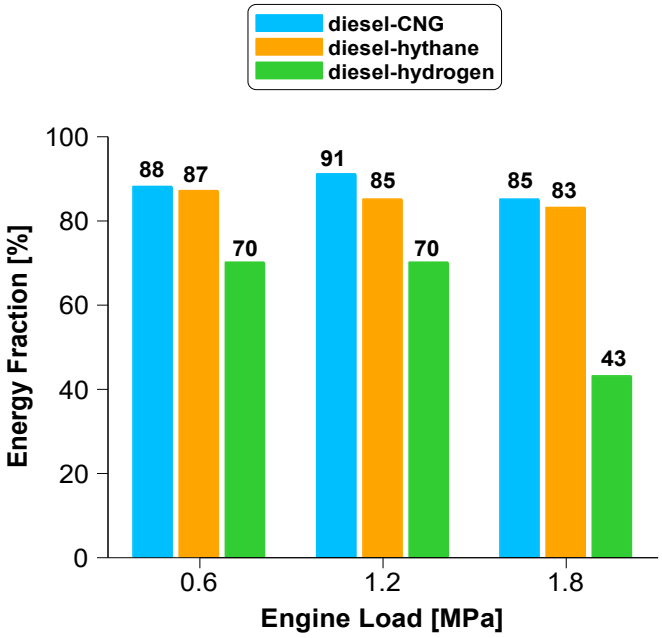

Figure 6.1. Maximum achievable energy fraction for each dual-fuel system at different engine loads.

Building on the maximisation of diesel replacement, it is noteworthy that the baseline energy substitution selected by Pedrozo et al. [120] was 80% on an energy basis. In contrast, the current study selected 76% energy substitution for the baseline diesel-hythane system, while the baseline diesel-hydrogen systems ranged between 36-70% energy substitution.

Table 6.1 summarises the engine operating conditions for the different combustion configurations investigated in this chapter. All dual-fuel cases are baseline configurations without additional optimisation, allowing a clearer isolation of fuel effects in the comparison. Moreover, it is important to note that only advanced dual-fuel combustion strategies were used for dual-fuel systems in this assessment, which fundamentally consists in the reduction of ECR via LIVC strategy.

Table 6.1. Engine operating conditions for the different dual-fuel systems.

Parameter	Unit	diesel-only	diesel-CNG	diesel-hythane	diesel-hydrogen
IMEP	MPa	0.6 – 1.8	0.6 – 1.8	0.6 – 1.8	0.6 – 1.8
Engine speed	rpm	1200	1200	1200	1200
Energy fraction	%	0	80	76	36 - 70
ECR	-	16.8	14.8	14.8	14.8
Intake air temperature	°C	40 - 43	42 - 44	40 - 43	40 - 43
Intake air pressure	kPa	125 - 260	125 - 260	125 - 260	125 - 260
Exhaust pressure	kPa	135 - 270	135 - 270	135 - 270	135 - 270
eEGR	%	0	0	0	0
iEGR	%	0	0	0	0
Water injection	-	No	No	No	No
Gas injection pressure	MPa	-	0.8	0.8	0.8
Diesel injection pressure	MPa	100 - 160	100 - 160	100 - 160	100 - 160
Diesel injection type	-	Non-premixed	Premixed	Premixed	Non-premixed

An additional key aspect to highlight is the variation in the diesel injection strategy employed across the different dual-fuel systems. The diesel-CNG and diesel-hythane configurations utilised a premixed combustion strategy, commonly referred to as

Reactivity-Controlled Compression Ignition (RCCI), which was achieved through an early split diesel injection. In contrast, due to safety concerns and timeframe limitation as approached in Chapter 5, the diesel-hydrogen configuration employed a non-premixed, conventional late diesel injection strategy near TDC. This difference in injection strategies could potentially influence the NO_x emissions, as the combustion characteristics for each system are distinct.

To ensure a reasonable comparison, the general test conditions – including engine load and speed, intake air temperatures, and fuel injection pressures – were strictly maintained the same between all dual-fuel systems.

The first metric compared across the different combustion systems is the indicated thermal efficiency at various engine loads, as shown in Figure 6.2.

Diesel-hythane operation generally exhibited the highest efficiency among the dual-fuel systems at low and medium loads, with an improvement of approximately 3% (absolute) at low load relative to CDC. At high load, the diesel-CNG dual-fuel configuration demonstrated the closest efficiency to CDC. In contrast, diesel-hydrogen showed the lowest efficiency across all loads, with reductions of 6%, 5%, and 4% at low, medium, and high loads, respectively, relative to diesel-only operation.

This performance gap can be attributed to differences in diesel injection strategies between diesel-hydrogen and the other two dual-fuel systems. While all dual-fuel configurations employed an advanced combustion approach through reduced effective compression ratio, only diesel-CNG and diesel-hythane utilised an early split diesel injection strategy. This approach is more effective at promoting a more homogeneous in-cylinder charge, thereby improving fuel conversion efficiency. In the case of diesel-hydrogen, a split late injection strategy near TDC was used due to safety concerns and time constraints in the current project.

Implementing a similar early injection approach could potentially narrow the efficiency gap between diesel-hydrogen and the other dual-fuel systems.

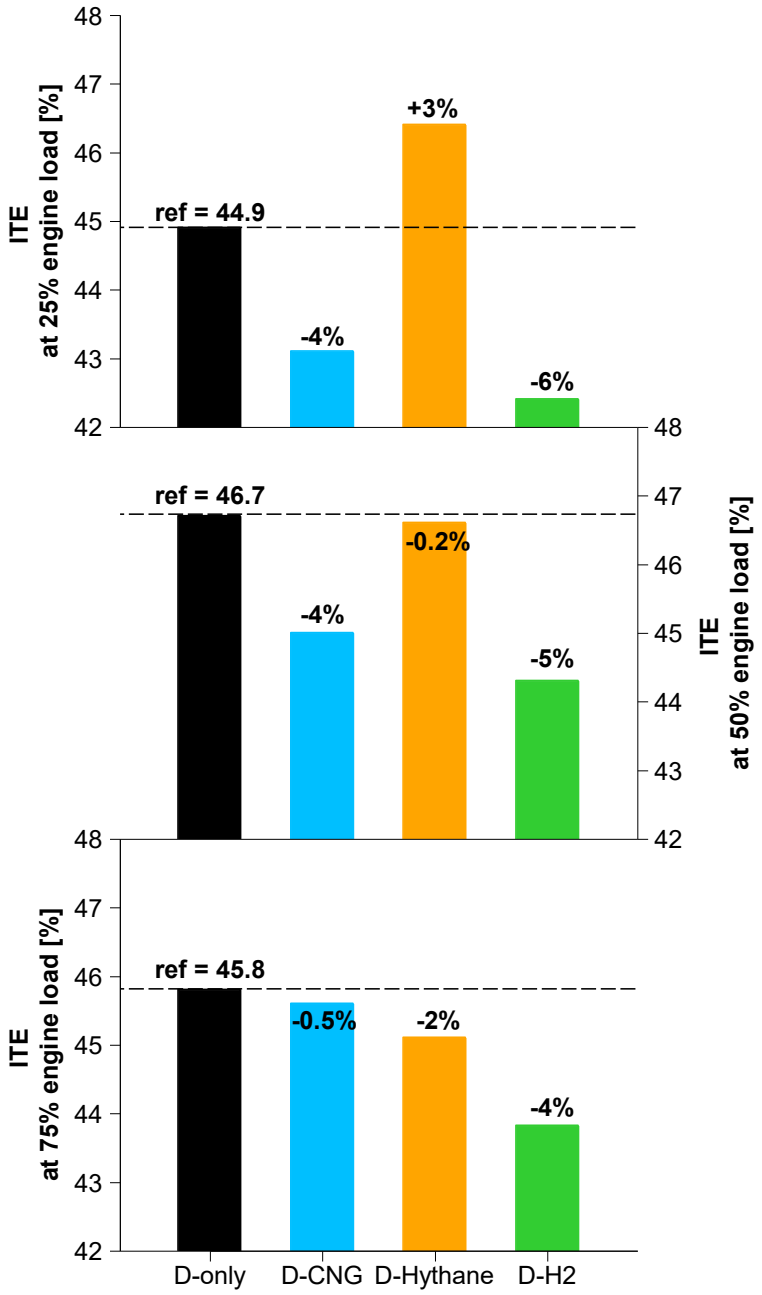

Figure 6.2. Indicated thermal efficiency of the combustion systems (diesel-only, diesel-CNG, diesel-hythane, and diesel-hydrogen) at low (top), medium (middle), and high (bottom) engine loads.

With regard to carbon emissions, Figure 6.3 illustrates the evolution of indicated specific CO_2 and total GHG emissions when replacing diesel with low- and zero-carbon fuels across the tested engine loads.

A clear trend is observed: diesel substitution with alternative gaseous fuels containing progressively lower carbon content leads to a gradual and effective reduction in CO_2 emissions.

The dual-fuel configuration using CNG achieved a total CO_2 reduction between 5% and 18%, depending on engine load. Diesel-hythane in-cylinder charge which included approximately 16% hydrogen on an energy basis, further enhanced this reduction, yielding CO_2 decreases ranging from 28% to 37%. This result demonstrates the decarbonisation potential of hythane for short-term applications.

Notably, the baseline diesel-hydrogen system – despite exhibiting the lowest diesel replacement among the dual-fuel configurations – achieved the greatest CO_2 reduction, ranging from 28% to 56%. This highlights the significant decarbonisation potential of hydrogen, even at moderate substitution levels. Importantly, this makes diesel-hydrogen the only configuration capable of meeting the 45% CO_2 reduction target set for 2030 under the updated EU CO_2 regulation [31], potentially allowing this solution to remain in operation until the end of 2034. However, further optimisation is still needed, particularly at high engine loads, as discussed in detail in Chapter 5.

However, a substantial reduction in CO_2 emissions does not always correspond to a reduction in overall GHG levels. This is particularly evident in dual-fuel configurations involving methane. In the diesel-CNG case, for example, a CO_2 reduction of 18% at low load resulted in a 10% increase in total GHG emissions compared to CDC.

This counterproductive effect is primarily due to methane slip – a known issue with methane-based systems – as CH_4's GWP is 27 times greater than that of CO_2 over a 100-year period [28]. Therefore, strict control of methane slip is essential for CNG and hythane systems to ensure that their CO_2 benefits are not offset by elevated GHG emissions.

Nevertheless, despite the impact of methane slip, the hythane configuration still demonstrated an effective GHG reduction of approximately 25% relative to diesel-only operation, proving to be a viable solution for short-term implementation.

It is important to note, however, that this GHG reduction may be slightly overestimated, since hydrogen's GWP – estimated to be 11 times greater than that of CO_2 over a 100-year lifetime [177] – has not been included in this calculation. This is because hydrogen slip was not measured during the diesel-hythane dual-fuel experiments.

On the other hand, hydrogen combustion is often associated with the formation of N_2O, a potent greenhouse gas with a GWP 273 times greater than that of CO_2 over a 100-year period [28]. However, as discussed in Chapter 5, the diesel-hydrogen configuration demonstrated residual levels of N_2O emissions.

Moreover, the low hydrogen slip measured during the diesel-hydrogen dual-fuel experiments resulted in negligible impact on GHGs. This outcome allowed GHG reduction potential to closely align with the observed CO_2 reduction, effectively maximising the climate benefits of hydrogen dual-fuel combustion and reinforcing its viability as a solution for short- and medium-term carbon footprint reduction.

Finally, it is relevant to note that CO_2 reductions tend to diminish as engine load increases. This occurs because higher loads improve thermodynamic conditions, leading to more efficient fuel conversion and more complete combustion, which in turn results in higher absolute CO_2 emissions from fuel oxidation.

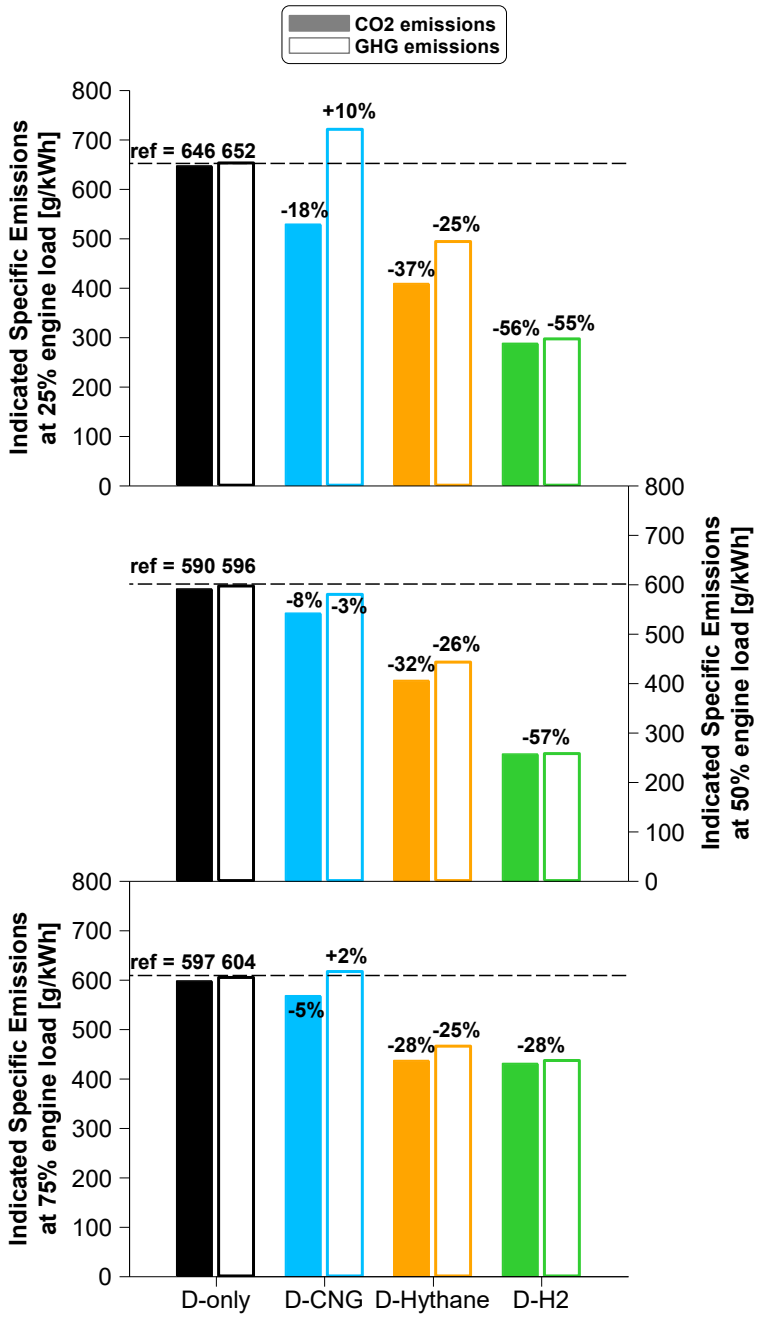

Figure 6.3. Comparison of indicated specific CO_2 and total GHG emissions for the combustion systems (diesel-only, diesel-CNG, diesel-hythane, and diesel-hydrogen) at low (top), medium (middle), and high (bottom) engine loads.

To provide a broader perspective on the impact of alternative fuels, a WTW analysis is presented, encompassing diesel, CNG, hythane, and hydrogen. This analysis includes both the Well-to-Tank (fuel production) and Tank-to-Wheel (engine operation) stages, following the methodology outlined in Section 4.5.3 of Chapter 4.

WTW emissions are expressed in grams of CO_{2eq} per MJ of fuel energy injected. Figure 6.4 presents the results for conventional diesel and dual-fuel combustion configurations based on fossil fuel pathways (grey and blue), including percentage differences relative to the diesel-only baseline. In contrast, Figure 6.5 illustrates the results for dual-fuel combustion systems utilising renewable fuel pathways (green), also showing percentage reductions compared to diesel-only mode to better highlight the potential impact of each decarbonisation strategy.

To provide a clearer understanding of each alternative fuel considered, Table 6.2 presents the estimated WTT CO_{2eq} emissions and associated sources for diesel and the various low-carbon fuel pathways.

Table 6.2. Estimated Well-to-Tank CO_{2eq} emissions for diesel and multiple alternative low-carbon fuel production pathways.

Fuel	Unit	WTT	Source
Diesel	gCO_{2eq}/MJ	18.9	Current fossil fuel [195]
Grey CNG	gCO_{2eq}/MJ	15.1	CNG coming from South West Asian locations with transport distance of 4000 km [195]
Green CNG	gCO_{2eq}/MJ	2.4	Synthetic CBM obtained from renewable electricity [195]
Grey hydrogen	gCO_{2eq}/MJ	113.0	SMR, natural gas feedstock [195]
Blue hydrogen	gCO_{2eq}/MJ	50.0	SMR with retrofit CCS, natural gas feedstock [202]
Green hydrogen	gCO_{2eq}/MJ	9.5	Electrolysis using renewable energy from wind and solar sources [195]
Grey hythane	gCO_{2eq}/MJ	21.9	Grey CNG and hydrogen
Green hythane	gCO_{2eq}/MJ	2.9	Green CNG and hydrogen

Figure 6.4 illustrates that among fossil-derived fuel combinations, the diesel-blue hydrogen configuration achieved the most significant GHG emissions reductions at low and medium loads, with decreases of 28% and 26%, respectively, compared to conventional diesel operation. At high load, the diesel-grey hythane setup offers the

highest reduction, reaching an 18% decrease in GHG emissions. The diminished effectiveness of blue hydrogen at high load may be attributed to a reduced gas energy fraction, constrained by the engine's operational limits.

Conversely, grey hydrogen produced via conventional SMR without CCS led to an increase in WTW GHG emissions at all loads of up to 19%, despite reductions observed during engine operation.

The diesel-CNG configuration provided only modest GHG mitigation, with reductions up to 9% across the cycle. Notably, at low engine load, this configuration leads to an increase in GHG emissions at low load, primarily due to low fuel conversion efficiency at these engine conditions. This outcome highlights the importance of considering the full fuel lifecycle as well as controlling methane slip control on decline these emissions, since high gas energy substitution does not necessarily translate to substantial GHG reductions.

Figure 6.5 depicts the WTW assessment for the conventional diesel baseline compared to renewable-derided fuel combinations, namely green CNG, green hythane, and green hydrogen, as outlined in Table 6.2.

The diesel–green hydrogen configuration proved to be the most effective in significantly reducing GHG emissions across all engine loads. The greatest reductions were observed at low and medium loads, reaching up to 56% relative to conventional diesel-only operation. At high load (75% of full engine capacity), the GHG reduction was less pronounced, reaching 35% reduction, primarily due to limited gas energy fraction obtained at such conditions. Nevertheless, this still marginally outperformed the hythane dual-fuel configuration.

The green CNG configuration, represented in this study as synthetic CBM, resulted in more modest GHG reductions – up to 20% compared to diesel-only operation – which is less than half of the potential offered by the diesel-green hydrogen system.

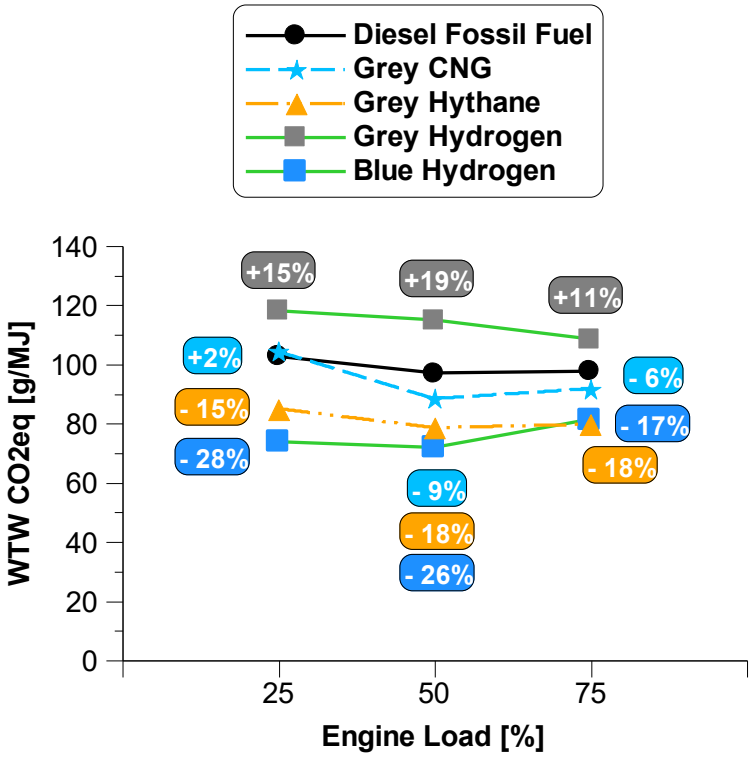

Figure 6.4. Well-to-Wheel assessment involving diesel and multiple alternative fuel production pathways from fossil sources.

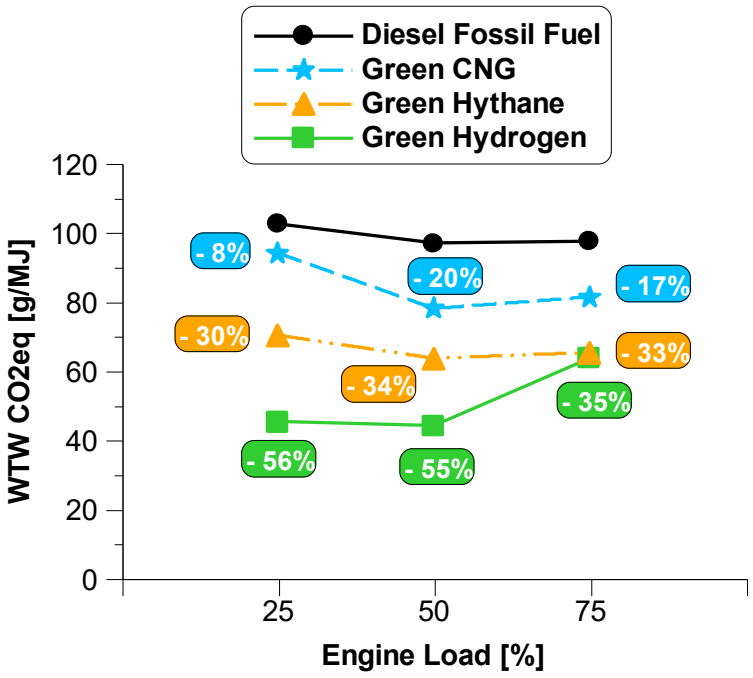

Figure 6.5. Well-to-Wheel assessment involving diesel and multiple alternative fuel production pathways from renewable sources.

The last topic of this chapter is the evaluation of NOx emissions for the different combustion systems at various engine loads. Figure 6.6 illustrates the evolution of indicated specific NOx emissions when replacing diesel with low- and zero-carbon fuels across the tested engine loads.

A clear trend was observed: the addition of hydrogen had a negative impact on NOx emissions. The diesel-hydrogen dual-fuel configuration produced the highest NOx levels among the dual-fuel systems, often matching or exceeding the NOx output of the diesel-only baseline. Compared to CDC, the diesel-hydrogen dual-fuel combustion produced 15-16% higher NOx emissions at low and medium loads, while similar concentrations at high load.

In contrast, both diesel-CNG and diesel-hythane operations exhibited significantly lower NOx emissions compared to conventional diesel, achieving reductions of over 80% at low load and above 40% at other loads.

While methane – the primary component in both operations – has a lower flame speed and leads to lower combustion temperatures compared to diesel and hydrogen, the primary reason behind these reductions was likely the alternative diesel injection strategy employed. Specifically, the early split injection used in these configurations promoted better premixing of the in-cylinder charge, leading to a more homogeneous mixture and, consequently, lower combustion temperatures and NOx formation.

Therefore, the diesel-hydrogen system could potentially benefit from adopting a similar diesel injection strategy to mitigate NOx emissions. Additional strategies for NOx reduction, such as the use of external EGR or water injection – discussed in Chapter 5 – also present promising option for in-cylinder NOx control.

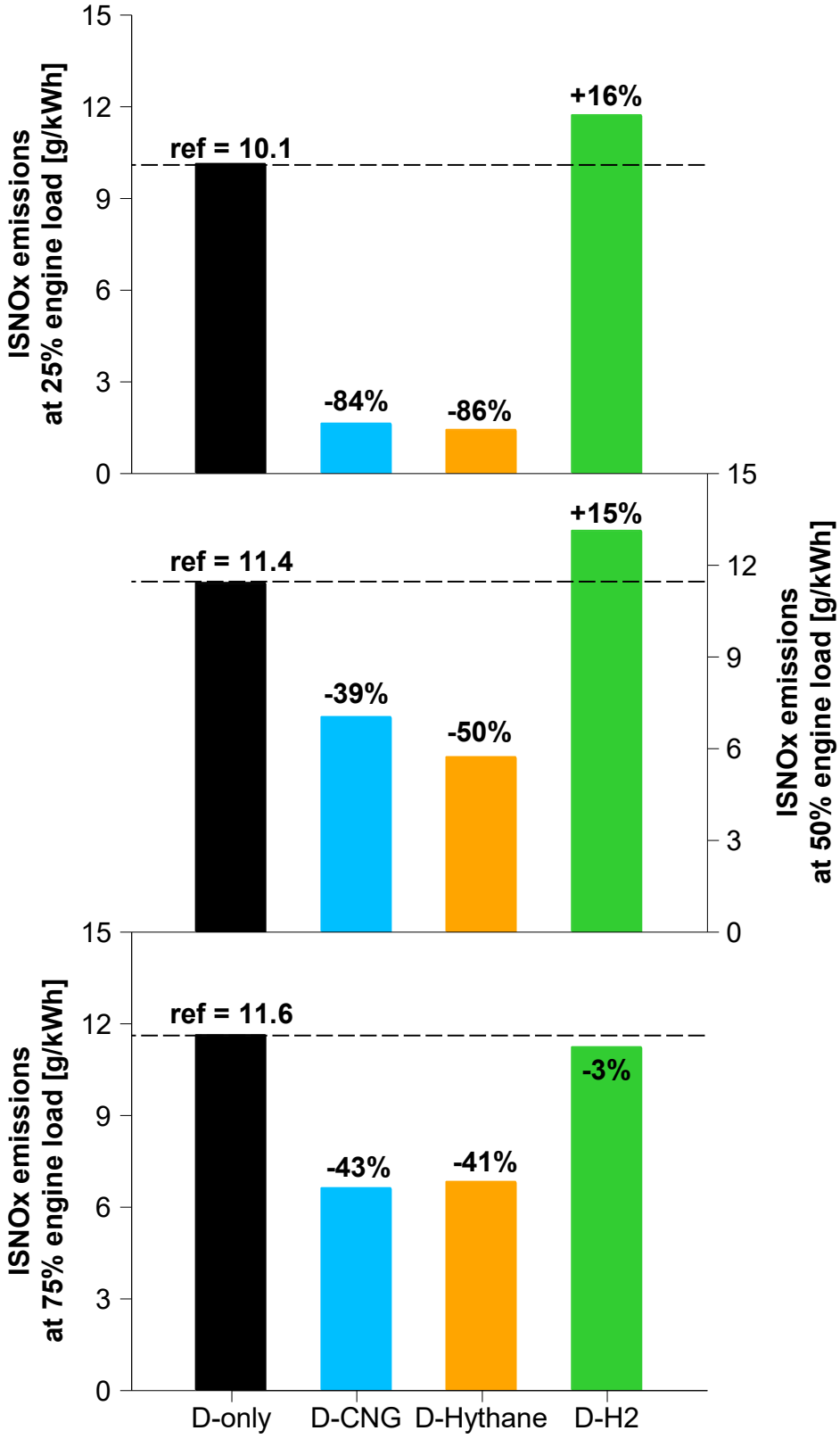

Figure 6.6. Indicated specific NOx emissions of the combustion systems at low (top), medium (middle), and high (bottom) engine loads.

This chapter provides a comprehensive comparison between conventional diesel operation and three dual-fuel configurations (diesel-CNG, diesel-hythane, and diesel-hydrogen), all tested on a single-cylinder heavy-duty engine across multiple engine loads. The analysis covers key performance metrics, including indicated thermal efficiency, CO_2 and total GHG emissions, and NOx emissions.

The primary findings from comparing conventional diesel combustion and dual-fuel operations in terms of engine efficiency and emissions are as follow:

- Diesel-CNG, although allowing the highest gas energy fraction among the dual-fuel configurations evaluated, delivered the least CO_2 reduction potential. Moreover, its CO_2 benefits were easily offset by elevated methane slip, limiting its overall effectiveness as a decarbonisation strategy.

- Diesel-hythane configuration demonstrated the best thermal efficiency and significant CO_2 reductions (28% to 37%). Total GHG emissions are, however lower due to the offset of methane slip, but still proving a GHG reduction of around 25% compared to diesel-only operation, showcasing its potential for decarbonisation in short-term applications.

- Diesel-hydrogen, despite lower diesel replacement levels, achieved the highest CO2 reduction (28% to 56%). Additionally, the overall GHG reduction potential closely matched CO_2 reduction, since this solution produced residual N_2O emissions. This reinforces the viability of diesel-hydrogen as a promising solution for medium-term carbon footprint reduction.

- The WTW assessment highlighted the importance of considering both fuel production and engine operation stages, with green hydrogen showing the most significant GHG reductions among renewable pathways, cutting full life-cycle GHG emissions by more than half compared to the conventional diesel solution.

- CH_4-based configurations (diesel-CNG and diesel-hythane) showed substantial reductions in NOx emissions – over 80% at low 40% at other loads – with a more advanced diesel injection strategy primarily contributing to the reduction. In contrast, the addition of hydrogen had a negative impact on NOx emissions.

In conclusion, while each alternative fuel demonstrated unique strengths and limitations, hythane and hydrogen configurations offer substantial potential in short- and medium-term decarbonisation, respectively, without considerably compromising engine performance.

Chapter 7
Conclusions and future work

Following a review of both experimental and modelling research on high-efficiency compression ignition engines, a single-cylinder heavy-duty engine and its fuelling systems were updated to achieve diesel-only, and diesel-hythane and diesel-hydrogen dual-fuel combustion modes. The experiments were carried out at a constant engine speed of 1200 rpm**,** across three load conditions: 0.6, 1.2, and 1.8 MPa IMEP**,** representing 25%, 50%, and 75% of the total engine load**,** respectively. Conventional and advanced combustion modes—based on variation of the effective compression ratio and multiple diesel injection strategies—were explored to achieve high efficiency and minimise exhaust emissions during dual-fuel operation. Alternative strategies were also proposed to address the challenges associated with fuel characteristics and to expand the operating range of dual-fuel systems. The findings and recommendations from this study are outlined below.

7.1 Conclusions

7.1.1 Diesel-hythane dual-fuel combustion

The diesel-hythane dual-fuel combustion study demonstrated that advanced dual-fuel (ADF) operation, combining early diesel injection with lower effective compression ratio (ECR) via employment of a late intake valve closure (LIVC), significantly enhanced combustion efficiency and reduced emissions compared to both conventional diesel combustion (CDC) and conventional dual-fuel (CDF) strategies, which employed a conventional diesel injection near top dead centre (TDC) and higher ECR. The ADF strategy enabled up to 87% diesel replacement with hythane at low loads, 85% at medium load, and 83% at high load, while improving indicated thermal efficiency (ITE) – by 17% at low load and up to 2.5% at medium load – over CDF mode. These gains were attributed to faster and more complete combustion near TDC, particularly at low and medium loads.

The ADF mode also delivered considerable emissions reductions. It reduced CO_2 emissions by up to 40% and total GHG emissions by 25% compared to CDC, with Well-to-Wheel (WTW) reductions reaching 34% when green hythane was used. NOx emissions were dropped by up to 89% at low load and remained significantly lower than CDC and CDF at all load conditions. Soot emissions were also reduced by up to 69%, and CO emissions by 72%, thanks to leaner, more homogeneous combustion. However, methane slip, particularly at low loads, remained a key challenge, limiting the full GHG benefit. Even so, ADF consistently outperformed CDF in GHG terms across all operating conditions.

To further optimise the ADF strategy, internal exhaust gas recirculation (iEGR) and external exhaust gas recirculation (eEGR) were explored. At low loads, iEGR improved combustion efficiency by increasing in-cylinder temperatures and promoting CO and CH_4 oxidation, while also raising EGTs above the catalysts light-off temperature threshold. When combined with eEGR, even greater reductions in methane slip and CO were achieved, resulting in an 11% total GHG reduction at low load compared to baseline ADF. Meanwhile, eEGR at medium and high loads helped to reduce NOx emissions and control excessive pressure rise rates – without compromising combustion stability – though this came at the cost of slightly higher GHG emissions due to increased CO_2 output.

From a practical standpoint, the ADF strategy – with high hythane energy fraction and optimised diesel injection – offers lower total fluid consumption of fuel and urea and reduced reliance on aftertreatment systems (ATS), especially at low loads where NOx targets may be met without SCR. This translates into lower operational costs, making diesel-hythane ADF an effective pathway for decarbonising heavy-duty transport when clean hythane is available.

7.1.2 Diesel-hydrogen dual-fuel combustion

The diesel-hydrogen dual-fuel combustion study showed that the ADF strategy, which used a lower ECR via a Miller cycle, allowed for significantly higher hydrogen substitution compared to the CDF mode. In ADF operation, the hydrogen energy

fraction (H2EF) reached up to 70% at low and medium loads, and up to 43% at high load after optimising the relative air-fuel ratio (λ). By contrast, CDF was limited to a maximum of 32% at low load and 20% at medium and high loads due to combustion instability. Although ADF resulted in a 4-5% reduction in thermal efficiency relative to CDC, it delivered better combustion efficiency than CDF, primarily due to significantly lower hydrogen slip.

The ADF mode resulted in substantial reductions in carbon-based emissions. CO_2 emissions decreased by up to 56% at low and medium loads – exceeding the 45% reduction target set for 2030 in the updated EU CO_2 regulation – and by 36% at high load after optimisation. Significant reductions were also achieved in carbon monoxide (up to 80%), total hydrocarbons (up to 47%), and soot (up to 68%) due to the reduced diesel input and enhanced mixture homogeneity. Nitrous oxide (N_2O) emissions dropped by as much as 75% at low and medium loads, with only moderate reductions observed at high load. In contrast, NOx emissions increased by 16% in the ADF baseline as a result of higher in-cylinder temperatures associated with greater hydrogen content.

To mitigate NOx emissions while preserving performance, three optimisation strategies were evaluated. eEGR proved most effective at low and medium loads, reducing NOx by over 50% without compromising indicated efficiency. At high load, water injection reduced NOx by 22% and improved thermal efficiency by 2.2%. Increasing λ also contributed to NOx reduction at low and medium loads (by 15–17%) and allowed for an additional 7% increase in H2EF at high load.

A WTW analysis confirmed that the climate benefit of this dual-fuel strategy depends strongly on hydrogen sourcing: green hydrogen enabled up to a 56% reduction in total GHG emissions relative to CDC, whereas grey hydrogen increased them. Overall, diesel-hydrogen dual-fuel combustion – especially under advanced operating strategies – offers strong potential for decarbonising heavy-duty transport, provided emissions control and hydrogen production pathways are carefully managed.

7.1.3 Multi-fuel comparison in dual-fuel operation

This final comparison chapter assessed diesel-only operation against three baseline dual-fuel configurations – diesel-CNG, diesel-hythane, and diesel-hydrogen – under identical engine conditions to evaluate their relative performance and emissions characteristics.

Among the options, diesel-hythane offered the best balance between efficiency and emissions. It delivered the highest thermal efficiency at low and medium loads and achieved notable CO_2 reductions (28–37%) with moderate GHG mitigation (~25%), despite some methane slip. Its NOx emissions were also significantly lower than diesel-only operation across all loads.

Diesel-hydrogen showed the highest potential for CO_2 and GHG reduction (up to 56%), successfully exceeding the EU's 2030 CO_2 reduction target. However, its thermal efficiency was lower due to the conventional late injection strategy employed, and NOx emissions increased, especially at low and medium loads. These trade-offs could be managed with further optimisation using eEGR and water injection.

Diesel-CNG, while allowing the highest diesel replacement, offered the least favourable results overall. Methane slip limited its GHG reduction potential, and at low load, it even increased total GHG emissions. However, it still achieved meaningful NOx reductions due to its early injection strategy.

In summary, diesel-hythane stands out as a strong short-term solution, offering a solid balance of efficiency and emissions benefits, while diesel-hydrogen holds the greatest promise for medium-term decarbonisation, provided NOx control and combustion strategies are further refined.

7.2 Recommendations for future work

From the present research, it is concluded that there is still room for further improvements, particularly in the diesel-hydrogen dual-fuel system. The following areas are recommended for future investigation:

- Exploration of early diesel injection strategies within diesel-hydrogen operation to enable reactivity-controlled compression ignition, with the aim of lowering NOx emissions while maintaining combustion stability.

- Modelling of the diesel-hythane and diesel-hydrogen dual-fuel combustions in order to capture the underlying thermodynamic and chemical kinetic mechanisms, and to provide clear insight into the combustion behaviour observed with the advanced dual-fuel strategies presented in this thesis.

- Experimental validation on a multi-cylinder turbocharged engine**,** across a wider range of engine speeds and loads, to assess the real-world efficiency and emissions performance of the dual-fuel concept under more representative conditions.

- Implementation of a gas fuel direct injection system to minimise diesel as a pilot fuel to ignite the hydrogen and other zero-carbon and carbon neutral fuels, in order to achieve simultaneous improvement in performance, efficiency and CO_2 emission by mitigate the risk of abnormal combustion at high load and incomplete combustion at low.

- Conduct a lifecycle cost and emissions assessment comparing diesel-hydrogen dual-fuel systems using bio-diesel with other decarbonisation pathways such as battery electric or fuel cell electric vehicles, especially in the heavy-duty transport sector.

Appendix A – Diesel fuel specifications

SPEEDY FUELS & LUBRICANTS

Gas Oil – EN590

Description

Gas Oil meets BS 2869 : 2017 : Class A2 and the EN590 specification. Gas oil is a dyed and marked product, and, from 1st April 2022, can only be used for HMRC permitted purposes, agriculture, horticulture, fish farming, forestry, rail, certain marine craft and non-commercial heating.

Specification

Parameter	Unit	Minimum	Maximum	Typical
Appearance	-	Clear & bright, Red. Free from visible sediment.		Pass
Density at 15°C	kg/m³	0.820	0.845	0.830
Kinematic viscosity at 40°C	mm²/s	2.0	4.5	2.90
Carbon residue (Ramsbottom on 10% residue)	% (m/m)	-	0.30(2)	<0.10
Distillation recovery at 250°C at 350°C 95% vol. recovered	 % (v/v) % (v/v) °C	 - 85 360	 65 - -	 37 93 355
Flash point (PMCC)	°C	>55	-	64
Water content	mg/kg	-	200	70
Particulate content	mg/kg	-	24	<12
Ash content	% (m/m)	-	0.01	<0.001
Sulphur	mg/kg	-	10.0	9
Copper corrosion (3 hrs at 50°C)	Class	-	1	1
Cold filter plugging point(1) Summer Winter	 °C °C	 - -	 -5 -15	 -8 -20
Oxidation stability	g/m³	-	25	5
Fatty acid methyl ester (FAME)	% (v/v)	-	7.0	6.5

Parameter	Unit	Minimum	Maximum	Typical
Cloud point(1) Summer Winter	 °C °C	 - -	 3 -5	 -2 -10
Lubricity (HFRR)	µm	-	460	390
Cetane number		51	-	53
Cetane index		46	-	55
Polycyclic aromatic hydrocarbons	% (m/m)	-	8	2.5
Carbon	% (m/m)	-	-	87
Hydrogen	% (m/m)	-	-	12.75
Nitrogen	% (m/m)	-	-	0.01 – 0.05
Gross specific energy	MJ/kg MJ/litre	- -	- -	45.4 37.7
Mean specific heat capacity over 0 - 100°C	KJ/kg°C	-	-	2.05

Notes:
1. Unless otherwise advised the following seasonal dates apply at point of sale:-
   Summer: 16th March – 15th November / Winter: 16nd November – 15th March
2. May contain an ignition improver in which case the MCR test in not valid.

Appendix B – Hythane fuel specifications

Certificate

BOC Limited
The Priestley Centre, 10 Priestley Road
The Surrey Research Park, Guildford GU2 7XY
www.BOConline.co.uk

BOC
A Member of The Linde Group

Orders and technical enquiries
Tel 0800 02 0800
Fax 0800 136 601
specialproducts@boc.com

From outside of the UK
Tel +44 1483 [illegible] 4067
Fax +44 1483 532 115

COMPONENT	NOMINAL COMPOSITION		CERTIFIED VALUE
METHANE	BAL	=	19.70 %
HYDROGEN	20 %		
At 15°C, 1013.25 millibar			
Net Wobbe number MJ	MAX	=	43.26 /M3
Net calorific value MJ	MAX	=	29.31 /M3
Gross Wobbe number MJ	MAX	=	48.27 /M3
Gross calorific value MJ	MAX	=	32.70 /M3
Relative density (Air=1)			
0.4589			

CERTIFICATE NO.: 21/012445
CERTIFICATE DATE: 10 MAY 2021
USE BY: 09 MAY 2026
APPROVED SIGNATORY Darren Powell

PROD ORDER	BARCODE NUMBER	CYLINDER NO.	MATERIAL	PAGE
2801824	21903110086844	S1664647FF	173892-L-C	1 of 2

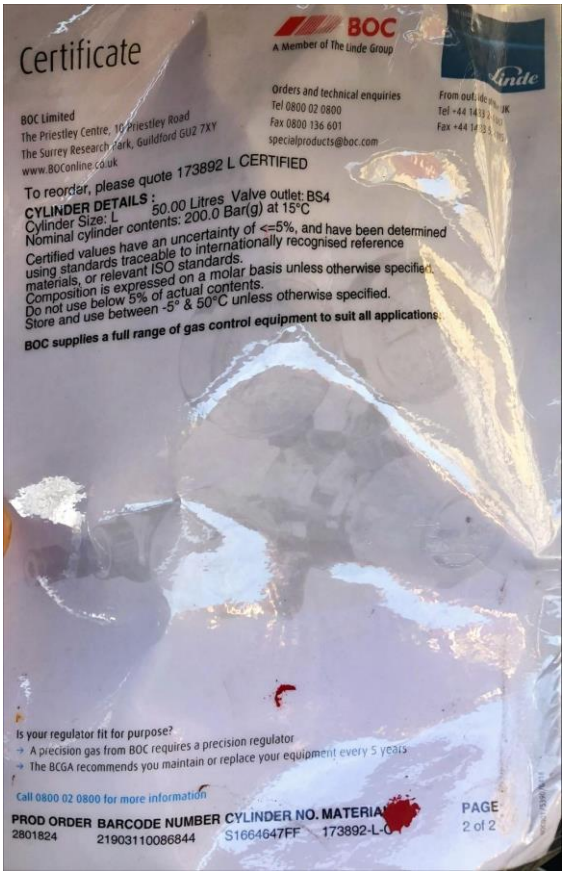

Certificate

BOC
A Member of The Linde Group

BOC Limited
The Priestley Centre, 10 Priestley Road
The Surrey Research Park, Guildford GU2 7XY
www.BOConline.co.uk

Orders and technical enquiries
Tel 0800 02 0800
Fax 0800 136 601
specialproducts@boc.com

From outside the UK
Tel +44 1483 [illegible]
Fax +44 1483 [illegible]

To reorder, please quote 173892 L CERTIFIED

CYLINDER DETAILS :
Cylinder Size: L 50.00 Litres Valve outlet: BS4
Nominal cylinder contents: 200.0 Bar(g) at 15°C
Certified values have an uncertainty of <=5%, and have been determined using standards traceable to internationally recognised reference materials, or relevant ISO standards.
Composition is expressed on a molar basis unless otherwise specified.
Do not use below 5% of actual contents.
Store and use between -5° & 50°C unless otherwise specified.

BOC supplies a full range of gas control equipment to suit all applications

Is your regulator fit for purpose?
→ A precision gas from BOC requires a precision regulator
→ The BCGA recommends you maintain or replace your equipment every 5 years

Call 0800 02 0800 for more information

PROD ORDER	BARCODE NUMBER	CYLINDER NO.	MATERIAL	PAGE
2801824	21903110086844	S1664647FF	173892-L-C	2 of 2

Appendix C – Hydrogen fuel specifications

→ Factsheet

BOC
A Linde company

Hydrogen

Specification → 99.99% minimum

Part number → 54-X (where 'X' indicates the relevant cylinder size)

Cylinder size	Cylinder contents volume (m^3)	Maximum filled pressure 15°C (bar)	Approx. dimensions incl. valve and guard where supplied (mm)	Approx. gross cylinder weight (kg)
WK	108.15	175	1290 x 1810 x 840	1500
K	7.21	175	1460 x 230	65
G20	4.98	300	660 x 320	26

Outlet connection → Please contact BOC

Key contact numbers For further product and safety information (including Safety Data Sheets)
Visit: bocgases.co.uk or bocgases.ie
Telephone: UK – 0800 111 333, Republic of Ireland – 1800 355 255 (24hr service)

BOC Limited
Customer Service Centre, Priestley Road, Worsley, Manchester M28 2UT, United Kingdom
UK Tel 0800 111 333, Fax 0800 111 555, ROI Tel 01 409 1800, Fax 01 409 1801, bocgases.co.uk, bocgases.ie

Making our world more productive

BOC/507350/NWD_Rev3/AS3/0125

8.2.3. Environmental exposure controls

Environmental exposure controls:
Refer to local regulations for restriction of emissions to the atmosphere. See section 13 for specific methods for waste gas treatment.

SECTION 9: Physical and chemical properties

9.1. Information on basic physical and chemical properties

Appearance		
Molecular mass	:	2 g/mol
Physical state	:	Gas
Form	:	Compressed gas
Colour	:	Colourless.
Odour	:	Odourless.
Odour threshold	:	Odour threshold is subjective and inadequate to warn of overexposure.
pH	:	Not applicable for gases and gas mixtures.
Relative evaporation rate (butylacetate=1)	:	No data available
Melting point	:	-259 °C
Freezing point	:	No data available
Boiling point	:	-253 °C
Flash point	:	Not applicable for gases and gas mixtures.
Critical temperature	:	-240 °C
Auto-ignition temperature	:	560 °C
Decomposition temperature	:	Not applicable.
Flammability (solid, gas)	:	Extremely flammable gas.
Vapour pressure	:	Not applicable.
Vapour pressure at 50°C	:	Not applicable.
Critical pressure	:	1293 kPa
Relative vapour density at 20°C	:	Not applicable.
Relative density	:	0.07
Density	:	Not applicable for gases and gas mixtures.
Relative gas density	:	0.07
Solubility in water	:	1.6 mg/l
Partition coefficient n-octanol/water (Log Pow)	:	Not applicable for gas mixtures.
Partition coefficient n-octanol/water (Log Kow)	:	Not applicable for inorganic products.
Viscosity, kinematic	:	No reliable data available.
Viscosity, dynamic	:	No reliable data available.
Explosive properties	:	No data available
Oxidising properties	:	No oxidising properties.
Explosive limits	:	Not known.
Lower explosive limit (LEL)	:	4 vol %
Upper explosive limit (UEL)	:	77 vol %
Particle characteristics	:	Not applicable for gases and gas mixtures. Nanoforms are not relevant for gases and gas mixtures.

9.2. Other information

Gas group	:	Compressed gas
Additional information	:	Burns with an invisible flame.

Appendix D – Measurement device specification

Measurement	Device	Manufacturer	Measurement range	Linearity/ Accuracy
Engine speed	AG 150 dynamometer	Froude Hofmann	0-8000 rpm	±1 rpm
Engine torque	AG 150 dynamometer	Froude Hofmann	0-500 Nm	±0.25% of FS
Clock Signal	EB58	Encoder Technology	0-25000 rpm	0.25 CAD
Diesel flow rate (supply)	Proline Promass 83A02	Endress+Hauser	0-20 kg/h	±0.10% of reading
Diesel flow rate (return)	Proline Promass 83A01	Endress+Hauser	0-100 kg/h	±0.10% of reading
Hythane flow rate	Proline Promass 80A02	Endress+Hauser	0-20 kg/h	±0.15% of reading
Hydrogen flow rate	Coriolis flowmeter K000000453	Alicat Scientific	0-10 kg/h	±0.20% of reading
Intake air mass flow rate	Proline T-mass 65F	Endress+Hauser	0-910 kg/h	±1.5% of reading
In-cylinder pressure	Piezoelectric pressure sensor Type 6125C	Kistler	0-30 MPa	≤ ±0.4% of FS
Intake and exhaust pressures	Piezoresistive pressure sensor Type 4049A	Kistler	0-1 MPa	≤ ±0.5% of FS
Oil pressure	Pressure transducer UNIK 5000	GE	0-1 MPa	< ±0.2% of FS
Temperature	Thermocouple K Type	RS	233-1473 K	≤ ±2.5 K
Fuel injector current signal	Current probe PR30	LEM	0-20 A	±2 mA
Smoke number	415SE	AVL	0-10 FSN	-
CO emission	MEXA-7170-DEGR (Non-Dispersive Infrared Detector)	Horiba	0-12 vol%	≤ ±1.0% of FS or ±2.0% of readings

CO_2 emission	MEXA-7170-DEGR (Non-Dispersive Infrared Detector)	Horiba	0-20 vol%	≤ ±1.0% of FS or ±2.0% of readings
THC emission	MEXA-7170-DEGR (Heated Flame Ionization Detector)	Horiba	0-500 ppm or 0-50k ppm	≤ ±1.0% of FS or ±2.0% of readings
CH_4 emission	MEXA-7170-DEGR (Non-Methane Cutter + Heated Flame Ionization Detector)	Horiba	0-0.25k ppm or 0-25k ppm	≤ ±1.0% of FS or ±2.0% of readings
NO/NOx emission	MEXA-7170-DEGR (Heated Chemiluminescence Detector)	Horiba	0-500 ppm or 0-10k ppm	≤ ±1.0% of FS or ±2.0% of readings
Hydrogen emissions	Air sens500	V&F	0-5000 ppm or 0-100%vol	0.5% of fs or 1%vol

List of references

[1] J. B. Heywood, Internal combustin engine fundamentals, McGraw-Hill, 1988.

[2] V. Kumar, D. Gupta and N. Kumar, “Hydrogen use in Internal Combustion Engine: A Review,” The International Journal of Advanced Culture Technology, 2015.

[3] T. Sandalci, O. Isin, S. Galata, Y. Karagoz and I. Guler, “Effect of hythane enrichment on performance, emission and combustion characteristics of an CI engine,” *International Journal of Hydrogen Energy,* vol. 44, pp. 3208-3220, 2019.

[4] Exxon Mobil Corporation, “Global Outlook - Energy supply,” 8 January 2024. [Online]. Available: https://corporate.exxonmobil.com/What-we-do/Energy-supply/Global-Outlook/Energy-supply?print=true#Liquids. [Accessed 5 May 2024].

[5] Exxon Mobil Corporation, “Global Outlook - Energy demand: Three drivers,” 8 January 2024. [Online]. Available: https://corporate.exxonmobil.com/what-we-do/energy-supply/global-outlook/energy-demand#Transportation. [Accessed 5 May 2024].

[6] Intergovernmental Panel on Climate Change (IPCC), “Climate Change 2023: Synthesis Report. Contribution of Working Groups I, II, and II to the Sixth Assessment Report of the Intergovernmental Panel on Climate Change,” Geneva, Switzerland, 2023.

[7] R. Lindsey, “Climate Change: Atmospheric Carbon Dioxide,” Climate.gov, 2024.

[8] H. Ritchie and M. Roser, “CO2 emissions,” Our World in Data, 2024.

[9] United Nations Framework Convention on Climate Change (UNFCCC), “Report of the Conference of the Parties serving as the meeting of the Parties to the Paris Agreement on its third session, held in Glasgow from 31 October to 13 November 2021,” Glasgow, Scotland, 2022.

[10] United Nations Framework Convention on Climate Change (UNFCCC), “Paris Agreement,” Paris, 2015.

[11] United Nations Framework Convention on Climate Change (UNFCCC), “Report of the Conference of the Parties serving as the meeting of the Parties to the Paris Agreement on its fifth session, held in the United Arab Emirates

from 30 November to 13 December 2023," Dubai, United Arab Emirates, 2024.

[12] European Comission, "The European Green Deal," Brussels, 2019.

[13] The European Parliament and the Council of the European Union, "Regulation (EU) 2021/1119," Official Journal of the European Union, 2021.

[14] Eurpoean Environment Agency, "Transport and mobility," 12 June 2024. [Online]. Available: https://www.eea.europa.eu/en/topics/in-depth/transport-and-mobility?activeTab=07e50b68-8bf2-4641-ba6b-eda1afd544be. [Accessed 8 July 2024].

[15] European Environment Agency, "Greenhouse gas emissions from transport in Europe," 23 October 2023. [Online]. Available: https://www.eea.europa.eu/en/analysis/indicators/greenhouse-gas-emissions-from-transport?activeAccordion=546a7c35-9188-4d23-94ee-005d97c26f2b. [Accessed 8 July 2024].

[16] Environmental Protection Agency, "Sources of Greenhouse Gas Emissions," 8 July 2024. [Online]. Available: https://www.epa.gov/ghgemissions/sources-greenhouse-gas-emissions. [Accessed 8 July 2024].

[17] D. Kodjak, "Policies to reduce fuel consumption, air pollution, and carbon emissions from vehicles in G20 nation," The International Council on Clean Transportation (ICCT), 2015.

[18] Y. Xie, T. Dallmann and R. Muncrief, "Heavy-duty zero-emission vehicles: Paceand opportunities for a rapid global transition," The International Council on Clean Transportation (ICCT), 24, 2022.

[19] World Health Organization, "WHO global air quality guidelines: particulate matter, ozone, nitrogen dioxide, sulfur dioxide and carbon monoxide," Bonn, Germany, 2021.

[20] European Environment Agency, "Air pollution in Europe: 2023 reporting status under the National Emission reduction Commitments Directive," 2023.

[21] Economic Commission for Europe of the United Nations (UN/ECE), "Regulation No 49 - Uniform provisions concerning the measures to be taken against the emission of gaseous and particulate pollutants from compression-ignition engines and positive-ignition engines for use in vehicles," Official Journal of the European Union, 2013.

[22] J. Dornoff and F. Rodriguez, "Euro 7: The new emission standard for light- and heavy-duty vehicles in the European Union," ICCT Policy Update, 2024.

[23] The European Parliament and the Council of the European Union, "Regulation (EC) No 595/2009," Official Journal of the European Union, 2009.

[24] The European Parliament and the Council of the European Union, “Comission Regulation (EU) No 582/2011,” Official Journal of the European Union, 2011.

[25] The European Parliament and the Council of the European Union, “Comission Regulation (EU) No 133/2014,” Official Journal of the European Union, 47, 2014.

[26] The European Parliament and the Council of the European Union, “Regulation (EU) 2024/1257,” Official Journal of the European Union, 2024.

[27] The Association for Emissions Control by Catalyst (AECC), “Heavy-Duty Vehicles,” May 2024. [Online]. Available: https://www.aecc.eu/legislation/heavy-duty-vehicles/#:~:text=The%20Euro%20VI%2DE%20entered,during%20the%20on%2Droad%20test.. [Accessed 2 July 2024].

[28] Intergovernmental Panel on Climate Change (IPCC), “Climate Change 2021: The Physical Science Basis - Working Group I Contribution to the Sixth Assessment Report of the Intergovernmental Panel on Climate Change,” 2021.

[29] Y. Shin, Y. Jung, C. P. Cho, Y. D. Pyo, J. Jang, G. Kim and T. M. Kim, “NOx abatement and N2O formation over urea-SCR systems with zeolite supported Fe and Cu catalysts in a nonroad diesel engine,” *Chemical Engineering Journal,* vol. 381, 2020.

[30] The European Parliament and the Council of the European Union, “Regulation (EU) No 2019/1242,” Official Journal of the European Union, 2019.

[31] The European Parliament and the Council of the European Union, “Regulation (EU) 2024/1610,” Official Journal of the European Union, 2024.

[32] R. D. Reitz, “Directions in internal combustion engine research,” *Combustion and Flame,* vol. 160, no. 1, pp. 1-8, 2013.

[33] R. Prasad and V. R. Bella, “A Review on Diesel Soot Emission, its Effect and Control,” *Bulletin of Chemical Reaction Engineering & Catalysis,* vol. 5, no. 2, pp. 69-86, 2010.

[34] J. B. Heywood, Internal Combustion Engine Fundamentals, Second ed., McGraw-Hill Education, 2018.

[35] A. J. Haagen-Smit, “Chemistry and Physiology of Los Angeles Smog,” *Industrial & Engineering Chemistry,* vol. 44, no. 6, pp. 1342-1346, 1952.

[36] I. A. Reşitoğlu, K. Altinişik and A. Keskin, “The pollutant emissions from diesel-engine vehicles and exhaust aftertreatment systems,” *Clean Technologies and Environmental Policy,* vol. 17, pp. 15-27, 2015.

[37] Y. Zhang, Y. Zhong, S. Lu, Z. Zhang and D. Tan, “A Comprehensive Review of the Properties, Performance, Combustion, and Emissions of the Diesel Engine Fueled with Different Generations of Biodiesel,” *MDPI,* 2022.

[38] C. W. Wu, R. H. Chen, J. Y. Pu and T. H. Lin, “The influence of air-fuel ratio on engine performance and pollutant emission of an SI engine using ethanol-gasoline-blended fuels,” *Atmospheric Environment,* vol. 38, no. 40, pp. 7093-7100, 2004.

[39] A. Faiz, C. S. Weaver and M. P. Walsh, “Air pollution from motor vehicles : standards and technologies for controlling emissions,” World Bank Group, Washington D.C., 1996.

[40] S. M. Corrêa and G. Arbilla, “Carbonyl emissions in diesel and biodiesel exhaust,” *Atmospheric Environment,* vol. 42, no. 4, pp. 769-775, 2008.

[41] W. Guan, “PhD thesis: Research of fuel injection and combustion control for maximum fuel efficiency and minimum emissions in a heavy-duty diesel engine,” Brunel University London, Uxbridge, 2019.

[42] M. Zheng, M. C. Mulenga, G. T. Reader, M. Wang, D. S.-K. Ting and J. Tjong, “Biodiesel engine performance and emissions in low temperature combustion,” *Fuel,* vol. 87, no. 6, pp. 714-722, 2008.

[43] H. Burtscher, “Physical characterization of particulate emissions from diesel engines: a review,” *Journal of Aerosol Science,* vol. 36, no. 7, pp. 896-932, 2005.

[44] M. Matti Maricq, “Chemical characterization of particulate emissions from diesel engines: A review,” *Journal of Aerosol Science,* vol. 38, no. 11, pp. 1079-1118, 2007.

[45] D. B. Kittelson, “Engines and nanoparticles: a review,” *Journal of Aerosol Science,* vol. 29, no. 5-6, pp. 575-588, 1998.

[46] Z. Han, A. Uludogan, G. Hampson and R. Reitz, “Mechanism of Soot and NOx Emission Reduction Using Multiple-injection in a Diesel Engine,” SAE Technical Paper 960633, 1996.

[47] V. Grewe, K. Dahlmann, S. Matthes and W. Steinbrencht, “Attributing ozone to NOx emissions: Implications for climate mitigation measures,” *Atmoshperic Environment,* vol. 59, pp. 102-107, 2012.

[48] S. L. Kokjohn, R. M. Hanson, D. Splitter and R. D. Reitz, “Fuel reactivity controlled compression ignition (RCCI): a pathway to controlled high-

efficiency clean combustion," *International Journal of Engine Research,* vol. 12, pp. 209-226, 2011.

[49] M. P. Musculus, P. C. Miles and L. M. Pickett, "Conceptual models for partially premixed low-temperature diesel combustion," *Progress in Energy and Combustion Science,* vol. 39, no. 2-3, pp. 246-283, 2013.

[50] M. Lewander, K. Ekholm, B. Johansson, P. Tunestak, N. Milovanovic, N. Keeler, T. Harcombe and P. Bergstrand, "Investigation of the Combustion Characteristics with Focus on Partially Premixed Combustion in a Heavy Duty Engine," *SAE Int. J. Fuels Lubr.,* vol. 1, no. 1, pp. 1063-1074, 2008.

[51] S. Imtenan, M. Varman, H. H. Masjuki, M. Kalam, H. Sajjad, M. I. Arbab and I. M. Rizwanul Fattah, "Impact of low temperature combustion attaining strategies on diesel engine emissions for diesel and biodiesels: A review," *Energy Conversion and Management,* vol. 80, pp. 329-356, 2014.

[52] U. Asad, M. Zheng, D.-K. Ting and J. Tjong, "Implementation Challenges and Solutions for Homogeneous Charge Compression Ignition Combustion in Diesel Engines," *Journal of Engineering for Gas Turbines and Power,* vol. 137, 2015.

[53] H. Bendu and S. Murugan, "Homogeneous charge compression ignition (HCCI) combustion: Mixture preparation and control strategies in diesel engines," *Renewable and Sustainable Energy Reviews,* vol. 38, 2014.

[54] S. Kook and C. Bae, "Combustion Control Using Two-Stage Diesel Fuel Injection in a Single-Cylinder PCCI Engine," SAE Technical Paper, 2004.

[55] S. Kook, C. Bae, P. C. Miles, D. Choi and L. M. Pickett, "The Influence of Charge Dilution and Injection Timing on Low-Temperature Diesel Combustion and Emissions," SAE Technical Paper, 2005.

[56] S. Kimura, O. Aoki, H. Ogawa, S. Muranaka and Y. Enomoto, "New Combustion Concept for Ultra-Clean and High-Efficiency Small DI Diesel Engines," SAE Technical Paper, 1999.

[57] R. Hasegawa and H. Yanagithara, "HCCI Combustion in DI Diesel Engine," SAE Technical Paper, 2003.

[58] G. D. Neely, S. Sasaki, Y. Huang, . J. Leet and D. W. Stewart, "New Diesel Emission Control Strategy to Meet US Tier 2 Emissions Regulations.," SAE Technical Paper, 2005.

[59] M. Sellnau, M. Foster, K. Hoyer, W. Moore, J. Sinnamon and H. Husted, "Development of a Gasoline Direct Injection Compression Ignition (GDCI) Engine," *SAE International Journal of Engines,* pp. 835-851, 2014.

[60] M. Sellnau, W. Moore, J. Sinnamon, K. Hoyer, M. Foster and H. Husted, “GDCI Multi-Cylinder Engine for High Fuel Efficiency and Low Emissions,” *SAE International Journal of Engines,* vol. 8, 2015.

[61] G. T. Kalghatgi, P. Risberg and H.-E. Ångström, “Partially Pre-Mixed Auto-Ignition of Gasoline to Attain Low Smoke and Low NOx at High Load in a Compression Ignition Engine and Comparison with a Diesel Fuel,” SAE Technical Paper, 2007.

[62] V. Manente, B. Johansson and W. Cannella, “Gasoline partially premixed combustion, the future of internal combustion engines?,” *International Journal of Engine Research,* vol. 12, p. 194.208, 2011.

[63] V. Manente, B. Johansson and P. Tunestal, “Characterization of Partially Premixed Combustion With Ethanol: EGR Sweeps, Low and Maximum Loads,” *Journal of Engineering for Gas Turbines and Power,* vol. 132, 2010.

[64] M. Shen, Yuner M and B. Johansson, “Close to Stoichiometric Partially Premixed Combustion - The Benefit of Ethanol in Comparison to Conventional Fuels,” SAE Technical Paper, 2013.

[65] D. W. Stanton, “Systematic Development of Highly Efficient and Clean Engines to Meet Future Commercial Vehicles Greenhouse Gas Regulations,” SAE Technical Paper 2013-01-2421, 2013.

[66] J. Liu, H. Wang, Z. Zheng, Z. Zou and M. Yao, “Effects of Different Turbocharging Systems on Performance in a HD Diesel Engine with Different Emission Control Technical Routes,” SAE Technical Paper 2016-01-2185, 2016.

[67] B. Mao, M. Yao, Z. Zunqing and H. Liu, “Effects of Dual Loop EGR and Variable Geometry Turbocharger on Performance and Emissions of a Diesel Engine,” SAE Technical Paper 2016-01-2340, 2016.

[68] V. Leek, K. Ekberg and L. Eriksson, “Development and Usage of a Continuously Differentiable Heavy Duty Diesel Engine Model Equipped with VGT and EGR,” SAE Technical Paper 2017-01-0611, 2017.

[69] S. Charlton, “Developing Diesel Engines to Meet Ultra-low Emission Standards,” SAE Technical Paper 2005-01-3628, 2005.

[70] M. Terada, Y. Sumida and D. Kawano, “Realization of HCCI Combustion by Internal EGR using CI Engine with Variable Valve Timing System (First Report),” SAE Technical Paper 2023-32-0021, 2023.

[71] A.-K. Jost, M. Günthner, F. Müller and A. Weigel, “Investigation of an Engine Concept for CNG-OME Dual Fuel Operation Using External and Internal EGR,” SAE Technical Paper 2022-32-0067, 2022.

[72] J. Balaji, G. M. V., L. Rao, B. Bandaru and A. Ramesh, “Modelling and Experimental Study of Internal EGR System for NOx Control on an Off-Road Diesel Engine,” SAE Technical Paper 2014-01-2645, 2014.

[73] P. A. Dittrich, F. Peter, G. Huber and M. Kuehn, “Thermodynamic Potentials of a Fully Variable Valve Actuation System for Passenger-Car Diesel Engines,” SAE Technical Paper 2010-01-119, 2010.

[74] M. Dahodwala, S. Joshi, E. W. Koehler and M. Franke, “Investigation of Diesel and CNG Combustion in a Dual Fuel Regime and as an Enabler to Achieve RCCI Combustion,” SAE Technical Paper 2014-01-1308, 2014.

[75] V. B. Pedrozo, I. May, T. D. M. Lanzanova and H. Zhao, “Potential of internal EGR and throttled operation for low load extension of ethanol–diesel dual-fuel reactivity controlled compression ignition combustion on a heavy-duty engine,” *Fuel,* vol. 175, pp. 391-405, 2016.

[76] W. Guan, H. Zhao, Z. Ban and T. Lin, “Exploring alternative combustion control strategies for low-load exhaust gas temperature management of a heavy-duty diesel engine,” *International Journal of Engine Research,* vol. 20, no. 4, pp. 381-392, 2018.

[77] T. Körfer, H. Busch, A. Kolbeck, C. Severin, T. Schnorbus and S. Honardar, “Advanced Thermal Management for Modern Diesel Engines: Optimized Synergy Between Engine Hardware and Software Intelligence,” ASME 2012 Internal Combustion Engine Division Spring Technical Conference, Torino, Italy, 2012.

[78] M. Baratta, R. Finesso, D. Misul and E. Spessa, “Comparison between Internal and External EGR Performance on a Heavy Duty Diesel Engine by Means of a Refined 1D Fluid-Dynamic Engine Model,” *SAE Int. J. Engines,* vol. 8, no. 5, pp. 1977-1992, 2015.

[79] J. Atkinson, “Gas Engine”. USA Patent 336505, 1886.

[80] J. Atkinson, “Gas Engine”. USA Patent 367496, 1887.

[81] R. Miller, “High-Pressure Supercharging System”. USA Patent 2670595, 1954.

[82] R. Miller, “High Expansion, Spark Ignited, Gas Burning, Internal Combustion Engines”. USA Patent 2773490, 1956.

[83] R. Miller, “Supercharged Engine”. USA Patent 2817322 A, 1957.

[84] S. Molina, A. García, J. Monsalve-Serrano and D. Estepa, “Miller cycle for improved efficiency, load range and emissions in a heavy-duty engine running under reactivity controlled compression ignition combustion,” *Applied Thermal Engineering,* vol. 136, pp. 161-168, 2018.

[85] J. Benajes, S. Molina, R. Novella and M. Riesco, “Improving pollutant emissions in diesel engines for heavy-duty transportation using retarded intake valve closing strategies,” *International Journal of Automotive Technology,* vol. 9, pp. 257-265, 2008.

[86] C. A. Rinaldini, E. Mattarelli and V. I. Golovitchev, “Potential of the Miller cycle on a HSDI diesel automotive engine,” *Applied Energy,* vol. 112, pp. 102-119, 2013.

[87] B. Wu, Q. Zhan, X. Yu, G. Lv, X. Nie and S. Liu, “Effects of Miller cycle and variable geometry turbocharger on combustion and emissions in steady and transient cold process,” *Applied Thermal Engineering,* vol. 118, pp. 621-629, 2017.

[88] Y. Wang, S. Zeng, J. Huang, Y. He, X. Huang, L. Lin and S. Li, “Experimental investigation of applying miller cycle to reduce NOx emission from diesel engine,” *Proceedings of the Institution of Mechanical Engineers, Part A: Journal of Power and Energy,* vol. 219, no. 8, pp. 631-638, 2005.

[89] R. Verschaeren, W. Schaepdryver, T. Serruys, M. Bastiaen, L. Vervaeke and S. Verhelst, “Experimental study of NOx reduction on a medium speed heavy duty diesel engine by the application of EGR (exhaust gas recirculation) and Miller timing,” *Energy,* vol. 76, pp. 614-621, 2014.

[90] D. Kovács and P. Eilts, “Potentials of the Miller Cycle on HD Diesel Engines Regarding Performance Increase and Reduction of Emissions,” SAE Technical Paper 2015-24-2440, 2015.

[91] W. Guan, V. Pedrozo, H. Zhao, Z. Ban and T. Lin, “Exploring the NOx Reduction Potential of Miller Cycle and EGR on a HD Diesel Engine Operating at Full Load,” SAE Technical Paper 2018-01-0243, 2018.

[92] A. Garg, M. Magee, C. Ding, L. Roberts, G. Shaver, E. Koeberlein, R. Shute, D. Koeberlein, J. McCarthy and D. Nielsen, “Fuel-efficient exhaust thermal management using cylinder throttling via intake valve closing timing modulation,” *Proceedings of the Institution of Mechanical Engineers, Part D: Journal of Automobile Engineering,* vol. 230, no. 4, p. 470–478, 2015.

[93] G. Gonca, “Investigation of the effects of steam injection on performance and NO emissions of a diesel engine running with ethanol–diesel blend,” *Energy Conversion and Management,* vol. 77, pp. 450-457, 2014.

[94] K. A. Subramanian, “A comparison of water–diesel emulsion and timed injection of water into the intake manifold of a diesel engine for simultaneous control of NO and smoke emissions,” *Energy Conversion and Management,* vol. 52, no. 2, pp. 849-857, 2011.

[95] G. P. Prabhukumar, S. Swaminathan, B. Nagalingam and K. V. Gopalakrishnan, “Water induction studies in a hydrogen-diesel dual-fuel

engine," *International Journal of Hydrogen Energy,* vol. 12, no. 3, pp. 177-186, 1987.

[96] B. Tesfa, R. Mishra, F. Gu and A. D. Ball, "Water injection effects on the performance and emission characteristics of a CI engine operating with biodiesel," *Renewable Energy,* vol. 37, no. 1, pp. 333-344, 2012.

[97] H. B. Mathur, L. M. Das and T. N. Patro, "Hydrogen-fuelled diesel engine: Performance improvement through charge dilution techniques," *International Journal of Hydrogen Energy,* vol. 18, no. 5, pp. 421-431, 1993.

[98] M. Chen and K. Schirmer, "A modelling approach to the design optimisation of catalytic converters of I. C. engines," in *Proceedings of ICEF03: 2003 fall technical conference of the ASME internal combustion engine division*, Erie, Pennsylvania, USA, 2003.

[99] T. J. Wang, S. W. Baek and J.-H. Lee, "Kinetic Parameter Estimation of a Diesel Oxidation Catalyst under Actual Vehicle Operating Conditions," *Industrial & Engineering Chemistry Research,* vol. 47, no. 8, pp. 2528-2537, 2008.

[100] B. K. Yun and M. Y. Kim, "Modeling the selective catalytic reduction of NOx by ammonia over a Vanadia-based catalyst from heavy duty diesel exhaust gases," *Applied Thermal Engineering,* vol. 50, no. 1, pp. 152-158, 2013.

[101] C. S. Sampara, E. J. Bissett, M. Chmielewski and D. Assanis, "Global Kinetics for Platinum Diesel Oxidation Catalysts," *Industrial & Engineering Chemistry Research,* vol. 46, no. 24, pp. 7993-8003, 2007.

[102] S. J. Lee, S. J. Jeong, W. S. Kim and C. B. Lee, "Computational study on the effects of volume ratio of DOC/DPF and catalyst loading on the PM and NOx emission control for heavy-duty diesel engines," *International Journal of Automotive Technology,* vol. 9, no. 6, pp. 659-670, 2008.

[103] T. Johnson, "Diesel Emissions in Review," *SAE International Journal of Engines,* vol. 4, no. 1, pp. 143-157, 2011.

[104] F. Posada, S. Chambliss and K. Blumberg, "Costs of emissions reduction technologies for heavy-duty diesel vehicles," The International Council on Clean Transportation, 2016.

[105] M. Eichelbaum, R. J. Farrauto and M. J. Castaldi, "Urea-SCR for NOx Diesel Emission Control: The influence of urea and its decomposition products on the SCR activity of zeolites," Hearth & Environmental Engineering (HKSM), New York.

[106] S. Charlton, T. Dollmeyer and T. Grana, "Meeting the US Heavy-Duty EPA 2010 Standards and Providing Increased Value for the Customer," *SAE Int. J. Commer,* vol. 3, no. 1, pp. 101-110, 2010.

[107] R. Hanson, A. Ickes and T. Wallner, “Comparison of RCCI Operation with and without EGR over the Full Operating Map of a Heavy-Duty Diesel Engine,” SAE Technical Paper 2016-01-0794, 2016.

[108] J. Benajes, A. Garcia, J. Monsalve-Serrano and V. Boronat, “Dual-Fuel Combustion for Future Clean and Efficient Compression Ignition Engines,” *Applied Sciences,* vol. 7, no. 1, 2017.

[109] M. E. J. Stettler, W. J. B. Midgley, J. J. Swanson, D. Cebon and A. M. Boies, “Greenhouse Gas and Noxious Emissions from Dual Fuel Diesel and Natural Gas Heavy Goods Vehicles,” *Environmental Science & Technology,* vol. 50, no. 4, 2016.

[110] R. D. Reitz and G. Duraisamy, “Review of high efficiency and clean reactivity controlled compression ignition (RCCI) combustion in internal combustion engines,” *Progress in Energy and Combustion Science,* vol. 46, pp. 12-71, 2015.

[111] M. Karczewski, J. Chojnowski and G. Szamrej, “A Review of Low-CO2 Emission Fuels for Dual-Fuel RCCI Engine,” *Energies,* vol. 14, 2021.

[112] K. Kuiken, “Principies; Target Global Energy Training,” in *Gas- and Dual-Fuel Engines I: for Ship Propulsion, Power Plants and Cogeneration from 0 to 100,000 kW*, Onnen, The Netherlands, 2016, p. 1–488.

[113] E. Monemian and A. Cairns, Hydrogen Fumigation on HD Diesel Engine: An Experimental and Numerical Study, IntechOpen, 2019.

[114] L. Wei and P. Geng, “A review on natural gas/diesel dual fuel combustion, emissions and performance,” *Fuel Processing Technology,* vol. 142, pp. 264-278, 2016.

[115] J. Zareei, M. Haseeb, K. Ghadamkheir, S. A. Farkhondeh, A. Yazdani and K. Ershov, “The effect of hydrogen addition to compressed natural gas on performance and emissions of a DI diesel engine by a numerical study,” *International Journal of Hydrogen Energy,* vol. 45, no. 58, pp. 34241-34253, 2020.

[116] N. R. Banapurmath, N. M. Gireesh, Y. H. Basavarajappa, R. S. Hosmath, V. S. Yaliwal, A. Pai, K. G. Navale, P. Jog and P. G. Tewari, “Effect of hydrogen addition to CNG in a biodiesel-operated dual-fuel engine,” *International Journal of Sustainable Engineering,* vol. 8, no. 6, pp. 332-340, 2015.

[117] N. R. Banapurmath, V. S. Yaliwal, R. S. Hosmath, M. R. Indudhar, S. Guluwadi and S. Bidari, “Dual fuel engines fueled with three gaseous and biodiesel fuel combinations,” *Biofuels,* vol. 9, no. 1, pp. 75-87, 2018.

[118] A. P. Singh, A. Pal and A. K. Agarwal, “Comparative particulate characteristics of hydrogen, CNG, HCNG, gasoline and diesel fueled engines,” *Fuel,* vol. 185, pp. 491-499, 2016.

[119] S. L. Kokjohn, M. P. B. Muscukus and R. D. Reitz, “Evaluating temperature and fuel stratification for heat-release rate control in a reactivity-controlled compression-ignition engine using optical diagnostics and chemical kinetics modeling,” *Combustion and Flame,* vol. 162, pp. 2729-2742, 2015.

[120] V. B. Pedrozo, X. Wang, W. Guan and H. Zhao, “The effects of natural gas composition on conventional dual-fuel and reactivity-controlled compression ignition combustion in a heavy-duty diesel engine,” *International Journal of Engine Research,* vol. 23, no. 3, pp. 397-415, 2022.

[121] M. Talibi, R. Balachandran and N. Ladommatos, “Influence of combusting methane-hydrogen mixtures on compression–ignition engine exhaust emissions and in-cylinder gas composition,” *Int J of Hydrogen Energy,* vol. 42, no. 4, pp. 2381-2396, 2017.

[122] S. Rotaru, C. Pana, N. Negurescu, A. Cernat, C. Nutu, D. Fuiorescu and G. Lazaroiu, “CNG impact on combustion quality of a diesel engine fueled in diesel-gas mode,” *Heliyon,* vol. 10, no. 15, 2024.

[123] J. Liu, X. Zhang, T. Wang, J. Zhang and H. Wang, “Experimental and numerical study of the pollution formation in a diesel/CNG dual fuel engine,” *Fuel,* vol. 159, pp. 418-429, 2015.

[124] I. May, V. P. Pedrozo, H. Zhao, A. Cairns, S. Whelan, H. Wong and P. Bennicke, “Characterization and Potential of Premixed Dual-Fuel Combustion in a Heavy Duty Natural Gas/Diesel Engine,” SAE Technical Paper 2016-01-0790, 2016.

[125] J. H. Zhou, C. S. Cheung and C. W. Leung, “Combustion, performance and emissions of a diesel engine with H2, CH4 and H2–CH4 addition,” International Journal of Hydrogen Energy 39(9):4611-4621, 2014.

[126] H. T. Arat, M. K. Baltacioglu, K. Aydin and M. Ozcanli, “Experimental investigation of using 30HCNG fuel mixture on a non-modified diesel engine operated with various diesel replacement rates,” *International Journal of Hydrogen Energy,* vol. 41, no. 4, pp. 3199-3207, 2016.

[127] M. R. A. Mansor, M. Abbood and T. I. Mohamad, “The influence of varying hydrogen-methane-diesel mixture ratio on the combustion characteristics and emissions of a direct injection diesel engine,” *Fuel,* vol. 190, pp. 281-291, 2017.

[128] L. De Simio and S. Iannaccone, “Gaseous and particle emissions in low-temperature combustion diesel–HCNG dual-fuel operation with double pilot injection,” *Applied Energy,* vol. 253, 2019.

[129] C. R. Parashuram, V. K. Shivaprasad and N. G. Kumar, “Use of Hydrogen in Internal Combustion Engines: A comprehensive Study,” Journal of Mechanical Engineering and Biomechanics, 2016.

[130] H. L. Yip, A. Srna, A. C. Y. Yuen, S. Kook, R. Taylor, G. H. Yeoh, P. Medwell and Q. N. Chan, “A Review of Hydrogen Direct Injection for Internal Combustion Engines: Towards Carbon-Free Combustion,” Applied Sciences, 2019.

[131] V. Edwin Geo, G. Nagarajan and B. Nagalingam, “Studies on dual fuel operation of rubber seed oil and its bio-diesel with hydrogen as the inducted fuel,” *International Journal of Hydrogen Energy,* vol. 33, no. 21, pp. 6357-6367, 2008.

[132] A. M. de Morais, M. A. Mendes Justino, O. S. Valente, S. d. M. Hanriot and J. R. Sodre, “Hydrogen impacts on performance and CO2 emissions from a diesel power generator,” *International Journal of Hydrogen Energy,* vol. 38, no. 16, pp. 6857-6864, 2013.

[133] H. B. Mathur, L. M. Das and T. N. Patro, “Hydrogen fuel utilization in CI engine powered end utility systems,” *International Journal of Hydrogen Energy,* vol. 17, no. 5, pp. 369-374, 1992.

[134] T. Korakianitis, A. M. Namasivayam, R. J. Crookes, S. Imran, B. Ihracska, A. Diez and N. A. Malik, “Compression-ignition engine performance and emissions in single and dual fuelling modes with sustainable fuels,” ACTA Press, 2011.

[135] T. Miyamoto, H. Hasegawa, M. Mikama, N. Kojima, H. Kabashima and Y. Urata, “Effect of hydrogen addition to intake gas on combustion and exhaust emission characteristics of a diesel engine,” *International Journal of Hydrogen Energy,* vol. 36, no. 20, pp. 13138-13149, 2011.

[136] Y. K. Wong and G. A. Karim, “A kinetic examination of the effects of the presence of some gaseous fuels and preignition reaction products with hydrogen in engines,” *International Journal of Hydrogen Energy,* vol. 24, no. 5, pp. 473-478, 1999.

[137] V. Chintala and K. A. Subramanian, “An effort to enhance hydrogen energy share in a compression ignition engine under dual-fuel mode using low temperature combustion strategies,” *Applied Energy,* vol. 146, pp. 174-183, 2015.

[138] G. A. Karim, “Combustion in gas fueled compression: Ignition engines of the dual fuel type,” *Journal of Engineering for Gas Turbines and Power,* vol. 125, no. 3, pp. 827-836, 2003.

[139] V. Chintala and K. A. Subramanian, “Experimental investigation on effect of enhanced premixed charge on combustion characteristics of a direct injection diesel engine,” *International Journal of Advances in Engineering Sciences and Applied Mathematics,* vol. 6, pp. 3-16, 2014.

[140] W. B. Santoso, R. A. Bakar and A. Nur, “Combustion Characteristics of Diesel-Hydrogen Dual Fuel Engine at Low Load,” *Energy Procedia,* vol. 32, pp. 3-10, 2013.

[141] C. Liew, H. Li, J. Nuszkowski, S. Liu, T. Gatts, R. Atkinson and N. Clark, “An experimental investigation of the combustion process of a heavy-duty diesel engine enriched with H2,” *International Journal of Hydrogen Energy,* no. 35, pp. 11357-11365, 2010.

[142] V. Chintala and K. A. Subramanian, “A comprehensive review on utilization of hydrogen in a compression ignition engine under dual fuel mode,” *Renewable and Sustainable Energy Reviews,* vol. 70, pp. 472-491, 2017.

[143] D. B. Lata, A. Misra and S. Medhekar, “Investigations on the combustion parameters of a dual fuel diesel engine with hydrogen and LPG as secondary fuels,” *International Journal of Hydrogen Energy,* vol. 36, no. 21, pp. 13808-13819, 2011.

[144] V. Chintala and K. A. Subramanian, “Assessment of maximum available work of a hydrogen fueled compression ignition engine using exergy analysis,” *Energy,* vol. 67, pp. 162-175, 2014.

[145] B. Nawaz, M. Nayer Nasim, S. K. Das, J. Landis, A. SubLaban, J. P. Trelles, D. Assanis, N. Van Dam and J. Hunter Mack, “Combustion characteristics and emissions of nitrogen oxides (NO, NO2, N2O) from spherically expanding laminar flames of ammonia–hydrogen blends,” *International Journal of Hydrogen Energy,* vol. 65, pp. 164-176, 2024.

[146] J. M. Gomes Antunes, R. Mikalsen and A. P. Roskilly, “An experimental study of a direct injection compression ignition hydrogen engine,” International Journal of Hydrogen Energy, 2009.

[147] T. Korakianitis, M. A. Namasivayam and J. R. Crookes, “Hydrogen dual-fueling of compression ignition engines with emulsified biodiesel as pilot fuel,” International Journal of Hydrogen ENergy, 2010.

[148] E. Monemian, A. Cairns, M. Gilmore and D. Newman, “Evaluation of intake charge hydrogen enrichment in a heavy-duty diesel engine,” Part D: Journal of Automobile Engineering, 2017.

[149] N. Saravanan and N. Govindan, “An experimental investigation of hydrogen-enriched air induction in a diesel engine system,” International Journal of Hydrogen Energy 33(6):1769-1775, 2008.

[150] Y. Karagoz, T. Sandalci, L. Yukset, A. S. Dalkilic and S. Wongwises, “Effects of hydrogen-diesel dual-fuel usage on pperformance, emissions and diesel combustion in diesel engines,” Adv. Mech. Eng., 2016.

[151] M. Masood, S. N. Mehdi and P. Ram Reddy, “Experimental Investigations on a Hydrogen-Diesel Dual Fuel Engine at Different Compression Ratios,” *Journal of Engineering for Gas Turbines and Power,* vol. 129, no. 2, pp. 572-578, 2007.

[152] B. J. Bora, U. K. Saha, S. Chatterjee and V. Veer, “Effect of compression ratio on performance, combustion and emission characteristics of a dual fuel diesel engine run on raw biogas,” *Energy Conversion and Management,* vol. 87, pp. 1000-1009, 2014.

[153] V. Chintala and K. A. Subramanian, “Experimental investigations on effect of different compression ratios on enhancement of maximum hydrogen energy share in a compression ignition engine under dual-fuel mode,” *Energy,* vol. 87, pp. 448-462, 2015.

[154] V. Chintala and K. A. Subramanian, “Experimental investigation of hydrogen energy share improvement in a compression ignition engine using water injection and compression ratio reduction,” *Energy Conversion and Management,* vol. 108, pp. 106-119, 2016.

[155] V. Chintala and K. A. Subramanian, “Hydrogen energy share improvement along with NOx (oxides of nitrogen) emission reduction in a hydrogen dual-fuel compression ignition engine using water injection,” *Energy Conversion and Management,* vol. 83, pp. 249-259, 2014.

[156] A. Sarvi, C.-J. Fogelholm and R. Zevenhoven, “Emissions from large-scale medium-speed diesel engines: 1. Influence of engine operation mode and turbocharger,” *Fuel Processing Technology,* vol. 89, no. 5, pp. 510-519, 2008.

[157] J. A. Schwoerer, K. Kumar, B. Ruggiero and B. Swanbon, “Lost-Motion VVA Systems for Enabling Next Generation Diesel Engine Efficiency and After-Treatment Optimization,” 2010.

[158] Y. Zhang, “Experimental investigation of CAI combustion in a two-stroke poppet valve DI engine,” 2014.

[159] N. Ladommatos and H. Zhao, Engine Combustion Instrumentation and Diagnostics, SAE International, 2001.

[160] E. Nadimi, G. Przybyła, M. T. Lewandowski and W. Adamczyk, “Effects of ammonia on combustion, emissions, and performance of the ammonia/diesel

dual-fuel compression ignition engine," *Journal of the Energy Institute,* vol. 107, 2023.

[161] F. Salek, M. Babaie, M. D. Redel-Macias, A. Ghodsi, S. V. Hosseini, A. Nourian, M. L. Burby and A. Zare, "The Effects of Port Water Injection on Spark Ignition Engine Performance and Emissions Fueled by Pure Gasoline, E5 and E10," *MDPI,* vol. 8 (10), 2020.

[162] Economic and Social Council of United Nations, "Proposal for Supplement 2 to the 07 series of amendments ti UN Regulation No. 49 (emissions of compression ignition and positive ignition (LPG and CNG) engines)," 2023.

[163] A. Wexler, "Vapor Pressure Formulation for Water in Range 0 to 100 C. A Revision.," *Journal of Research of the National Bureau of Standards Section A: Physics and Chemistry,* pp. 775-785, 1976.

[164] AVL, "AVL Smoke Meter - Product Guide," Graz, Austria, 2013.

[165] The European Parliament and the Council of the European Union, "Regulation (EC) No 1999/96/EC," Official Journal of the European Union, 1999.

[166] T. Tsujimura and Y. Suzuki, "The utilization of hydrogen in hydrogen/diesel dual fuel engine," *Int J of Hydrogen Energy,* vol. 42, no. 19, pp. 14019-14029, 2017.

[167] A. Ickes, R. Hanson and T. Wallner, "Impact of Effective Compression Ratio on Gasoline-Diesel Dual-Fuel Combustion in a Heavy-Duty Engine Using Variable Valve Actuation," 2015.

[168] J. Benajes, J. R. Serrano, S. Molina and R. Novella, "Potential of Atkinson cycle combined with EGR for pollutant control in a HD diesel engine," *Energy Conversion and Management,* vol. 50, no. 1, pp. 174-183, 2009.

[169] K. Longo, X. Wang and H. Zhao, "Comparison of conventional vs reactivity-controlled compression ignition diesel-hythane dual-fuel combustion: An investigation on engine performance and emissions at low-load," SAE Technical Paper 2023-01-1203, 2023.

[170] K. Longo, X. Wang and H. Zhao, "Impact of diesel-hythane dual-fuel combustion on engine performance and emissions in a heavy-duty engine at low-load condition," *International Journal of Engine Research,* vol. 25, no. 2, 2023.

[171] I. Smith, E. Jimenez, T. Briggs, C. Sharp, G. Bartley and J. Chiu, "Achieving Fast Catalyst Light-Off from a Heavy-Duty Stoichiometric Natural Gas Engine Capable of 0.02 g/bhp-hr NOX Emissions," SAE Technical Paper 2018-01-1136, 2018.

[172] W. Guan, V. B. Pedrozo, H. Zhao, Z. Ban and T. Lin, “Variable valve actuation-based combustion control strategies for efficiency improvement and emissions control in a heavy-duty diesel engine,” *International Journal of Engine Research,* vol. 21, no. 4, pp. 578-591, 2020.

[173] J. A. Caton, “Maximum efficiencies for internal combustion engines: Thermodynamic limitations,” *Int J Engine Res.,* vol. 19, no. 10, pp. 1005-1023, 2017.

[174] J. Liu, F. Yang, H. Wang, M. Ouyang and S. Hao, “Effects of pilot fuel quantity on the emissions characteristics of a CNG/diesel dual fuel engine with optimized pilot injection timing,” *Applied Energy,* vol. 110, pp. 201-206, 2013.

[175] D. R. Tree and K. I. Svensson, “Soot processes in compression ignition engines,” *Progress in Energy and Combustion Science,* vol. 33, no. 3, pp. 272-309, 2007.

[176] S. R. Turns, An Introduction to Combustion: Concepts and Applications, 2nd ed., McGraw-Hill Companies, 2000.

[177] N. Warwick, P. Griffiths, J. Keeble, A. Archibald and J. Pyle, “Atmospheric implications of increased Hydrogen use,” Open Government Licence, 2022.

[178] R. G. Derwent, D. S. Stevenson, S. R. Utembe, M. E. Jenkin, A. H. Khan and D. E. Shallcross, “Global modelling studies of hydrogen and its isotopomers using STOCHEM-CRI: Likely radiative forcing consequences of a future hydrogen economy,” *International Journal of Hydrogen Energy,* vol. 45, no. 15, pp. 9211-9221, 2020.

[179] R. A. Field and R. G. Derwent, “Global warming consequences of replacing natural gas with hydrogen in the domestic energy sectors of future low-carbon economies in the United Kingdom and the United States of America,” *International Journal of Hydrogen Energy,* vol. 46, no. 58, pp. 30190-30203, 2021.

[180] D. W. Stanton, “Systematic Development of Highly Efficient and Clean Engines to Meet Future Commercial Vehicle Greenhouse Gas Regulations,” *SAE Int. J. Engines,* vol. 6, no. 3, pp. 1395-1480, 2013.

[181] H. Zhao, Advanced Direct Injection Combustion Engine Technologies and Development, vol. 2. Diesel engines, Woodhead Publishing Limited, 2010.

[182] M. Schaefer, L. Hofmann, P. Girot and R. Rohe, “Investigation of NOx- and PM-reduction by a Combination of SCR-catalyst and Diesel Particulate Filter for Heavy-duty Diesel Engine,” *SAE Int. J. Fuels Lubr.,* vol. 2, no. 1, pp. 386-398, 2009.

[183] J. V. Timothy, “Diesel Emissions in Review,” *SAE Int. J. Engines,* vol. 4, no. 1, pp. 143-157, 2011.

[184] V. B. Pedrozo, I. May, W. Guan and H. Zhao, “High efficiency ethanol-diesel dual-fuel combustion: A comparison against conventional diesel combustion from low to full engine load,” *Fuel,* pp. 440-451, 2018.

[185] V. B. Perdozo, “An experimental study of ethanol-diesel dual-fuel combustion for high efficiency and clean heavy-duty engines,” 2017.

[186] N. Watson, A. Pilley and M. Marzouk, “A Combustion Correlation for Diesel Engine Simulation,” SAE Technical Paper, 1980.

[187] D. Klos, D. Janecek and S. Kokjohn, “Investigation of the Combustion Instability-NOx Tradeoff in a Dual Fuel Reactivity Controlled Compression Ignition (RCCI) Engine,” *SAE International Journal of Engines,* vol. 8, pp. 821-830, 2015.

[188] R. Stone, Introduction to Internal Combustion Engines, 4th ed., Palgrave Macmillan, 2012.

[189] J. A. Caton, “Combustion phasing for maximum efficiency for conventional and high efficiency engines,” *Energy Conversion and Management,* vol. 77, pp. 564-576, 2014.

[190] H. Zhao, HCCI and CAI engines for automotive industry, Elsevier, 2007.

[191] V. Y. Prikhodko, S. J. Curran, J. E. Parks and R. M. Wagner, “Effectiveness of Diesel Oxidation Catalyst in Reducing HC and CO Emissions from Reactivity Controlled Compression Ignition,” *SAE International Journal of Fuels and Lubricants,* vol. 6, 2013.

[192] U. Asad and M. Zheng, “Exhaust gas recirculation for advanced diesel combustion cycles,” *Applied Energy,* vol. 123, pp. 242-252, 2014.

[193] S. Ramachandran and U. Stimming, “Well to wheel analysis of low carbon alternatives for road traffic,” *Energy & Environmental Science,* vol. 8, no. 11, pp. 3313-3324, 2015.

[194] J. Savage and G. Esposito, “Hydrogen Vehicle Well-to-Wheel GHG and Energy Study,” Zemo Partnership, London, 2021.

[195] M. Prussi, M. Yugo, L. De Prada, M. Padella and Edwards, “JEC Well-To-Wheels report v5. EUR 30284 EN,” Publications Office of the European Union, Luxembourg, 2020.

[196] D. A. Splitter and R. D. Reitz, “Fuel reactivity effects on the efficiency and operational window of dual-fuel compression ignition engines,” *Fuel,* vol. 118, 2014.

[197] K. S. Varde and G. A. Frame, “Hydrogen aspiration in a direct injection type diesel engine-its effects on smoke and other engine performance

parameters," *International Journal of Hydrogen Energy,* vol. 8, no. 7, pp. 549-555, 1983.

[198] S. Arrhenius, "On the reaction velocity in the inversion of cane sugar by acids," *Journal of Physical Chemistry,* vol. 4, no. 1, pp. 226-248, 1889.

[199] V. S. Yadav, S. L. Soni and D. Sharma, "Engine performance of optimized hydrogen-fueled direct injection engine," *Energy,* vol. 65, pp. 116-122, 2014.

[200] Y. Shi and R. D. Reitz, "Optimization study of the effects of bowl geometry, spray targeting, and swirl ratio for a heavy-duty diesel engine operated at low and high load," *International Journal of Engine Research,* vol. 9, no. 4, pp. 325-346, 2008.

[201] S. Kook, C. Bae, P. C. Miles, D. Choi, M. Bergin and R. D. Reitz, "The Effect of Swirl Ratio and Fuel Injection Parameters on CO Emission and Fuel Conversion Efficiency for High-Dilution, Low-Temperature Combustion in an Automotive Diesel Engine," SAE Technical Paper 2006-01-0197, 2006.

[202] G. Esposito, J. McGeachie, C. Cluzel, S. Baltac, W. Nock, O. Robinson and W. Drake, "Executive Summary: Low Carbon Hydrogen Well-to-Tank Pathways Study," Zemo Partnership, London, 2021.

[203] H. B. Mathur, L. M. Das and T. N. Patro, "Hydrogen fuel utilization in CI engine powered end utility systems," *International Journal of Hydrogen Energy,* vol. 17, no. 5, pp. 369-374, 1992.